Elemental Fluxes to the Seafloor: Pleistocene Climate and Submarine Hydrothermal Activity

Elemental Fluxes to the Seafloor:

Pleistocene Climate and Submarine Hydrothermal Activity

A dissertation presented

by

Jennifer L. Middleton

to

The Department of Earth and Planetary Sciences

in partial fulfillment of the requirements

for the degree of

Doctor of Philosophy

in the subject of

Earth and Planetary Sciences

Harvard University

Cambridge, Massachusetts

October 2017

Dissertation Advisors:
Professor Sujoy Mukhopadhyay
Professor Charles H. Langmuir

Jennifer L. Middleton

Elemental Fluxes to the Seafloor:

Pleistocene Climate and Submarine Hydrothermal Activity

Abstract

Marine sedimentary records of major and trace element deposition provide a means to examine the temporal variability and interactions between a wide variety of Earth processes, including fluctuations in atmospheric and oceanographic circulation as well as variations in the hydrothermal fluid output of mid-ocean ridges. The extensive advance and retreat of continental ice sheets during Pleistocene glacial-interglacial cycles drives variations in sea level on the order of a hundred meters that may provide a sufficient forcing pressure to modulate the degree of submarine hydrothermal circulation. This work presents new records of hydrothermal flux variability from the Mid-Atlantic Ridge and the Juan de Fuca Ridge that span the past 50,000 years and 600,000 years, respectively, to provide observational constraints with which to examine the potential relationship between glacially-driven sea level changes and submarine hydrothermal activity.

Hydrothermal iron fluxes recorded in sediments from both the Mid-Atlantic Ridge and the Juan de Fuca Ridge suggest two to eight-fold variability in the elemental output of hydrothermal systems on timescales ranging from thousands to hundreds of thousands of years. If representative of a global trend, as the limited suite of exiting studies suggest, variations in

dissolved hydrothermal iron flux from mid-ocean ridges to the deep ocean over glacial timescales may introduce significant levels of variability into the global biogeochemical cycling of iron.

The generation of long-term hydrothermal flux records from marine sediment cores provides an opportunity to investigate additional sources of variability in elemental fluxes to the seafloor and examine the climatic signal deposited in such records. Accordingly, this work presents new records of wind-blown dust deposition to the Mid-Atlantic spanning the past 70,000 years. The Mid-Atlantic dust flux data suggest that millennial-scale changes in wind-strength and continental aridity generate higher levels of North African dust emissions than are observed during orbital-scale climate extremes, such as the Last Glacial Maximum or Marine Isotope Stage 4.

The hydrothermal records examined in this work suggest that the potential relationship between sea level changes and submarine hydrothermal activity are likely to be complex. Nonetheless, significant correlations are observed between hydrothermal iron fluxes and sea level over multiple glacial cycles on the Juan de Fuca Ridge. The results of this work encourage continued investigation into the proposed relationship between Pleistocene sea level variability and submarine hydrothermal circulation.

Table of Contents

List of Figures

Chapter 4: Constant flux proxy comparison and a 600 ka record of hydrothermal flux variability on the Cleft Segment of the Juan de Fuca Ridge

Appendix A: Supplemental material for Chapter 1

Appendix C: Supplemental material for Chapter 3

List of Tables

Acknowledgements

I would like to thank my co-advisors, Sujoy Mukhopadhyay and Charles Langmuir, as well as the additional members of my thesis committee, Jerry Mitrovica and Peter Huybers, for their guidance, support, and feedback throughout my graduate career. I thank Charles Langmuir particularly for fostering my interests in mid-ocean ridges and introducing me to the joys of collecting samples at sea. I am especially grateful for the thoughtful mentorship of Sujoy Mukhopadhyay, who has been inspiring, patient, and encouraging ever since I first joined his lab as an undergraduate, even (and especially) when things did not go according to plan.

I additionally thank the many individuals and institutions who helped contribute to my scientific development and the logistical execution of my graduate research. Specifically, this includes my sedimentary collaborators Jerry McManus, Kassandra Costa, Gisela Winckler, and the rest of the SeaVOICE team, for many stimulating discussions; Robert Ackert, Seth Campbell, and Jen Erxleben for sharing their knowledge and enthusiasm for Antarctic research and for keeping me cool on the ice; Robert Ackert and Zhongxing Chen for extensive technical support, as well as Ariana Saxby, Alex Tyra, Zachary Mason, Francisco Apen, and Marcelle D'Almeida for their assistance in sample preparation. I have also benefitted tremendously from the comradery of the additional members of the Harvard/UC Davis Noble Gas Laboratories and the Langmuir Group at Harvard, including Rita Parai, Jonathan Tucker, Curtis Williams, Maria Pető, Atreyee Battacharya, Michael Huh, Cole Bishop, Stephen Turner, and Jocelyn Fuentes. This work could not have been completed without the generous support of the students, faculty, and staff of the Harvard Department of Earth and Planetary Sciences, or the generous hospitality of the

Department of Earth and Planetary Sciences at the University of California Davis. This work was funded by the National Science Foundation and its Graduate Research Fellowship Program.

Finally, I am grateful to the those who have provided great moral support over the years, including the numerous friends who have graciously lent their shoulders to lean on and couches to sleep on, as well as my family, Martin Middleton, Jim Middleton, and Lynne Wilcox, who have graciously indulged my enthusiasm for geoscience since the beginning.

Chapter 0

Introduction

Elemental fluxes to the seafloor are governed by variations in the deposition of lithogenic, biogenic, and hydrothermal material, among others. Consequently, temporal records of marine sedimentary fluxes inform our understanding of many aspects of the climate system, including continental dust emissions, continental aridity, atmospheric transport, nutrient cycling, and biologic productivity. In addition, marine sedimentary records of hydrothermal flux variability provide a means to evaluate the proposed connection between glacially-driven changes in sea level and submarine hydrothermal circulation. Thus, elemental fluxes to the seafloor provide valuable insights into both the climate system itself and into feedbacks and interactions between the climate system and the Solid Earth. The chapters in this thesis, summarized below, present new records of major and trace element flux variability in sediments from both the Atlantic and the Pacific and examine their implications for Pleistocene climate and its effects on submarine hydrothermal activity.

Chapter 1 presents new records of hydrothermal Fe and Cu fluxes over the past 50,000 years in a sediment core from the Mir zone hydrothermal area of the TAG segment of the Mid-Atlantic Ridge. The Mir records exhibit 6 to 8-fold increases in hydrothermal deposition coincident with the Last Glacial Maximum and a sharp decrease in hydrothermal deposition coincident with the onset of major deglaciation. The timing of increased hydrothermal output recorded in the Mir sediments is consistent with hydrothermal records from the Galapagos Microplate, the East Pacific Rise, and elsewhere on the Mid-Atlantic Ridge, and is interpreted to reflect the influence

of rapid sea level changes on submarine hydrothermal activity. This chapter further explores the biogeochemical implications of a globally synchronous hydrothermal response to glacially-driven changes in sea level. Proposed variations in the total dissolved hydrothermal Fe flux from mid-ocean ridges into oceans are estimated to rival the glacial-interglacial variations in dissolved Fe flux associated with wind-blow dust and consequently provide a significant fertilization effect for the marine biological carbon pump. Thus, the results of this chapter suggest that climate variability can affect solid-Earth processes and subsequently stimulate additional feedbacks within the carbon cycle on timescales of ~1000 to 10000's of years.

Chapter 2 presents additional records of major and trace element fluxes to the Mir zone hydrothermal sediments and compares Mir zone patterns of elemental deposition with those observed over the past 70,000 years in a sediment core recovered from the Broken Spur segment of the Mid-Atlantic Ridge. This chapter focuses on the sedimentary fluxes of P, V, Fe, Zn, Cu, Pb, and U at both study sites in an in-depth exploration of the compositional variability in hydrothermal deposition on the Mid-Atlantic Ridge. Elemental flux records are complemented by new high-resolution concentration data for Fe, Ti, and Cu, that allow for examination of millennial-scale changes in hydrothermal deposition. Weak evidence of significant hydrothermal deposition to the Broken Spur sediments is interpreted to result from bathymetric shielding of the study site from the local hydrothermal plume and suggests that the occurrence of megaplumes, as have been observed on the Juan de Fuca Ridge, is rare along the Broken Spur segment. Where previous analyses of the Mir zone sediments resolved a broad glacial peak in hydrothermal deposition, the high-resolution data presented here reveal two distinct intervals of intense hydrothermal activity between 15,000 and 30,000 years ago. A revised interpretation of the Mir

zone hydrothermal record suggests that the relationship between sea level changes and submarine hydrothermal at this location may be more complicated than previously observed.

Chapter 3 explores the signal of dust deposition to the subtropical Atlantic over the past 70,000 years using the flux patterns of terrigenous ^{4}He, Th, and Ti measured in the Mid-Atlantic Ridge sediment cores analyzed in Chapters 2 and 3. The new dust data provide exciting new constraints on North African dust delivery to the Atlantic, where long-term dust flux records determined using constant flux proxies were previously limited to the past 20,000 and represented sparse spatial coverage. Similarities in the patterns of dust deposition observed in the Mid-Atlantic records compared with those from the Northwest African continental margin support previous interpretations of dust flux variability from the Last Glacial Maximum through the Holocene and highlight the ability of the Mid-Atlantic records to capture millennial-scale changes in dust deposition. Despite average sedimentation rates of less than 2 cm per 1000 years at the Mid-Atlantic study sites, biologic mixing of the sedimentary column does not appear to overly obscure interpretations of millennial-scale dust flux variability. The dust flux records presented in this chapter reveal clear peaks in dust deposition coincident with millennial-scale North Atlantic cold periods such as the Younger Dryas and multiple Heinrich Stadial Events. Further, the Mid-Atlantic dust flux suggest that the highest rates of North African dust emissions occur during these millennial-scale events, rather than during orbital-scale climate extremes such as the Last Glacial Maximum or Marine Isotope Stage 4. Comparison of the new 70,000 year Atlantic dust flux record with previous studies of North African aridity supports the hypothesis that dust emissions are governed by variable wind strength and continental aridity over changing climatic conditions.

Chapter 4 shifts discussion to the Northeast Pacific and presents new records of extraterrestrial ^{3}He-derived vertical sediment rain rates extending over 600,000 years ago as determined in two sediment cores from the Cleft Segment of the Juan de Fuca Ridge. Comparison of the sedimentary fluxes derived using extraterrestrial ^{3}He and those previously derived using excess ^{230}Th over the past 440,000 years demonstrate good agreement between these two constant flux proxies over glacial-interglacial timescales. On suborbital timescales, fluxes calculated using extraterrestrial ^{3}He exhibit high frequency variability that is not observed in the flux records constrained by excess ^{230}Th. This difference in constant flux proxy behavior may reflect a distinct advantage of one system over the other at suborbital timescales and motivates additional investigation in order to determine the most appropriate methods to evaluate millennial-scale depositional variability in future studies. The extraterrestrial ^{3}He-derived records are combined with previous determinations of hydrothermal Fe and Cu concentrations to extend constraints on hydrothermal fluxes to the Cleft Segment sediments beyond the 500,000 year temporal limit of the excess ^{230}Th constant flux proxy. Finally, the hydrothermal records of the Cleft Segment sediments are used to examine the proposed relationship between sea level changes and hydrothermal activity on the intermediate-spreading Juan de Fuca Ridge. Statistical comparison of Cleft Segment hydrothermal Fe and Cu fluxes with a global proxy record of sea level variability do not find a simple and consistent relationship between hydrothermal deposition and sea level change, however positive correlations are observed between rising seas and increasing hydrothermal Fe deposition over the past 250 ka. The Cleft Segment hydrothermal records encourage further investigation into the proposed relationship between sea level variability and submarine hydrothermal activity.

Chapter 1

Hydrothermal iron flux variability following rapid sea level changes

The contents of this chapter have been published as:

Middleton, J.L., Langmuir, C.H., Mukhopadhyay, S., McManus, J.F., Mitrovica, J.X., 2016. Hydrothermal iron flux variability following rapid sea level changes. Geophysical Research Letters, 43, doi:10.1002/2016GL068408.

Abstract

Sea-level changes associated with Pleistocene glacial cycles have been hypothesized to modulate melt production and hydrothermal activity at ocean ridges, yet little is known about fluctuations in hydrothermal circulation on timescales longer than a few millennia. We present a high resolution record of hydrothermal activity over the past 50 ka using elemental flux data from a new sediment core from the Mir zone of the TAG hydrothermal field at 26°N on the Mid-Atlantic Ridge. Mir sediments reveal 6 to 8-fold increases in hydrothermal iron and copper deposition during the Last Glacial Maximum, followed by a rapid decline during the sea-level rise associated with deglaciation. Our results, along with previous observations from Pacific and Atlantic spreading centers, indicate that rapid sea-level changes influence hydrothermal output on mid-ocean ridges. Thus, climate variability may discretize volcanic processing of the solid-Earth on millennial timescales and subsequently stimulate variability in biogeochemical interactions with volcanic systems.

1.1. Introduction

Recent studies propose that pressure changes due to rapid sea-level fluctuations associated with Pleistocene glacial cycles may influence submarine volcanic activity, with falling sea-level driving increased melt production (Huybers and Langmuir, 2009; Lund and Asimow, 2011; Crowley et al., 2015). Glacially driven changes in submarine volcanism might generate variations in crustal thickness associated with abyssal hills (Huybers and Langmuir, 2009; Crowley et al., 2015; Tolstoy, 2015) and may induce global variations in both magmatic CO_2 emissions (Burley and Katz, 2015) and hydrothermal element fluxes across glacial-interglacial cycles (Lund and Asimow, 2011). Hydrothermal circulation provides a deep source of dissolved Fe and other metals to the global oceans (Conway and John, 2014; Fitzsimmons et al., 2014; Resing et al., 2015). If rapid sea-level changes modulate hydrothermal activity, then the global hydrothermal iron flux to nutrient-limited surface waters, and resulting carbon export (e.g., Tagliabue et al., 2010), may vary substantially across glacial cycles.

Near-vent sediment cores containing hydrothermal plume precipitates provide continuous, spatially integrated, and datable records to examine the long term behavior of hydrothermal vent systems (e.g., Frank et al., 1994; Cherkashev, 1995; Auffret et al., 1996; German et al., 1997; Cave et al., 2002). Few published studies, however, contain the appropriate temporal resolution over a sufficiently long time interval to capture hydrothermal changes across a glacial interval. This work examines a new sediment core from the relict Mir hydrothermal zone neighboring the TAG hydrothermal field at 26°N on the Mid-Atlantic Ridge (e.g., Rona et al., 1993) to provide such a record of hydrothermal activity for the last 50 ka. The new high resolution record of Mir

zone hydrothermal activity is then used to examine millennial-scale climatic forcing of hydrothermal venting and its implications for hydrothermal Fe fertilization across the Last Glacial Maximum (LGM).

1.2. Sampling and Methods

Gravity core KN207-2-GGC3 (26.14°N, 44.80°W, 3433 m water depth, 82 cm core length) was collected proximal to the relict Mir zone in the axial valley of the Mid-Atlantic Ridge, with the aim of investigating temporal variations in hydrothermal activity, during cruise KN207-2 of the *R/V Knorr* in June 2012 (Figure 1.1). GGC3 sediments are typically carbonaceous oozes, with carbonate content ranging from 70 to 90 wt.% (Table A1). Small basalt fragments (<255 μm) are sparsely scattered throughout the core. The full core length was sampled in continuous 1 to 2 cm intervals and reported measurements reflect the average value over the time-depth interval sampled.

Hydrothermal deposition to the Mir zone was constrained using Fe, Cu, Ti and Th concentrations, obtained using solution nebulized inductively coupled mass spectrometry (ICP-MS; Table A1), and helium isotope analyses (Table A2, Table A3). Sediment chronology was determined from benthic foraminiferal oxygen isotope ($\delta^{18}O$) stratigraphy measured in *C. wuellerstorfi* (Table A4), with absolute age control from radiocarbon measurements of the planktonic foraminifer *G. ruber* (Table A5).

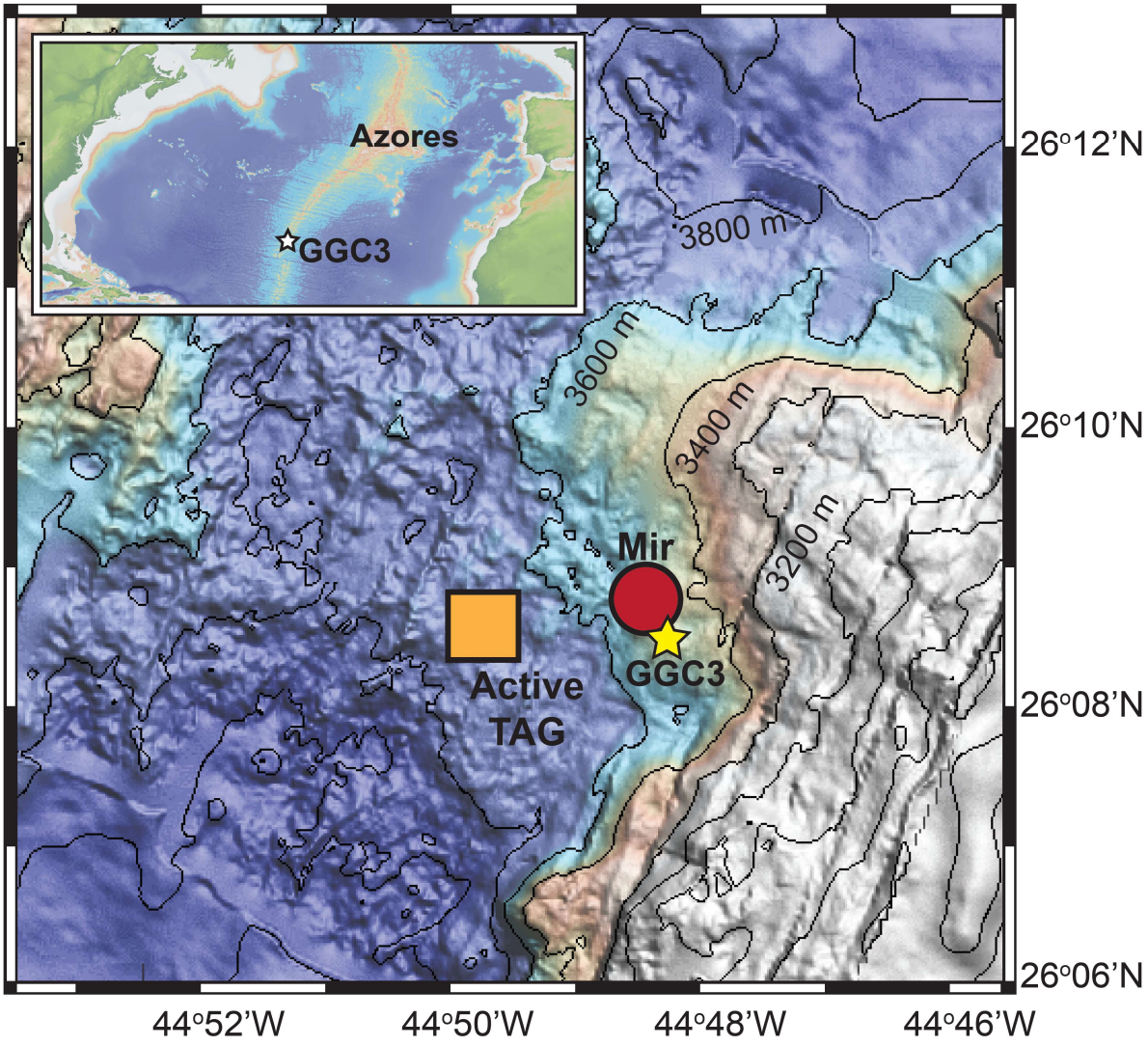

Figure 1.1. Sediment core location on the Mid-Atlantic Ridge. Gravity core KN207-2-GGC3 (yellow star), the Mir hydrothermal zone (red circle), and the active TAG mound (orange square) within the TAG hydrothermal vent field at 26°N on the Mid-Atlantic Ridge. Contours are shown at 200 m depth intervals. Inset shows location of GGC3 within the broader context of the Northern Mid-Atlantic Ridge.

1.2.1. Elemental Flux Determination

Fe, Cu, Ti, and Th concentrations were measured using solution nebulized ICP-MS analyses on a Thermo X series quadrupole at Harvard University (e.g., Gale et al., 2011) (Table A1). ICP-MS

analyses were performed separately for the carbonate and carbonate-free components of each sample. Initial ICP-MS sample aliquots varied from ~70 to 200 mg in order that the carbonate-free component had a dry mass of ~25 mg. Carbonate components were isolated from bulk sediments using a 24 hr leach in 10% acetic acid at 25°C. Some fraction of hydrothermal Fe and Cu may have dissolved during the acetic acid leach and may be detectable within the carbonate leachate composition rather than the carbonate-free sediment composition (Table A1). To reduce uncertainties associated with this possible fractionation, reported elemental concentrations and fluxes refer to the bulk sediment composition and thus account for both the acetic acid leachate and carbonate-free sediment compositions. Carbonate-free sediments were further digested over several days in a mixture of 0.8 mL of 48% hydrofluoric acid (HF) and 2 mL of 8N nitric acid (HNO_3) at ~150°C. Once dissolved, the carbonate-free sediments were evaporated at ~100°C and dissolved again with 2.5 mL of 8N HNO_3, twice, to eliminate residual HF. All acids used in ICP-MS sample preparation were ultrapure grade and double distilled to avoid trace element contamination. Prior to analysis, the acetic acid leachate and the dissolved carbonate-free sediments were each diluted 1:5000 with an internal standard solution of 0.2N HNO_3 spiked with Ge (10 ppb), Rh (5 ppb), In (5 ppb), Tm (5 ppb), and Bi (5 ppb). ICP-MS sensitivity to the internal standard elements was used to correct for instrumental drift. Elemental concentrations were calculated from ICP-MS results using calibration curves determined from the standards BCR-2, BHVO-2, DNC-1, W-2, and JB-2 (each digested following the procedure for carbonate-free sediments and analyzed in the same instrumental runs as the sediment samples). Aliquots of the in-house standard K1919 were analyzed between every three samples. 1σ uncertainties in elemental concentrations were calculated from inter-run reproducibility of K1919 and were 0.1 wt.%, 0.5 wt.%, 4 ppm, and 0.1 ppm for Fe, Ti, Cu, and Th, respectively.

Elemental fluxes were calculated by multiplying concentration values with sediment rain rates derived using extraterrestrial ^{3}He [$^3He_{ET}$] as a constant flux proxy (e.g., Marcantonio et al., 2001; McGee and Mukhopadhyay, 2013). The term 'rain rate' describes the vertical sediment flux as distinct from the total mass accumulation rate that includes laterally advected material. $^3He_{ET}$ accumulates in marine sediments via the delivery of interplanetary dust particles (IDPs) bearing high $^3He/^4He$ ratios from implanted solar wind. While IDPs dominate the ^{3}He component of deep-sea sediments, terrigenous dust dominates that of ^{4}He (Patterson et al., 1999). The 5 orders of magnitude difference in $^3He/^4He$ ratios between IDPs (~170 R_A, where R_A is the ratio normalized to the atmospheric $^3He/^4He$ ratio of 1.39×10^{-6}) and terrigenous materials (~0.01 R_A) allows for the determination of both $^3He_{ET}$ and terrigenous ^{4}He ($^4He_{terr}$) concentrations in marine sediments under the assumption of two-component mixing (McGee and Mukhopadhyay, 2013) (see Appendix A).

Sediment concentrations of $^3He_{ET}$ are controlled by both the IDP $^3He_{ET}$ flux from space (f) and the sediment rain rate (Φ) through the relationship [3HeET] = fR /Φ, where R is the fraction of He retained within the sediments (McGee and Mukhopadhyay, 2013). $^3He_{ET}$ retention in ~480 Ma limestone deposits suggests that variations in R over relatively short geologic intervals are negligible (Patterson et al., 1998). Thus, when the IDP $^3He_{ET}$ flux is known, [$^3He_{ET}$] can be inverted to compute sediment rain rates independent of age-model tie points. Previous work has demonstrated a constant Quaternary IDP $^3He_{ET}$ flux (Higgins, 2001; Marcantonio et al., 2001; Winckler and Fischer, 2006) and a value of $7.7 \pm 1.7 \times 10^{-13}$ cm^3 STP cm^{-2} ka^{-1} (Higgins, 2001) was used here.

Natural variability in the distribution of rare, helium-rich IDPs within marine sediments can generate uncertainties when using limited sample sizes to determine representative sediment [$^3He_{ET}$]. Such uncertainties are a function of the area-time product of the sediment aliquots analyzed, determined by dividing the sample mass (in g) by the mass accumulation rate (in g m^{-2} a^{-1}), and are reduced by increasing sample masses and analyzing replicate samples (Farley et al., 1997). A typical area-time product of 0.25 m^2a yields a 1σ uncertainty in sediment [$^3He_{ET}$] of ~20%, much larger than the 1-2% analytical uncertainties for each sample (Farley et al., 1997; Patterson and Farley, 1998). In contrast, sediment concentrations of terrigenous ^4He are well constrained, with 1σ values reflecting the analytical uncertainties of 1-2% (Table A2).

Sample aliquots of 1.5 g and the bulk sedimentation rates of GGC3 sediments lead to an area-time product of 0.15 m^2a. To constrain the $^3He_{ET}$ uncertainties associated with such an area-time product, replicate helium analyses were performed on 108 samples from GGC3 and an additional Mid-Atlantic core, KN207-2-GGC6 (29.21°N, 43.23°W, 3018 m water depth), with a similar mass accumulation rate (Table A2). A Gaussian fit to the distribution of fractional difference in measured [$^3He_{ET}$] within the replicated sample population yields estimated 1σ uncertainties of 28% for single analyses of sediment [$^3He_{ET}$]. Applying the 28% uncertainty to the average [$^3He_{ET}$] of the replicated sample population yields a 1σ uncertainty of 0.66 pcc STP $^3He_{ET}$ g^{-1}.

The 28% 1σ uncertainty in sediment [$^3He_{ET}$] is reduced for replicated samples by $n^{-1/2}$, where n is the number of replicated analyses for a given sample. To further reduce uncertainties associating with sampling rare He-rich particles, sediment fluxes reported in the main text represent a 3-

point running mean through the $^3He_{ET}$-derived sediment rain rates. Propagation of additional uncertainties in the IDP $^3He_{ET}$ flux from space ($7.7 \pm 1.7 \times 10^{-13}$ cm^3 STP cm^{-2} ka^{-1}; Higgins, 2001) leads to typical 1σ values for $^3He_{ET}$-derived sediment rain rates of 30% for each sampled depth and 18% for the 3-point running mean.

Computation of $^3He_{ET}$ concentrations requires negligible helium contributions from mantle sources ($^3He/^4He \sim 8$ R_A for average mid-ocean ridge basalts (MORB); Graham, 2002) such as gas-bearing basalt fragments or vent fluid-bearing sulfides. Mantle-like $^3He/^4He$ ratios have been observed in near-vent deposits (Jean-Baptiste and Fouquet, 1996; Stuart et al., 1994), but there is no correlation between high concentrations of hydrothermal Fe and $^3He_{ET}$ (Figure A1) in the GGC3 sediment core.

Some basalt fragments occur in GGC3 sediments and the upper limit of MORB ^3He contamination from these fragments was constrained as follows. Basalt fractions (f_{basalt}) in the carbonate-free sediments were calculated using Mg/Rb ratios assuming a two component mixture of MORB (Mg/Rb = 2.54 wt.%/ppm; Gale et al., 2013; Table A1) and a hypothetical zero-Mg endmember. Resulting f_{basalt} values range from 1 to 3%. Calculations of f_{basalt} made using the MORB Mg/Th ratio of 18.7 (Gale et al., 2013) also ranged from 1 to 3%. These values overestimate basalt concentrations within He analyzed aliquots as non-basalt sediment is not completely Mg-free and ICP aliquots were not sieved at the 64 μm level, which systematically removed coarse basalt chips relative to the finer terrigenous sediments.

Representative He concentrations and isotope ratios for the fine basalt fragments were determined from the average values of 3 MORB glass samples (KN207-2 D4-1, D42-4, and D57-1; Table A3) dredged from the TAG and Broken Spur segments of the Mid-Atlantic Ridge on the same cruise as the GGC3 and GGC6 sediment core retrievals. Sample D42-4 is known to be gas rich due to its popping behavior when recovered from the seafloor. MORB samples were crushed and sieved to the <200 μm level and He was extracted by heating under vacuum at 1285°C following the same procedure as the sediment samples (yielding a $^3He/^4He$ ratio of 8.19 R_A and a $^3He_{MORB}$ concentration of 2.85 x 10^{-11} cc STP g_{basalt}^{-1}).

$^3He_{ET}$ concentrations were then recalculated, using the same two component assumption as above, after subtracting maximum $^3He_{MORB}$ and $^4He_{MORB}$ contributions proscribed for each sample based on the Mg/Rb-derived f_{basalt} values. Resulting basalt-corrected $^3He_{ET}$ concentrations were only 1 to 7% lower than original $^3He_{ET}$ estimates. Thus, the fractional $^3He_{ET}$ correction due to basalt contamination is lower than natural uncertainty of the uncorrected $^3He_{ET}$ measurements and does not affect interpretation of $^3He_{ET}$-derived sediment rain rates. We conclude that a two-component mixture of IDP and terrigenous helium remains a valid assumption for the GGC3 sediment core.

Helium concentrations and isotope ratios were measured in the <64 μm fraction of initial 1.5 g aliquots of dry bulk sediment. The He aliquots were sieved to provide material for $\delta^{18}O$ and radiocarbon measurements and to reduce possible contamination from mid-ocean ridge basalt glass (see Appendix A). Sieving does not affect determination of sediment $^3He_{ET}$ because >80%, and possibly >95%, of $^3He_{ET}$-bearing particles reside within the <64 μm sediment fraction

(Mukhopadhyay and Farley, 2006; Brook et al., 2009; Torfstein, 2012). Samples were decarbonated using 10% acetic acid, rinsed three times with distilled water, frozen with liquid nitrogen, wrapped in tin foil, and dried for 4 hours at 100°C prior to loading into the gas extraction line of the Harvard Noble Gas Laboratory. Sediment helium was extracted under vacuum at 1285°C and measured in a Nu Noblesse mass spectrometer under established protocols (Mukhopadhyay and Kreycik, 2008).

Concentrations of $^3He_{ET}$ and $^4He_{terr}$ were calculated assuming a two component mixture of 170 R_A IDP helium ($(^3He/^4He)_{ET}$; Nier and Schlutter, 1992) and a typical 0.01 R_A terrigenous source ($(^3He/^4He)_{terr}$; Farley and Patterson, 1995) using the following relationship:

$$^3He_{ET} = {}^3He_{msr}\left(\frac{1-\frac{(^3He/^4He)_{terr}}{(^3He/^4He)_{msr}}}{1-\frac{(^3He/^4He)_{terr}}{(^3He/^4He)_{ET}}}\right)$$

where *msr* denotes the measured sample value (Tables A2, A3; Figure A1). 1σ uncertainties in sediment concentrations of $^3He_{ET}$ and $^4He_{terr}$ were 28% and 1-2%, respectively, and were determined from 108 replicated sample analyses (see Appendix A).

1.2.2. Sediment Chronology

Benthic $\delta^{18}O$ measurements were collected on a dual-inlet Thermo Delta V+ mass spectrometer at the Lamont-Doherty Earth Observatory of Columbia University. Whole *C. wuellerstorfi* tests were sonicated in distilled H_2O prior to analysis. Approximately 50 to 90 µg allotments of *C. wuellerstorfi* were dissolved in ~105% phosphoric acid (H_3PO_4) in a KIEL IV device. The resulting CO_2 gas was then purified and analyzed. The NBS-19 international standard was

analyzed every ~10 samples. The long-term standard deviation for $\delta^{18}O$ of NBS-19 measured on this instrument is 0.06 ‰. The average difference in $\delta^{18}O$ between replicated samples was 0.24 ‰ (Table A4).

Radiocarbon measurements were conducted at the National Ocean Sciences Accelerator Mass Spectrometry (NOSAMS) Facility at the Woods Hole Oceanographic Institution (Table A5). Whole *G. ruber* tests were sonicated for 30 seconds in ethanol, followed by >1 min of sonication in distilled H_2O prior to submission to the NOSAMS facility to reduce sedimentary contamination. NOSAMS radiocarbon sample ages were corrected for a 400 year North Atlantic surface ocean reservoir age (Bard, 1988). Sediment core age models were then calculated between radiocarbon dated depths assuming constant sedimentation rates between tie-points. One radiocarbon sample (GGC3: 64-66 cm) yielded an age >35 ka and was not included in age model calculations. Ages for sediment core depths lower than the oldest tie-point were estimated using the same constant sedimentation rate as the previous tie-point bounded sediment interval. The radiocarbon-derived timing of LGM matches the maximum values of the $\delta^{18}O$ stratigraphy in GGC3.

1.2.3. Relative Sea-Level Curve

The sea-level history at the TAG hydrothermal field site was computed across the last glacial cycle using a gravitationally self-consistent theory that accounts for Maxwell viscoelastic adjustment of the solid-Earth, time-varying shoreline geometry, and changes in Earth rotation (Mitrovica and Milne, 2003; Kendall et al., 2005), using a pseudo-spectral algorithm with

truncation at spherical harmonic degree and order 256 (Kendall et al., 2005). The predicted sea-level history for the TAG hydrothermal field is relatively insensitive to changes in the ice history and Earth model, including the incorporation of lateral variations in lithospheric thickness and mantle viscosity (Figure A4).

1.3. Results

Hydrothermal contributions to Mir sediments were identified using Fe and Cu, as both are enriched in near-vent (≤ 5 km) hydrothermal deposits (Cave et al., 2002). Total sediment Fe and Cu contents, however, can also reflect contributions from terrigenous dust and mid-ocean ridge basalt fragments. The terrigenous component was constrained using $^{4}He_{terr}$ and Th, both excellent tracers of dust (Patterson et al., 1999; Winckler et al., 2008). In addition, Fe/Ti and Cu/Ti ratios were used to distinguish hydrothermal material from Fe and Cu associated with dust and basalt fragment.

The highest Fe and Cu concentrations occur between 30 and 50 cm depth and coincide with the LGM, as indicated by the heaviest $\delta^{18}O$ values (Figure 1.2). The LGM peak in Fe and Cu requires enhanced hydrothermal deposition because the synchronous Fe and Cu patterns are distinct from the dust proxies, Th and $^{4}He_{terr,}$ which broadly oscillate throughout the core (Figure 1.2). The background Fe/Ti ratio of 13 to 22 suggests a small, but near continuous, hydrothermal sediment contribution as the Fe/Ti ratios of dust and basalt are ~11.7 (Taylor and McLennan,

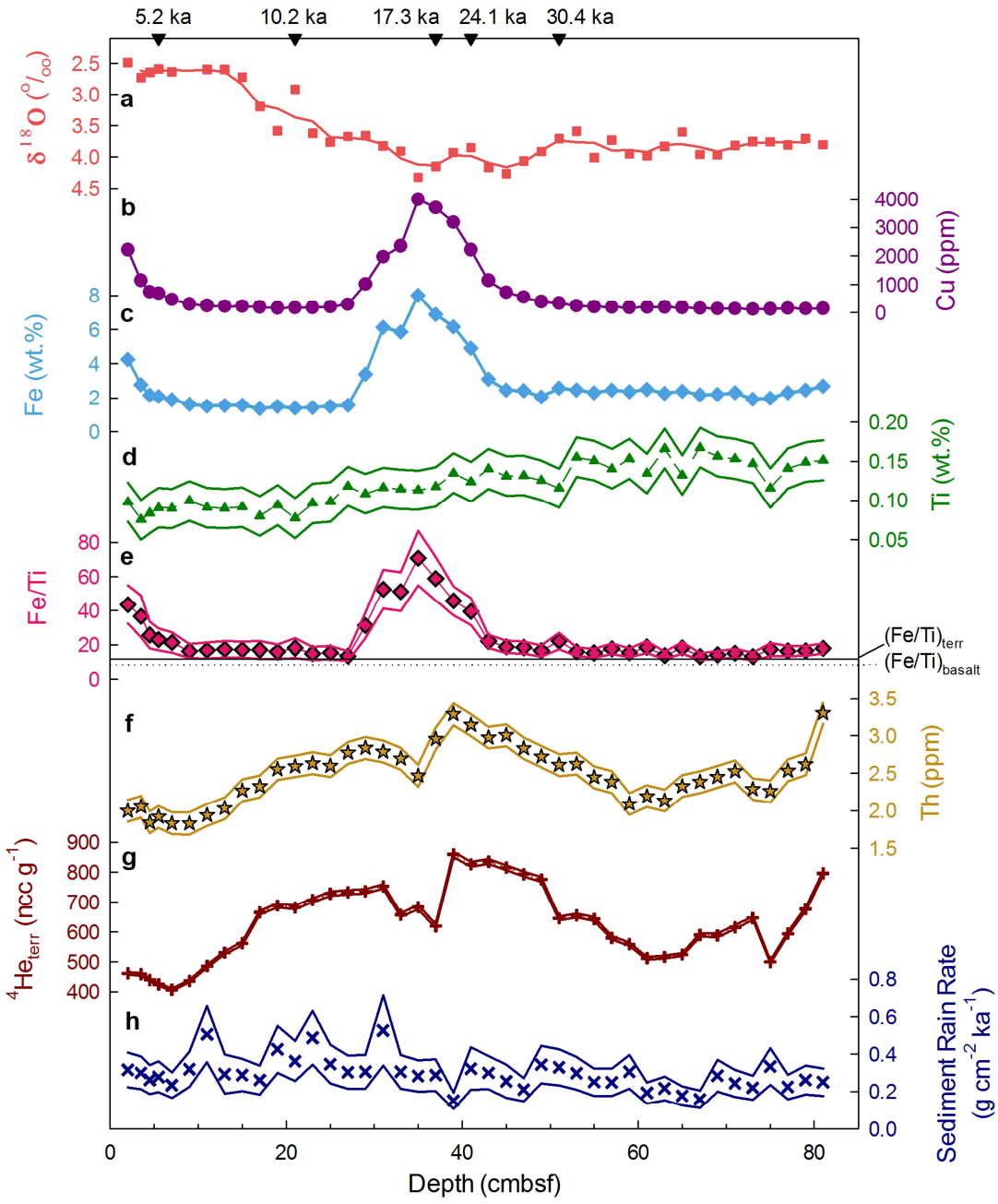

Figure 1.2. Sediment composition as a function of depth. a, Benthic $\delta^{18}O$ values from *C. wuellerstorfi* for each depth (squares), along with the $\delta^{18}O$ 3-point running mean (solid line), and depths with planktonic *G. ruber* radiocarbon dates (black triangles). Bulk sediment concentrations of Cu (b), Fe (c), Ti (d), the Fe/Ti ratio (e), and bulk sediment Th (f), and terrigenous ^4He ($^4He_{terr}$; g) for each depth (points) within 1σ uncertainty envelope (solid lines). h, extraterrestrial ^3He [$^3He_{ET}$]-derived sediment rain rates for each depth (points) within a 1σ uncertainty envelope (solid lines). The Fe/Ti values for terrigenous material (11.7, solid black line) and mid-ocean ridge basalt (8.3, dashed black line) are highlighted in panel e (Taylor and McLennan, 1995; Gale et al., 2013).

1995) and ~8.3 (Gale et al., 2013), respectively. The pronounced peak in the Fe/Ti ratio to 71 ± 16 across the LGM (Figure 1.2e), therefore, requires a significant increase in hydrothermal Fe deposition.

Fe and Cu fluxes confirm an increase in hydrothermal deposition across the LGM (Figure 1.3). The LGM peak in Fe and Cu concentrations represents a 4-fold increase in total Fe flux and a 7-fold increase in total Cu flux between 28 and 15 ka (Figure 1.3a,b). In contrast, the dust fluxes, as constrained by Th and $^4He_{terr}$, remain relatively constant between 28 and 15 ka. The dust fluxes peak, instead, between 15 and 10 ka, when Fe and Cu fluxes are in decline (Figure 1.3d,e). Thus, the elemental flux data indicate that increased Fe and Cu deposition during the LGM must come from enhanced hydrothermal activity and not from enhanced terrigenous input.

Hydrothermal fluxes (X_{HT}) were more precisely distinguished from total Fe and Cu fluxes (X_{total}) following the relationship $X_{HT} = X_{total} - (X/Ti)_{nonHT}*Ti_{total}$, where $(X/Ti)_{nonHT}$ represents the X/Ti ratio of non-hydrothermal components (dust and basalt; Figure 1.3a,c). $(Cu/Ti)_{nonHT}$ can be estimated using the terrigenous Cu/Ti value (83 ppm/wt.%) (Taylor and McLennan, 1995) because terrigenous Cu/Ti and mid-ocean ridge basalt Cu/Ti (80 ppm/wt.%) (Gale et al., 2013) are vastly lower than the highest measured hydrothermal sediment values in GGC3 (>30,000 ppm/wt.%). $(Fe/Ti)_{nonHT}$ can similarly be approximated using the terrigenous Fe/Ti value of ~ 11.7 (Taylor and McLennan, 1995). Dust and basalt corrections to the elemental fluxes are minor, as hydrothermal Fe and Cu compose >80% and >90% of total Fe and Cu fluxes,

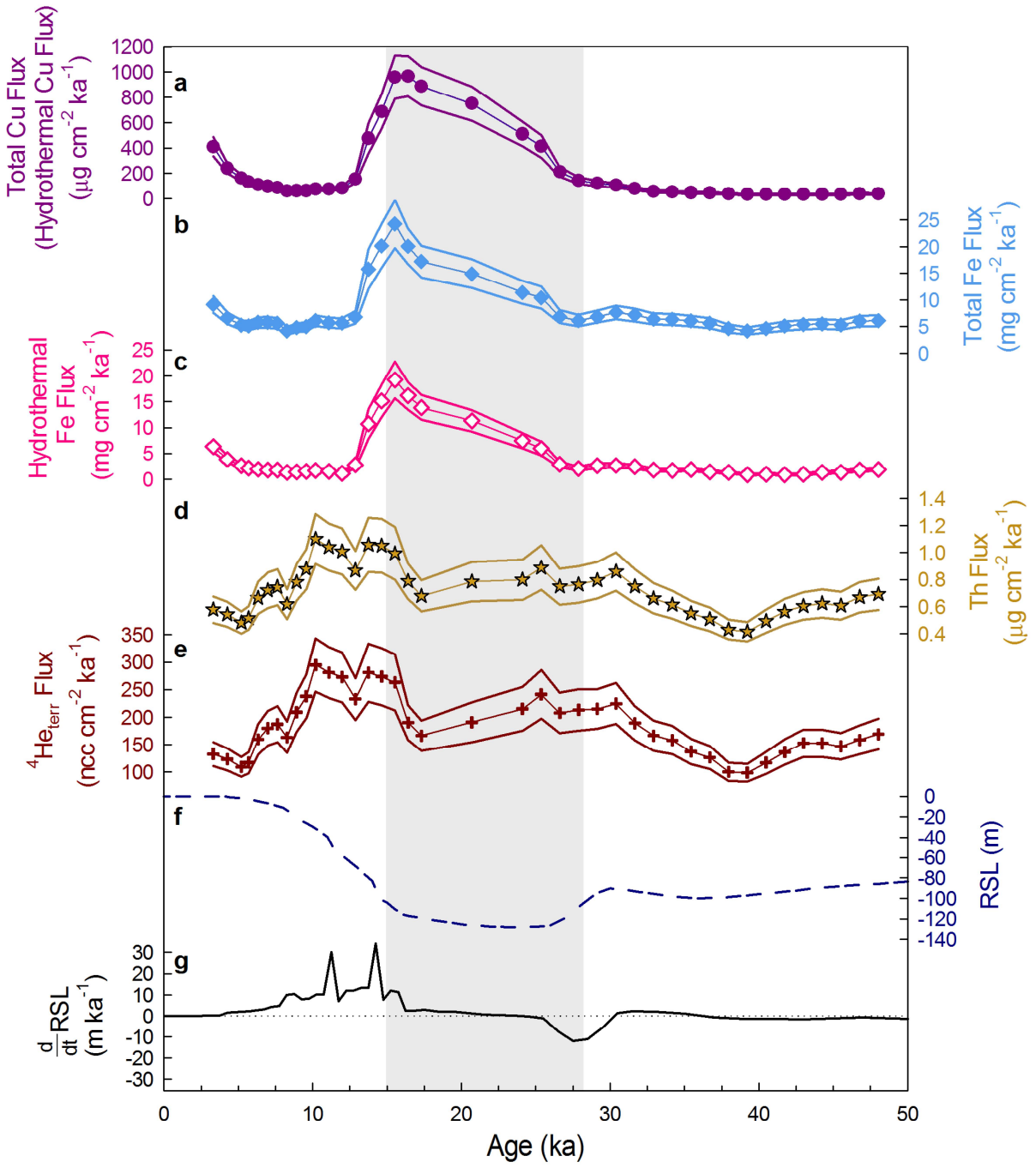

Figure 1.3. Comparison of elemental flux data and sea-level history. 3-point running mean elemental fluxes (points) of total Cu and hydrothermal Cu, which completely overlap on the figure scale (a), total Fe (b), hydrothermal Fe (c), and dust proxies Th (d), and $^{4}He_{terr}$ (e) within 1σ uncertainty envelope (solid lines). Relative sea-level curve (RSL; f) and rate of sea-level change ($^{d}/_{dt}$ RSL; g) computed for TAG hydrothermal field at 26°N on the Mid-Atlantic Ridge. Gray bar highlights the concurrent changes in the rate of sea-level fall and rise with the respective rise and fall of hydrothermal fluxes across the LGM (28-15 ka).

respectively, during the LGM-hydrothermal peak (Figure A2). With the non-hydrothermal background removed, corrected fluxes indicate a 6 to 8-fold increase in hydrothermal Fe and Cu deposition between 28 and 15 ka.

1.4. Discussion

We interpret observed variations in hydrothermal deposition to reflect changes in hydrothermal output from the Mir vent field. Discrete uranium-series dates of Mir zone sulfides demonstrate active intervals of Mir hydrothermal venting at 0.7 – 3 ka and at 18-20 ka (Lalou et al., 1995) that align with both periods of enhanced hydrothermal deposition observed in GGC3 sediments. Conceivably, repeated debris flow deposition of weathered sulfides from the Mir vent field, rather than mineral precipitation from an overlying hydrothermal plume, could generate the hydrothermal signal observed in GGC3. However, there is no sedimentological evidence for debris flow deposition within the core and neither the radiocarbon data, nor the benthic $\delta^{18}O$ stratigraphy, nor the $^{3}He_{ET}$-derived mass accumulation rates of GGC3 sediments show signs of significant disruption in sediment chronology or accumulation (Figure 1.2). Varying bottom currents could change the directionality of the Mir hydrothermal plume and potentially provide an alternate explanation for variable hydrothermal deposition to the core. However, comparison of the down-core Fe contents of GGC3 and of 4 neighboring Mir zone sediment cores (Cherkashev, 1995) reveals a spatially consistent pattern of hydrothermal deposition on all sides of the Mir hydrothermal system (Figure A3). Though sampling resolution and sedimentation rates vary slightly among the suite of Mir cores, the 4 Cherkashev (1995) cores contain both a core top Fe peak and a 30-50 cm depth Fe peak, as observed in GGC3. If the variations in

hydrothermal deposition to GGC3 sediments were driven by changes in debris flow activity, or by plume directionality alone, then there should not be a reproducible Fe pattern in multiple directions surrounding the Mir zone. Ultimately, net changes in Mir hydrothermal output provide the best explanation for the hydrothermal sedimentation fluctuations observed in GGC3.

Absolute age control allows for comparison of the Mir zone hydrothermal record with a relative sea-level (RSL) curve calculated for the TAG hydrothermal field across the last glacial cycle (Figure 1.3f,g). The RSL time series presented in Figure 1.3 was computed using the ICE-5G (version 1.2) ice model and the VM2 mantle viscosity profile (Peltier, 2004) (Figure A4).

The amplitude and timing of Mir zone hydrothermal variability suggests a relationship between rapid sea-level change and hydrothermal activity. Fe and Cu fluxes reveal increased hydrothermal deposition between 28-15 ka and again between 7- 2 ka. The smaller peak in hydrothermal activity between 7 to 2 ka does not coincide with rapid sea-level changes and may be driven by local tectonic or magmatic factors (Lalou et al., 1995). However, the largest hydrothermal signal observed in GGC3 (28 to 15 ka) clearly coincides with the sea-level minimum associated with LGM (Figure 1.3).

The data suggest a relatively swift hydrothermal response following a rapid sea-level change. The onset of increased hydrothermal deposition at 28 ka coincides with the fastest rate of sea-level fall, and thus the fastest rate of sea-level pressure decrease, during the last 50 ka. The end of the enhanced hydrothermal period, marked by the maximum hydrothermal sediment flux at 15 ka, occurs at the onset of rapid sea-level rise associated with global scale deglaciation. A major

reduction in hydrothermal activity follows and coincides with Meltwater Pulse 1A (MWP-1A) at ~14.5 ka, during which global mean sea-level rose ~15 m in less than 340 years (Deschamps et al., 2012). Both the increase in hydrothermal activity associated with rapid sea-level fall and the decrease associated with rapid sea-level rise are consistent with the hypothesis that hydrothermal circulation responds to sea-level change.

Enhanced hydrothermal activity across the LGM and across Marine Isotope Stage 4 has also been observed in sediment cores from the Galapagos Microplate (Frank et al., 1994) and from 38°N on the Mid-Atlantic Ridge (Auffret et al., 1996), suggesting a global ridge response to sea-level change (Lund and Asimow, 2011). Further evidence for a global ridge response to sea-level change comes from recent analyses of sediment cores from the Southern East Pacific Rise that reveal peaks in hydrothermal deposition following LGM and the previous glaciation (Lund et al., 2016). At the Mir zone, the onset of the LGM-associated increase in hydrothermal activity occurs at ~27 ka, near-concurrently with the fastest rate of sea-level fall. In contrast, the onset of the LGM-associated increase in hydrothermal activity at 6°S on the Southern East Pacific Rise appears to lag the sea-level signal by up to 5 ka. Such variations in timing merit further investigation into the diverse manifestation of hydrothermal responses to sea-level change. However, it is notable that the peak hydrothermal fluxes at both locations occur at ~15 ka, just before the onset of major deglaciation.

While climatic and volcanic interactions are known to occur on multi-million year timescales, as with the deep carbon cycle, a global LGM hydrothermal peak suggests volcanic sensitivity to millennial-scale climate variability. Furthermore, climate modulation of the chemical cycling and

redox exchange at submarine volcanic settings could stimulate additional variability in biogeochemical interactions with the solid-Earth. The 2 to 4-fold increases in hydrothermal deposition from ~35 ka to the LGM observed in the previous studies (Frank et al., 1994; Auffret et al., 1996; Lund and Asimow, 2011; Lund et al., 2016) are lower than the 6 to 8-fold Mir increase, yet even a conservative 3-fold LGM spike in global hydrothermal output would be comparable in Fe flux magnitude to the 2 to 4-fold increase in global dust flux during the last glacial period (Mahowald et al., 2006; Winckler et al., 2008).

Globally synchronous hydrothermal variation could have dramatic effects on hydrothermal Fe availability, biological carbon export, and the drawdown of atmospheric CO_2 in the Southern Ocean and other Fe-limited waters. Organic ligand complexation permits transport of dissolved hydrothermal Fe both high into the water column and far (>4000 km) from its vent source (Bennett et al., 2008; Toner et al., 2009; Conway and John, 2014; Fitzsimmons et al., 2014; Resing et al., 2015). Recent biogeochemical models including such transport suggest that the modern hydrothermal flux yields 4 Gmol yr^{-1} of dissolved hydrothermal Fe and may stimulate ~15-30% of carbon export in parts of the Southern Ocean (Tagliabue et al., 2010; Saito et al., 2013; Resing et al., 2015).

If the modern hydrothermal flux represents the global background at 30 ka, then a 3-fold increase in hydrothermal Fe output may have delivered significantly more dissolved Fe to the global oceans and could have enhanced carbon export in otherwise Fe-limited surface waters. Full quantification of the resulting dissolved Fe flux is beyond the scope of this work, as Fe stabilizing ligands may saturate with increased Fe flux, or, if they are produced by hydrothermal

ecosystems, may vary in concentration with increased hydrothermal activity (Bennett et al., 2008; Toner et al., 2009). Assuming a constant fraction of hydrothermal Fe is stabilized in the dissolved phase, however, a 3-fold increase in the global hydrothermal output of ~4 Gmol yr^{-1} (Resing et al., 2015) would yield a dissolved hydrothermal Fe flux of ~12 Gmol yr^{-1}. Wind-blown dust provides the largest Fe source to the open ocean and, assuming a terrigenous Fe solubility of 5%, the modern dust flux to the ocean yields a comparable value of ~14 Gmol yr^{-1} of dissolved Fe (Jickells et al., 2005). Although enhanced carbon export may not scale linearly with increased hydrothermal flux (e.g., Tagliabue et al., 2010), a 3-fold increase in hydrothermal activity during the LGM suggests that hydrothermal Fe does not buffer the ocean from glacial-interglacial variations in dust deposition as previously proposed, but may instead vary to a similar degree, and should therefore be considered in future calculations and modeling efforts.

1.5. Conclusions

We examine hydrothermal flux variations over the past 50 ka in a Mir zone sediment core from the TAG vent field on the Mid-Atlantic Ridge to test the hypothesis that Pleistocene sea-level fluctuations modulate submarine hydrothermal activity. Hydrothermal fluxes were constrained using $^{3}He_{ET}$-derived sediment rain rates and measurements of Fe, Cu, Th, $^{4}He_{terr}$ and Ti. The Mir sediments record a 6 to 8-fold increase in hydrothermal Fe and Cu deposition between 28 and 15 ka, coinciding with the LGM. The onset of the Mir hydrothermal peak occurs at ~28 ka and coincides with the fastest rate of sea-level fall entering LGM. Hydrothermal deposition quickly returns to baseline after 15 ka, during the main phase of global deglaciation that includes the MWP-1A event.

Our results, along with previous sediment analyses from the Galapagos Microplate, from the Southern East Pacific Rise, and from 38°N on the Mid-Atlantic Ridge, indicate that hydrothermal systems respond to rapid sea-level changes and suggest that the global hydrothermal Fe flux may have been significantly higher during the LGM than observed today. Increased hydrothermal Fe output during the LGM could lead to enhanced Fe fertilization, carbon export, and the drawdown of atmospheric CO_2 in the Southern Ocean and other Fe-limited waters. Ultimately, the magnitude of global hydrothermal emissions and resulting effects on marine biogeochemical cycles may vary in pace with Pleistocene glacial variability.

References

Auffret, G. A., et al. (1996), Record of hydrothermal activity in sediments from the Mid-Atlantic Ridge south of the Azores, *C. R. Acad. Sci.*, *323*(7), 583-590.

Bard, E. (1988), Correction of accelerator mass spectrometry ^{14}C ages measured in planktonic foraminifera: Paleoceanographic implications, *Paleoceanography*, *3*(6), 635-645.

Bennett, S. A., E. P. Achterberg, D. P. Connelly, P. J. Statham, G. R. Fones, and C. R. German (2008), The distribution and stabilisation of dissolved Fe in deep-sea hydrothermal plumes, *Earth Planet. Sci. Lett.*, *270*(3), 157-167.

Brook, E. J., M. D. Kurz, and J. Curtice (2009), Flux and size fractionation of ^{3}He in interplanetary dust from Antarctic ice core samples, *Earth Planet. Sci. Lett.*, *286*(3-4), 565-569.

Burley, J., and R. F. Katz (2015), Variations in mid-ocean ridge CO_2 emissions driven by glacial cycles, *Earth Planet. Sci. Lett.*, *426*, 246-258.

Cave, R. R., C. R. German, J. Thomson, and R. W. Nesbitt (2002), Fluxes to sediments underlying the Rainbow hydrothermal plume at 36°14'N on the Mid-Atlantic Ridge, *Geochim. Cosmochim. Ac.*, *66*(11), 1905-1923.

Cherkashev, G. (1995), Hydrothermal input into sediments of the Mid-Atlantic Ridge, *Geol. Soc. London Sp.*, *87*(1), 223-229.

Conway, T. M., and S. G. John (2014), Quantification of dissolved iron sources to the North Atlantic Ocean, *Nature*, *511*(7508), 212-215.

Crowley, J. W., R. F. Katz, P. Huybers, C. H. Langmuir, and S.-H. Park (2015), Glacial cycles drive variations in the production of oceanic crust, *Science*, *347*(6227), 1237-1240.

Deschamps, P., N. Durand, E. Bard, B. Hamelin, G. Camoin, A. L. Thomas, G. M. Henderson, J. i. Okuno, and Y. Yokoyama (2012), Ice-sheet collapse and sea-level rise at the Bolling warming 14,600 years ago, *Nature*, *483*(7391), 559-564.

Farley, K. A., and D. B. Patterson (1995), A 100-kyr periodicity in the flux of extraterrestrial ^{3}He to the sea floor, *Nature*, *378*(6557), 600-603.

Farley, K., S. Love, and D. Patterson (1997), Atmospheric entry heating and helium retentivity of interplanetary dust particles, *Geochim. Cosmochim. Ac.*, *61*(11), 2309-2316.

Fitzsimmons, J. N., E. A. Boyle, and W. J. Jenkins (2014), Distal transport of dissolved hydrothermal iron in the deep South Pacific Ocean, *Proceedings of the National Academy of Sciences*, *111*(47), 16654-16661.

Frank, M., J.-D. Eckhardt, A. Eisenhauer, P. W. Kubik, B. Dittrich-Hannen, M. Segl, and A. Mangini (1994), Beryllium 10, thorium 230, and protactinium 231 in Galapagos microplate sediments: Implications of hydrothermal activity and paleoproductivity changes during the last 100,000 years, *Paleoceanography*, *9*(4), 559-578.

Gale, A., S. Escrig, E. J. Gier, C. H. Langmuir, and S. L. Goldstein (2011), Enriched basalts at segment centers: The Lucky Strike (37°17′ N) and Menez Gwen (37°50′ N) segments of the Mid-Atlantic Ridge, *Geochem. Geophys. Geosyst.*, *12*(Q06016).

Gale, A., C. A. Dalton, C. H. Langmuir, Y. Su, and J.-G. Schilling (2013), The mean composition of ocean ridge basalts, *Geochem. Geophys. Geosyst.*, *14*(3), 489-518.

German, C. R., et al. (1997), Hydrothermal scavenging on the Juan de Fuca Ridge: Th-230(xs), Be-10, and REEs in ridge-flank sediments, *Geochim. Cosmochim. Ac.*, *61*(19), 4067-4078.

Graham, D. W. (2002), Noble gas isotope geochemistry of mid-ocean ridge and ocean island basalts: Characterization of mantle source reservoirs, *Rev. Mineral Geochem.*, *47*(1), 247-318.

Higgins, S. (2001), Extraterrestrial tracer in the sea: evaluation and application of ^{3}He in interplanetary dust particles as a 'constant flux' tracer in marine sediments, Columbia University, New York, New York.

Huybers, P., and C. Langmuir (2009), Feedback between deglaciation, volcanism, and atmospheric CO_2, *Earth Planet. Sci. Lett.*, *286*(3), 479-491.

Jean-Baptiste, P., and Y. Fouquet (1996), Abundance and isotopic composition of helium in hydrothermal sulfides from the East Pacific Rise at 13°N, *Geochim. Cosmochim. Ac.*, *60*(1), 87-93.

Jickells, T., Z. An, K. K. Andersen, A. Baker, G. Bergametti, N. Brooks, J. Cao, P. Boyd, R. Duce, and K. Hunter (2005), Global iron connections between desert dust, ocean biogeochemistry, and climate, *Science*, *308*(5718), 67-71.

Kendall, R. A., J. X. Mitrovica, and G. A. Milne (2005), On post-glacial sea level–II. Numerical formulation and comparative results on spherically symmetric models, *Geophys. J. Int.*, *161*(3), 679-706.

Lalou, C., J. L. Reyss, E. Brichet, P. A. Rona, and G. Thompson (1995), Hydrothermal activity on a 10^5-year scale at a slow-spreading ridge, TAG hydrothermal field, Mid-Atlantic Ridge 26°N, *J. Geophys. Res.*, *100*(B9), 17855-17862.

Lund, D. C., and P. D. Asimow (2011), Does sea level influence mid-ocean ridge magmatism on Milankovitch timescales?, *Geochem. Geophys. Geosyst.*, *12*(Q12009).

Lund, D.C., P.D. Asimow, K.A. Farley, T.O. Rooney, E. Seeley, E.W. Jackson, and Z.M. Durham (2016), Enhanced East Pacific Rise hydrothermal activity during the last two glacial terminations, *Science*, *351*(6273), 478-482.

Mahowald, N. M., D. R. Muhs, S. Levis, P. J. Rasch, M. Yoshioka, C. S. Zender, and C. Luo (2006), Change in atmospheric mineral aerosols in response to climate: Last glacial period, preindustrial, modern, and doubled carbon dioxide climates, *J. Geophys. Res.*, *111*(D10202).

Marcantonio, F., R. F. Anderson, S. Higgins, M. Stute, P. Schlosser, and P. Kubik (2001), Sediment focusing in the central equatorial Pacific Ocean, *Paleoceanography*, *16*(3), 260-267.

McGee, D., and S. Mukhopadhyay (2013), Extraterrestrial He in sediments: From recorder of asteroid collisions to timekeeper of global environmental changes, in *The Noble Gases as Geochemical Tracers*, edited, pp. 155-176, Springer-Verlag, Hiedelberg, Heidelberg.

Mitrovica, J. X., and G. A. Milne (2003), On post-glacial sea level: I. General theory, *Geophys. J. Int.*, *154*(2), 253-267.

Mukhopadhyay, S., and K. Farley (2006), New insights into the carrier phase (s) of extraterrestrial ^{3}He in geologically old sediments, *Geochim. Cosmochim. Ac.*, *70*(19), 5061-5073.

Mukhopadhyay, S., and P. Kreycik (2008), Dust generation and drought patterns in Africa from helium-4 in a modern Cape Verde coral, *Geophys. Res. Lett.*, *35*(L20820).

Nier, A., and D. Schlutter (1992), Extraction of helium from individual interplanetary dust particles by step-heating, *Meteoritics*, *27*(2), 166-173.

Patterson, D., K. Farley, and B. Schmitz (1998), Preservation of extraterrestrial ^{3}He in 480-Ma-old marine limestones, *Earth Planet. Sci. Lett.*, *163*(1), 315-325.

Patterson, D., K. Farley, and M. Norman (1999), ^{4}He as a tracer of continental dust: A 1.9 million year record of aeolian flux to the west equatorial Pacific Ocean, *Geochim. Cosmochim. Ac.*, *63*(5), 615-625.

Peltier, W. (2004), Global glacial isostasy and the surface of the ice-age Earth: the ICE-5G (VM2) model and GRACE, *Annu. Rev. Earth Planet. Sci.*, *32*, 111-149.

Rona, P.A., Y.A. Bogdanov, E.G. Gurvich, B.A. Rimski-Korsakov, A.M. Sagalevitch, M.D. Hannington, and G. Thompson (1993), Relict hydrothermal zones in the TAG Hydrothermal Field, Mid-Atlantic Ridge 26°N, 45°W, *J. Geophys. Res., 98*(B6), 9715-9730.

Resing, J. A., P. N. Sedwick, C. R. German, W. J. Jenkins, J. W. Moffett, B. M. Sohst, and A. Tagliabue (2015), Basin-scale transport of hydrothermal dissolved metals across the South Pacific Ocean, *Nature*, *523*(7559), 200-203.

Saito, M.A., A.E. Noble, A. Tagliabue, T.J. Goepfert, C.H. Lamborg, and W.J. Jenkins (2013), Slow-spreading submarine ridges in the South Atlantic as a significant oceanic iron source, *Nature Geosci., 6*(9), 775-779.

Tagliabue, A., L. Bopp, J.-C. Dutay, A. R. Bowie, F. Chever, P. Jean-Baptiste, E. Bucciarelli, D. Lannuzel, T. Remenyi, and G. Sarthou (2010), Hydrothermal contribution to the oceanic dissolved iron inventory, *Nature Geosci.*, *3*(4), 252-256.

Taylor, S. R., and S. M. McLennan (1995), The geochemical evolution of the continental crust, *Rev. Geophys.*, *33*(2), 241-265.

Tolstoy, M. (2015), Mid-ocean ridge eruptions as a climate valve, *Geophys. Res. Lett., 42,* 1346-1351.

Toner, B. M., S. C. Fakra, S. J. Manganini, C. M. Santelli, M. A. Marcus, J. W. Moffett, O. Rouxel, C. R. German, and K. J. Edwards (2009), Preservation of iron (II) by carbon-rich matrices in a hydrothermal plume, *Nature Geosci.*, *2*(3), 197-201.

Torfstein, A. (2012), Size fractionation, reproducibility and provenance of helium isotopes in north-equatorial pacific pelagic clays, *Earth Planet. Sci. Lett.*, *339–340*(0), 151-163.

Winckler, G., and H. Fischer (2006), 30,000 years of cosmic dust in Antarctic ice, *Science*, *313*(5786), 491-491.

Winckler, G., R. F. Anderson, M. Q. Fleisher, D. McGee, and N. Mahowald (2008), Covariant glacial-interglacial dust fluxes in the equatorial Pacific and Antarctica, *Science*, *320*(5872), 93-96.

Chapter 2

Millennial-scale major and trace element depositional variability over the last glacial period in hydrothermal sediments from the Mid-Atlantic Ridge

Abstract

Slow spreading mid-ocean ridges, such as the Mid-Atlantic Ridge, account for nearly one quarter of the globally detected hydrothermal vent fields and represent a vast chemical diversity of hydrothermal environments. Sedimentary records of hydrothermal deposition provide a means to evaluate the long-term chemical and physical behavior of hydrothermal systems and thus investigate interactions at the interface between Earth's surface and its exterior. Hydrothermal Fe and Cu flux variability observed over the past 50 ka in sediments recovered within the Mir Zone of the TAG segment of the Mid-Atlantic Ridge have been interpreted to reflect the influence of glacially-driven variations in sea level on submarine hydrothermal circulation. This study presents new major and trace element data for the Mir zone sediments and an additional core recovered from the Broken Spur segment of the Mid-Atlantic Ridge that spans the past 70 ka. Focusing on the sedimentary fluxes of Fe, Cu, Zn, Pb, P, V, and U, this study evaluates the depositional and compositional variability of hydrothermal material within the two study sites. The Broken Spur sediments contain little evidence to suggest significant hydrothermal deposition over the past 70 ka and may be perpetually shielded by the surrounding bathymetry, which exceeds 300 m above the height of the modern plume. Significant bathymetry shielding by a height of 300 m suggests that megaplumes, as have been observed on the Juan de Fuca Ridge, are rare occurrences along the Broken Spur ridge segment. The new data presented for the Mir zone sediments include high resolution analyses of Fe, Ti, Cu, and Zn variability and reveal two

distinct peaks in hydrothermal activity during the Last Glacial Maximum and the onset of deglaciation, where only one was previously identified. The revised Mir zone record remains consistent with the hypothesis that sea level changes can affect the output of submarine hydrothermal systems, however the new data suggest that sea level is not the only driver of variability within the Mir zone.

2.1. Introduction

Submarine hydrothermal circulation plays a critical role in the chemical and thermal exchange between Earth's interior and its surface, regulates seawater chemistry and provides the redox potential required for entire ecosystems to exist independent of solar input (Kelley et al., 2002). An increasing number of studies suggest that pressure fluctuations caused by glacially driven variations in sea level may modulate magmatic and hydrothermal output at submarine volcanic centers, with falling sea level driving increased volcanic activity (Huybers and Langmuir, 2009; Lund and Asimow, 2011; Crowley et al., 2015; Lund et al., 2016; Middleton et al., 2016). In turn, glacially paced changes in submarine volcanism could induce globally synchronous variations in the delivery of bioavailable iron and CO_2 from mid-ocean ridges and thus provide solid-Earth feedbacks into the climate system (Burley and Katz, 2015; Middleton et al., 2016; Huybers and Langmuir, 2017).

Despite relatively low levels of magmatic input, ~25% of globally detected hydrothermal vent sites occur on slow-spreading mid-ocean ridges (Beaulieu, 2015). Further, hydrothermal plumes emanating from the slow-spreading southern Mid-Atlantic Ridge appear to contain up to ~80x more dissolved iron than plumes originating from the faster spreading East Pacific Rise (Saito et al., 2013). Thus, the biogeochemical importance of mid-ocean ridge hydrothermal circulation may not scale directly with ridge spreading rate. Consequently, understanding the physical and chemical processes that govern hydrothermal circulation in slow-spreading environments is essential to our understanding of the global impact of hydrothermal circulation.

A 50-ka sedimentary record of hydrothermal deposition within the Mir Zone of the TAG hydrothermal region reveals increased rates of hydrothermal iron and copper deposition coincident with the Last Glacial Maximum and is used to support the hypothesized relationship between Pleistocene sea level changes and submarine hydrothermal activity (Middleton et al., 2016). This study presents an updated hydrothermal record for the Mir Zone sediment core (KN207-2-GGC3) with new major and trace element analyses, including P, V, Mn, Zn, Pb, and U, and increased temporal resolution obtained from x-ray fluorescence scanning to further explore the relationship between sea level change and hydrothermal variability at the Mir Zone. Mir zone sediments are additionally compared to a new 70 ka sedimentary record from the Broken Spur segment of the Mid-Atlantic Ridge, constrained using the same methods of elemental analyses and extraterrestrial helium-3 derived sedimentary fluxes.

Weak hydrothermal deposition within the Broken Spur core, likely resulting from bathymetric shielding from the Broken Spur plume, precludes its ability to record the possible effects of sea level change on Mid-Atlantic Ridge hydrothermal activity. However, the Broken Spur sediments provide a local reference for the background elemental variability expected along the Mid-Atlantic Ridge in the absence of clear hydrothermal deposition. The new Mir Zone hydrothermal record suggests multi-thousand year shifts in the composition and variability of hydrothermal deposition proximal to the extinct Mir mound. The revised Mir zone hydrothermal record suggests that, while sea level may influence hydrothermal circulation at the Mir zone, it is unlikely to be the dominant driver of hydrothermal flux variability over the past 50 ka.

2.2. Sampling and Methods

2.2.1. Geologic Setting

The Mid-Atlantic Ridge is the most intensively studied of the slow-spreading centers in the global ridge system. High temperature hydrothermal systems on the Mid-Atlantic Ridge manifest in a diverse variety of settings and include both ultramafic-hosted systems, such as Rainbow (36°N) and Lost City (30°N), as well as basalt-hosted systems more typical of faster spreading ridges (e.g., German and Seyfried, 2014). Of the basalt-hosted Atlantic hydrothermal systems, some, such as Broken Spur (29°N) and Snakepit/MARK (23°N) are located within the neovolcanic zone of their ridge segments and are driven by the heat of shallow magma bodies (Karson et al., 1987; Murton et al., 1994).

In contrast, the enigmatic TAG hydrothermal field (26°N) is a basalt-hosted system situated > 2 km east of the neovolcanic zone and along a large detachment fault within an asymmetric spreading segment of the Mid-Atlantic Ridge (Rona, 1980). TAG vent fluids are chemically comparable to those of neovolcanic systems (Kelley et al., 2002; Foustoukos and Seyfried, 2005) and the heat flux emanating from TAG suggests the presence of a magmatic heat source 4 to 7 km below its surface. However, seismic survey data reveals no such magma body (Canales et al., 2007; deMartin et al., 2007). Isotopic dating of TAG mound deposits reveals episodic periods of hydrothermal activity over the past 140 ka that may be governed by variable magmatic activity or by tectonic faulting and the activation of new fluid-flow pathways (Lalou et al., 1990, 1995; Humphris and Tivey, 2000; Cherkashov et al., 2017).

The gravity core KN207-2-GGC3 (26.14°N, 44.80°W, 3433 water depth, 82 cm core length) was collected proximal to (<1 km) the relict Mir zone of the TAG hydrothermal area (e.g., Rona et al., 1993) in the axial valley of the Mid-Atlantic Ridge during cruise KN207-2 of the *R/V Knorr* in June 2012 (Figure 2.1). Hydrothermal Fe and Cu fluxes suggest a broad peak in hydrothermal deposition within the Mir zone core from from ~30 to ~15 ka and a smaller hydrothermal peak starting at ~7 ka and increasing towards the core top (Middleton et al., 2016).

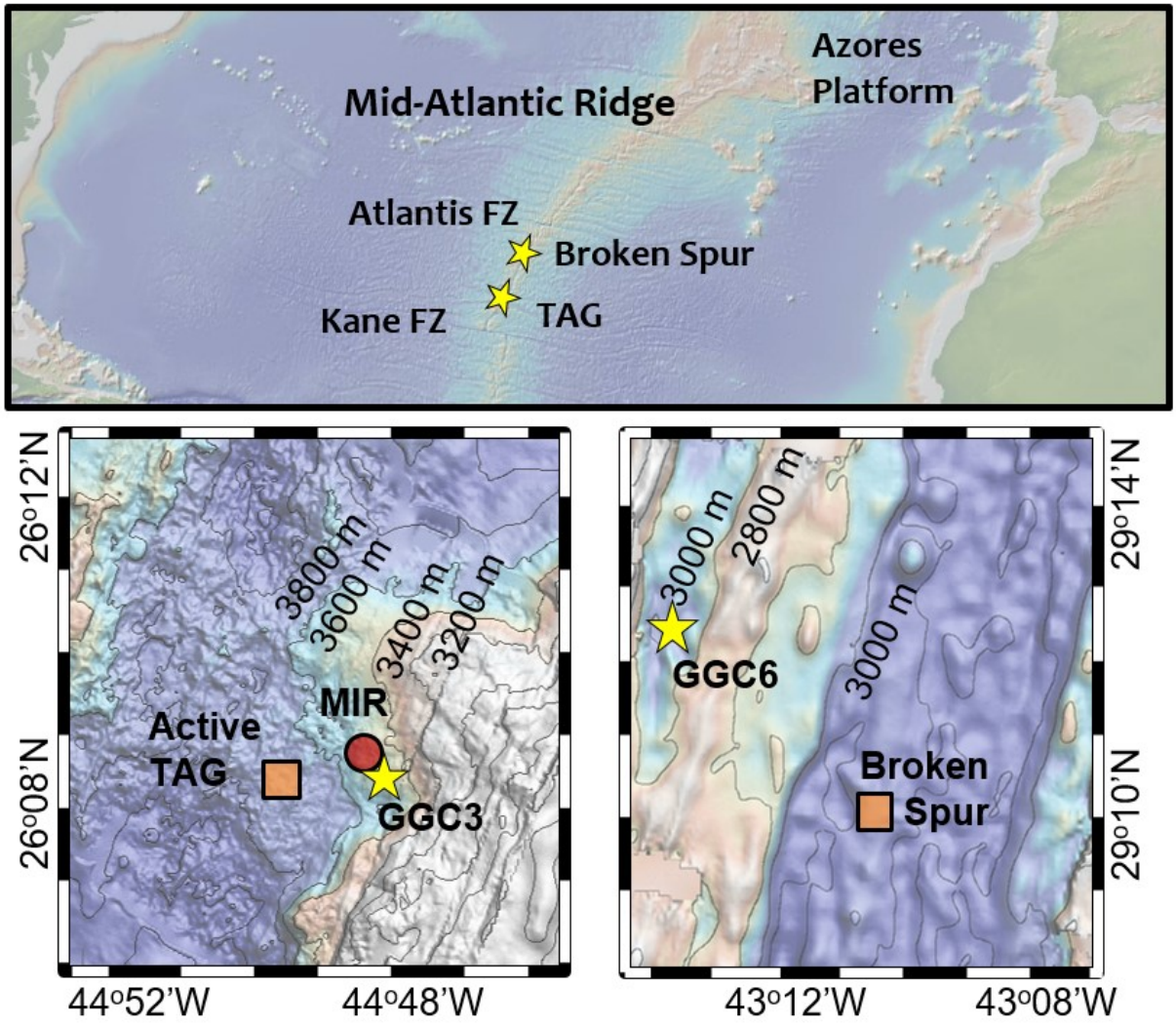

Figure 2.1. Map and insets of KN207-2-GGC3 (Mir sediment core, left panel) and KN207-2-GGC6 (Broken Spur sediment core, right panel). Sediment core retrieval sites (yellow stars), active hydrothermal fields (orange square) and the relict Mir zone (red circle) are indicted. Black lines indicate 200 m bathymetric contours. Maps generated in GeoMapApp.

The gravity core KN207-2-GGC6 (29.21°N, 43.23°W, 3018 water depth, 147 cm core length) was recovered from the axial valley of the Broken Spur segment of the Mid-Atlantic Ridge on the same cruise (Figure 2.1). The Broken Spur sediment core was collected > 6 km from the active Broken Spur hydrothermal field in a location outside of the path of the modern Broken Spur hydrothermal plume (German et al., 1999).

The age models for both sediment cores were determined using radiocarbon analyses and stratigraphic correlations in bulk carbonate content and are as reported in Middleton et al. (*in press*). It is noted that the age model for GGC3 is slightly revised from the original age model of Middleton et al. (2016).

2.2.2. Elemental indicators of hydrothermal deposition

The elemental composition of hydrothermal vent fluids is variable among vent sites and can vary temporally within a single vent field (Fouquet et al., 2010 and references therein; Edmond et al., 1995; Campbell et al., 1988). On the Mid-Atlantic Ridge, basalt-hosted high temperature vent fluids are typically enriched relative to seawater in Fe, Mn, Cu, Zn, and Pb, among other elements (Fouquet et al., 2010 and references therein). When the acidic and reduced vent fluids mix with cold oxidized seawater, the dissolved metals begin to precipitate as sulfide phases or as part of Fe-oxyhydroxides and Mn-oxide phases (e.g., German et al., 1991a; Rona et al., 1993). These plume precipitates provide a sedimentary proxy for the past presence of hydrothermal activity.

Hydrothermal sediments are identifiable by their relatively high concentrations of trace metals. Hydrothermal sulfide phases are rich in vent fluid elements like Fe, Cu, Zn, and Pb, and are preferentially deposited in close proximity to the vent itself (German et al., 1991a; Rona et al., 1993). Oxidized Fe and Mn particles settle out of the neutrally buoyant hydrothermal plume less rapidly and, in the Pacific, have been detected up to 4000 km from their originating mid-ocean ridge (Resing et al., 2015; Fitzsimmons et al., 2017). The formation of Fe-oxyhydroxides within hydrothermal plumes scavenges additional non-hydrothermal elements from the surrounding seawater, such as V, P, and U, and delivers these elements to the sediments below (Feely et al., 1991; German et al., 1991a,b). Although Mid-Atlantic Ridge hydrothermal vent fluids emit high concentrations of dissolved Mn, Mn oxidation and removal from the neutrally buoyant plume is slow. Consequently, near-vent (< 1 km) hydrothermal sediments do not always contain high Mn concentrations (German et al., 1991a). Sedimentary evidence of hydrothermal Mn deposition may be additionally complicated by the remobilization of Mn associated with redox-driven diagenesis (Shimmield and Price, 1986; Froelich et al., 1979). Such redox-driven remobilization and precipitation may also significantly affect the sedimentary records of U, V, and P (Klinkhammer and Palmer, 1991; Mangini et al., 2001; Mills et al., 2010; Dunk and Mills, 2006).

Many hydrothermally sensitive elements, such as Fe, Cu, and Zn, are additionally present in lithogenic material, such as wind-blown dust. Consequently, a lithogenic correction is required to distinguish hydrothermally driven changes in elemental deposition from the effects of variable dust delivery to the Mid-Atlantic (e.g., Middleton et al., *in press*). The lithogenic-corrected, or excess (XS), concentration of each element was calculated using the following equation:

$$X_{XS} = X_{total} - (X/L)_{lith} * L_{total} \quad \text{EQ. 2.1}$$

where X indicates the element in question, L indicates the lithogenic proxy element, and (X/L)_lithogenic refers to the X/L ratio in average upper continental crust (UCC; Taylor and McLennan, 1995). The term 'excess' is used to refer to the lithogenic-corrected component of each element in this study to highlight the potential for some elements to be associated with sedimentary components that are neither hydrothermal nor lithogenic (See Section 2.4). Both titanium and thorium-232 (common Th) are regularly employed as lithogenic proxies due to the high concentrations of these elements within the continental crust relative to other marine sedimentary inputs (e.g., Murray et al., 2000; Adkins et al., 2006; Middleton et al., 2016; Winckler et al., 2008). Unlike Th, the total Ti in the Mid-Atlantic Ridge sediment cores likely derives from small fragments of mid-ocean ridge basalt in addition to wind-blown North African dust (Middleton et al., 2016; Middleton et al., *in press*). As a result, the assumed UCC values may not represent the true lithogenic endmember composition throughout each core. The differences in X/Ti between North African dust, mid-ocean ridge basalt, and the residual hydrothermal component of each element, however, are typically large enough that estimated hydrothermal components are relatively insensitive to the presumed lithogenic endmember. Where Th data are available, excess elemental concentrations were separately computed using Ti-based and Th-based corrections for lithogenic input in order to examine the sensitivity of the excess elemental records to the lithogenic correction. While x-ray fluorescence scanning yields high-resolution Ti data in the Mid-Atlantic cores, Th concentration data are limited to the temporal resolution of analyses performed using inductively coupled mass spectrometry (see Section 2.2.3).

This study examines the temporal variability of excess Fe, Cu, Zn, Pb, V, P, U, and Mn within the Mir and Broken Spur sediment cores to evaluate the presence or absence and the magnitude of hydrothermal deposition at these locations. Where hydrothermal deposits are detected, the compositional variability of hydrothermal input to the Mid-Atlantic Ridge sediments is additionally examined.

2.2.3 Determination of elemental concentrations and fluxes

Major and trace elemental concentrations were determined in each sediment core using inductively coupled plasma mass spectrometry (ICP-MS) and x-ray fluorescence (XRF) scanning.

Major and trace elemental concentrations were determined from homogenized 1 to 2 cm sediment intervals throughout the length of each core using solution nebulized ICP-MS analyses performed with a Thermo X series quadrupole at Harvard University following the methods described in Middleton et al. (2016). ICP-MS analyses were performed separately on the carbonate and carbonate-free components of each sample determined by an 24 h leach in 10% acetic acid at 25ºC. The carbonate content of each sample was determined from the mass difference between dry initial bulk sediments and dry residual sediments following the acetic acid leach. Elemental concentrations for bulk sediment samples were then calculated by mass balance. While this study focuses discussion on the hydrothermally sensitive elements listed above, the ICP-MS data for Na, Mg, Al, K, Ca, Fe, Li, P, Sc, Ti, V, Cr, Mn, Co, Ni, Cu, Zn, Sr, Rb, Y, Zr, Cs, Ba, rare earth elements (REEs), Hf, Ta, Pb, Th, and U concentrations in both

sediment cores are included in the supplementary tables for completeness of the record (Appendix B).

Additional bulk sediment Ti, V, Fe, Cu, Zn, and Pb concentration analyses were performed for each core at 4-mm resolution using x-ray fluorescence scanning (XRF) performed at the Woods Hole Oceanographic Institution. Cores were scanned with a Cox Analytical Itrax core scanner using a 10 sec exposure time and a Mo-tube. Elemental intensities as measured by XRF in counts per second were calibrated to units of wt.% or ppm by linearly regressing the XRF data against the ICP-MS results for each element (Figures 2.2 and 2.3). For the calibration calculations, the 4-mm resolution XRF data were smoothed over 2 cm intervals to better reflect the sampling resolution of the ICP-MS data. XRF scanning is not without error and is sensitive to matrix effects (Rousseau et al., 1996). Accordingly, the XRF-derived data for the elements exhibiting weak correlations ($R^2 < 0.5$) with the data derived from ICP-MS and were thus excluded from further consideration (Figures 2.2 and 2.3). The remaining XRF-based elemental concentration records include Ti, Fe, Cu, and Zn in the Mir sediments (GGC3) and Ti and Fe in the Broken Spur sediments (GGC6).

Total elemental and excess elemental fluxes were calculated by multiplying sediment concentration values with vertical sediment rain rates (Φ_{sed}) derived using extraterrestrial helium-3 ($^3He_{ET}$) as a constant flux proxy (Takayanagi and Ozima, 1987; Marcantonio et al., 1995;

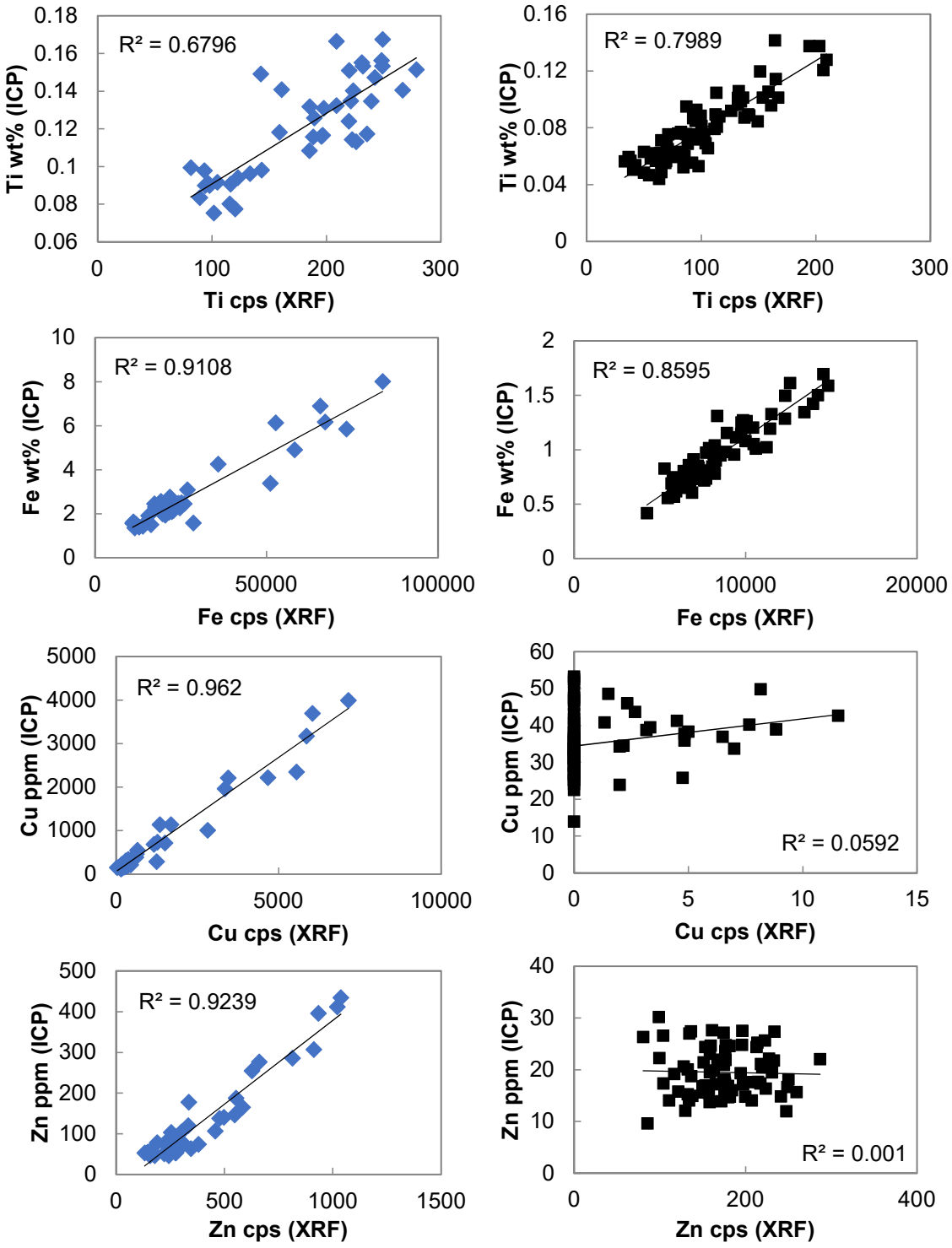

Figure 2.2: Calibration curves for determination of XRF-based elemental concentration values in GGC3 (Mir; blue diamonds in left column) and GGC6 (Broken Spur; black squares in right column). Cu concentrations in Broken Spur sediments are typically below the XRF detection threshold. XRF-based Cu and Zn data in Broken Spur exhibit weak correlations ($R^2 < 0.5$) with ICP-based values and are excluded from further discussion.

Farley and Patterson, 1995; Farley, 1995; Marcantonio et al., 2001) using the following equation:

$$\Phi_x = [X]_{sed} * \Phi_{sed} \quad \text{EQ. 2.2}$$

where Φ_x and $[X]_{sed}$ refer to the vertical flux and bulk sediment concentration of the component of interest. Helium isotope data and vertical sediment rain rates for the Mir and Broken Spur sediment cores are as reported in Middleton et al. (2016) and Middleton et al. (*in press*), respectively. The $^3He_{ET}$-derived vertical sediment rain rates were determined at the same 1 to 2 cm sampling resolution as the ICP-MS analyses. Mantle-derived helium, potentially associated with basalt fragments and hydrothermal deposits in the Mid-Atlantic cores, was not found to significantly bias the application of $^3He_{ET}$ as a constant flux proxy in these sediments (Middleton et al., 2016). All sedimentary fluxes presented in this study are reported as 3-point running-means unless otherwise stated.

2.3. Hydrothermal deposition in Mir vs. Broken Spur

2.3.1. Compositional differences between Mir and Broken Spur sediment cores

Evaluation of the carbonate-free sediment component highlights compositional variability beyond the effects of carbonate dilution and reveals distinct patterns between the Mir zone and Broken Spur sediment cores (Figures 2.4 and 2.5). A subset of elements representing the range of patterns expressed is elaborated upon below.

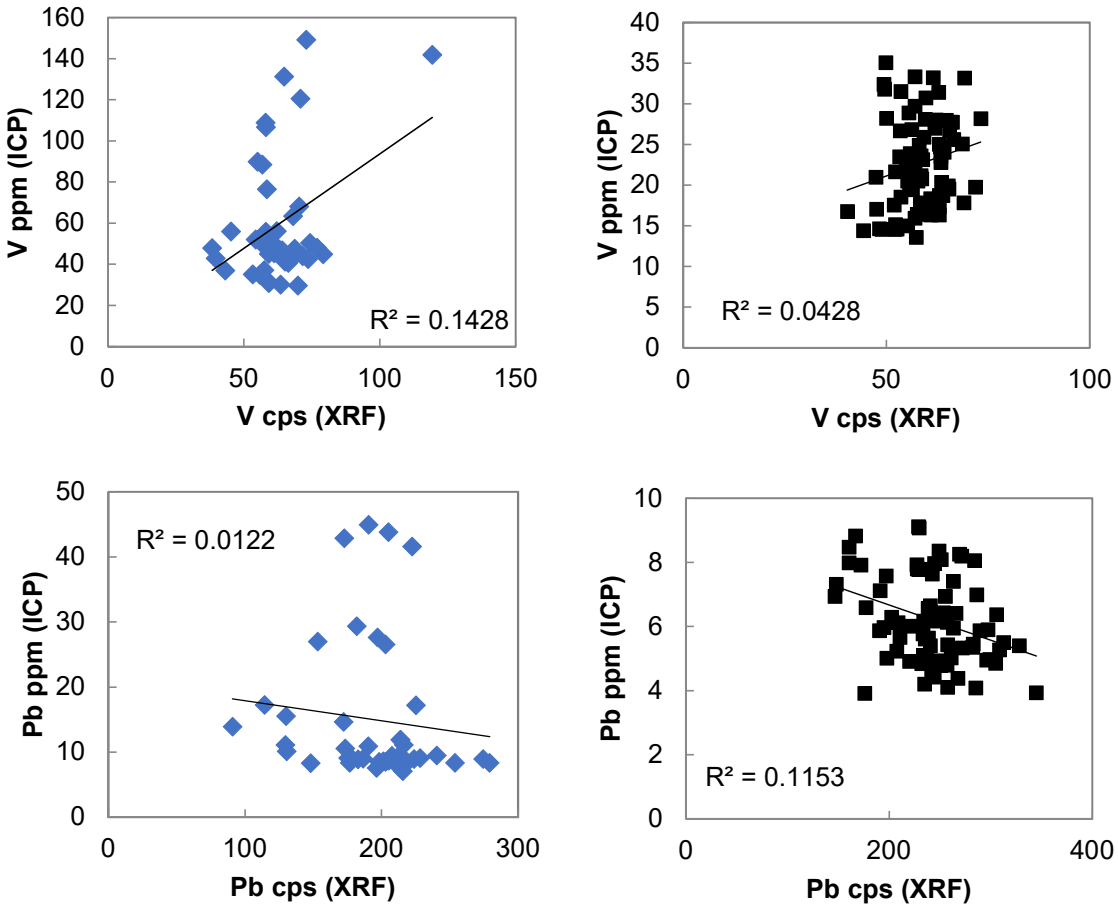

Figure 2.3: Additional calibration curves for determination of XRF-based elemental concentration values in GGC3 (Mir; blue diamonds, left column) and GGC6 (Broken Spur; black squares, right column). XRF-based V and Pb data in both Mid-Atlantic cores exhibit weak correlations ($R^2 < 0.5$) with ICP-based values and are excluded from further discussion.

2.3.1.1. Lithogenic pattern- Ti and Th

The magnitudes and patterns of temporal variability of carbonate-free Ti and Th concentrations are relatively similar between the Mir and Broken Spur sediment cores (Figure 2.4). Similarity in the concentrations of these lithogenic proxies between the Mid-Atlantic cores is expected as the two cores are thought to receive similar levels of lithogenic input from wind-blown dust (Middleton et al., *in press*). While the majority of lithophile elements in Mir sediments exhibit

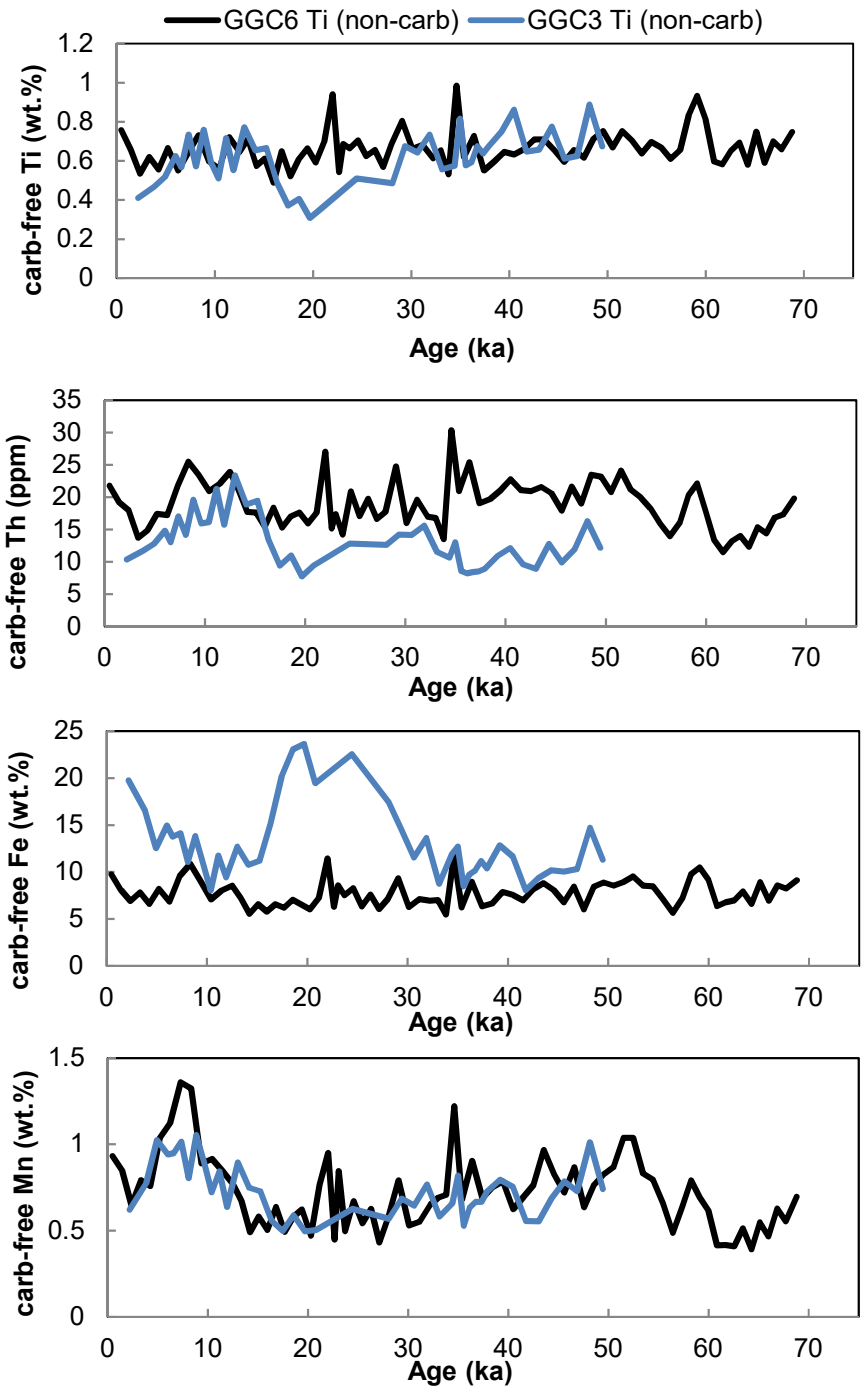

Figure 2.4: Down-core variability in the composition of carbonate-free sediments from the Mir zone (GGC3, blue) and Broken Spur (GGC6, black). The carbonate-free concentration records of Ti and Th, Fe, and Mn were chosen to highlight the distinct temporal patterns of elements dominated by lithogenic contributions (Ti and Th), hydrothermal contributions (Fe), and non-lithogenic non-hydrothermal contributions (Mn).

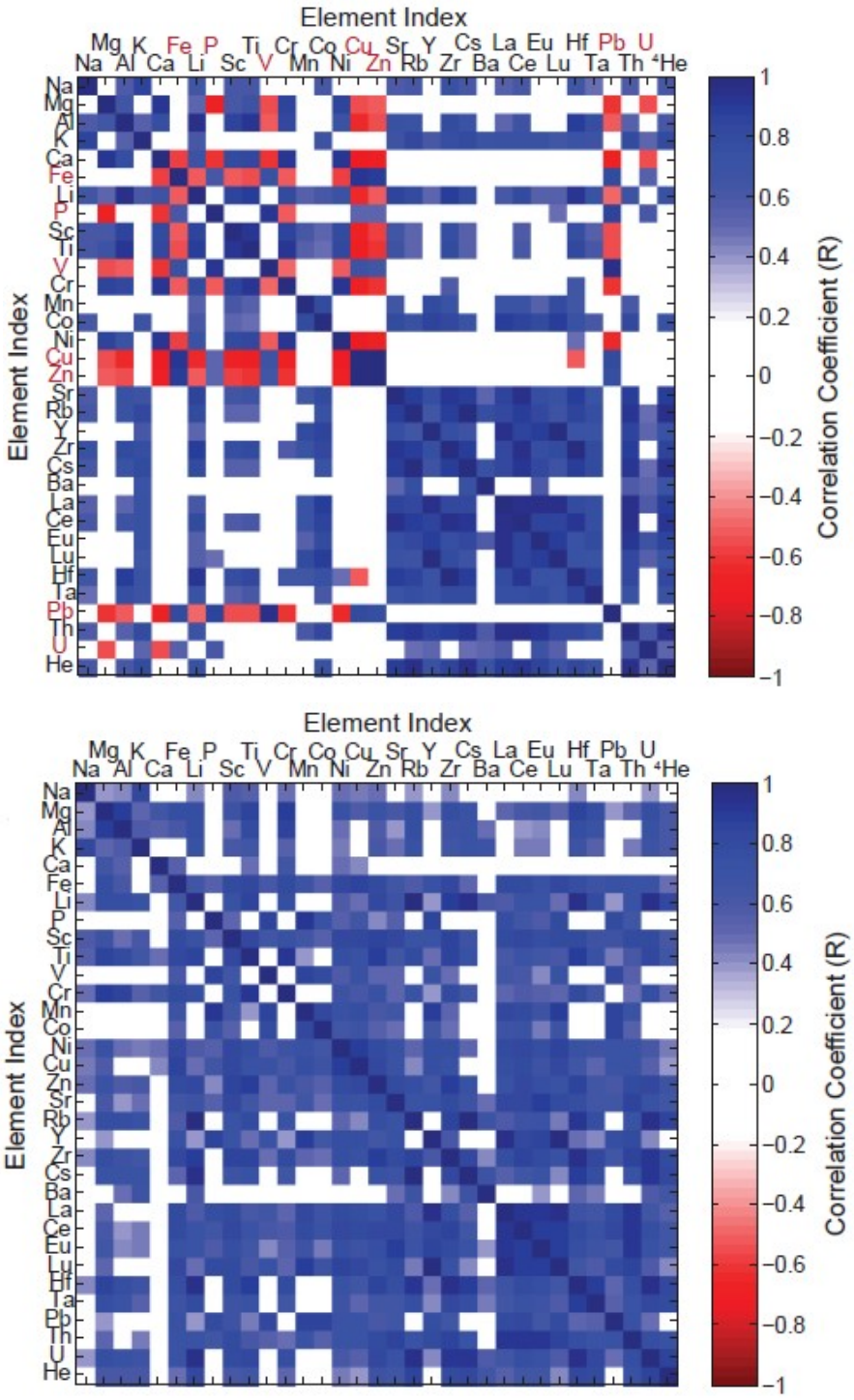

Figure 2.5: Elemental correlations within the carbonate-free sediment components of GGC3 (upper) and GGC6 (lower). Elements strongly correlated with hydrothermal deposition (Fe, P, V, Cu, Zn, Pb, and U) in GGC3 labeled in red. Note the distinction between elemental correlations in GGC3, where a strong hydrothermal signal is apparent, and in GGC6, where lithogenic material is the dominant carbonate-free sediment input.

carbonate-free concentration patterns that are positively correlated with Ti and Th, many of the elements examined do not, demonstrating a strong influence of a non-lithogenic sedimentary component (Figure 2.5; see below). The majority of the elements measured in Broken Spur sediments, however, are positively correlated with the lithogenic pattern expressed by Ti and Th, suggesting that lithogenic variability is the dominant driver of sediment composition at this location (Figure 2.5).

2.3.1.2. Hydrothermal pattern- Fe

The magnitudes and patterns of temporal variability in the carbonate-free concentrations of Fe are quite distinct between the Mir sediments and those from Broken Spur (Figures 2.4 and 2.5). In the Mir zone sediments, Fe concentrations increase from a background of ~10 wt.% to ~25 wt.% between 30 and 20 ka and again from 10 to 0 ka, consistent with known increases in hydrothermal deposition to this location (Middleton et al., 2016). The pattern of Fe variability is clearly distinct from that of the lithogenic pattern in the Mir sediments and carbonate-free Fe concentrations are found to correlate negatively with those of Ti and Th. As expected due to their sensitivity to hydrothermal activity, carbonate-free concentrations of P, V, Cu, Zn, Pb, and U in the Mir sediments are all found to positively correlate with the hydrothermal pattern expressed by Fe.

In contrast, Fe concentrations in the Broken Spur sediment core are typically lower than the lowest Fe concentrations in the Mir zone sediments and remain between ~5 and 11 wt.% over the past 70 ka. Similarities between the carbonate-free Fe concentration pattern at Broken Spur and

those of the lithogenic proxies Ti and Th (Figures 2.4 and 2.5) suggest that Broken Spur Fe is likely to be primarily derived from lithogenic inputs.

2.3.1.3. Non-lithogenic non-hydrothermal pattern - Mn

The carbonate-free concentration pattern exhibited by Mn is distinct from the lithogenic pattern expressed by Ti and Th and the hydrothermal pattern expressed by Fe in the Mir sediments. However, the magnitudes and patterns of temporal variability in carbonate-free Mn contents are similar between the Mid-Atlantic cores (Figure 2.4). Carbonate-free Mn concentrations are low during glacial periods, such as the Last Glacial Maximum (~21 ka) and Marine Isotope Stage 4 (~64 ka), and high in the mid-Holocene (~5 to 9 ka). Mn is sensitive to variations in redox conditions and similarities in the temporal Mn variability between the Mid-Atlantic cores may be caused by basin-wide changes in bottom water oxygen conditions (Mangini et al., 2001), rather than coincidental changes in local hydrothermal Mn input. Of the elements focused on in this work (P, Ti, V, Fe, Cu, Zn, Pb, Th, U, and Mn), the carbonate-free Mn concentration pattern is weakly correlated with Ti and Th in both cores (Figure 2.5). In the Broken Spur sediments, where a hydrothermal sedimentation pattern is not clearly observed, carbonate-free Mn is well correlated with P. Similarities in the behavior of Mn and P at Broken Spur highlight the sensitivity of P to changing redox conditions within the sediments.

2.3.2. "Excess" elemental fluxes and sensitivity to the lithogenic-correction

Examination of excess elemental fluxes allows for investigation into the depositional behavior of hydrothermally sensitive elements in the absence of the lithogenic pattern of variability (see Section 2.2.3). Such investigation allows for the potential detection of hydrothermal deposition in sedimentary localities where lithogenic input appears to dominant the carbonate-free elemental composition, as observed at Broken Spur.

In the Mir sediment core, the magnitudes and patterns of excess elemental fluxes were mostly insensitive to Ti- vs. Th-based lithogenic corrections (Figure 2.6). The primary difference between the Ti- vs. Th-corrected Mir flux records is that the Th-corrected records suggest slightly higher fluxes, relative to the Ti-corrected records, prior to ~30 ka. With the exception of this offset, the temporal pattern of excess elemental flux variability is unaffected by the choice of lithogenic correction. However, it is noted that the use of Ti leads to overcorrection for lithogenic input in the cases of U and Pb, yielding unphysical negative values. Thus, the Th-based lithogenic corrections are preferred.

In the Broken Spur sediments (Figure 2.7), the excess Mn, P, V, Cu, and Pb flux records are also relatively insensitive to the Ti- vs. Th-based lithogenic corrections. However, the use of a Ti- vs. Th-based lithogenic correction yields distinct patterns of variability in the excess Fe, Zn, and U fluxes at this site. The sensitivity of the excess Fe, Zn, and U flux records to the lithogenic correction suggests that perceived patterns of variability in the excess components of these elements may not be robust in the Broken Spur sediments. As observed in the Mir sediments, Ti-

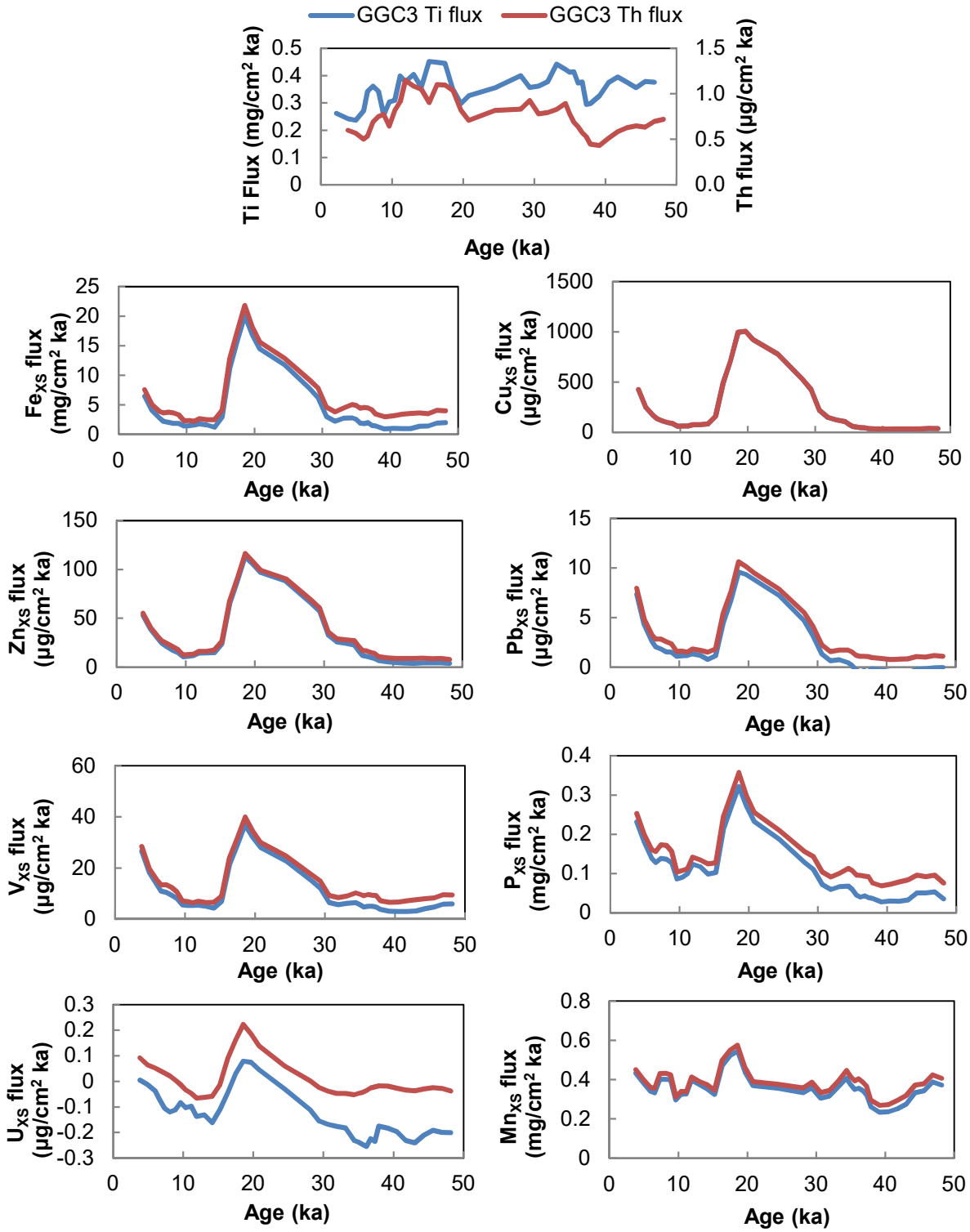

Figure 2.6: Comparison of excess elemental fluxes resulting from Ti -based (blue) and Th-based (red) lithogenic corrections in the Mir sediment core. With the exception of U, resulting fluxes are relatively insensitive to elemental choice for lithogenic corrections. However, Th-based lithogenic corrections are preferred as they yield fewer negative excess flux values.

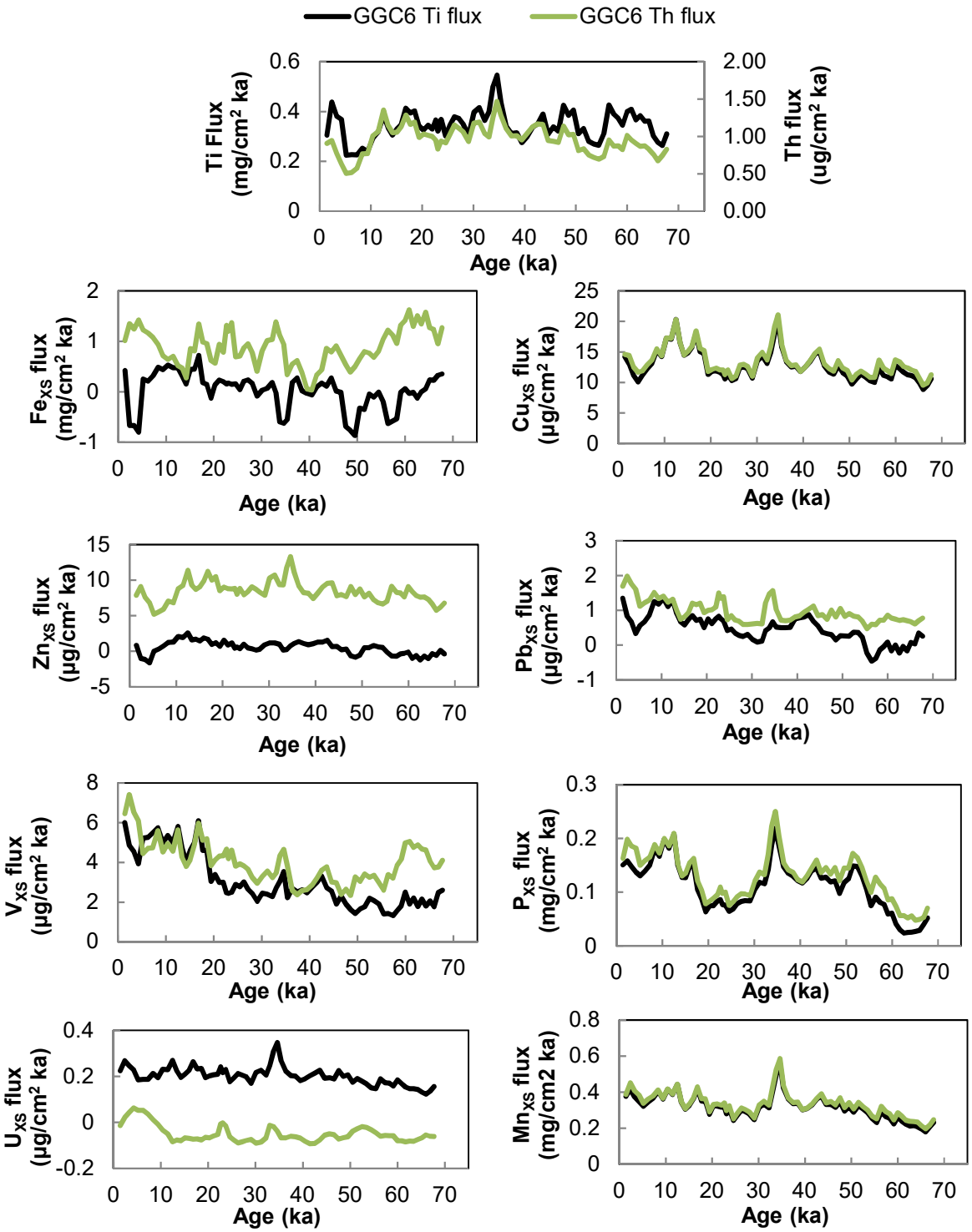

Figure 2.7: Comparison of excess elemental fluxes resulting from Ti-based (black) vs. Th-based (green) lithogenic corrections in the Broken Spur sediment core. Lower levels of excess elemental fluxes at the Broken Spur site result in increased sensitivity to Ti vs. Th-based lithogenic corrections (e.g., Fe, Zn, Pb, V, and U). Note the change in y-axes scale between Broken Spur sediments and Mir zone sediments (Figure 2.6)

based lithogenic corrections appear to lead to overcorrection for lithogenic input and yield negative excess flux values for Pb, U, Zn, and Fe. Notably, Th-based lithogenic corrections also yield negative flux values for U in both sediment cores. For consistency, the remaining discussion of ICP-MS derived data exclusively refers to excess elemental fluxes calculated using a Th-based lithogenic correction.

2.3.3. Mir zone vs. Broken Spur sedimentary records of hydrothermal deposition

In the Broken Spur sediments, excess fluxes of the hydrothermally sensitive Fe, Cu, P, V, Zn, Pb, and U do not follow the same pattern of variability (Figure 2.7), suggesting the occurrence of little to no hydrothermal deposition at this study site. Rather, the computed excess elemental fluxes in the Broken Spur sediments may result from variations in non-hydrothermal sedimentary mechanisms that uniquely affect each element such as diagenetic mobilization, paleoproductivity, or small deviations in the X/Th ratio of the local lithogenic input (e.g., Klinkhammer and Palmer, 1991; Mangini et al., 2001; Mills et al., 2010; Dunk and Mills, 2006; Schoepfer et al., 2015; Castillo et al., 2008). While weak evidence for hydrothermal deposition within the Broken Spur sediment core preclude its ability to reliably record potential responses of the Broken Spur hydrothermal field to changes in sea level, the Broken Spur sediments provide a good reference for background, non-hydrothermal, elemental variability in Mid-Atlantic Ridge sediments.

In the Mir zone sediments, excess P, V, Zn, Pb, and U fluxes clearly follow the hydrothermal Fe and Cu flux pattern observed by Middleton et al. (2016; and Figure 2.6). Consequently, the

excess fluxes of these elements are interpreted to reflect hydrothermal deposition. Excess Fe, P, V, Cu, Zn, Pb, and U fluxes each record a broad hydrothermal peak from ~30 to 15 ka and a second hydrothermal peak starting at ~10 ka and increasing towards the ~4 ka core top (Figures 2.6, 2.8 and 2.9). The excess U flux record drops below zero for prolonged intervals of the Mir sedimentary record (Figures 2.6 and 2.9). Given the redox sensitivity of sedimentary U, negative excess elemental flux values may result from either uncertainty in U concentrations within the lithogenic endmember or from intervals of U depletion from the sediment column (Mangini et al., 2001).

During the two hydrothermal peaks in Mir sediments, the magnitude of excess V, Fe, Cu, Zn, and Pb fluxes dwarfs both the background fluxes of these elements in the Mir core and the total range of these fluxes observed in the Broken Spur sediments (Figure 2.8). In contrast, excess P and U fluxes do not (Figure 2.9). For example, excess V fluxes in the Mir hydrothermal maximum are ~6x higher than the maximum excess V fluxes observed at Broken Spur, while peak excess P fluxes at Mir are less than 2x higher than peak excess P fluxes at Broken Spur. During the glacial hydrothermal peak, excess P and U fluxes in the Mir sediments are higher than coincident fluxes of these components at Broken Spur. However, the magnitudes of excess P and U fluxes during the Holocene hydrothermal peak are similar to those observed in contemporaneous Broken Spur sediments (Figure 2.9). The clear difference in the relative magnitudes of hydrothermal peaks in excess P and U deposition compared to excess V, Fe, Cu, Zn, and Pb fluxes suggest that non-hydrothermal sedimentary mechanisms, such as the deposition of organic matter (Schoepfer et al., 2015) and/or redox-driven remobilization

(Mangini et al., 2001) likely represent an important component of the computed excess P and U fluxes in the Mid-Atlantic sediments.

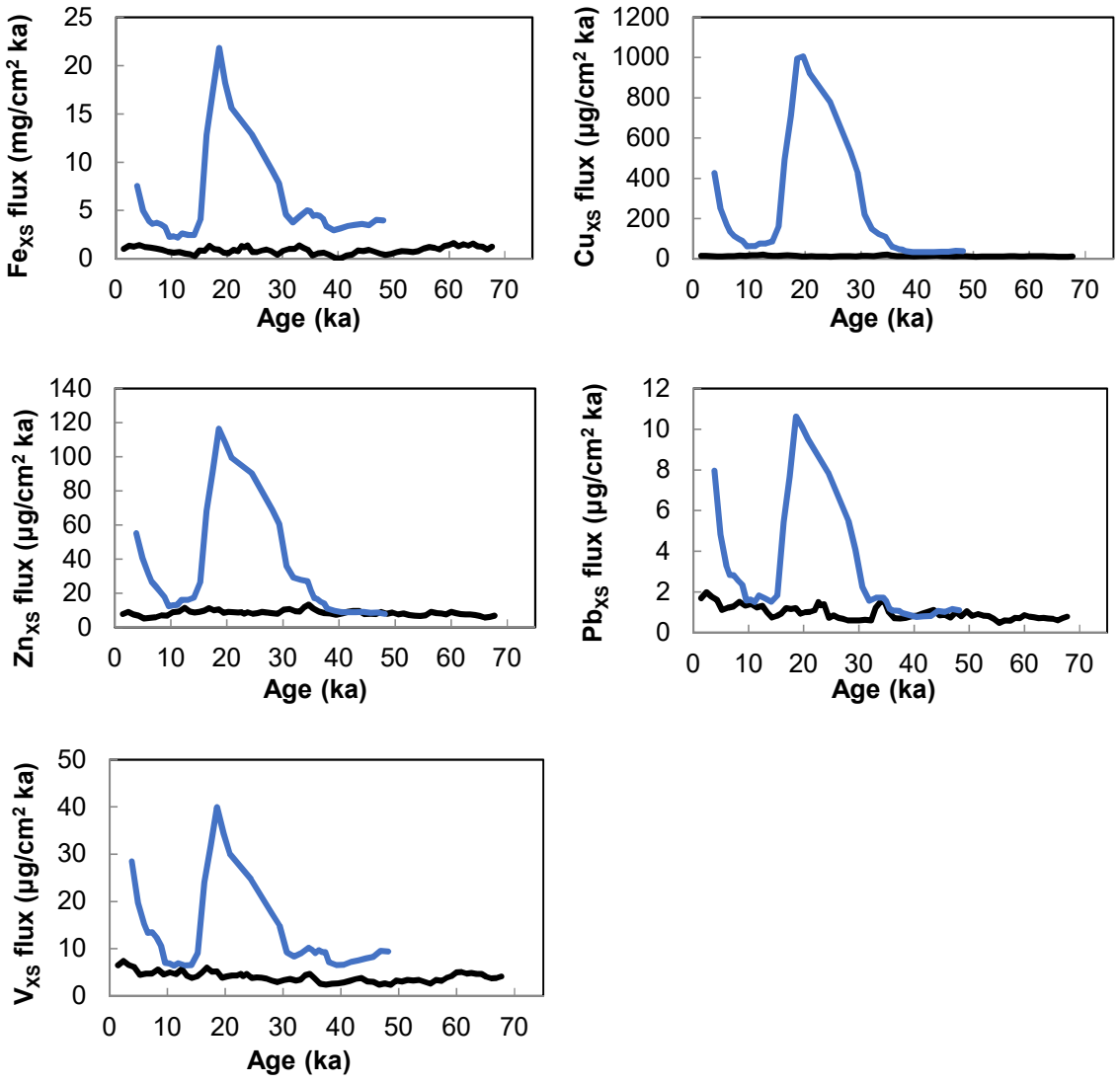

Figure 2.8: Lithogenic-corrected excess elemental fluxes in sediments from the Mir zone (GGC3, blue) and Broken Spur (GGC6, black). Flux values represent 3-pt running means of $^{3}He_{ET}$-based elemental flux values after a Th-based correction for lithogenic deposition. The excess flux values of Fe, Cu, Zn, Pb, and V in Mir sediments are significantly larger than observed at Broken Spur.

In contrast to the elements discussed above, excess Mn fluxes are dissimilar from the hydrothermal indicators and follow a similar pattern in both the Mir zone and Broken Spur sediments (Figures 2.8 and 2.9). Lack of correlation between the excess Mn and excess Fe, P, V, Cu, Zn, Pb, and U suggests that the excess Mn fluxes do not reflect changes in hydrothermal deposition in the Mir zone sediments. Such Mn behavior is consistent with prior observations in Mid-Atlantic Ridge hydrothermal sediments (German et al., 1991a).

2.3.4. Implications of the limited hydrothermal activity recorded at Broken Spur

Low excess Fe, Cu, Zn, Pb, and V flux values and dissimilarities in the temporal variability of these elements within the Broken Spur sediment core suggest that this site has received little to no hydrothermal deposition over the past 70 ka. This weak record of hydrothermal accumulation likely results from bathymetric shielding of the GGC6 sediment core location from the Broken Spur hydrothermal plume (Figure 2.10). A bathymetric high reaching ~300 m above the active Broken Spur vent field prevents the modern extent of the hydrothermal plume from reaching the core site and depositing hydrothermal precipitates (e.g., German et al., 1999).

The absence of a clear hydrothermal signal within the GGC6 sedimentary record suggests that the Broken Spur hydrothermal plume has not risen significantly in excess of 300 m above its originating vent field within the past 70 ka. While elevations in excess of 300 m above the seafloor are not expected from a typical hydrothermal plume (Rudnicki et al., 1994; Lilley et al., 1995), episodic hydrothermal megaplumes, as found on the Juan de Fuca Ridge in the Northeast Pacific, have been observed at heights of ~1000 m above the seafloor (Baker et al., 1987; 1989). A Juan de Fuca Ridge megaplume mapped within days of fluid release was found to span a

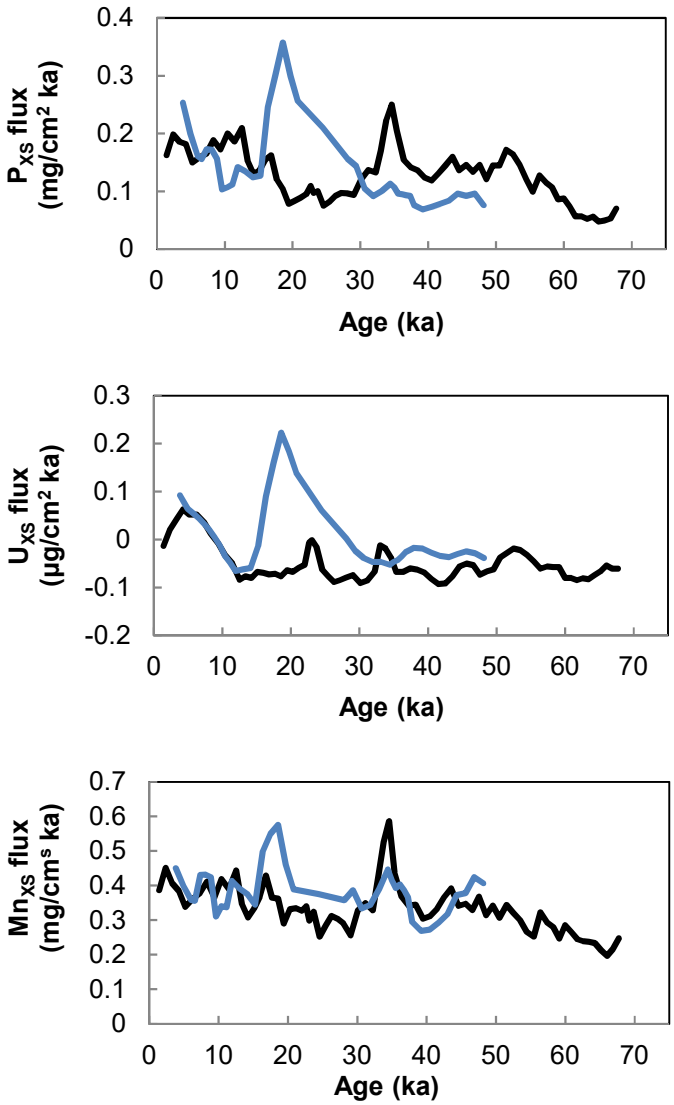

Figure 2.9: Lithogenic-corrected excess elemental fluxes in sediments from the Mir zone (GGC3, blue) and Broken Spur (GGC6, black). Flux values represent 3-pt running means of $^{3}He_{ET}$-based elemental flux values after a Th-based correction for lithogenic deposition. The range of excess flux values of P, U, and Mn in Mir sediments are relatively similar to those at Broken Spur.

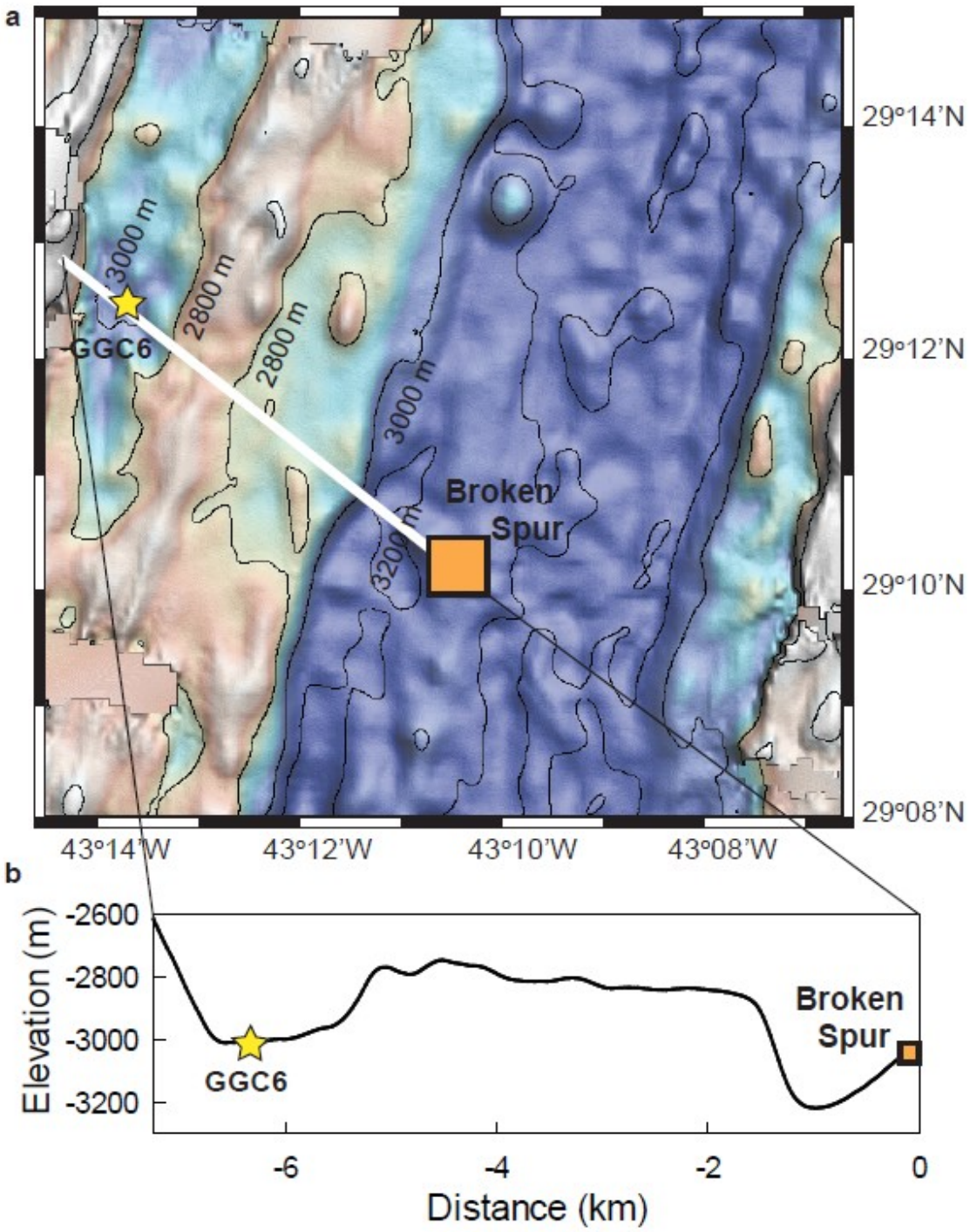

Figure 2.10: Broken Spur sediment core setting. (a) Locations of KN207-2 GGC6 gravity core (yellow star) and the active Broken Spur hydrothermal field (orange square) at 29°N on the Mid-Atlantic Ridge. Contours are shown at 200 m depth intervals. (b) Bathymetric profile between GGC6 and Broken Spur following the white transect in (a).

radially symmetric plume of ~20 km in diameter (Baker et al., 1989). The eruption of such a megaplume from the Broken Spur hydrothermal field would likely reach even the shielded location of the Broken Spur sediment core retrieval site and thus provide the opportunity for the deposition of hydrothermal material. The lack of significant hydrothermal deposition within the GGC6 sediments suggests that the occurrence of such megaplumes within the Broken Spur segment of the Mid-Atlantic Ridge may have been extremely rare over the past 70 ka.

2.4. Elemental variability in Mir hydrothermal deposits

Both the ICP-MS and the XRF derived concentration data suggest temporal variability in the elemental composition of hydrothermal deposits in the Mir sedimentary record (Figures 2.11 and 2.12). Given the significant increase in excess Fe, Cu, Zn, Pb, and V fluxes within peak hydrothermal layers, variability in excess Cu/Fe, Zn/Fe, Pb/Fe and V/Fe ratios may reflect changes in the chemical and physical nature of hydrothermal output of Mir zone vents and subsequent particle precipitation from the resulting hydrothermal plume.

The Cu/Fe, Zn/Fe, and Pb/Fe ratios of hydrothermal fluids are dependent on the temperature, pressure, and substrate conditions of the reaction zone within the hydrothermal system as well as the fluid pathway as it ascends back into the water column (e.g., Von Damm et al., 1998; Seewald and Seyfried, 1990; Kelley et al., 2002). However, these ratios are further modified within the hydrothermal plume due to varying sensitivities of each element to precipitation and scavenging (German et al., 1991a). In contrast to Fe, Cu, Zn, and Pb, the majority of V in hydrothermal sediments is sourced from seawater itself, rather than from hydrothermal vent

fluids and variations in V/Fe ratios may reflect changing interactions between sea water and the hydrothermal plume (Feely et al., 1991; German et al., 1991a). While excess P and U fluxes may be significantly influenced by non-hydrothermal sedimentary mechanisms (see section 2.3.3), excess P/Fe and excess U/Fe ratios are additionally presented for comparison. Observed compositional variations and possible implications for the Mir zone hydrothermal system and surrounding environment are elaborated upon below.

2.4.1. Elemental variability resolved by ICP-MS analyses

The temporal patterns of variability in ICP-MS derived excess elemental ratios are relatively insensitive to the choice of Ti-based versus Th-based lithogenic corrections, with the exception of a distinct peak marked by a single sample at ~15 ka and high frequency variability observed prior to ~35 ka in Ti-based excess Cu/Fe, Zn/Fe, and V/Fe that is not observed in the Th-based elemental records (Figures 2.11 and 2.12). The high frequency variability recorded in Ti-based excess elemental ratios may result from amplified uncertainties associated with the determination of excess elemental concentrations during intervals where hydrothermal deposition is low or may result from the heterogenous presence of basalt fragments within the sediments (Section 2.2.2). Due to the likely overcorrection of lithogenic material associated with the Ti-based excess values (See Section 2.3.2), the following discussion will focus on variations in the Th-based excess elemental records unless otherwise noted.

2.4.1.1. Cu, Zn, and Pb

Variability in the relative Fe, Cu, Zn, and Pb concentrations of a hydrothermal fluid may result from chemical and physical changes in the water-rock reaction pathway of circulating hydrothermal fluids associated with magmatic and volcanic activity, the opening of new crustal fractures associated with tectonic activity, or with the alteration of the substrate rock following prolonged intervals of fluid circulation (Kelley et al., 2002; German and Seyfried, 2014). Once injected into the water column, variable rates of precipitation of these elements will further change their relative concentrations within the resulting hydrothermal precipitates. Thus, changing proximity of the nearest active vent may also influence observed Cu/Fe, Zn/Fe, and Pb/Fe ratios in hydrothermal sediments (German et al., 1991a,b). Variations in the excess Cu/Fe, Zn/Fe, and Pb/Fe ratios of Mir zone hydrothermal sediments suggest that multiple such processes are likely to be occurring over the duration of the 50 ka record.

Broadly, excess Cu/Fe, Zn/Fe, and Pb/Fe ratios are each lowest in the oldest Mir sediments (prior to 35 ka) and exhibit a peak during the glacial period (Figure 2.11). Otherwise, however, the three ratios follow distinct patterns over the last 50 ka and maximum values of excess Cu/Fe, Zn/Fe, and Pb/Fe ratios occur at different times throughout each record. Excess Cu/Fe values are relatively flat (90 to 112 ppm/wt%) from 50 ka to ~35 ka, when they increase to a broad maximum value of 622 ppm/wt% lasting from ~25 to 21 ka. Excess Cu/Fe values then gradually decline to 244 ppm/wt.% at ~ 9 ka before rising once more to 612 ppm/wt.% in the top of the core. Excess Zn/Fe values gradually increase from 50 ka to ~35 ka (18 to 35 ppm/wt.%), where they increase more rapidly to peak at ~31 ka (86 ppm/wt%). Following the peak at ~31 ka,

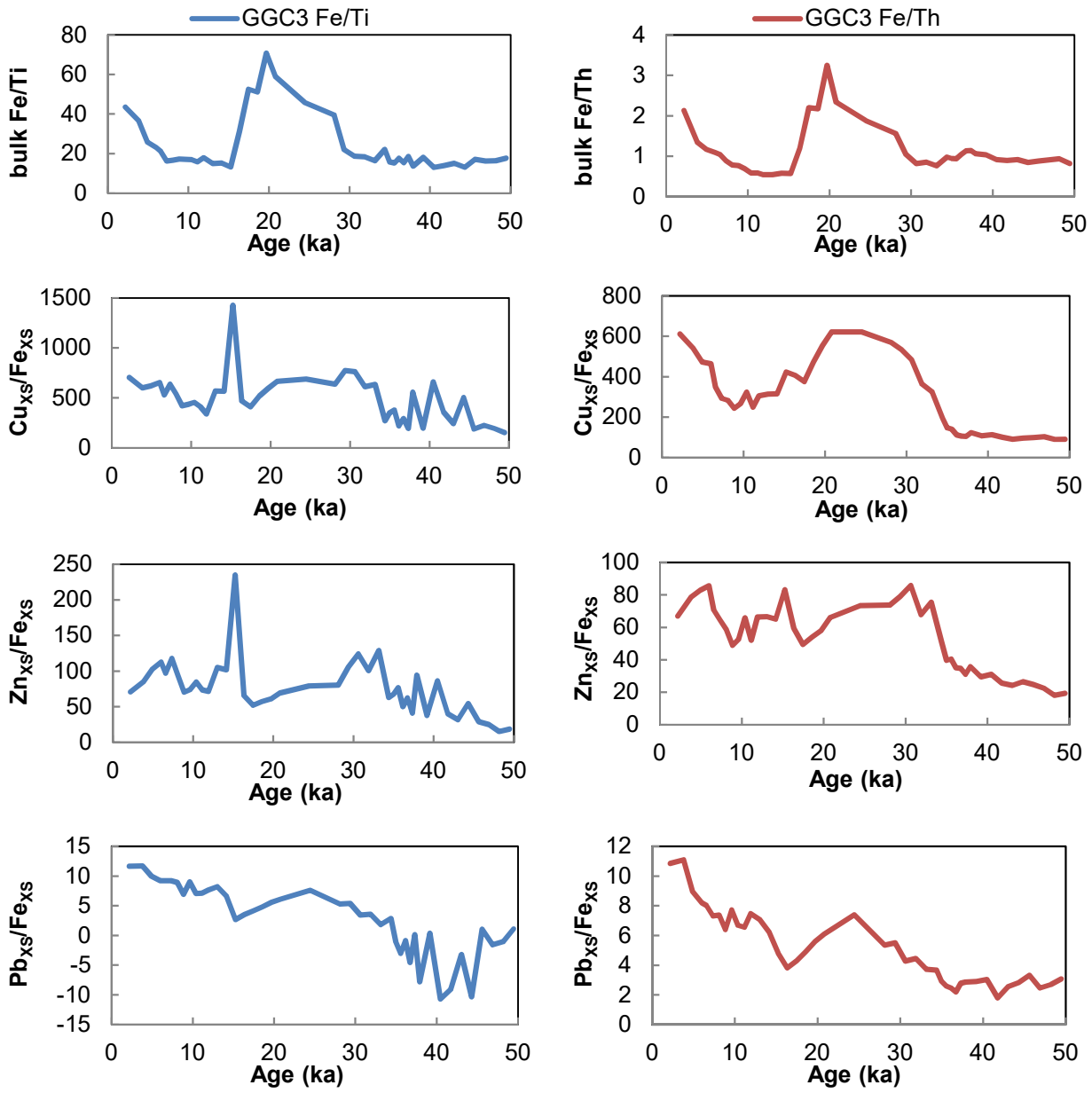

Figure 2.11: Temporal variability in excess elemental concentrations with respect to excess Fe in sediments from Mir zone. Bulk sediment Fe/Ti and Fe/Th ratios demonstrate relative concentrations of hydrothermal to lithogenic material for reference. Ratios are calculated following Ti-based (blue) and Th-based (red) lithogenic corrections. Note variations in the y-axis scale between left and right panels. Th-based lithogenic corrections are preferred as they yield fewer negative excess elemental values. Variations in excess Cu/Fe, Zn/Fe, and Pb/Fe may reflect variations in the conditions of hydrothermal reactions within the crust.

excess Zn/Fe oscillate about a higher baseline (54 to 84 ppm/wt%), peaking again at ~15 and ~6 ka. The excess Pb/Fe pattern more closely resembles that of Cu/Fe compared to Zn/Fe, with a relatively flat range prior to 35 ka (1.8 to 3.3 ppm/wt%), followed by a gradual increase to a peak at ~25 ka (7.8 ppm/wt%) and a gradual decline to ~16 ka (3.8 ppm/wt%). However, in contrast to excess Cu/Fe, excess Pb/Fe reaches its highest value in the Holocene hydrothermal peak at ~4 ka (11 ppm/wt%). The diversity of peak excess Cu/Fe, Zn/Fe, and Pb/Fe values is in stark contrast to the $^{3}He_{ET}$-derived excess Fe, Cu, Zn, and Pb flux records, which all peak at ~19 ka (Figure 2.8). This suggest that the mechanisms driving variations in vent fluid chemistry are not dominating the total hydrothermal output of the Mir zone vent field.

The observed Cu/Fe values are typically an order of magnitude lower than the average Cu/Fe value of 5900 ppm/wt% measured in Mir sulfide deposits retrieved from the vents themselves (Rona et al., 1993). The relatively low excess Cu/Fe values in the Mir sediment core are consistent with decreasing Cu deposition with distance from the vent source as sulfide phases are depleted from the hydrothermal plume (e.g., German et al., 1991a). The Mir sediment Zn/Fe ratios are also typically an order of magnitude lower than the average Zn/Fe value of 3800 ppm/wt% for Mir chimney fragments, but are well within the <30 to 114 ppm/wt% range of Ze/Fe ratios observed in the Mir massive sulfide talus (Rona et al., 1993). The pattern of generally higher Holocene excess Cu/Fe, Zn/Fe, and Pb/Fe values, relative to >35 ka, is similar to the trend observed in excess Cu, Zn, and Pb fluxes, which sit at a higher baseline value in the Holocene relative to >35 ka (Figure 2.8). The higher Holocene background in hydrothermal flux and associate high ratios of excess Cu/Fe, Zn/Fe, and Pb/Fe may reflect enhanced hydrothermal deposition associated with the opening of a new vent in close proximity to the Mir sediment core

location. The formation of new chimneys may occur when new fluid pathways are generated through crustal fracturing or the sealing of old pathways caused by mineral precipitation (Humphris and Tivey, 2000).

2.4.1.2. V and P

Variability in excess V/Fe and P/Fe is likely to be driven by changes within the oxidation and precipitation of material from the hydrothermal plume, rather than as a direct result of changes in fluid reactions with the ocean crust, because V and P are scavenged from surrounding seawater by Fe-oxyhydroxide formation within the plume (Feely et al., 1991; German et al., 1991a,b). Thus, V/Fe and P/Fe variability may reflect changes in the chemistry of the hydrothermal plume (e.g., German et al., 1991a) or larger scale changes in seawater chemistry (Feely et al., 1998; Cave et al., 2002).

Unlike the sulfide-associated Cu, Zn, and Pb, Mir sediment excess V/Fe ratios are lowest during the glacial hydrothermal peak (~30 to 18 ka; Figure 2.13). The narrow range of excess V/Fe ratios observed during the glacial hydrothermal peak (18 to 20 ppm/wt%) is lower than the average V/Fe ratio of ~45 ppm/wt% observed in hydrothermal sediments from the TAG hydrothermal field (Trocine and Trefry, 1988) and may reflect the relative dilution of V scavenged by Fe-oxyhydroxides by increased deposition of sulfide hosted Fe (e.g., Trefry and Metz, 1989). In stark contrast to the glacial hydrothermal peak, the Holocene hydrothermal peak coincides with the highest excess V/Fe values observed in Mir sediments, which increase from 18 ppm/wt% at ~18 ka to 43 ppm/wt% at ~5 ka. Thus, the Holocene hydrothermal peak recorded

in Mir sediments may reflect distinct hydrothermal plume depositional processes than those occurring during the increased hydrothermal activity of the glacial period.

Alternatively, variations in the V/Fe ratios of hydrothermal particulates have been hypothesized to reflect changes in the local seawater P, because V and P compete with each other for Fe-oxyhydroxide particle adsorption sites (Feely et al., 1998). Sedimentary analyses from the Rainbow hydrothermal field (36°N on the Mid-Atlantic Ridge) reveal higher V/Fe and lower P/Fe values in Holocene hydrothermal deposits relative to hydrothermal deposits during the Last Glacial Maximum and deglacial periods (Cave et al., 2002). Following the Feely et al. (1998) hypothesis, the Rainbow data would suggest that the deep water feeding the axial valley of the Mid-Atlantic Ridge had higher P concentrations during the glacial period than during the Holocene that may be associated with an increased proportion of P-rich Labrador Deep Water incorporated into the formation of North East Atlantic Deep Water (Cave et al., 2002). However, while excess V/Fe ratios in the Mir sediments follow the same temporal trend as those observed at Rainbow, excess P/Fe ratios in the Mir sediments decidedly do not (Figure 2.12). As with excess V/Fe, excess P/Fe ratios are lowest during the glacial hydrothermal peak (~30 to 18 ka). The coinciding minimum in Mir zone excess V/Fe and excess P/Fe ratios during the glacial hydrothermal peak supports the interpretation that the sulfide phases dominant the hydrothermal sedimentary fluxes at this time. Notably, Mir excess P/Fe ratios do exhibit inverse behavior to excess V/Fe ratios after the glacial hydrothermal peak. In contrast to the gradual increase from ~18 ka to the core top observed in excess V/Fe, excess P/Fe ratios peak at ~12 ka and gradually decline towards the core top. The Holocene excess P/Fe trend may reflect changes in non-hydrothermal excess P deposition within the Mid-Atlantic, however, as indicated by a peak in

Broken Spur excess P fluxes at ~12 ka, despite weak evidence for hydrothermal deposition in the Broken Spur sediments (Figure 2.9).

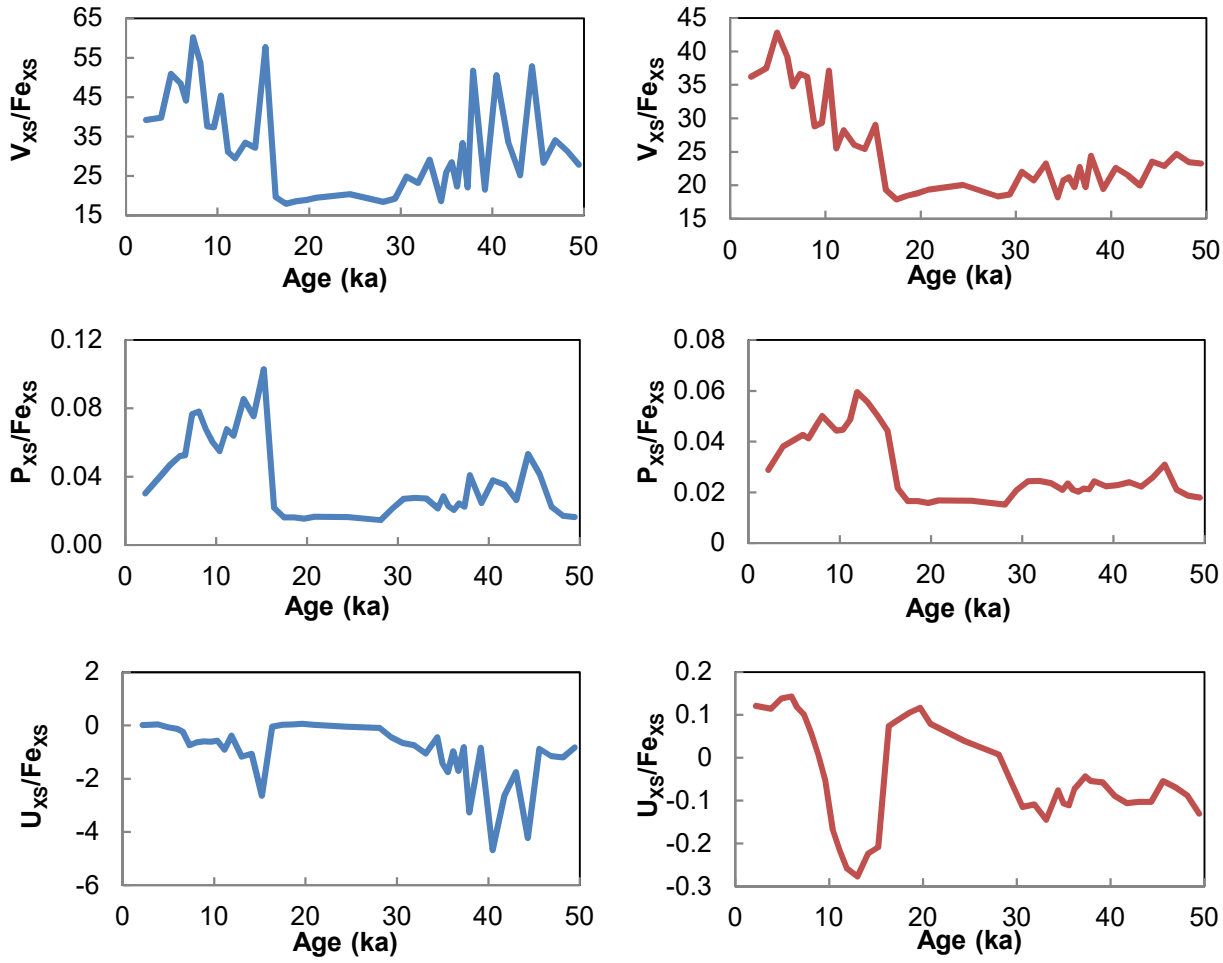

Figure 2.12: Temporal variability in excess elemental concentrations with respect to excess Fe in sediments from Mir zone. Ratios are calculated following Ti-based (blue) and Th-based (red) lithogenic corrections. Note variations in the y-axis scale between left and right panels. Th-based lithogenic corrections are preferred as they yield fewer negative excess elemental values. Variations in excess V/Fe, P/Fe and U/Fe may reflect variations seawater interactions with the hydrothermal plume and redox conditions within the sediments.

2.4.2 High-resolution elemental variability resolved by XRF analyses

High resolution XRF derived Mir elemental data are additionally available for Fe, Ti, Cu, and Zn. In the absence of XRF Th data, high resolution XRF derived records of compositional variability are limited to Ti-based excess elemental determinations (Figure 2.13).

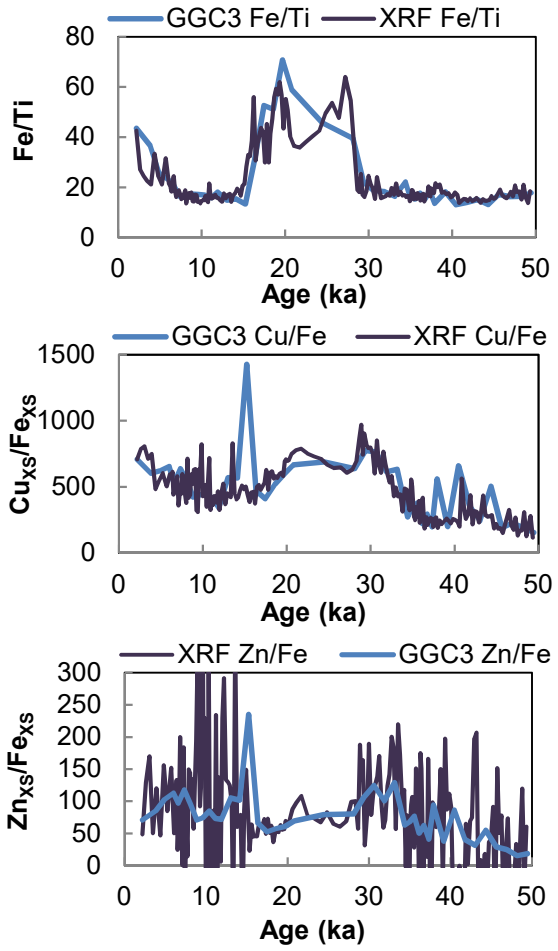

Figure 2.13: Comparison of ICP-based (thick blue line) and XRF-based (thin navy line) bulk sediment Fe/Ti and excess Cu/Fe and Zn/Cu ratios in Mir sediments. The high-resolution XRF-based data reveals to two peaks during the glacial hydrothermal maximum. The ICP-based excess Cu/Fe at ~15 ka and the XRF-based high frequency noise in Zn/Fe ratios prior to ~30 ka and after ~16 ka are interpreted to be analytical artifacts.

There are two major differences between the ICP-MS-based and XRF-based excess elemental ratio records that are interpreted to reflect analytical artifacts within the data (Figure 2.13). First, the obvious peak in the excess Cu/Fe ratio observed in the Ti-based ICP-MS records (Figure 2.12) at ~15 ka is not observed in the high-resolution XRF records. Accordingly, this inferred peak may not reflect representative sediment compositions. Second, XRF-derived excess Zn/Fe ratios exhibit very high amplitude and high frequency variability prior to ~30 ka and after ~16 ka. This high frequency variability likely reflects noise in the XRF derived excess Zn/Fe signal during intervals with low concentrations of hydrothermal Zn rather than significant changes in the Zn/Fe ratio of Mir hydrothermal deposits. The remaining distinctions between the excess elemental ratio records constrained by the two analytical methods are interpreted to reflect the difference in sampling resolution (see Section 2.2.3).

The high-resolution bulk sediment Fe/Ti records indicate that the initially observed broad glacial peak in hydrothermal deposition actually reflects two distinct intervals of intense hydrothermal activity (Figure 2.13). Rather than a single peak at ~20 ka, the XRF-derived Fe/Ti record exhibits a rapid increase from 18 wt.%/wt.% at ~29 ka up to a peak of 63 wt.%/wt.% at ~ 27 ka. The Fe/Ti values then decrease to a local minimum of 36 wt.%/wt.% at ~21 ka before increasing again to 62 wt.%/wt.% at ~19 ka. Finally, glacial period of hydrothermal deposition ends with a sharp decline in Fe/Ti values from ~40 wt.%/wt.% at ~17 ka to ~20 wt.%/wt.% at ~15 ka. The remainder of the XRF derived Fe/Ti record is similar to that indicated by the ICP-MS data (Figure 2.13). Bulk sediment XRF-derived Cu/Ti and Zn/Ti records similarly exhibit double peak behavior across the glacial hydrothermal maximum, although the Zn/Ti peak at ~27 ka is distinctly higher than the second peak at ~19 ka (Figure 2.14). The consistent pattern observed

between bulk Fe/Ti, bulk Cu/Ti, and bulk Zn/Ti values suggest that the bulk depositional patterns of excess Fe, Cu, and Zn are governed by the same general trend in hydrothermal variability during the glacial double peak.

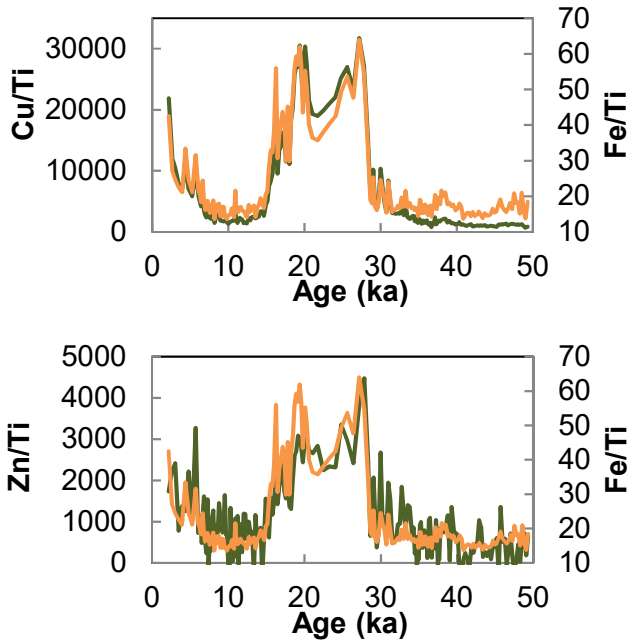

Figure 2.14: Comparison of bulk sediment Fe/Ti (orange), Cu/Ti (green, upper panel), and Zn/Ti ratios (green, lower panel) in the Mir zone sediments. The high-resolution XRF-based data reveals to two peaks during the glacial hydrothermal maximum, where ICP-based data resolved only one.

Examination of the excess Cu/Fe and Zn/Fe ratios provides clues as to the mechanisms driving the glacial double peak in hydrothermal activity. The excess Cu/Fe ratio begins to rise and clearly peaks before the occurrence of maximum hydrothermal concentrations as indicated by the bulk Fe/Ti ratio (Figure 2.15). Excess Cu/Fe values then decline before the Fe/Ti ratio peak at ~27 ka and rise again to peak at ~20 ka, again before the Fe/Ti maximum at ~19 ka. The inverted behavior between excess Cu/Fe and bulk Fe/Ti is unlikely to be related to uncertainties in the Ti-based lithogenic correction used to calculate excess Cu/Fe, because the bulk sediment Cu/Fe

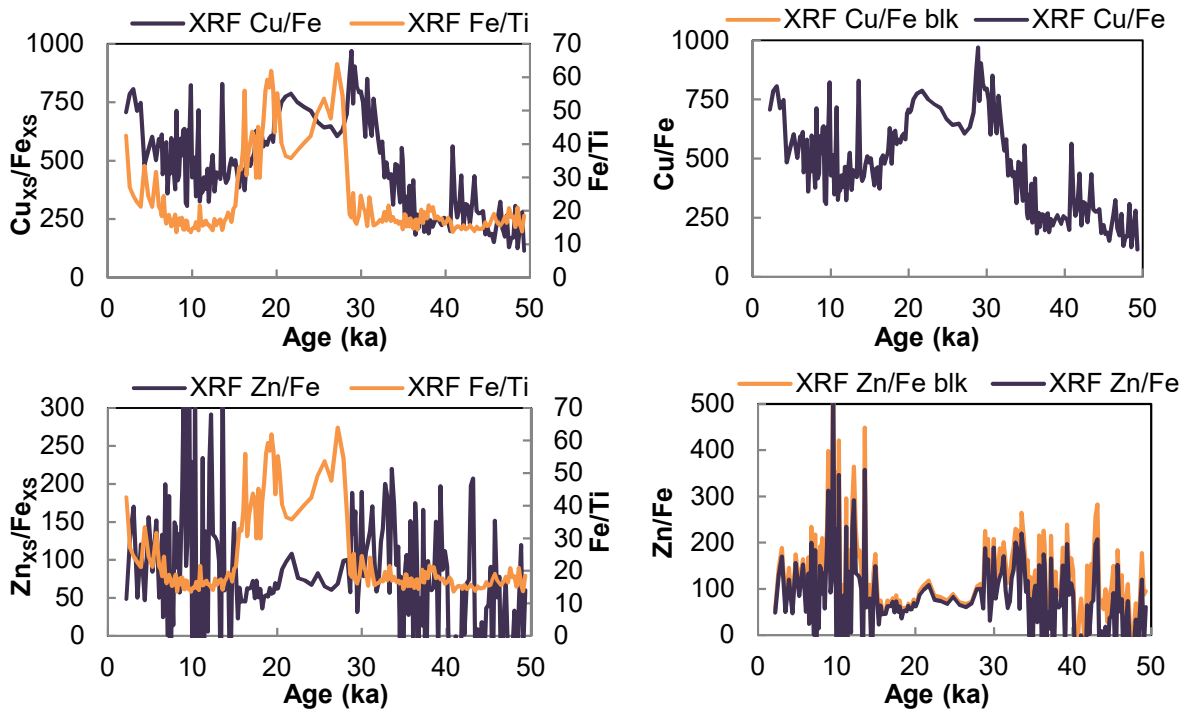

Figure 2.15: Comparison of Cu/Fe (upper panels) and Zn/Fe (lower panels) with Fe/Ti. Left panels compare excess Cu/Fe and Zn/Fe ratios (navy) to bulk sediment Fe/Ti ratios (orange). Bulk sediment Fe/Ti is used an indicator of the relative hydrothermal and lithogenic contributions to the Mir zone sediments. Right panels compare excess Cu/Fe and Zn/Fe values with bulk sediment Cu/Fe and Zn/Fe. Bulk sediment ratios for these elements appear to be governed by the hydrothermal input in the Mir sediments.

values are nearly identical to the excess Cu/Fe Mir sedimentary record (Figure 2.15). In marked contrast to the compositional variability during the glacial hydrothermal peak, the Holocene increase in hydrothermal deposition exhibits contemporaneous increased in Fe/Ti and Cu/Fe (Figure 2.13). Although Zn/Fe ratios outside of the glacial hydrothermal periods are difficult to interpret, both excess Zn/Fe and bulk Zn/Fe ratios also peak prior to the maximum occurrence of hydrothermal deposition (Figure 2.15). Accordingly, the observed compositional variability in the high-resolution Mir record suggest that each hydrothermal Fe peak during the glacial period may be preceded by a ~5 kyr phase of low level, yet increasing, hydrothermal activity yielding relatively Cu-rich hydrothermal material. Such episodes could result from low levels of very

high temperature venting associated with limited fluid flow through regions through hot crust potentially associated with recent magmatic migration. As the crust cools and fractures, enhanced hydrothermal circulation may follow yielding higher total fluxes of all hydrothermal elements, yet lower excess Cu/Fe ratios due to the decreased temperature of the reaction zone.

2.5. Sea level change and a revised record of Mir zone hydrothermal activity

The high resolution XRF concentration data suggest that the Mir zone hydrothermal flux record is more variable that as reported by Middleton et al. (2016). Thus, the comparison between sea level variability and hydrothermal output at the Mir zone vent field merits reevaluation.

Although $^{3}He_{ET}$-derived elemental flux data are only available at the 1 to 2 cm sampling resolution of the ICP-MS records, an approximate record of 4-mm resolution hydrothermal fluxes can be estimated from the XRF derived Fe/Ti record. Despite temporal variability in the total Ti flux to the Mir zone sediments (Middleton et al., *in press*), the unsmoothed $^{3}He_{ET}$ -derived excess Fe flux record in the Mir sediments is very strongly correlated (R = 0.93) with the bulk Fe/Ti record determined using ICP-MS (Figure 2.16). Assuming a linear relationship between hydrothermal Fe deposition within the Mir sediments and resulting Fe/Ti ratios, high resolution hydrothermal Fe fluxes (Φ_{FeHT*}) can be estimated from the XRF derived Fe/Ti record using the following empirical equation:

$$\Phi_{FeHT*} = (0.37) * (Fe/Ti) - 4.5 \qquad \text{EQ. 2.3}$$

where units Φ_{FeHT*} are mg/cm^2 ka and Fe/Ti units are wt.%/wt.%. It is noted that this empirical approach is viable in the Mir zone sediments due to the high magnitude of hydrothermal Fe deposition relative to variations in lithogenic input and may not be applicable in sediments with relatively lower hydrothermal fluxes. The empirically estimated hydrothermal Fe flux record provides a means to resolve the apparent double peak in Mir zone hydrothermal activity within the glacial period and provides a more nuanced record with which to investigate the relationship between sea level change and hydrothermal activity (Figure 2.17).

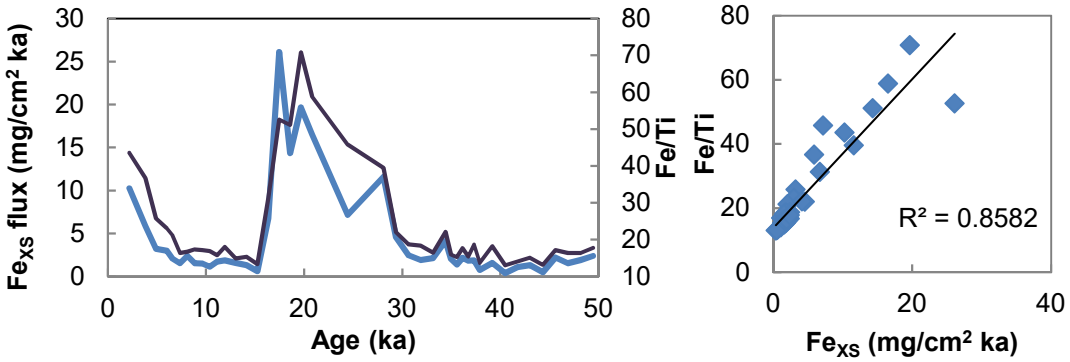

Figure 2.16: Temporal correlations between bulk sediment Fe/Ti ratios derived using ICP-MS (thin navy line) and the coincident Fe_{XS} flux in Mir zone sediments (thick blue line). Plotted excess Fe fluxes represent the unsmoothed flux record to match the resolution of Fe/Ti data. High correlation (R = 0.93) between these values suggests that hydrothermal Fe deposition dominantly drives variability in Fe/Ti.

The revised hydrothermal Fe flux record suggests that the possible relationship between rapid sea level changes and hydrothermal activity at the Mir zone may be more complicated than previously understood (e.g., Middleton et al., 2016; Figure 2.17). Middleton et al. (2016) suggested that the rapid sea level fall expected at ~28 ka coincided with the increased hydrothermal deposition to the Mir sediments that then ceased began to decline at ~15 ka,

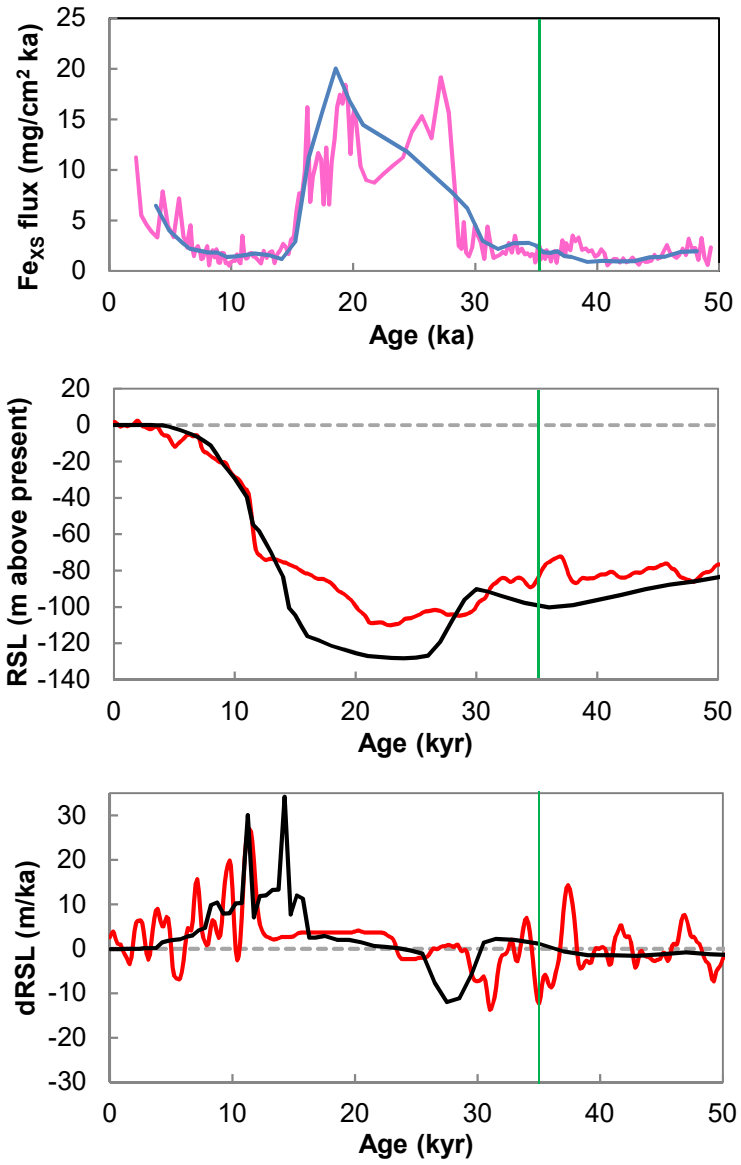

Figure 2.17: Comparison of Mir hydrothermal Fe flux with sea level changes over the past 50 ka. The 4 mm resolution XRF-based Mir excess Fe flux estimate (pink) is plotted against the 2 cm resolution $^{3}He_{ET}$-derived hydrothermal Fe flux record (blue; Middleton et al., 2016) on the revised timescale of Middleton et al. (*in press*). Relative sea level (RSL) and rate of sea level change (dRSL) curves are from Middleton et al. (2016; black) and Grant et al. (2014; red). Green line indicates 35 ka, where hydrothermal Cu/Fe ratios begin to increase.

coincident with the onset of rapid sea level rise associated with deglaciation. One complication of this analysis is that the relative sea level curve (RSL) and the derivative relative sea level curve (dRSL) used by Middleton et al. (2016) was computed in 2 kyr time-steps and consequently does not resolve higher frequency variations in sea level that may be associated with rapid sea level rise or fall (Figure 2.17; Grant et al., 2014). In turn, the higher resolution RSL curve presented by Grant et al. (2014) may exclude some rapid sea level changes, such as meltwater pulse 1A (Deschamps et al., 2012), that could have significant influence on submarine hydrothermal activity. Thus, the dRSL curves used to examine potential connections between hydrothermal activity and sea level change are sensitive to the methods used in their determination.

One might suggest that the onset of the glacial increase in hydrothermal activity recorded in the Mir record occurs at ~29 ka, when hydrothermal Fe fluxes rapidly increase, and is thus coincident with the rapid sea level fall estimated by Middleton et al. (2016). Alternatively, one might interpret the onset of the glacial increase in Mir hydrothermal activity to occur at ~35 ka, when the hydrothermal Cu/Fe ratio begins to climb, coincident with an interval of rapid sea level fall estimated by Grant et al. (2014). Either explanation could be used to support a connection between sea level change and hydrothermal output, but the offset in the timing between records of the rapid sea level fall preceding the Last Glacial Maximum renders these explanations less satisfactory.

Regardless of the RSL curve examined, the double peak across the glacial interval resolved in the revised hydrothermal Fe flux record indicates distinct changes in hydrothermal activity from

~27 ka to ~23 ka to ~19 ka that are not coincident with any major sea level change (Figure 2.17). Such hydrothermal variability must be driven by a more localized control on heat flux to the Mir hydrothermal zone, such as tectonic activity or variations in local magmatic supply (e.g., Humphris and Tivey, 2000). Thus, while sea level may not be the only driver of Mir zone hydrothermal output, the revised Mir zone record is not inconsistent with the hypothesis that sea level variability influences submarine hydrothermal activity.

2.6. Conclusions

This study constrains the magnitude and compositional variability (including Fe, Cu, P, V, Mn, Zn, Pb, and U) of hydrothermal sediment fluxes in two sediment cores from the Mir Zone of the TAG segment and from the Broken Spur segment of the Mid-Atlantic Ridge over the past glacial period. Hydrothermal fluxes were computed from major and trace element concentration data after corrections for lithogenic input and using extraterrestrial helium-3 derived vertical sediment rain rates.

The lack of significant hydrothermal deposition within the GGC6 sediments suggests that the occurrence of such megaplumes within the Broken Spur segment of the Mid-Atlantic Ridge may have been extremely rare over the past 70 ka. The Broken Spur sediment core exhibits little to no hydrothermal deposition over the past 70 ka and is likely shielded from typical Broken Spur vent field activity due to bathymetric barriers. Weak hydrothermal deposition within the Broken Spur core precludes its ability to record the possible effects of sea level change on Mid-Atlantic Ridge

hydrothermal activity. However, the Broken Spur record provides a compositional reference for the background elemental variability expected along the Mid-Atlantic Ridge.

High temporal resolution hydrothermal Fe fluxes were empirically estimated from XRF-derived bulk sediment Fe/Ti ratios to provide a revised record Mir Zone hydrothermal activity over the past 50 ka. In contrast to the previous work by Middleton et al. (2016), the revised Mir record suggests the occurrence of two distinct peaks in hydrothermal deposition between ~30 and ~15 ka in addition to a late Holocene increase in hydrothermal deposition. Holocene hydrothermal deposits represent a distinct composition differences from those deposited during the glacial period. Excess Cu/Fe and Zn/Fe ratios within the Mir sediments demonstrate additional compositional variability within the hydrothermal sediments associated with each of the two glacial peaks in hydrothermal deposition. The additional variability in hydrothermal deposition revealed by the high-resolution excess Fe flux record suggests that sea level is not the only cause of variability in Mir zone hydrothermal activity. However, the high resolution hydrothermal record of Mir zone remains consistent with the hypothesis that rapid sea level changes can affect mid-ocean ridge hydrothermal circulation.

References

Adkins, J., Demenocal, P., Eshel, G., 2006. The "African humid period" and the record of marine upwelling from excess ^{230}Th in Ocean Drilling Program Hole 658C. Paleoceanography 21.

Baker, E., Lavelle, J., Feely, R., Massoth, G., Walker, S., Lupton, J., 1989. Episodic venting of hydrothermal fluids from the Juan de Fuca Ridge. Journal of Geophysical Research: Solid Earth 94, 9237-9250.

Baker, E.T., Massoth, G.J., Feely, R.A., 1987. Cataclysmic hydrothermal venting on the Juan de Fuca Ridge. Nature 329, 149-151.

Beaulieu, S.E., 2015, InterRidge Global Database of Active Submarine Hydrothermal Vent Fields: prepared for InterRidge, Version 3.3. World Wide Web electronic publication. Version 3.X accessed 2017-10-01, http://vents-data.interridge.org

Burley, J.M., Katz, R.F., 2015. Variations in mid-ocean ridge CO_2 emissions driven by glacial cycles. Earth and Planetary Science Letters 426, 246-258.

Campbell, A., Palmer, M., Klinkhammer, G., Bowers, T., Edmond, J., Lawrence, J., Casey, J., Thompson, G., Humphris, S., Rona, P., 1988. Chemistry of hot springs on the Mid-Atlantic Ridge. Nature 335, 514-519.

Canales, J.P., Sohn, R.A., Demartin, B.J., 2007. Crustal structure of the Trans-Atlantic Geotraverse (TAG) segment (Mid-Atlantic Ridge, 26° 10′ N): Implications for the nature of hydrothermal circulation and detachment faulting at slow spreading ridges. Geochemistry, Geophysics, Geosystems 8.

Castillo, S., Moreno, T., Querol, X., Alastuey, A., Cuevas, E., Herrmann, L., Mounkaila, M., Gibbons, W., 2008. Trace element variation in size-fractionated African desert dusts. Journal of Arid Environments 72, 1034-1045.

Cave, R., German, C., Thomson, J., Nesbitt, R., 2002. Fluxes to sediments underlying the Rainbow hydrothermal plume at 36° 14′ N on the Mid-Atlantic Ridge. Geochimica et Cosmochimica Acta 66, 1905-1923.

Cherkashov, G., Kuznetsov, V., Kuksa, K., Tabuns, E., Maksimov, F., Bel'tenev, V., 2017. Sulfide geochronology along the Northern Equatorial Mid-Atlantic Ridge. Ore Geology Reviews 87, 147-154.

Crowley, J.W., Katz, R.F., Huybers, P., Langmuir, C.H., Park, S.-H., 2015. Glacial cycles drive variations in the production of oceanic crust. Science 347, 1237-1240.

deMartin, B.J., Sohn, R.A., Pablo Canales, J., Humphris, S.E., 2007. Kinematics and geometry of active detachment faulting beneath the Trans-Atlantic Geotraverse (TAG) hydrothermal field on the Mid-Atlantic Ridge. Geology 35, 711-714.

Deschamps, P., Durand, N., Bard, E., Hamelin, B., Camoin, G., Thomas, A.L., Henderson, G.M., Okuno, J.i., Yokoyama, Y., 2012. Ice-sheet collapse and sea-level rise at the Bølling warming 14,600 years ago. Nature 483, 559.

Dunk, R.M., Mills, R.A., 2006. The impact of oxic alteration on plume-derived transition metals in ridge flank sediments from the East Pacific Rise. Marine geology 229, 133-157.

Edmond, J., Campbell, A., Palmer, M., Klinkhammer, G., German, C., Edmonds, H., Elderfield, H., Thompson, G., Rona, P., 1995. Time series studies of vent fluids from the TAG and MARK sites (1986, 1990) Mid-Atlantic Ridge: a new solution chemistry model and a mechanism for Cu/Zn zonation in massive sulphide orebodies. Geological Society, London, Special Publications 87, 77-86.

Farley, K., 1995. Cenozoic variations in the flux of interplanetary dust recorded by 3He in a deep-sea sediment. Nature 376, 153.

Farley, K., Patterson, D., 1995. A 100-kyr periodicity in the flux of extraterrestrial ^{3}He to the sea floor. Nature 378, 600.

Feely, R.A., Trefry, J.H., Lebon, G.T., German, C.R., 1998. The relationship between P/Fe and V/Fe ratios in hydrothermal precipitates and dissolved phosphate in seawater. Geophysical Research Letters 25, 2253-2256.

Feely, R.A., Trefry, J.H., Massoth, G.J., Metz, S., 1991. A comparison of the scavenging of phosphorus and arsenic from seawater by hydrothermal iron oxyhydroxides in the Atlantic and Pacific Oceans. Deep Sea Research Part A. Oceanographic Research Papers 38, 617-623.

Fitzsimmons, J.N., John, S.G., Marsay, C.M., Hoffman, C.L., Nicholas, S.L., Toner, B.M., German, C.R., Sherrell, R.M., 2017. Iron persistence in a distal hydrothermal plume supported by dissolved-particulate exchange. Nature Geoscience 10, 195-201.

Fouquet, Y., Cambon, P., Etoubleau, J., Charlou, J.L., Ondréas, H., Barriga, F.J., Cherkashov, G., Semkova, T., Poroshina, I., Bohn, M., 2010. Geodiversity of Hydrothermal Processes Along the Mid-Atlantic Ridge and Ultramafic-Hosted Mineralization: a New Type Of Oceanic Cu-Zn-Co-Au Volcanogenic Massive Sulfide Deposit. Diversity of hydrothermal systems on slow spreading ocean ridges, 321-367.

Foustoukos, D.I., Seyfried, W., 2005. Redox and pH constraints in the subseafloor root zone of the TAG hydrothermal system, 26° N Mid-Atlantic Ridge. Earth and Planetary Science Letters 235, 497-510.

Froelich, P.N., Klinkhammer, G., Bender, M.L., Luedtke, N., Heath, G.R., Cullen, D., Dauphin, P., Hammond, D., Hartman, B., Maynard, V., 1979. Early oxidation of organic matter in pelagic sediments of the eastern equatorial Atlantic: suboxic diagenesis. Geochimica et Cosmochimica Acta 43, 1075-1090.

German, C., Campbell, A., Edmond, J., 1991a. Hydrothermal scavenging at the Mid-Atlantic Ridge: modification of trace element dissolved fluxes. Earth and Planetary Science Letters 107, 101-114.

German, C., Fleer, A., Bacon, M., Edmond, J., 1991b. Hydrothermal scavenging at the Mid-Atlantic Ridge: radionuclide distributions. Earth and Planetary Science Letters 105, 170-181.

German, C., Rudnicki, M., Klinkhammer, G., 1999. A segment-scale survey of the Broken Spur hydrothermal plume. Deep Sea Research Part I: Oceanographic Research Papers 46, 701-714.

German, C., Seyfried, W., 2014. Hydrothermal processes. In 'Treatise on Geochemistry'.(Eds H. Holland and K. Turekian.) pp. 191–233. Elsevier: Amsterdam, Netherlands.

Grant, K., Rohling, E., Ramsey, C.B., Cheng, H., Edwards, R., Florindo, F., Heslop, D., Marra, F., Roberts, A., Tamisiea, M.E., 2014. Sea-level variability over five glacial cycles. Nature communications 5, ncomms6076.

Humphris, S.E., Tivey, M.K., 2000. A synthesis of geological and geochemical investigations of the TAG hydrothermal field: Insights into fluid-flow and mixing processes in a hydrothermal system. Special Papers-Geological Society of America, 213-236.

Huybers, P., Langmuir, C., 2009. Feedback between deglaciation, volcanism, and atmospheric CO_2. Earth and Planetary Science Letters 286, 479-491.

Huybers, P., Langmuir, C.H., 2017. Delayed CO_2 emissions from mid-ocean ridge volcanism as a possible cause of late-Pleistocene glacial cycles. Earth and Planetary Science Letters 457, 238-249.

Karson, J., Thompson, G., Humphris, S., Edmond, J., Bryan, W., Brown, J., Winters, A., Pockalny, R., Casey, J., Campbell, A., 1987. Along-axis variations in seafloor spreading in the MARK area. Nature 328, 681-685.

Kelley, D.S., Baross, J.A., Delaney, J.R., 2002. Volcanoes, fluids, and life at mid-ocean ridge spreading centers. Annual Review of Earth and Planetary Sciences 30, 385-491.

Klinkhammer, G., Palmer, M., 1991. Uranium in the oceans: where it goes and why. Geochimica et Cosmochimica Acta 55, 1799-1806.

Lalou, C., Reyss, J.L., Brichet, E., Rona, P.A., Thompson, G., 1995. Hydrothermal activity on a 105-year scale at a slow-spreading ridge, TAG hydrothermal field, Mid-Atlantic Ridge 26° N. Journal of Geophysical Research: Solid Earth 100, 17855-17862.

Lalou, C., Thompson, G., Arnold, M., Brichet, E., Druffel, E., Rona, P., 1990. Geochronology of TAG and Snakepit hydrothermal fields, Mid-Atlantic Ridge: witness to a long and complex hydrothermal history. Earth and Planetary Science Letters 97, 113-128.

Lilley, M.D., Feely, R.A., Trefry, J.H., 1995. Chemical and biochemical transformations in hydrothermal plumes. Seafloor hydrothermal systems: physical, chemical, biological, and geological interactions, 369-391.

Lund, D., Asimow, P., Farley, K., Rooney, T., Seeley, E., Jackson, E., Durham, Z., 2016. Enhanced East Pacific Rise hydrothermal activity during the last two glacial terminations. Science 351, 478-482.

Lund, D.C., Asimow, P.D., 2011. Does sea level influence mid-ocean ridge magmatism on Milankovitch timescales? Geochemistry, Geophysics, Geosystems 12.

Mangini, A., Jung, M., Laukenmann, S., 2001. What do we learn from peaks of uranium and of manganese in deep sea sediments? Marine Geology 177, 63-78.

Marcantonio, F., Anderson, R.F., Higgins, S., Stute, M., Schlosser, P., Kubik, P., 2001. Sediment focusing in the central equatorial Pacific Ocean. Paleoceanography 16, 260-267.

Marcantonio, F., Kumar, N., Stute, M., Anderson, R.F., Seidl, M.A., Schlosser, P., Mix, A., 1995. A comparative study of accumulation rates derived by He and Th isotope analysis of marine sediments. Earth and Planetary Science Letters 133, 549-555.

Middleton, J.L., Langmuir, C.H., Mukhopadhyay, S., McManus, J.F., Mitrovica, J.X., 2016. Hydrothermal iron flux variability following rapid sea level changes. Geophysical Research Letters 43, 3848-3856.

Mills, R.A., Taylor, S.L., Pälike, H., Thomson, J., 2010. Hydrothermal sediments record changes in deep water oxygen content in the SE Pacific. Paleoceanography 25.

Murray, R., Knowlton, C., Leinen, M., Mix, A.C., Polsky, C., 2000. Export production and carbonate dissolution in the central equatorial Pacific Ocean over the past 1 Myr. Paleoceanography 15, 570-592.

Murton, B.J., Klinkhammer, G., Becker, K., Briais, A., Edge, D., Hayward, N., Millard, N., Mitchell, I., Rouse, I., Rudnicki, M., 1994. Direct evidence for the distribution and occurrence of hydrothermal activity between 27° N–30° N on the Mid-Atlantic Ridge. Earth and Planetary Science Letters 125, 119-128.

Resing, J.A., Sedwick, P.N., German, C.R., Jenkins, W.J., Moffett, J.W., Sohst, B.M., Tagliabue, A., 2015. Basin-scale transport of hydrothermal dissolved metals across the South Pacific Ocean. Nature 523, 200.

Rona, P., 1980. TAG hydrothermal field: Mid-Atlantic Ridge crest at latitude 26° N. Journal of the Geological Society 137, 385-402.

Rona, P.A., Bogdanov, Y.A., Gurvich, E.G., Rimski-Korsakov, N.A., Sagalevitch, A.M., Hannington, M.D., Thompson, G., 1993. Relict hydrothermal zones in the TAG Hydrothermal Field, Mid-Atlantic Ridge 26° N, 45° W. Journal of Geophysical Research: Solid Earth 98, 9715-9730.

Rousseau, R.M., Willis, J.P., Duncan, A.R., 1996. Practical XRF calibration procedures for major and trace elements. X-Ray Spectrometry 25, 179-189.

Rudnicki, M., James, R., Elderfield, H., 1994. Near-field variability of the TAG non-buoyant plume, 26° N, Mid-Atlantic Ridge. Earth and Planetary Science Letters 127, 1-10.

Saito, M.A., Noble, A.E., Tagliabue, A., Goepfert, T.J., Lamborg, C.H., Jenkins, W.J., 2013. Slow-spreading submarine ridges in the South Atlantic as a significant oceanic iron source. Nature Geoscience 6, 775.

Schoepfer, S.D., Shen, J., Wei, H., Tyson, R.V., Ingall, E., Algeo, T.J., 2015. Total organic carbon, organic phosphorus, and biogenic barium fluxes as proxies for paleomarine productivity. Earth-Science Reviews 149, 23-52.

Seewald, J.S., Seyfried, W.E., 1990. The effect of temperature on metal mobility in subseafloor hydrothermal systems: constraints from basalt alteration experiments. Earth and Planetary Science Letters 101, 388-403.

Shimmield, G., Price, N., 1986. The behaviour of molybdenum and manganese during early sediment diagenesis—offshore Baja California, Mexico. Marine Chemistry 19, 261-280.

Takayanagi, M., Ozima, M., 1987. Temporal variation of $^{3}He/^{4}He$ ratio recorded in deep-sea sediment cores. Journal of Geophysical Research: Solid Earth 92, 12531-12538.

Taylor, S.R., McLennan, S.M., 1995. The geochemical evolution of the continental crust. Reviews of Geophysics 33, 241-265.

Trefry, J.H., Metz, S., 1989. Role of hydrothermal precipitates in the geochemical cycling of vanadium. Nature 342, 531-533.

Trocine, R.P., Trefry, J.H., 1988. Distribution and chemistry of suspended particles from an active hydrothermal vent site on the Mid-Atlantic Ridge at 26° N. Earth and Planetary Science Letters 88, 1-15.

Von Damm, K., Bray, A., Buttermore, L., Oosting, S., 1998. The geochemical controls on vent fluids from the Lucky Strike vent field, Mid-Atlantic Ridge. Earth and Planetary Science Letters 160, 521-536.

Winckler, G., Anderson, R.F., Fleisher, M.Q., McGee, D., Mahowald, N., 2008. Covariant glacial-interglacial dust fluxes in the equatorial Pacific and Antarctica. Science 320, 93-96.

Chapter 3

Millennial-scale variations in dustiness recorded in Mid-Atlantic sediments from 0 to 70 ka

The contents of this chapter have been submitted for publication as:

Middleton, J.L., Mukhopadhyay, S., Langmuir, C.H., McManus, J.F., Huybers, P.J., 2017. Millennial-scale variations in dustiness recorded in Mid-Atlantic sediments from 0 to 70 ka. Earth and Planetary Science Letters (*in press*).

Abstract

Sedimentary records of dust deposition in the subtropical Atlantic provide important constraints on millennial- and orbital-scale variability in atmospheric circulation and North African aridity. Constant flux proxies, such as extraterrestrial helium-3, yield dust flux records that are independent of the biases caused by lateral sediment transport and limited resolution that may be associated with age-model-derived mass accumulation rates. However, Atlantic dust records constrained using constant flux proxies are sparsely distributed and generally limited to the past 20 ka. Here we extend the Atlantic record of North African dust deposition to 70 ka using extraterrestrial helium-3 and measurements of titanium, thorium, and terrigenous helium-4 in two sediment cores collected at 26°N and 29°N on the Mid-Atlantic Ridge and compare results to model estimates for dust deposition in the subtropical North Atlantic. Dust proxy fluxes between 26°N and 29°N are well correlated, despite variability in lateral sediment transport, and underscore the utility of extraterrestrial helium-3 for constraining millennial-scale variability in dust deposition. Similarities between Mid-Atlantic dust flux trends and those observed along the Northwest African margin corroborate previous interpretations of dust flux variability over the past 20 ka and suggest that long distance transport and depositional processes do not overly

obscure the signal of North African dust emissions. The 70 ka Mid-Atlantic record reveals a slight increase in North African dustiness from Marine Isotope Stage 4 through the Last Glacial Maximum and a dramatic decrease in dustiness associated with the African Humid Period. On the millennial-scale, the new records exhibit brief dust maxima coincident with North Atlantic cold periods such as the Younger Dryas, and multiple Heinrich Stadials. The correlation between Mid-Atlantic dust fluxes and previous constraints on North African aridity is high. However, precipitation exerts less control on dust flux variability prior to the African Humid Period, when wind variability governs dust emissions from consistently dry dust source regions. Thus, the Mid-Atlantic dust record supports the hypothesis that both aridity and wind strength drive dust flux variability across changing climatic conditions.

3.1. Introduction

Aeolian dust is an influential component of the climate system due to its radiative effects (Miller and Tegen, 1998; Rosenfeld et al., 2001) and the nutritional boon it brings to otherwise limited ecosystems (Bristow et al., 2010; Jickells et al., 2005; Martin, 1990). Constraints on variable dust emissions through changing climatic regimes are essential to understand the past and to forecast future scenarios (Albani et al., 2015; Albani et al., 2016; Evan et al., 2016; Mahowald et al., 2009; Mahowald et al., 2006; Pausata et al., 2016). The Sahel and Sahara regions of North Africa provide the largest contribution to modern global dust emissions (Goudie and Middleton, 2001; Prospero et al., 2002) and generate dust plumes that influence African and Atlantic surface temperatures, precipitation, and tropical cyclone development (Booth et al., 2012; Dunion and Velden, 2004; Evan et al., 2011).

Twentieth century records of Atlantic dustiness demonstrate a strong correlation between decreased North African rainfall and increased dust emissions on inter-annual timescales (Chiapello et al., 2005; Mukhopadhyay and Kreycik, 2008; Prospero and Lamb, 2003). Wind strength, however, also influences dustiness and recent studies suggest that wind strength, rather than aridity, is the primary driver of inter-annual variability in North African dust emissions (Ridley et al., 2014; Rodríguez et al., 2015). On millennial and orbital timescales, significant restructuring of atmospheric circulation may alter the relative importance of wind strength versus aridity in driving dust emissions. Separating these two effects, however, has been difficult because there are few records (Adkins et al., 2006; Bradtmiller et al., 2007; McGee et al., 2013; Tjallingii et al., 2008; Williams et al., 2016) that constrain North African dust deposition with

sufficient resolution to evaluate the changing distribution and drivers of emissions associated with millennial-scale climatic oscillations.

Marine sedimentary records of dust deposition can constrain climatic variability in continental aridity, wind strength, and the spatial pattern of atmospheric circulation (Grousset et al., 1998; Kohfeld and Harrison, 2001; McGee et al., 2010a; Parker et al., 2016; Rea, 1994; Ruddiman, 1997; Werner et al., 2002; Winckler et al., 2008). Sedimentary dust records, however, have often been calculated using mass accumulation rates estimated from the sediment core age-model and dry bulk density (Adkins et al., 2006; deMenocal et al., 2000; Ruddiman, 1997). Such accumulation estimates are limited to the temporal resolution of the age-model and typically assume constant sedimentation rates between chronostratigraphic tie-points. Age-model-derived fluxes are additionally subject to biases introduced by lateral sediment transport. These biases complicate the interpretation of age-model-derived records because the magnitude of sediment winnowing or focusing at a given location can vary across climatic cycles (Suman and Bacon, 1989; Costa and McManus, 2017; Higgins et al., 2002; Marcantonio et al., 1996).

In contrast, constant flux proxies, such as excess thorium-230 (Bacon, 1984; Francois et al., 2004; Marcantonio et al., 2001a) and extraterrestrial helium-3 ($^3He_{ET}$; McGee and Mukhopadhyay, 2013), can be used to constrain vertical sediment rain rates that are independent of age-model tie-points and lateral sediment transport. The increased resolution of dust records determined using constant flux proxies permits improved quantification and evaluation of dust flux variability. However, existing records of North African dustiness constrained using constant flux proxies are sparse and limited to the past 20 ka (Adkins et al., 2006; Bradtmiller et al., 2007;

McGee et al., 2013; Williams et al., 2016). These records indicate a broad mid-Holocene dust flux minimum (~5 to 11 ka) in the equatorial Atlantic, the western tropical Atlantic, and along the Northwest African margin, that is coincident with the African Humid Period. On millennial timescales, however, there is less agreement. Dust maxima are observed along the continental margin during the Younger Dryas and Heinrich 1 (McGee et al., 2013), yet the far-field records from the equatorial Atlantic and the Bahamas exhibit a singular early Holocene peak (Bradtmiller et al., 2007; Williams et al., 2016). Increased Atlantic coverage is essential to determine if such far-field locations provide clear records of continental dust generation or if they are affected by long distance transport and depositional processes. Furthermore, new and longer records improve constraints on African emissions in global dust cycle models (Albani et al., 2015; Albani et al., 2016; Mahowald et al., 2009) and are required to determine whether the past 20 ka are representative of typical dust flux variability prior to the Last Glacial Maximum.

Here we present new records of dust flux from two subtropical North Atlantic sediment cores collected at 26°N and 29°N on the Mid-Atlantic Ridge. Dust fluxes are determined from analyses of terrigenous helium-4 using extraterrestrial helium-3 as a constant flux proxy. Flux records of common thorium-232 and titanium are additionally examined to evaluate reproducibility between dust proxies in the Mid-Atlantic sediments. The new data extend the subtropical North Atlantic dust record to 70 ka and allow for evaluation of orbital- and millennial-scale variations in dust generation and long-distance transport through the last glacial period.

3.2. Geochemical Background

3.2.1 Dust proxies

Marine sediments include biogenic, authigenic, and lithogenic inputs. Thorium-232 (common Th), terrigenous helium-4 ($^4He_{terr}$), and titanium have all been used to constrain the lithogenic component of marine sediments due to relatively high concentrations of these tracers in continental crust (Marcantonio et al., 2001a; Mukhopadhyay and Kreycik, 2008; Murray et al., 2000; Patterson et al., 1999; Winckler et al., 2005). Thorium and $^4He_{terr}$ are distinctly advantageous as dust proxies because sedimentary concentrations of Th and $^4He_{terr}$ are less sensitive than Ti to the presence of volcanic inputs (Gale et al., 2013; Graham, 2002; Patterson et al., 1999). Consequently, Th and $^4He_{terr}$ have been increasingly utilized in combination with the excess ^{230}Th and extraterrestrial ^3He constant flux proxies to constrain aeolian dust fluxes (Adkins et al., 2006; Anderson et al., 2006; Kienast et al., 2016; Marcantonio et al., 2001a; Serno et al., 2014; Winckler et al., 2008; Winckler et al., 2005).

Ideally, the conversion of sedimentary Th or $^4He_{terr}$ concentrations into absolute dust concentrations would be based on tightly constrained values of Th or $^4He_{terr}$ in the dust end-member. However, $^4He_{terr}$ concentrations of North African dust sources are seldom measured (McGee et al., 2016; Mukhopadhyay and Kreycik, 2008) and dust concentrations of $^4He_{terr}$, Th, and Ti are each known to vary with grain size and among source regions (Castillo et al., 2008; McGee et al., 2016). Thus, absolute concentrations of sedimentary dust are difficult to constrain from analysis of a single lithogenic proxy. We examine $^4He_{terr}$, Th, and Ti fluxes in the Mid-

Atlantic sediments to evaluate the sensitivity of proxy-based dust records to each element of interest.

3.2.2 Extraterrestrial helium-3 as a constant flux proxy

Helium-4 accumulates in marine sediments primarily via the delivery of terrigenous dust, whereas ^{3}He is primarily delivered to the seafloor via interplanetary dust particles (IDPs; Farley, 1995; Nier and Schlutter, 1992; Takayanagi and Ozima, 1987). Sediment concentrations of extraterrestrial ^{3}He (^{3}He$_{ET}$) are determined by correcting total ^{3}He for its small terrigenous contribution (see Section 3.3.3). Previous work has shown that ^{3}He$_{ET}$ can be utilized as a constant flux proxy to calculate vertical sediment rain rates throughout much of the Cenozoic (Farley and Eltgroth, 2003; Farley, 1995; Marcantonio et al., 2001b; Marcantonio et al., 1995; Mukhopadhyay et al., 2001; Winckler et al., 2005). The term 'rain rate' refers to the vertical sediment flux as distinct from the traditional mass accumulation rate that may reflect the addition or subtraction of laterally advected material.

When the influx of IDP ^{3}He$_{ET}$ from space (f) is known, the vertical sediment rain rate (Φ_{sed}) can be determined through the relationship:

$$\Phi_{sed} = \frac{fR}{[3HeET]} \qquad \text{EQ. 3.1}$$

where R is the fraction of deposited He retained within the sediments (Farley, 1995). Observations of ^{3}He$_{ET}$ retention in ~480 Ma limestones suggest negligible variations in R over relatively short geologic intervals (Patterson et al., 1998). Previous studies of marine sediments and ice core records have demonstrated a constant Quaternary IDP ^{3}He$_{ET}$ flux and a value of 8.0

± 1.2 x 10^{-13} cm^3 STP cm^{-2} ka^{-1}, reflecting the mean and standard error of compiled marine studies, was used here (McGee and Mukhopadhyay, 2013). Distinct fluxes for individual elements and sedimentary components (Φ_x) are computed from vertical rain rates as follows:

$$\Phi_x = [X]_{sed} * \Phi_{sed} \quad \text{EQ. 3.2}$$

where $(X)_{sed}$ is the measured sediment concentration of the element or component of interest.

Constant flux proxies, such as $^3He_{ET}$, can also be used to calculate the sediment focusing factor (Ψ) and thus provide a quantitative constraint on the degree of lateral sediment redistribution affecting a marine sedimentary column (Francois et al., 2004; Higgins et al., 2002; Suman and Bacon, 1989). We adapt the original definition of Ψ, based on ^{230}Th, to define a Ψ_{He} as follows:

$$\Psi_{He} = \frac{\int_{z_1}^{z_2} [3HeET]\rho_b dz}{f(t_2 - t_1)} \quad \text{EQ. 3.3}$$

where z is depth in the core, ρ_b is the sediment dry bulk density, f is the known $^3He_{ET}$ influx from space as above, and t_1 and t_2 are the sediment ages at depths z_1 and z_2.

3.3. Sampling and Methods

Gravity cores KN207-2-GGC3 (26.14°N, 44.80°W, 3433 water depth, 82 cm core length) and KN207-2-GGC6 (29.21°N, 43.23°W, 3018 water depth, 147 cm core length) were recovered within the axial valley of the Mid-Atlantic Ridge during cruise KN207-2 of the *R/V Knorr* in June 2012 (Figure 3.1). The cores are located ~2500 km from the Northwest African coast and ~2000 km north of the center of the African dust plume, allowing for investigation into both the pattern of Mid-Atlantic dust deposition and long distance aeolian transport over the past 70 ka.

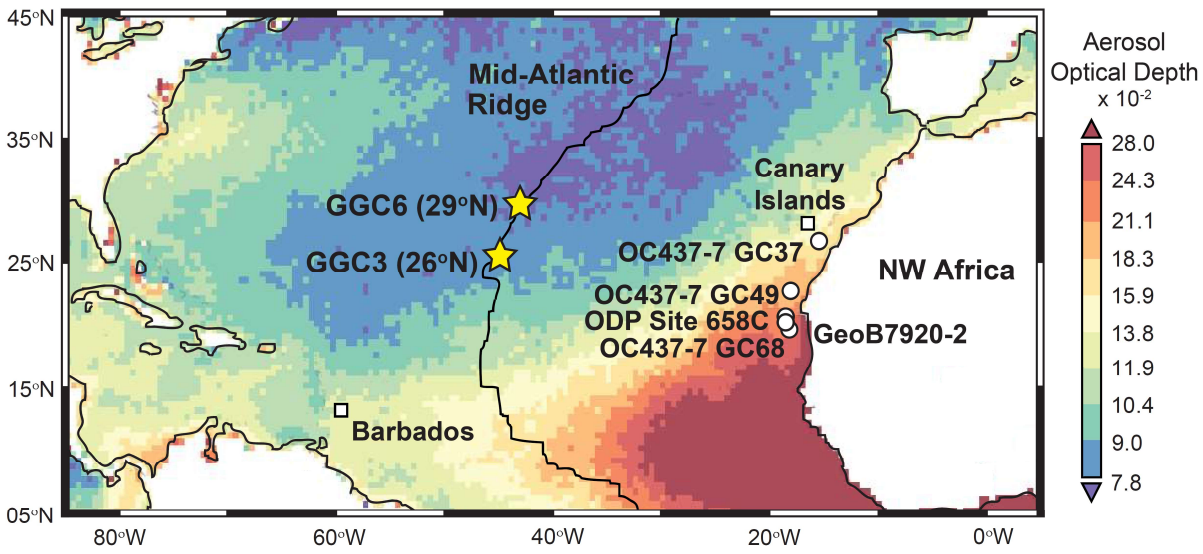

Figure 3.1: Map of sediment core locations. Sites for KN207-2 sediment cores used in this study (GGC6 and GGC3) are indicated by yellow stars. Core locations of previous work on Northwest African dust or aridity from ODP Site 658 (deMenocal et al., 2000; Adkins et al., 2006), select OC437-7 cores (McGee et al., 2013; Tierney et al., 2017) and GeoB7920-2 (Tjallingii et al., 2008) are indicated by white circles. Aerosol Optical Depth (AOD) values indicate the time averaged daily 670 nm SeaWiFS satellite data product from January 2004 to December 2009, downloaded from the Giovanni online data system of the NASA Goddard Earth Sciences Data and Information Services Center. AOD values are plotted on a logarithmic-scale to highlight contrasts across the Atlantic.

Both cores are dominantly carbonaceous oozes, with carbonate content ranging from 70 to 90 wt.% in GGC3 and from 80 to 95 wt.% in GGC6. Three carbonate-rich coarse layers are observed in GGC6 at 6-8 cm, 49-50 cm, and 71-73 cm and may result from small scale sediment redistribution events during which the fine sediment fraction was lost. No such coarse layers are observed in GGC3 (Figure C1). Iron and copper enrichments indicate intense hydrothermal deposition in GGC3 between 0-10 cm and 30-50 cm (Middleton et al., 2016), but analogous examination of GGC6 suggests little to no hydrothermal deposition in the 29°N sediments. Proximity to hydrothermal activity was not found to interfere with utilization of $^{3}He_{ET}$ as a constant flux proxy in GGC3 (Middleton et al., 2016). The full length of each core was sampled

in continuous 1 to 2 cm intervals and reported values reflect the sampled interval average. Contiguous sampling ensures that any millennial-scale excursion in dust flux preserved within the sediments is captured within the analytical record and thus precludes potential interpretation biases associated with unsampled intervals. However, the observed magnitude of each excursion is likely to be underrepresented due to bioturbation and sampling-associated smoothing of the record.

Terrigenous dust concentrations were evaluated using $^{4}He_{terr}$, Th, and Ti. Vertical sediment rain rates were constrained using $^{3}He_{ET}$ and were used to calculate dust fluxes following Equation 3.2. Sediment core age-models were determined using a combination of radiocarbon analyses and basin-scale correlations in bulk carbonate content stratigraphy. Additional chronostratigraphic context for the sedimentary records was provided by benthic foraminiferal oxygen isotope ($\delta^{18}O$) and carbon isotope ($\delta^{13}C$) analyses.

3.3.1 Sediment chronology and age-model-derived mass accumulation rates

The GGC6 age-model and an updated GGC3 age-model were determined using tie-points from radiocarbon analyses and from stratigraphic correlations of bulk carbonate contents. Radiocarbon measurements were performed on whole *G. ruber* tests at the National Ocean Sciences Accelerator Mass Spectrometry (NOSAMS) Facility at the Woods Hole Oceanographic Institution (See Supplementary Materials). Tests were sonicated for 30 sec in ethanol and for >1 min in distilled H_2O to reduce sedimentary contamination prior to submission to the NOSAMS facility. NOSAMS reported radiocarbon sample ages were converted to calendar years using

Calib 7.1 Marine 13 (Reimer et al., 2013; Stuiver and Reimer, 1993) which includes a time-dependent reservoir age that averages ~400 years. Two radiocarbon samples (GGC3: 64-66 cm and GGC6: 106-108 cm) yielded ages >38 ka and were not included in age-model calculations due to increased levels of uncertainty.

Given the high signal to noise ratio of bulk carbonate contents in GGC3 and GGC6 relative to benthic oxygen isotope values, millennial-scale variability in bulk carbonate contents was used to determine tie-points beyond the radiocarbon limit (Figure C2). Local carbonate concentration maxima were correlated with carbonate peaks in the high-resolution stratigraphy observed in KNR31-GPC-5 (33.67°N, 57.63°W, 4500 m water depth) from the northeast Bermuda Rise, where millennial-scale changes in local terrigenous input and basin-wide carbonate dissolution are thought to drive carbonate variability (Keigwin and Jones, 1994). The KNR31-GPC-5 chronology was determined using radiocarbon dates and $\delta^{18}O$ stratigraphy (Keigwin and Jones, 1994).

Chronologies for GGC3 and GGC6 were calculated assuming a linear distribution of time between tie-points. Ages for depths below the oldest tie-point were estimated assuming the same sedimentation rate as the previous tie-point bounded interval. Stratigraphic similarities between the benthic $\delta^{18}O$ and $\delta^{13}C$ records in GGC3 and GGC6 suggest that the Mid-Atlantic cores record unperturbed sediment chronologies (Figure 3.2). The radiocarbon-derived timing of the Last Glacial Maximum (LGM) matches the occurrence of maximum $\delta^{18}O$ in both GGC3 and GGC6. The carbonate content-derived timing of Marine Isotope Stage 4 (MIS 4) coincides with

local minimum values of the $\delta^{13}C$ stratigraphy. The estimated chronologies suggest average sedimentation rates of ~2 cm/ka in both cores.

Traditional mass accumulation rates were also determined in order to compare age-model-derived dust fluxes with dust fluxes derived using $^{3}He_{ET}$. Mass accumulation rates (*MAR*) were calculated from the relationship:

$$MAR = \rho_b * \frac{z_2 - z_1}{t_2 - t_1} \qquad \text{EQ. 3.4}$$

where ρ_b, t_1, t_2,z_1 and z_2 are as in Equation 3 and using an average dry bulk density for the Mid-Atlantic cores of 0.65 g cm^{-3} determined by weighing 5 sediment samples of known initial volume.

3.3.2. Stable Isotope and Elemental Analyses

Benthic oxygen isotope ($\delta^{18}O$) and carbon isotope ($\delta^{13}C$) analyses were performed on a dual-inlet Thermo Delta V+ mass spectrometer at the Lamont-Doherty Earth Observatory of Columbia University (see Appendix C). After sonication in distilled H_2O, approximately 50 to 90 µg aliquots of whole *C. wuellerstorfi* tests were dissolved in ~105% phosphoric acid (H_3PO_4) in an automated KIEL IV sample-preparation device utilizing individual reaction vessels. The resulting carbon dioxide gas was then purified and analyzed. The NBS-19 international standard was analyzed every ~10 samples. The long-term standard deviations for $\delta^{18}O$ and $\delta^{13}C$ of NB-19 measured on this instrument are 0.06‰ and 0.04‰, respectively. The average difference in $\delta^{18}O$ and in $\delta^{13}C$ values between replicated samples from this study was 0.24‰ for both isotopic systems.

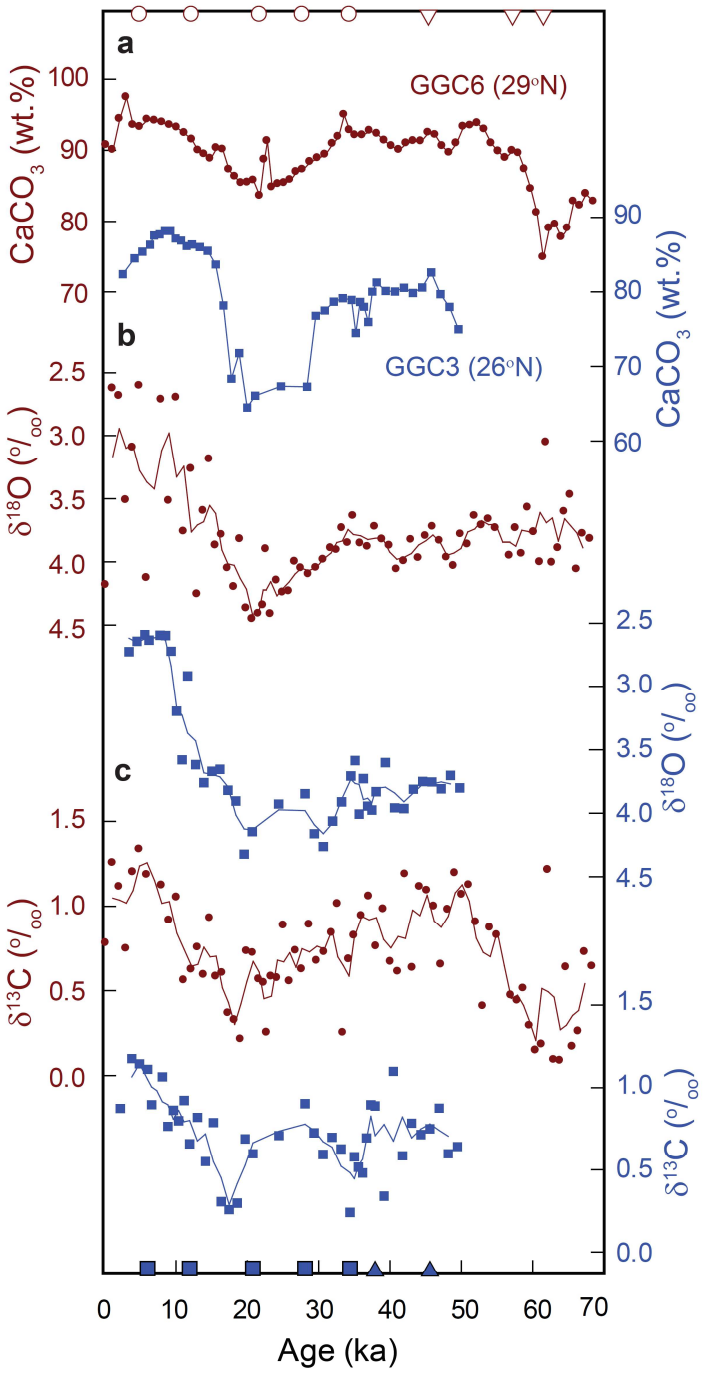

Figure 3.2: Sediment core age-models and stable isotope values for KN207-2-GGC3 (26°N, blue squares) and KN207-2GGC6 (29°N, brown circles). (a) Bulk carbonate content. Data points indicate the average value of a sedimentary interval spanning ~1 ka of time. GGC6 carbonate peaks at 3.3, 23.0, and 33.8 ka are associated with anomalously coarse sedimentary layers. The 28 to 15 ka GGC3 carbonate minimum is coincident with significant accumulation of hydrothermal material (Middleton et al., 2016). **(Caption continued on next page.)**

Figure 3.2 caption (continued): (b) Individual aliquot (points) and three-point running mean values (lines) of benthic $\delta^{18}O$ and (c) $\delta^{13}C$ measured in *C. wuellerstorfi*. Age-model tie-points from radiocarbon data (circles and squares) and from carbonate stratigraphy (triangles; see Appendix C) are indicated along the x-axes for GGC6 (top axis) and for GGC3 (bottom axis). Age uncertainties span the width of tie-point markers. Chronological uncertainty increases with distance from the age-model tie-points.

Concentrations of Ti and Th were determined using solution nebulized ICP-MS analyses following the methods of Middleton et al. (2016) and performed on a Thermo X series quadrupole at Harvard University (See Appendix C).

Although the carbonate and carbonate-free components of each sample were analyzed separately, reported elemental concentrations and fluxes refer to the bulk composition determined from mass balance. Elemental concentrations were calculated from the ICP-MS results using calibration curves determined from the standards BCR-2, BHVO-2, DNC-1, W-2, and JB-2. Aliquots of the in-house standard K1919 (Escrig et al., 2012) were analyzed between every three samples to monitor and correct for instrumental drift. The 1σ uncertainties in elemental concentrations were determined from interrun reproducibility of K1919 and were 0.05 wt. % and 0.07 ppm for Ti and Th, respectively.

3.3.3. Helium isotope analyses

Helium sample preparation, heated gas extraction, and analyses were performed on 1.5 g sediment aliquots in the Harvard Noble Gas Laboratory following the procedure reported by Middleton et al. (2016). Median hot blank values were 7.8×10^{-10} cm^3 STP of ^4He and 7.9×10^{-16}

cm^3 STP of ^3He, equivalent to < 0.1 % of the sample contents of each isotope. Repeated heating steps yielded hot blank values for both ^4He and ^3He, ensuring quantitative sediment helium extraction. Helium concentrations and isotope ratios were determined with respect to routine analysis of a high helium-3 standard (HH3) with a $^3He/^4He$ ratio of 8.8 R_A (Gayer et al., 2008). During the course of sample measurements, standard deviations of 0.28% for ^4He and 0.29% for the $^3He/^4He$ ratio were observed in a population of 146 analyses of HH3 aliquots containing volumes of ^3He comparable to the sample suite.

Sample $^3He_{ET}$ and $^4He_{terr}$ concentrations were calculated assuming a two component mixture of IDP helium ($(^3He/^4He)_{ET}$) with a $^3He/^4He$ ratio of 170 R_A (where R_A denotes the ratio normalized to the atmospheric $^3He/^4He$ value of 1.39 x 10^{-6}; Nier and Schlutter, 1992) and a typical terrigenous source ($(^3He/^4He)_{terr}$ with a $^3He/^4He$ ratio of 0.01 R_A; Farley and Patterson, 1995) using the following relationships:

$$[\,^3He_{ET}] = (^3He_{msr})\left(\frac{1-\frac{(^3He/^4He)_{terr}}{(^3He/^4He)_{msr}}}{1-\frac{(^3He/^4He)_{terr}}{(^3He/^4He)_{ET}}}\right) \qquad \text{EQ. 3.5}$$

and

$$(^4He_{terr}) = (^4He_{msr})\left(\frac{(^3He/^4He)_{msr}-(^3He/^4He)_{ET}}{(^3He/^4He)_{terr}-(^3He/^4He)_{ET}}\right) \qquad \text{EQ. 3.6}$$

where *msr* denotes the measured sample value (see Appendix C). Using the IDP and terrigenous $^3He/^4He$ end-member values listed above, $^3He_{ET}$ represents >98% of total ^3He and $^4He_{terr}$ represents >93% of total ^4He in all samples measured. Interpretations of the Mid-Atlantic samples are not sensitive to the presumed value of $(^3He/^4He)_{terr}$. For example, assuming a 10x higher $(^3He/^4He)_{terr}$ value of 0.10 R_A (Marcantonio et al., 1998), $^3He_{ET}$ would represent >88% of

total ^{3}He in all samples and 94% of total ^{3}He in the sample mean. Calculated values of $^{4}He_{terr}$ would change by less than 0.1%.

Reproducibility in ($^{4}He_{terr}$) is comparable to analytical uncertainty and replicated samples indicate 1σ values of 1-2%. In contrast, [$^{3}He_{ET}$] reproducibility is influenced by the distribution of unusually large, helium-rich IDPs that are rare and are consequently not representatively sampled in typical sediment aliquots. This 'nugget effect' is independent of sedimentary smoothing associated with bioturbation and increases the uncertainty in [$^{3}He_{ET}$] substantially beyond that of the analytical uncertainty (Farley et al., 1997).

The uncertainties in sediment [$^{3}He_{ET}$] values associated with natural variability in the distribution of helium-rich IDPs are a function of the area-time product of the sediment aliquots analyzed, determined by dividing the sample mass (in g) by the mass accumulation rate (in g m^{-2} a^{-1}), and are reduced by increasing sample masses and analyzing replicate samples (Farley et al., 1997). A 20% 1σ uncertainty in sediment [$^{3}He_{ET}$], determined by a Gaussian fit to the distribution of fractional differences in replicated analyses, is representative for a typical area-time product of 0.25 $m^{2}a$ (Farley et al., 1997). The bulk sedimentation rates observed in the Mid-Atlantic sediment cores and the 1.5 g sample aliquot masses of this study yield an area-time product of 0.15 $m^{2}a$. The lower area-time product of the Mid-Atlantic sediments results in the higher 28% 1σ [$^{3}He_{ET}$] uncertainty observed in the population of 108 replicated sample analyses (Figure C7). Assuming normality, the 1σ uncertainty in [$^{3}He_{ET}$] in individual samples scaled as $0.28/\sqrt{n}$, where *n* is the number of aliquots analyzed. Note that this level of uncertainty does not compromise the conclusions of this study.

Elemental fluxes were calculated by multiplying elemental concentrations with the $^{3}He_{ET}$-derived sediment rain rates following Equation 3.2. Propagation of uncertainties associated with the $^{3}He_{ET}$ flux from space (*f* in Equation 3.1), elemental concentration data, and the determination of [$^{3}He_{ET}$] yield an average 1σ uncertainty of 25% and a maximum uncertainty of 32% in the Mid-Atlantic elemental fluxes. To reduce the statistical noise introduced by under-sampling of rare IDPs, elemental fluxes are reported as 3-point running means, representing a smoothing window of ~6 cm or ~3 ka, unless otherwise stated.

3.4. Results

3.4.1. Dust proxy flux patterns

To first order, the elemental flux patterns of the dust proxies ($^{4}He_{terr}$ and Th) and the lithogenic proxy (Ti) exhibit similar patterns of variability *within* each sediment core (Figure 3.3, see Figure C3 for unsmoothed flux records). $^{4}He_{terr}$, Th, and Ti fluxes are all low during the mid-Holocene (4-7 ka) and high during the early Holocene, including distinct peaks at ~8, ~12, and ~17 ka. In detail, $^{4}He_{terr}$ and Th have the highest correlation (Figure C4) and exhibit increased variability relative to Ti fluxes. Between the 17 ka peak and the 6 ka minimum, $^{4}He_{terr}$ and Th fluxes decrease by a factor of ~3 to 4, while Ti fluxes decrease only by a factor of 2. Depending on the element in the 70 ka record from 29°N, there is either a slightly increasing ($^{4}He_{terr}$, Th) or a steady (Ti) level of dustiness from MIS 4 through the LGM and into the early Holocene. Thus, while there is a generally consistent flux pattern suggested by each dust proxy element, the exact

magnitude of flux variation and relative peak heights vary between $^4He_{terr}$, Th, and Ti. Such variations in dust proxy fluxes may be associated with changes in the integrated provenance and composition of dust delivered to the Mid-Atlantic (Castillo et al., 2008; McGee et al., 2016) or with the presence of non-dust components of sedimentary Th and Ti.

Despite slight elemental differences, $^4He_{terr}$, Th, and Ti additionally exhibit similar absolute fluxes *between* the 26°N and the 29°N sediment cores (Figure 3.3). With the exception of 35 to 45 ka, when $^4He_{terr}$ and Th fluxes at 26°N fall to mid-Holocene levels, the $^4He_{terr}$ and Th fluxes of 26°N and 29°N overlap within error between cores over the past 50 ka. Ti fluxes overlap within error throughout the entirety of the coinciding records.

Linear interpolation of $^4He_{terr}$, Th, and Ti flux records from each core to a uniform time series allows for direct comparison of contemporaneous dust accumulation and highlights the similarities between Mid-Atlantic locations (Figure 3.4; see Appendix C). Flux values from the time span covered by both Mid-Atlantic records (2-50 ka) were linearly interpolated to a uniform time series of 48 points between 4.1 and 47.8 ka. The 0.9 ka time step of the interpolated data series equals the total duration of time contained within the 29°N sedimentary record divided by the number of sediment intervals analyzed and was chosen to best approximate the temporal resolution of original data sets. The same linear interpolation methods were employed to compare the Mid-Atlantic dust flux stack with the grain size-based humidity index calculated by Tjallingii et al. (2008; See Section 3.5.5). For each time series comparison, a correlation coefficient (R) and accompanying p-value is presented. Traditional p-values calculated using a t-distribution overestimate the significance of correlations between the time series evaluated in this

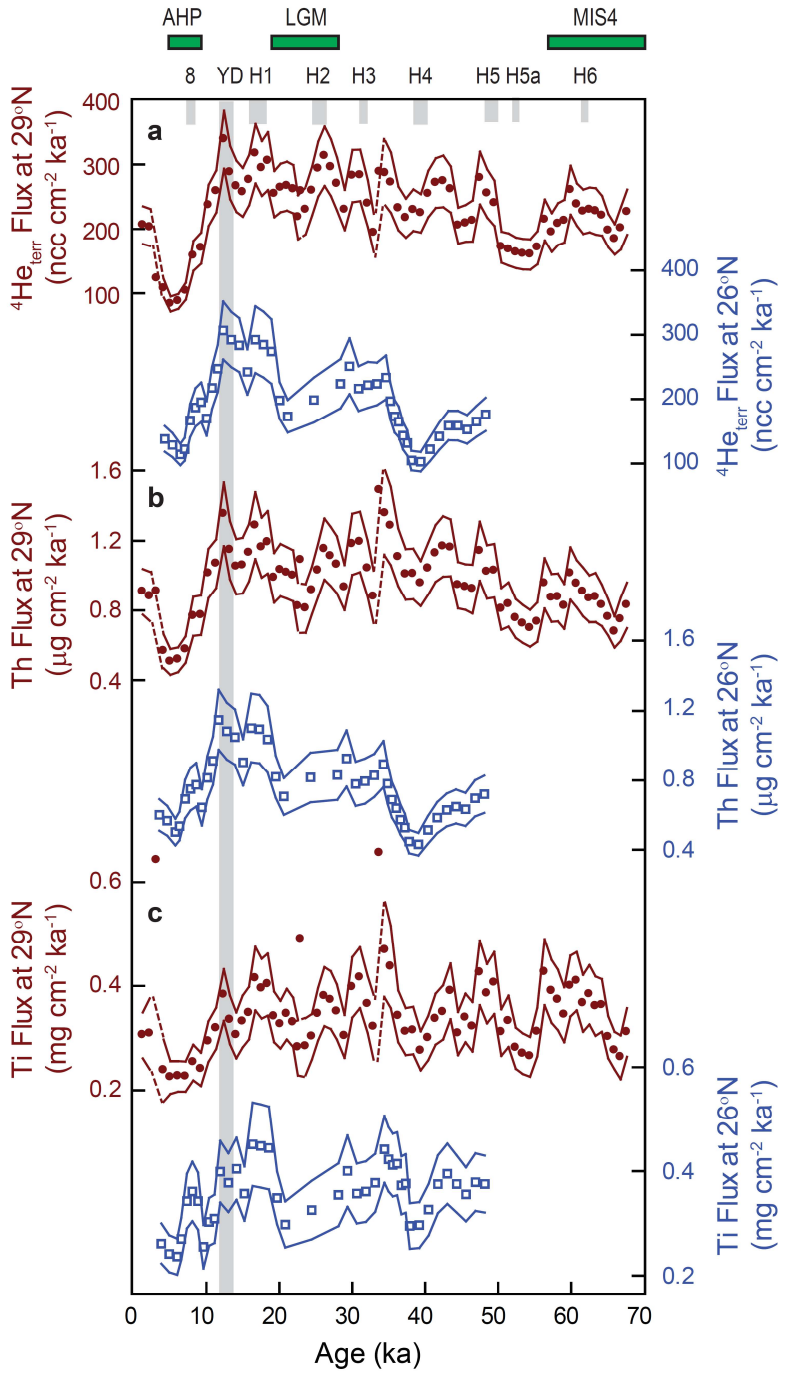

Figure 3.3: Mid-Atlantic $^3He_{ET}$-derived dust ($^4He_{terr}$, Th) and lithogenic (Ti) proxy fluxes. (a) $^4He_{terr}$, (b) Th, and (c) Ti fluxes for 26°N (GGC3, blue squares) and for 29°N (GGC6, brown circles) as a function of time. Flux values indicate a three point-running mean of sedimentary intervals spanning ~1 ka (data points) within a 1σ error envelope (solid lines). Coarse carbonate layers of GGC6 are excluded from the three point-running mean. **(Caption continued on the next page.)**

Figure 3.3 caption (continued): Green bands indicate the timing of the African Humid Period (AHP), the Last Glacial Maximum (LGM), and Marine Isotope Stage 4 (MIS4). Gray bands indicate the timing of 8 ka, the Younger Dryas (YD), and Heinrich events (H1-H6) from Tierney et al. (2017), Rashid et al. (2013), and Sanchez Goñi and Harrison (2010). GGC3 flux data (Middleton et al., 2016) are presented on a revised age-model. The timing of the YD is highlighted through the suite of flux records for ease of comparison.

study due to autocorrelation within each marine sedimentary record. To improve constraints on the significance of each correlation, reported p-values were computed from a null distribution of R-values generated from 10,000 comparisons of phase randomized surrogate data (e.g., Theiler et al., 1992).

Linear interpolations of the $^{4}He_{terr}$ fluxes demonstrate a good correlation between the two sediment cores over the entire interval of comparison ($R = 0.59$, $p = 0.04$), a strong correlation over the past 35 ka ($R = 0.81$, $p < 0.01$), and an exceptional correlation over the past 20 ka ($R = 0.96$, $p < 0.01$).

Observed flux similarities between the Mid-Atlantic cores are notable given the variations in sediment focusing within each core (Figure 3.5). Sediment focusing factors in the Mid-Atlantic cores range from 2 to 8 and are comparable to values of 1 to 16 observed in Quaternary sediments in the Western subtropical Atlantic (Bacon, 1984; McGee et al., 2010b). The Mid-Atlantic focusing factors fluctuate out of sync, with the strongest sediment focusing occurring at ~10 and ~37 ka at 26°N and at ~25 and ~65 ka at 29°N. It is possible that the high level of sediment focusing observed from 35 to 40 ka at 26°N could fractionate $^{3}He_{ET}$-bearing IDPs from bulk sediment on the seafloor and thus explain the difference in elemental flux patterns between the 26°N and 29°N records at this time (Figure 3.3). However, evaluation of $^{3}He_{ET}$ performance

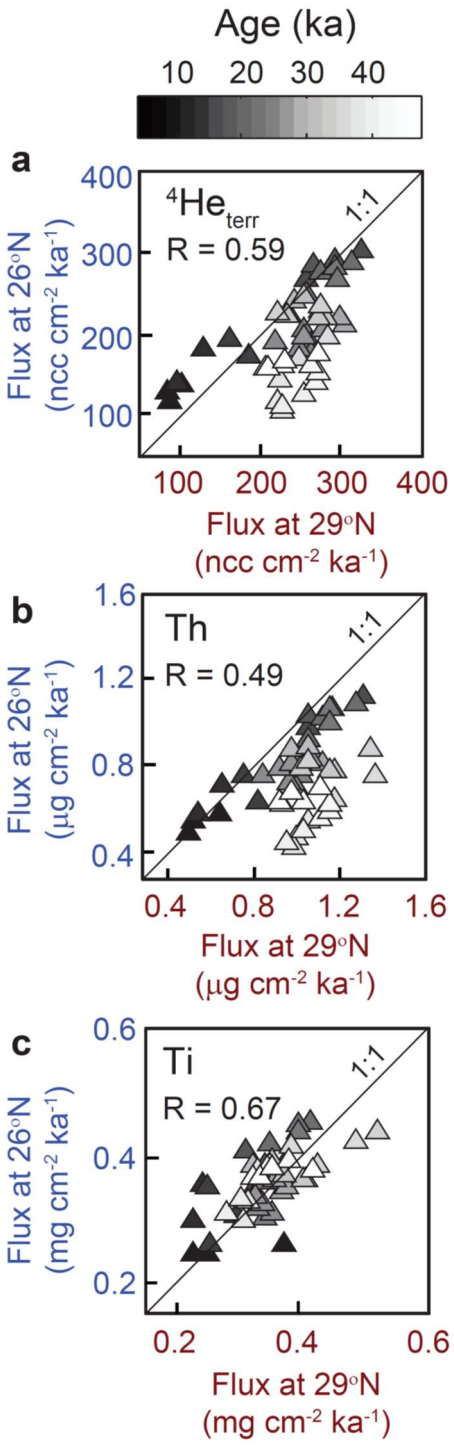

Figure 3.4: Correlation of elemental flux records between Mid-Atlantic sediment cores. (a) $^4He_{terr}$, (b) Th, and (c) Ti flux record comparisons between 26°N (y-axes) and 29°N (x-axes) after linear interpolation to a uniform time series (see Appendix C). P-values are 0.04, 0.06, and <0.01, for the correlations reported in a, b, and c, respectively. Grayscale shading indicates the age of each flux data point. A 1:1 line is indicated on each plot for comparison.

in the highly advected sediments of the Blake Ridge found little evidence for such fractionation (McGee et al., 2010b). The strong correlation in dust proxy fluxes observed between cores, despite distinct variability in the sediment focusing at each location, emphasizes the utility of the $^{3}He_{ET}$ constant flux proxy to constrain millennial-scale vertical dust deposition rates in complex sedimentary environments.

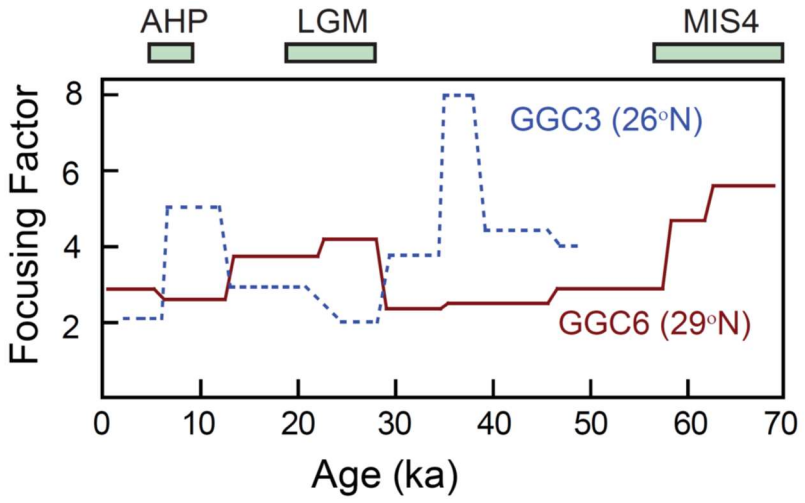

Figure 3.5: Extraterrestrial helium-3 based sediment focusing factors calculated between age model tie-points for GGC3 (26°N, blue dashed line) and GG6 (29°N, red solid line) following Equation 3.3. The timing of the African Humid Period (AHP), the Last Glacial Maximum (LGM), and Marine Isotope Stage 4 (MIS4) are as in Figure 3.3.

3.4.2. Absolute dust fluxes

Absolute Mid-Atlantic dust fluxes were estimated from the $^{4}He_{terr}$ flux (Figure 3.6) using a constant endmember dust $^{4}He_{terr}$ concentration of 5600 ncc g^{-1} (ODP Site 658C; Mukhopadhyay and Kreycik, 2008). Over the past 70 ka, Mid-Atlantic $^{4}He_{terr}$-based dust flux values range from 15 to 60 mg cm^{-2} ka^{-1} (or 0.15 to 0.60 g m^{-2} yr^{-1}). At 29°N, the $^{4}H_{terr}$-based dust fluxes account

for 60-100% of the total non-carbonate sediment flux, which ranges from 25 to 70 mg cm^{-2} ka^{-1}. Dust fluxes were also computed from the Th and Ti data using average endmember Northwest African dust concentrations of 14 ppm for Th (Castillo et al., 2008; McGee et al., 2016) and 0.50 wt.% for Ti (Castillo et al., 2008). However, the prescribed endmember Th and Ti values yield absolute dust fluxes that range from 35 to 105 mg cm^{-2} ka^{-1} and 45 to 110 mg cm^{-2} ka^{-1}, respectively, and consistently exceed the total non-carbonate sediment flux in 29°N sediments younger than 60 ka (Figure C5).

Overestimation of Th and Ti-derived dust fluxes likely results from an underestimation of the representative Th and Ti concentrations within dust delivered to the subtropical North Atlantic. Th and Ti concentrations vary by grain size and among localities within North African dust source regions and span 10 to 37 ppm Th and 0.36 to 0.78 wt.% Ti (Castillo et al., 2008). Alternatively, Ti-bearing sedimentary basalt chips or the deposition of authigenic Th supplied by the advection of Th-rich bottom waters (e.g., Rowland et al., 2017) could potentially supply significant components of non-dust Ti and Th to the Mid-Atlantic sediments. However, significant components of non-dust Th are not consistent with the excellent correlations between $^4He_{terr}$ and Th observed in both cores. As the exact Ti and Th concentrations of the North African endmember within the core sites remain uncertain, remaining discussion will focus exclusively on $^4He_{terr}$-based dust flux values. Importantly, the relative pattern of Mid-Atlantic dust variability is not affected by the choice of $^4He_{terr}$-based versus Th-based dust concentrations.

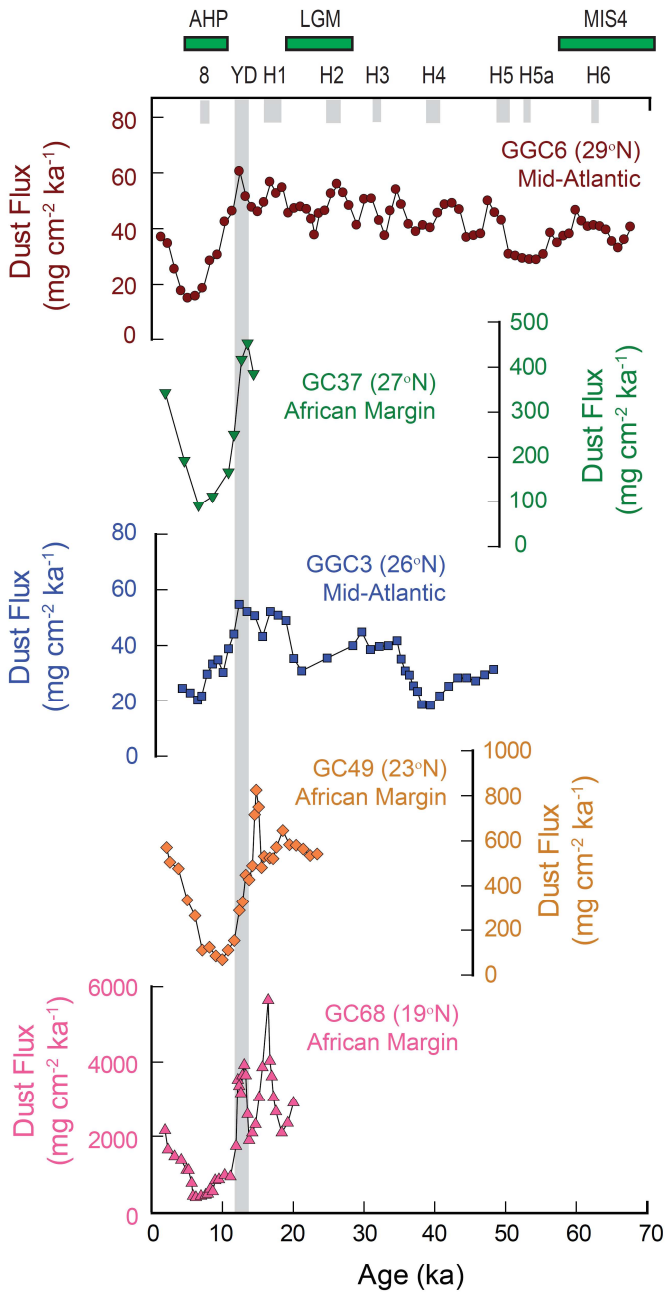

Figure 3.6: Comparison of Atlantic dust flux records. $^{4}He_{terr}$-based dust records from the Mid-Atlantic constrained using the $^{3}He_{ET}$ constant flux proxy (GGC3 and GGC6, this study) and select dust flux records from the Northwest African Margin (GC27, GC49, and GC68; Figure 3.1) constrained using grain size analysis and the excess ^{230}Th constant flux proxy (McGee et al., 2013). The timing of the African Humid Period (AHP), the Last Glacial Maximum (LGM), Marine Isotope Stage 4 (MIS4), 8 ka, the Younger Dryas (YD), and Heinrich events (H1-H6) are as in Figure 3.3. Error bars have been removed for clarity. Despite ~2500 km of separation, the Mid-Atlantic dust flux records exhibit similar patterns of variability to those from the continental margin over the past 20 ka.

3.5. Discussion

3.5.1. Helium-based Mid-Atlantic records reflect North African dust emissions

Mid-Atlantic dust fluxes derived using the $^{3}He_{ET}$ constant flux proxy yield a high resolution, spatially consistent pattern of dustiness that is similar to the dust flux patterns constrained using excess ^{230}Th along the Northwest African margin over the past 20 ka (Figure 3.6; Adkins et al., 2006; McGee et al., 2013). The Mid-Atlantic records and those from the margin each exhibit a mid-Holocene dust minimum at ~6ka and prominent dust peaks coinciding with the Younger Dryas (YD) and Heinrich 1. Further, the Mid-Atlantic records at 26°N and 29°N indicate YD dust fluxes of 54 ± 8 and 60 ± 8 mg cm^{-2} ka^{-1} that are 3 to 4-fold higher than minimum dust fluxes at ~ 6ka of 20 ± 3 and 15 ± 2 mg cm^{-2} ka^{-1}, respectively. The amplitude of variability recorded in the slowly accumulating (~2 cm/ka) Mid-Atlantic cores may be relatively muted by the effects of bioturbation or temporal smoothing of the $^{3}He_{ET}$-derived data (see Section 3.5.5). Nonetheless, these values are comparable to those observed from 23°N to 31°N along the continental margin, where dust deposition rates are 1.5 to 7.5-fold higher during the YD than at ~6 ka (McGee et al., 2013). The relative change in Mid-Atlantic dustiness is notably similar to the contemporaneous 4.5-fold change from 415 to 90 mg cm^{-2} ka^{-1} observed on the margin at 27°N (McGee et al., 2013).

Although absolute dust flux values are somewhat sensitive to the presumed dust endmember composition (see Section 4.2), the 15 to 60 mg cm^{-2} ka^{-1} range of the helium-based dust fluxes is reasonable, given the distance between the cores and the center of the African dust plume (Figure

3.1). The Mid-Atlantic dust fluxes are approximately ten times lower than coincident dust fluxes from similar latitudes on the Northwest African margin, which range from 70 to 950 mg cm^{-2} ka^{-1} (Figure 3.6; McGee et al., 2013). This apparent tenfold reduction between the continental margin and the Mid-Atlantic is comparable to modern atmospheric observations. Aerosol collection data from 2004 to 2009 reveal an average fivefold decrease in dust concentrations between the Canary Islands, located at 28°N on the African margin, and Barbados, located at 13°N in the Caribbean (Gelado-Caballero et al., 2012; Prospero and Mayol-Bracero, 2013). While comparable aerosol collection data is unavailable for the Mid-Atlantic, aerosol optical depth (AOD) values from satellite observations suggest that the Mid-Atlantic core sites (AOD of 0.07 and 0.08) receive much lower dust levels than either the Canary Islands (AOD of 0.14) or Barbados (AOD of 0.13; Figure 3.1; Kaufman et al., 2005). Hence, the observed tenfold decrease in dust deposition between the continental margin and the subtropical Mid-Atlantic agrees with the predicted spatial gradient of at least a fivefold change.

Agreement in relative changes in dust deposition between the Mid-Atlantic records and those closer to the continental dust sources suggests that Mid-Atlantic dust flux variability is heavily influenced by changes in North African dust emissions.

3.5.2 Extraterrestrial helium-3 vs. age-model derived Mid-Atlantic dust records

In contrast to the dust fluxes determined using $^3He_{ET}$, Mid-Atlantic dust fluxes estimated using age-model-derived mass accumulation rates (Equation 3.4) yield spatially inconsistent patterns of dustiness with dramatically different climatic implications (Figure 3.7). While the $^3He_{ET}$-

derived dust fluxes of both sites peak during millennial-scale events coincident with those on the North African margin (Figure 3.6), the age-model-derived dust fluxes do not. At 26°N, age-model-derived dust flux peaks occur prior to the LGM (36 ka) and in the early Holocene (11 ka). At 29°N, however, the age-model-derived dust fluxes peak twice across the LGM (25 and 20 ka). Further, while the $^{3}He_{ET}$-derived dust fluxes range from 15 to 60 mg cm^{-2} ka^{-1} over the past 70 ka, the age-model-based dust fluxes are typically four times higher and range from 45 to 250 mg cm^{-2} ka^{-1}. Subsequently, evaluation of the past 70 ka of Mid-Atlantic dustiness based on the age-model-derived dust fluxes from these cores would lead to persistent overestimation of total dust deposition and an underestimation of the importance of millennial-scale events in governing dust supply.

We highlight the differences in the pattern and magnitude of inferred dust flux variability between the age-model-based and the $^{3}He_{ET}$-based dust records to emphasize the critical importance of utilizing a constant flux proxy to constrain vertical sediment rain rates. Interpretation of Atlantic dustiness based solely on the age-model-derived dust flux records would suggest large variations in the patterns of dust deposition between 29°N and 26°N on the ten-thousand-year timescale, possibly governed by changes in Earth's orbital configuration (Figure 3.7). Such interpretation is discordant with the more reliable $^{3}He_{ET}$-derived dust fluxes. Thus, we exclusively refer to the $^{3}He_{ET}$-derived dust fluxes for the remainder of the discussion.

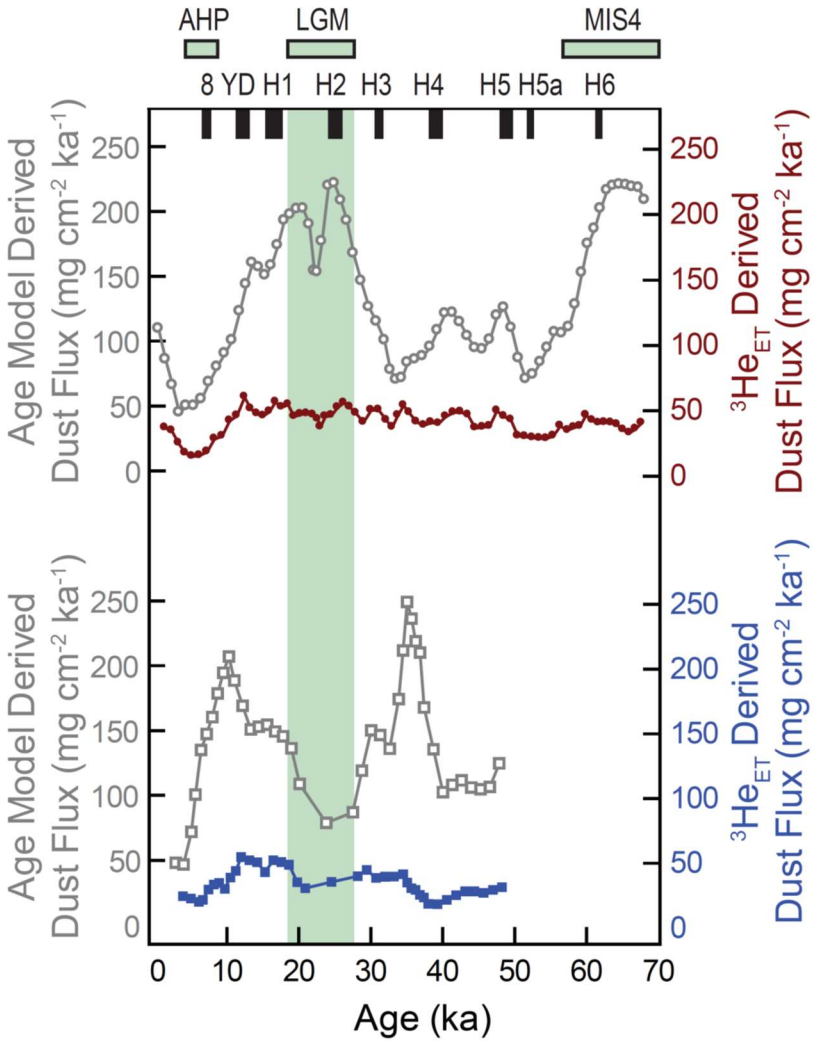

Figure 3.7: Comparison of Mid-Atlantic dust fluxes derived using the age-model (left axes, open points) and using $^{3}He_{ET}$ as a constant flux proxy (right axes, solid points) for 29°N (upper panel) and 26°N (lower panel). All plots represent three point-running mean fluxes. The timing of the African Humid Period (AHP), the Last Glacial Maximum (LGM), Marine Isotope Stage 4 (MIS4), 8 ka, the Younger Dryas (YD), and Heinrich events (H1-H6) are as in Figure 3.3. A green band highlights the timing of the LGM for ease of comparison between the records. Note that age-model derived dust fluxes, which are sensitive to climatically driven changes in lateral sediment transport, suggest significantly higher rates of dust deposition with more spatial variability and a weaker influence of millennial-scale events than those determined using $^{3}He_{ET}$.

3.5.3 Glacial variability

The new Mid-Atlantic data extend the record of North African dust emissions from 20 to 70 ka and suggest major fluctuations in Atlantic dustiness coincident with known variations in Northern Hemisphere climate (Figure 3.6). On the orbital timescale, dust fluxes to the Mid-Atlantic generally increase from MIS 4 through the LGM and into the early Holocene. Millennial-scale dust peaks in the Mid-Atlantic records centered at ~13, 17, 27, 31, 42, 48, and 61 ka appear to coincide, within reasonable age-model uncertainty, with short-term Northern Hemisphere cold periods such as the YD and many of the past seven Heinrich Stadial events (Rashid et al., 2003; Sanchez Goñi and Harrison, 2010). Excluding the dust peak at ~61 ka, the 29°N record indicate a MIS 4 dust flux of 40 ± 6 mg cm^{-2} ka^{-1}, ~80% of the LGM value of 50 ± 7 mg cm^{-2} ka^{-1}. Notably, the highest levels of Mid-Atlantic dustiness occur during the millennial-scale cold periods, rather than during the LGM or the near-glacial MIS 4 (see Section 3.5.5).

The most dramatic feature of the Mid-Atlantic records is the decrease in dust fluxes from the YD to 6 ka. This mid-Holocene dust decrease is coincident with the African Humid Period (AHP; ~5 to 11 ka), when lake levels, West African river output, and fossil pollen records suggest a wet and vegetated continent (Gasse, 2000; Jolly et al., 1998; Ritchie et al., 1985; Street and Grove, 1976; Weldeab et al., 2007). The AHP is also associated with significant decreases in dust flux in multiple sedimentary records from the Northwest African margin (deMenocal et al., 2000; Gasse, 2000; Adkins et al., 2006; McGee et al., 2013; Tierney et al., 2017).

The AHP is associated with increased low-latitude insolation and sea surface temperatures in the tropical North Atlantic and is thought to reflect changes in the West African monsoon (Kutzbach and Liu, 1997). Sedimentary proxies of Northwest African aridity all indicate that the AHP was the wettest interval of the past 70 ka (Tjallingii et al., 2008; Weldeab et al., 2007). Feedbacks between increased precipitation and vegetation cover and decreased mineral aerosol concentrations may have amplified dust emissions reductions associated with the wet AHP (Claussen et al., 1999; Pausata et al., 2016). The effect of such a decrease in continental dust sources is consistent with the low dust fluxes observed during the mid-Holocene at both 26°N and 29°N. Interestingly, dust fluxes at 26°N at ~40 ka appear comparably low to the mid-Holocene minimum, despite the absence of an equivalent period of African humidity, while those at 29°N do not. This divergence in dust fluxes at ~40 ka may be related to a change in dust emission conditions within the southern Sahara and Sahel regions relative to northern dust sources. However, additional long-term dust flux records from more southern latitudes in the North Atlantic are required to evaluate this hypothesis

3.5.4. Comparison to model estimates for Mid-Atlantic dust deposition

The subtropical Mid-Atlantic flux estimates provide new temporal and spatial constraints on Atlantic dustiness that can be used to test and improve models of atmospheric transport and aeolian iron deposition across climatic changes (e.g., Albani et al., 2016, 2015; Mahowald et al. 2009). For example, recent modeling efforts have employed existing dust flux records and the Community Earth System Model to estimate variability in the global dust cycle and fine grained

(<10 μm) aeolian deposition to the oceans from the LGM to the preindustrial period (Albani et al., 2016; 2015).

The Mid-Atlantic data reveal subtropical North Atlantic dust fluxes that are at least three times lower than estimates from the Albani et al. (2016) model over the past 21 ka. During the LGM (at 21 ka), the Albani et al. model predicts dust deposition rates of 180 and 160 mg cm^{-2} ka^{-1} to the grid cells hosting the 26°N and 29°N cores, respectively. These predicted values are three to six times higher than the LGM values of 30 ± 5 (at 26°N) and 50 ± 7 (at 29°N) mg cm^{-2} ka^{-1} recorded in the Mid-Atlantic sediments at 21 ka. The model-data offset is slightly higher during the dust minimum of the AHP. At 6 ka, the Albani et al. model estimates dust deposition rates of 135 (at 26°N) and 100 mg cm^{-2} ka^{-1} (at 29°N), whereas the Mid-Atlantic records reflect dust fluxes of only 20 ± 4 mg cm^{-2} ka^{-1}. Thus, the global dust model suggests a ~30% drop in subtropical North Atlantic dust deposition from the LGM into the AHP, while the sedimentary data suggest a larger decrease of ~50% over the same interval. Consequently, although the amplitude of dust flux variability recorded in the Mid-Atlantic sediments may have been smoothed by bioturbation, the data suggest larger changes in Northwest African dust emissions over the past 21 ka than the recent model predicts. Muted variability of North African dust emissions within the Albani et al. global model suggests that incorporation of additional processes, such as dynamic vegetation and variable flooding of dry lake beds (Tegen et al., 2002), could be important for improving model representation of dust emissions across variable climatic conditions.

3.5.5 Millennial-scale variability in Atlantic dustiness

The occurrence of millennial-scale dust peaks within the Mid-Atlantic records is consistent with previous observations from the African margin and allows for the evaluation of the effects of short-term climatic variability on North African dust emissions prior to the LGM. While temporal averaging of $^{3}He_{ET}$-derived flux data, as employed above, allows for examination of distinct spatial patterns between the Mid-Atlantic core locations, temporal averaging decreases the perceived magnitude of dust flux changes across millennial-scale events. Similarly, spatial averaging of the sedimentary dust flux data preserves temporal resolution at the expense of spatial variability. Thus, to better examine the occurrence of millennial-scale variability in North African dust emissions, the unsmoothed dust flux data from 26°N and 29°N were averaged together to generate a Mid-Atlantic dust flux stack (Figure 3.8, Figure C3).

Over the past 50 ka, millennial-scale peaks in Mid-Atlantic dust deposition occur at ~13, 17, 27, 31, 34, 42 and 48 ka, reaching maximum dust fluxes equivalent to 150%, 155%, 130%, 110%, 115%, 95%, and 105% of the LGM (21 ka) flux of 45 ± 6 mg cm^{-2} ka^{-1}, respectively. Excluding the peaks at 34 and 42 ka, these events coincide with the YD and Heinrich Stadials 1-3 and 5 (Sanchez Goñi and Harrison, 2010). The dramatic decrease in Mid-Atlantic dust flux into the AHP is punctuated at ~8 ka. This feature may be related to a pronounced dry spell that interrupted the relatively wet conditions of the AHP (Tierney et al., 2017). The apparent absence of a Mid-Atlantic dust peak during Heinrich Stadial 4 (38-40 ka) may result from either weak emission conditions particular to this event or from age model error in the chronology of the ~42 ka dust peak. The increasing trend in maximum dust emissions during millennial-scale Northern

Hemisphere cold periods from 50 ka through the LGM is consistent with the general increase in background dustiness across this interval.

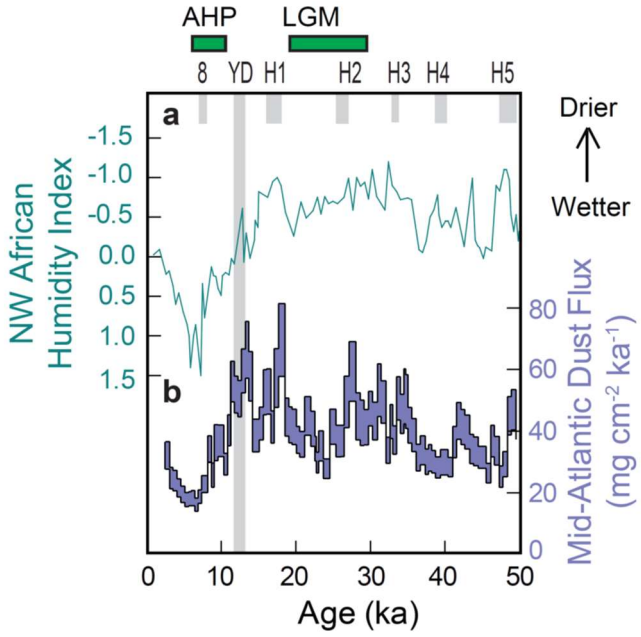

Figure 3.8: Comparison of Mid-Atlantic dust record to a Northwest African Humidity Index from GEOB7920-2 (Figure 3.1). (a) Humidity Index determined using grain size analysis of fluvial versus aeolian input to sediments at 21°N on the Northwest African continental margin (Tjallingii et al., 2008). The y-axis has been inverted such that drier conditions are pointing up. (b) Spatially averaged $^{4}He_{terr}$-based Mid-Atlantic dust flux stack (within the 1σ error envelope) constrained using the $^{3}He_{ET}$ constant flux proxy. The timing of the African Humid Period (AHP), the Last Glacial Maximum (LGM), 8 ka, the Younger Dryas (YD), and Heinrich events (H1-H5) are as in Figure 3.3. The records of Mid-Atlantic dust flux and Northwest African Humidity Index are correlated with an R = -0.57 and p = 0.03.

The effects of bioturbation on the Mid-Atlantic records were examined using a simple bioturbation model (e.g., Berger and Heath, 1968; McGee et al., 2013; See Appendix C). An input dust flux signal of abritrary units was deposited in 0.005 ka timesteps onto an accumulating sediment column. The input signal was prescribed to approximate, with ~1 ka of smoothing, the

high-resolution dust flux record observed in a more rapidly accumulating sediment core from 19°N on the Northwest African margin (OC437-7-GC68; McGee et al., 2013). The recorded dust flux and ages of sediments within the mixed layer were completely and linearly homogenized. The mixed layer depth was varied to generate bioturbated records representing 1 to 4 ka of sedimentary smoothing, equivalent to mixed layer depths of 2 to 8 cm in the Mid-Atlantic cores (Figure 3.9).

Complete homoginization of the mixed layer may not lead to a linear homogenization of the input dust flux signal in an actual sedimentary environment, however, because proxy estimates for dust flux are directly related to dust concentrations and inversely related to concentrations of $^{3}He_{ET}$. In order to examine the sensitivity of model output to the assumption of linear homogenization, an additional bioturbation model was evaluated, in which the inverse of the GC68-based input dust signal was used to prescribe an input accumulation of $^{3}He_{ET}$ in arbitrary units (Figure C9).

In this model, the $^{3}He_{ET}$ concentrations were completely and linearly homogenized within the mixed layer and the resulting dust flux signals were computed as $1/[^{3}He_{ET}]$. This approach yields bioturbated dust flux records that are less damped and more shifted towards older ages than the dust flux records estimated from a linear homogenization of the input dust flux signal itself (as above, Figure 3.9). As with the original model, these results suggest that the Mid-Atlantic sediments have experienced less than ~2 ka of sedimentary smoothing and express a decreased amplitude of variability, relative to 19°N on the Northwest African margin, than is predictred

from bioturbation alone. Thus, the primary conclusions of the bioturbation analyses are insenstive to the assumption of linear homogenization.

The bioturbation model demonstrates that as smoothing increases, the amplitude of variability decreases and the timing of peaks and troughs shift towards older ages. The timing of the AHP minimum and the YD maximum in the Mid-Atlantic dust flux stack (~6 and ~13 ka, respectively) is similar to the predicted occurrence of these events following 1 to 2 ka of smoothing to the input signal (5.9-6.9 ka for the AHP and 12.8-13.8 ka for the YD; Figure 3.9). This suggests that the Mid-Atlantic records did not experience more than 2 ka (or ~4 cm) of smoothing via bioturbation. However, the relative magnitude of the YD to AHP decrease in Mid-Atlantic dust fluxes is much lower than predicted by 2 ka of smoothing to the input signal (Figure 3.9). Therefore, the perceived amplitude of variability recorded in the Mid-Atlantic sediments may reflect decreased variability in the actual dust input to the subtropical Mid-Atlantic, relative to 19°N on the African margin, in addition to the smoothing effects of bioturbation. Such decreased dust variability may result from changes in long-distance dust transport or from a latitudinal gradient in the intensity of emission peaks (e.g., Figure 3.6).

Both continental aridity and wind speed are known to govern long-term regional dustiness (Grousset et al., 1998; McGee et al., 2010a; Rea, 1994; Ruddiman, 1997), but the Mid-Atlantic record suggests that the relative influence of aridity versus wind strength varies over orbital- and millennial-timescales. Tjallingii et al. (2008) estimated a Humidity Index for Northwest Africa over the past 120 ka using grain size analysis and the relative deposition of fluvial versus aeolian material in the GEOB7920-2 core from 21°N on the continental margin (Figure 3.1). Over the

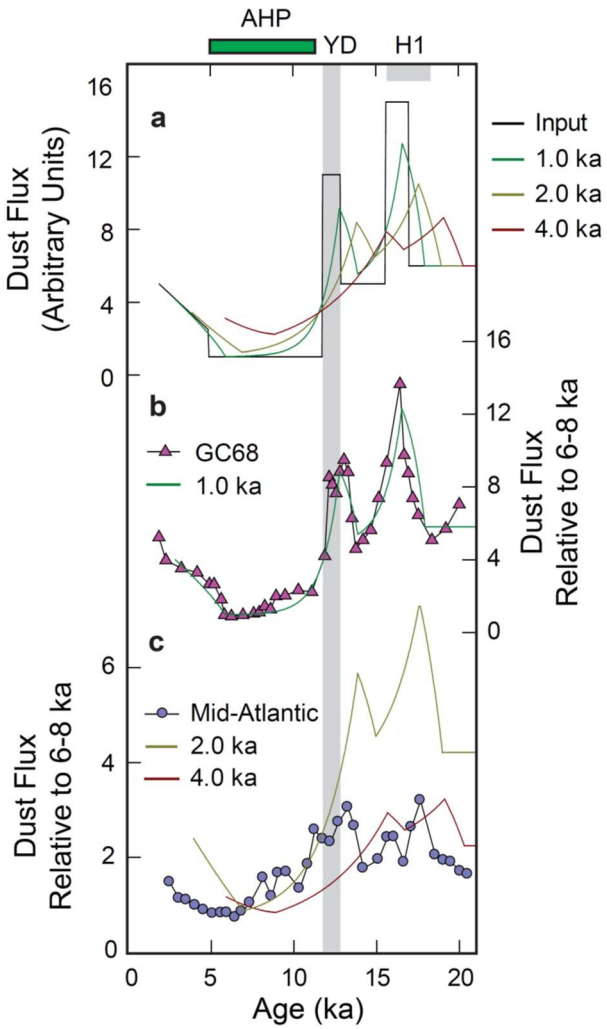

Figure 3.9: Estimated effects of bioturbation on sedimentary records of millennial-scale dust flux variability. (a) Input dust flux signal (black) and bioturbation model outputs for mixed layer depths equivalent to 1 ka (green), 2 ka (yellow), and 4 ka (red) of smoothing. (b) Comparison of the high-resolution OC437-7-GC68 dust flux record (triangles) from 19°N on the Northwest African continental margin (McGee et al., 2013) with the bioturbation model output for 1 ka of smoothing (green line). (c) Comparison of the Mid-Atlantic dust flux stack (circles) with bioturbation model outputs for 2 ka (yellow line) and 4 ka (red line) of smoothing. Error bars are excluded from the Mid-Atlantic stack for clarity. Dust fluxes in (b) and (c) are plotted relative to their 6-8 ka average. Listed ages for the African Humid Period (AHP), the Younger Dryas (YD), and Heinrich event 1 (H1) are as in Figure 3.3. The timing of the AHP minimum and the YD maximum dust fluxes in the Mid-Atlantic (~6 and ~13 ka, respectively) is slightly younger than the predicted timing of these events (6.9 and 13.8 ka, respectively) with 2 ka of smoothing of the input signal. With 4 ka smoothing of the input signal, these events are shifted too far downcore (to 8.9 and 15.6 ka, respectively) to fit the Mid-Atlantic record.

past 50 ka, their Humidity Index and the Mid-Atlantic dust flux stack are relatively well-correlated ($R = -0.57$, $p = 0.03$; Figure 3.8; Figure C6). However, if one excludes the AHP (~5 to 11 ka), the correlation between the humidity index and dust is reduced ($R = -0.40$, $p = 0.16$). This reduced correlation may arise during glacial periods because minor variations in humidity over the desiccated continent will not dramatically alter the extent of dust provenance regions. Rather, increased surface wind speeds and subsequently enhanced aeolian transport driven by increased meridional temperature gradients during Northern Hemisphere cold periods (Broccoli et al., 2006; Chiang and Friedman, 2012) likely explain the general increase in Mid-Atlantic dustiness from 50 ka to the LGM and amplify the millennial-scale dust peaks associated with the YD and multiple Heinrich Stadials (e.g., McGee et al., 2010a; McGee et al., 2013).

The $^{3}He_{ET}$-derived Mid-Atlantic dust stack additionally highlights the ability of sediments with accumulation rates of ~2 cm/ka to resolve the occurrence of millennial-scale peaks in dust deposition. The techniques used in this study could be applied to many existing Atlantic sediment cores to fill in gaps in the spatial coverage of Atlantic dust records and to extend the temporal coverage of dust flux variability beyond the past 70 ka.

3.6. Conclusions

We present new dust flux records constrained using the extraterrestrial helium-3 constant flux proxy and measurements of $^{4}He_{terr}$, Th, and Ti for the subtropical Mid-Atlantic at 26°N and 29°N over the past 70 ka. The new data extend the limit of existing constant flux proxy normalized Atlantic dust records from 20 ka to 70 ka. The presented dust records are remarkably similar to each other and to those from the Northwest African margin, indicating that, while the amplitude of variability may be muted, marine sediments far removed from African dust sources can record the occurrence of millennial-scale changes in continental dust emissions.

The observed Mid-Atlantic dust fluxes are at least a factor of three lower than recent model estimates to the subtropical North Atlantic over the past 21 ka (Albani et al., 2015; Albani et al., 2016). Over longer timescales, the Mid-Atlantic dust records reveal a general increase in dustiness from Marine Isotope Stage 4 through the Last Glacial Maximum, ending only at the onset of the mid-Holocene African Humid Period. Overlying orbital-scale dust trends, millennial-scale dust peaks coincide with Northern Hemisphere cold periods, such as the Younger Dryas, and multiple Heinrich Stadials.

Comparison of a 50 ka Mid-Atlantic dust flux stack to Northwest African humidity estimates (Tjallingi et al., 2008) suggest that decreasing aridity during the African Humid Period was a major driver of decreased dust emissions from 11 to 5 ka. However, precipitation does not appear to exert the exclusive control on millennial-scale dust flux variability during Northern Hemisphere cold periods when dust source regions are already very dry. Thus, the Mid-Atlantic dust record is consistent with the hypothesis that both aridity and wind strength are important regulators of African dust emissions.

References

Adkins, J., Demenocal, P., Eshel, G., 2006. The "African humid period" and the record of marine upwelling from excess 230Th in Ocean Drilling Program Hole 658C. Paleoceanography 21, PA4203.

Albani, S., Mahowald, N.M., Murphy, L.N., Raiswell, R., Moore, J.K., Anderson, R.F., McGee, D., Bradtmiller, L.I., Delmonte, B., Hesse, P.P., Mayewski, P.A., 2016. Paleodust variability since the Last Glacial Maximum and implications for iron inputs to the ocean. Geophysical Research Letters 43, 3944-3954.

Albani, S., Mahowald, N.M., Winckler, G., Anderson, R.F., Bradtmiller, L.I., Delmonte, B., Francois, R., Goman, M., Heavens, N.G., Hesse, P.P., Hovan, S.A., Kang, S.G., Kohfeld,

K.E., Lu, H., Maggi, V., Mason, J.A., Mayewski, P.A., McGee, D., Miao, X., Otto-Bliesner, B.L., Perry, A.T., Pourmand, A., Roberts, H.M., Rosenbloom, N., Stevens, T., Sun, J., 2015. Twelve thousand years of dust: the Holocene global dust cycle constrained by natural archives. Climate of the Past 11, 869-903.

Anderson, R.F., Fleisher, M.Q., Lao, Y., 2006. Glacial–interglacial variability in the delivery of dust to the central equatorial Pacific Ocean. Earth and Planetary Science Letters 242, 406-414.

Bacon, M.P., 1984. Glacial to interglacial changes in carbonate and clay sedimentation in the Atlantic Ocean estimated from 230Th measurements. Isotope Geoscience 46, 97-111.

Berger, W.H., Heath, G.R., 1968. Vertical mixing in pelagic sediments. J. Mar. Res. 26, 134.

Booth, B.B., Dunstone, N.J., Halloran, P.R., Andrews, T., Bellouin, N., 2012. Aerosols implicated as a prime driver of twentieth-century North Atlantic climate variability. Nature 484, 228-232.

Bradtmiller, L.I., Anderson, R.F., Fleisher, M.Q., Burckle, L.H., 2007. Opal burial in the equatorial Atlantic Ocean over the last 30 ka: Implications for glacial-interglacial changes in the ocean silicon cycle. Paleoceanography 22, PA4216.

Bristow, C.S., Hudson-Edwards, K.A., Chappell, A., 2010. Fertilizing the Amazon and equatorial Atlantic with West African dust. Geophysical Research Letters 37.

Broccoli, A.J., Dahl, K.A., Stouffer, R.J., 2006. Response of the ITCZ to Northern Hemisphere cooling. Geophysical Research Letters 33, L01702.

Castillo, S., Moreno, T., Querol, X., Alastuey, A., Cuevas, E., Herrmann, L., Mounkaila, M., Gibbons, W., 2008. Trace element variation in size-fractionated African desert dusts. Journal of Arid Environments 72, 1034-1045.

Chiang, J.C.H., Friedman, A.R., 2012. Extratropical cooling, interhemispheric thermal gradients, and tropical climate change. Annual Review of Earth and Planetary Sciences 40, 383-412.

Chiapello, I., Moulin, C., Prospero, J.M., 2005. Understanding the long-term variability of African dust transport across the Atlantic as recorded in both Barbados surface concentrations and large-scale Total Ozone Mapping Spectrometer (TOMS) optical thickness. Journal of Geophysical Research 110.

Claussen, M., Kubatzki, C., Brovkin, V., Ganopolski, A., Hoelzmann, P., Pachur, H.J., 1999. Simulation of an abrupt change in Saharan vegetation in the mid-Holocene. Geophysical Research Letters 26, 2037-2040.

Costa, K., McManus, J., 2017. Efficacy of 230Th normalization in sediments from the Juan de Fuca Ridge, northeast Pacific Ocean. Geochimica et Cosmochimica Acta 197, 215-225.

deMenocal, P., Ortiz, J., Guilderson, T., Adkins, J., Sarnthein, M., Baker, L., Yarusinsky, M., 2000. Abrupt onset and termination of the African Humid Period: rapid climate responses to gradual insolation forcing. Quaternary Science Reviews 19, 347-361.

Dunion, J.P., Velden, C.S., 2004. The impact of the Saharan air layer on Atlantic tropical cyclone activity. Bulletin of the American Meteorological Society 85, 353-365.

Escrig, S., Bézos, A., Langmuir, C.H., Michael, P.J., Arculus, R., 2012. Characterizing the effect of mantle source, subduction input and melting in the Fonualei Spreading Center, Lau Basin: Constraints on the origin of the boninitic signature of the back-arc lavas. Geochemistry, Geophysics, Geosystems 13.

Evan, A.T., Flamant, C., Gaetani, M., Guichard, F., 2016. The past, present and future of African dust. Nature 531, 493-495.

Evan, A.T., Foltz, G.R., Zhang, D., Vimont, D.J., 2011. Influence of African dust on ocean-atmosphere variability in the tropical Atlantic. Nature Geoscience 4, 762-765.

Farley, K.A., 1995. Cenozoic variations in the flux of interplanetary dust recorded by ^{3}He in a deep-sea sediment. Nature 376, 153-156.

Farley, K.A., Eltgroth, S.F., 2003. An alternative age model for the Paleocene–Eocene thermal maximum using extraterrestrial 3He. Earth and Planetary Science Letters 208, 135-148.

Farley, K.A., Love, S.G., Patterson, D.B., 1997. Atmospheric entry heating and helium retentivity of interplanetary dust particles. Geochimica et Cosmochimica Acta 61, 2309-2316.

Farley, K.A., Patterson, D.B., 1995. A 100-kyr periodicity in the flux of extraterrestrial ^{3}He to the sea floor. Nature 378, 600-603.

Francois, R., Frank, M., Rutgers van der Loeff, M.M., Bacon, M.P., 2004. 230Th normalization: An essential tool for interpreting sedimentary fluxes during the late Quaternary. Paleoceanography 19, PA1018.

Gale, A., Dalton, C.A., Langmuir, C.H., Su, Y., Schilling, J.-G., 2013. The mean composition of ocean ridge basalts. Geochemistry Geophysics Geosystems 14, 489-518.

Gasse, F., 2000. Hydrological changes in the African tropics since the Last Glacial Maximum. Quaternary Science Reviews 19, 189-211.

Gayer, E., Mukhopadhyay, S., Meade, B.J., 2008. Spatial variability of erosion rates inferred from the frequency distribution of cosmogenic 3He in olivines from Hawaiian river sediments. Earth and Planetary Science Letters 266, 303-315.

Gelado-Caballero, M.D., López-García, P., Prieto, S., Patey, M.D., Collado, C., Hérnández-Brito, J.J., 2012. Long-term aerosol measurements in Gran Canaria, Canary Islands: Particle concentration, sources and elemental composition. Journal of Geophysical Research 117, D03304.

Goudie, A.S., Middleton, N.J., 2001. Saharan dust storms: nature and consequences. Earth-Science Reviews 56, 179-204.

Graham, D.W., 2002. Noble gas isotope geochemistry of mid-ocean ridge and ocean island basalts: Characterization of mantle source reservoirs. Rev. Mineral Geochem. 47, 247-318.

Grousset, F.E., Parra, M., Bory, A., Martinez, P., Bertrand, P., Shimmield, G., Ellam, R.M., 1998. Saharan wind regimes traced by the Sr–Nd isotopic composition of subtropical Atlantic sediments: Last Glacial Maximum vs Today. Quaternary Science Reviews 17, 395-409.

Higgins, S., 2001. Extraterrestrial tracer in the sea: evaluation and application of ^{3}He in interplanetary dust particles as a 'constant flux' tracer in marine sediments, Columbia University, New York. Columbia University, New York, New York.

Higgins, S.M., Anderson, R.F., Marcantonio, F., Schlosser, P., Stute, M., 2002. Sediment focusing creates 100-ka cycles in interplanetary dust accumulation on the Ontong Java Plateau. Earth and Planetary Science Letters 203, 383-397.

Jickells, T.D., An, Z.S., Andersen, K.K., Baker, A.R., Bergametti, G., Brooks, N., Cao, J.J., Boyd, P.W., Duce, R.A., Hunter, K.A., Kawahata, H., Kubilay, N., LaRoche, J., Liss, P.S., Mahowald, N., Prospero, J.M., Ridgwell, A.J., Tegen, I., Torres, R., 2005. Global iron connections between desert dust, ocean biogeochemistry, and climate. Science 308, 67-71.

Jolly, D., Prentice, I.C., Bonnefille, R., Ballouche, A., Bengo, M., Brenac, P., Buchet, G., Burney, D., Cazet, J.P., Cheddadi, R., Edorh, T., Elenga, H., Elmoutaki, S., Guiot, J., Laarif, F., Lamb, H., Lezine, A.-M., Maley, J., Mbenza, M., Peyron, O., Reille, M., Reynaud-Farrera, I., Riollet, G., Ritchie, J.C., Roche, E., Scott, L., Ssemmanda, I., Straka, H., Umer, M., Van Campo, E., Vilimumbalo, S., Vincens, A., Waller, M., 1998. Biome reconstruction from pollen and plant macrofossil data for Africa and the Arabian peninsula at 0 and 6000 years. Journal of Biogeography 25, 1007-1027.

Kaufman, Y.J., Koren, I., Remer, L.A., Tanré, D., Ginoux, P., Fan, S., 2005. Dust transport and deposition observed from the Terra-Moderate Resolution Imaging Spectroradiometer (MODIS) spacecraft over the Atlantic Ocean. Journal of Geophysical Research 110, D10S12.

Keigwin, L.D., Jones, G.A., 1994. Western North Atlantic evidence for millennial-scale changes in ocean circulation and climate. Journal of Geophysical Research 99, 12397-12410.

Kienast, S.S., Winckler, G., Lippold, J., Albani, S., Mahowald, N.M., 2016. Tracing dust input to the global ocean using thorium isotopes in marine sediments: ThoroMap. Glob. Biogeochem. Cycle 30, 1526-1541.

Kohfeld, K.E., Harrison, S.P., 2001. DIRTMAP: the geological record of dust. Earth-Science Reviews 54, 81-114.

Kutzbach, J.E., Liu, Z., 1997. Response of the African monsoon to orbital forcing and ocean feedbacks in the middle Holocene. Science 278, 440-443.

Mahowald, N.M., Engelstaedter, S., Luo, C., Sealy, A., Artaxo, P., Benitez-Nelson, C., Bonnet, S., Chen, Y., Chuang, P.Y., Cohen, D.D., Dulac, F., Herut, B., Johansen, A.M., Kubilay, N., Losno, R., Maenhaut, W., Paytan, A., Prospero, J.M., Shank, L.M., Siefert, R.L., 2009. Atmospheric Iron Deposition: Global Distribution, Variability, and Human Perturbations. Annual Review of Marine Science 1, 245-278.

Mahowald, N.M., Muhs, D.R., Levis, S., Rasch, P.J., Yoshioka, M., Zender, C.S., Luo, C., 2006. Change in atmospheric mineral aerosols in response to climate: Last glacial period, preindustrial, modern, and doubled carbon dioxide climates. J. Geophys. Res. 111.

Marcantonio, F., Anderson, R.F., Higgins, S., Fleisher, M.Q., Stute, M., Schlosser, P., 2001a. Abrupt intensification of the SW Indian Ocean monsoon during the last deglaciation: constraints from Th, Pa, and He isotopes. Earth and Planetary Science Letters 184, 505-514.

Marcantonio, F., Anderson, R.F., Higgins, S., Stute, M., Schlosser, P., Kubik, P., 2001b. Sediment focusing in the central equatorial Pacific Ocean. Paleoceanography 16, 260-267.

Marcantonio, F., Higgins, S., Anderson, R.F., Stute, M., Schlosser, P., Rasbury, E.T., 1998. Terrigenous helium in deep-sea sediments. Geochimica et Cosmochimica Acta 62, 1535-1543.

Marcantonio, F., Anderson, R.F., Stute, M., Kumar, N., Schlosser, P., Mix., A., 1996. Extraterrestrial 3He as a tracer of marine sediment transport and accumulation. Nature 383, 705-707.

Marcantonio, F., Kumar, N., Stute, M., Anderson, R.F., Seidl, M.A., Schlosser, P., Mix, A., 1995. A comparative study of accumulation rates derived by He and Th isotope analysis of marine sediments. Earth and Planetary Science Letters 133, 549-555.

Martin, J.H., 1990. Glacial-interglacial CO2 change: The iron hypothesis. Paleoceanography 5, 1-13.

McGee, D., Broecker, W.S., Winckler, G., 2010a. Gustiness: The driver of glacial dustiness? Quaternary Science Reviews 29, 2340-2350.

McGee, D., Marcantonio, F., McManus, J.F., Winckler, G., 2010b. The response of excess 230Th and extraterrestrial 3He to sediment redistribution at the Blake Ridge, western North Atlantic. Earth and Planetary Science Letters 299, 138-149.

McGee, D., Mukhopadhyay, S., 2013. Extraterrestrial He in sediments: From recorder of asteroid collisions to timekeeper of global environmental changes, The Noble Gases as Geochemical Tracers. Springer-Verlag, Hiedelberg, Heidelberg, pp. 155-176.

McGee, D., Winckler, G., Borunda, A., Serno, S., Anderson, R.F., Recasens, C., Bory, A., Gaiero, D., Jaccard, S.L., Kaplan, M., McManus, J.F., Revel, M., Sun, Y., 2016. Tracking eolian dust with helium and thorium: impacts of grain size and provenance. Geochimica et Cosmochimica Acta 175, 47-67.

McGee, D., Winckler, G., Stuut, J.B.W., Bradtmiller, L.I., 2013. The magnitude, timing and abruptness of changes in North African dust deposition over the last 20,000 yr. Earth and Planetary Science Letters 371, 163-176.

Middleton, J.L., Langmuir, C.H., Mukhopadhyay, S., McManus, J.F., Mitrovica, J.X., 2016. Hydrothermal iron flux variability following rapid sea level changes. Geophysical Research Letters 43, 3848-3856.

Miller, R., Tegen, I., 1998. Climate response to soil dust aerosols. Journal of Climate 11, 3247-3267.

Mukhopadhyay, S., Farley, K.A., Montanari, A., 2001. A short duration of the Cretaceous-Tertiary boundary event: Evidence from extraterrestrial helium-3. Science 291, 1952-1955.

Mukhopadhyay, S., Kreycik, P., 2008. Dust generation and drought patterns in Africa from helium-4 in a modern Cape Verde coral. Geophysical Research Letters 35.

Murray, R.W., Knowlton, C., Leinen, M., Mix, A.C., Polsky, C.H., 2000. Export production and carbonate dissolution in the central equatorial Pacific Ocean over the past 1 Myr. Paleoceanography 15, 570-592.

Nier, A.O., Schlutter, D.J., 1992. Extraction of helium from individual interplanetary dust particles by step-heating. Meteoritics 27, 166-173.

Parker, A.O., Schmidt, M.W., Jobe, Z.R., Slowey, N.C., 2016. A new perspective on West African hydroclimate during the last deglaciation. Earth and Planetary Science Letters 449, 79-88.

Patterson, D.B., Farley, K.A., Norman, M.D., 1999. ^{4}He as a tracer of continental dust: A 1.9 million year record of aeolian flux to the west equatorial Pacific Ocean. Geochimica Et Cosmochimica Acta 63, 615-625.

Patterson, D.B., Farley, K.A., Schmitz, B., 1998. Preservation of extraterrestrial ^{3}He in 480-Ma-old marine limestones. Earth and Planetary Science Letters 163, 315-325.

Pausata, F.S., Messori, G., Zhang, Q., 2016. Impacts of dust reduction on the northward expansion of the African monsoon during the Green Sahara period. Earth and Planetary Science Letters 434, 298-307.

Prospero, J.M., Ginoux, P., Torres, O., Nicholson, S.E., Gill, T.E., 2002. Environmental characterization of global sources of atmospheric soil dust identified with the Nimbus 7 Total Ozone Mapping Spectrometer (TOMS) absorbing aerosol product. Reviews of Geophysics 40.

Prospero, J.M., Lamb, P.J., 2003. African droughts and dust transport to the Caribbean: Climate change implications. Science 302, 1024-1027.

Prospero, J.M., Mayol-Bracero, O.L., 2013. Understanding the transport and impact of African dust on the Caribbean basin. Bulletin of the American Meteorological Society 94, 1329-1337.

Rashid, H., Hesse, R., Piper, D.J.W., 2003. Evidence for an additional Heinrich event between H5 and H6 in the Labrador Sea. Paleoceanography 18, 1077.

Rea, D.K., 1994. The paleoclimatic record provided by eolian deposition in the deep sea: The geologic history of wind. Reviews of Geophysics 32, 159-195.

Reimer, P.J., Bard, E., Bayliss, A., Beck, J.W., Blackwell, P.G., Bronk Ramsey, C., Buck, C.E., Cheng, H., Edwards, R.L., Friedrich, M., Grootes, P.M., Guilderson, T.P., Haflidason, H., Hajdas, I., Hatte, C., Heaton, T.J., Hoffmann, D.L., Hogg, A.G., Hughen, K.A., Kaiser, K.F., Kromer, B., Manning, S.W., Niu, M., Reimer, R.W., Richards, D.A., Scott, E.M., Southon, J.R., Staff, R.A., Turney, C.S.M., van der Plicht, J., 2013. IntCal13 and Marine13 radiocarbon age calibration curves 0-50,000 years cal BP. Radiocarbon 55, 1869-1887.

Ridley, D.A., Heald, C.L., Prospero, J.M., 2014. What controls the recent changes in African mineral dust aerosol across the Atlantic? Atmospheric Chemistry and Physics 14, 5735-5747.

Ritchie, J.C., Eyles, C.H., Haynes, C.V., 1985. Sediment and pollen evidence for an early to mid-Holocene humid period in the eastern Sahara. Nature 314, 352-355.

Rodríguez, S., Cuevas, E., Prospero, J.M., Alastuey, A., Querol, X., López-Solano, J., García, M.I., Alonso-Pérez, S., 2015. Modulation of Saharan dust export by the North African dipole. Atmospheric Chemistry and Physics 15, 7471-7486.

Rowland, G.H., Ng, H.C., Robinson, L.F., McManus, J.F., Mohamed, K.J., McGee, D., 2017. Investigating the use of $^{232}Th/^{230}Th$ as a dust proxy using co-located seawater and sediment samples from the low-latitude North Atlantic. Geochimica et Cosmochimica Acta 214, 143-156.

Rosenfeld, D., Rudich, Y., Lahav, R., 2001. Desert dust suppressing precipitation: A possible desertification feedback loop. Proceedings of the National Academy of Sciences 98, 5975-5980.

Ruddiman, W.F., 1997. Tropical Atlantic terrigenous fluxes since 25,000 yrs BP. Marine Geology 136, 189-207.

Sanchez Goñi, M.F., Harrison, S.P., 2010. Millennial-scale climate variability and vegetation changes during the Last Glacial: Concepts and terminology. Quaternary Science Reviews 29, 2823-2827.

Serno, S., Winckler, G., Anderson, R.F., Hayes, C.T., McGee, D., Machalett, B., Ren, H., Straub, S.M., Gersonde, R., Haug, G.H., 2014. Eolian dust input to the Subarctic North Pacific. Earth and Planetary Science Letters 387, 252-263.

Street, F.A., Grove, A.T., 1976. Environmental and climatic implications of late Quaternary lake-level fluctuations in Africa. Nature 261, 385-390.

Stuiver, M., Reimer, P.J., 1993. Extended 14 C data base and revised CALIB 3.0 14 C age calibration program. Radiocarbon 35, 215-230.

Suman, D.O., Bacon, M.P., 1989. Variations in Holocene sedimentation in the North-American Basin determined from Th-230 measurements. Deep-Sea Research Part a-Oceanographic Research Papers 36, 869-878.

Takayanagi, M., Ozima, M., 1987. Temporal variation of $^{3}He/^{4}He$ ratio recorded in deep-sea sediment cores. Journal of Geophysical Research 92, 12531-12538.

Tegen, I., Harrison, S.P., Kohfeld, K., Prentice, I.C., Coe, M., Heimann, M., 2002. Impact of vegetation and preferential source areas on global dust aerosol: Results from a model study. Journal of Geophysical Research 107, 4576, doi:10.1029/2001JD000963.

Theiler, J., Eubank, S., Longtin, A., Galdrikian, B., Farmer, J.D., 1992. Testing for nonlinearity in time series: the method of surrogate data. Physica D 58, 77-94.

Tierney, J.E., Pausata, F.S.R., deMenocal, P.B., 2017. Rainfall regimes of the Green Sahara. Science Advances 3, e1601503.

Tjallingii, R., Claussen, M., Stuut, J.-B.W., Fohlmeister, J., Jahn, A., Bickert, T., Lamy, F., Röhl, U., 2008. Coherent high-and low-latitude control of the northwest African hydrological balance. Nature Geoscience 1, 670-675.

Weldeab, S., Lea, D.W., Schneider, R.R., Andersen, N., 2007. 155,000 years of West African monsoon and ocean thermal evolution. Science 316, 1303-1307.

Werner, M., Tegen, I., Harrison, S.P., Kohfeld, K.E., Prentice, I.C., Balkanski, Y., Rodhe, H., Roelandt, C., 2002. Seasonal and interannual variability of the mineral dust cycle under present and glacial climate conditions. Journal of Geophysical Research: Atmospheres 107.

Williams, R.H., McGee, D., Kinsley, C.W., Ridley, D.A., Hu, S., Fedorov, A., Tal, I., Murray, R.W., deMenocal, P.B., 2016. Glacial to Holocene changes in trans-Atlantic Saharan dust transport and dust-climate feedbacks. Science Advances 2, e1600445.

Winckler, G., Anderson, R.F., Fleisher, M.Q., McGee, D., Mahowald, N., 2008. Covariant glacial-interglacial dust fluxes in the Equatorial Pacific and Antarctica. Science 320, 93-96.

Winckler, G., Anderson, R.F., Schlosser, P., 2005. Equatorial Pacific productivity and dust flux during the mid-Pleistocene climate transition. Paleoceanography 20, PA4025.

Chapter 4: Constant flux proxy comparison and a 600 ka record of hydrothermal flux variability on the Cleft Segment of the Juan de Fuca Ridge

Abstract

Marine sedimentary mass accumulation rates are commonly used to construct records of lithogenic, biogenic, and hydrothermal deposition to the seafloor over time. Variations in the mass fluxes of these sedimentary components help to decipher changes in continental aridity, atmospheric dynamics, biologic productivity, and submarine hydrothermal activity over myriad climatic conditions. Constant flux proxies, such as extraterrestrial helium-3 ($^{3}He_{ET}$) and excess thorium-230 ($^{230}Th_{XS}$), provide a means to constrain vertical sediment rain rates that are independent of the biases associated with lateral sediment transport and limited age model resolution. While the application of $^{230}Th_{XS}$ is limited to the past ~500 ka by its 75,700-year half-life, $^{3}He_{ET}$ can be utilized to constrain depositional variability throughout much of the Cenozoic. While the $^{230}Th_{XS}$ and $^{3}He_{ET}$ constant flux proxy systems provide valuable tools with which to investigate a wide range of climatic variability, few studies have directly compared their performance in the same sedimentary samples. This study uses new measurements of $^{3}He_{ET}$ in two sediment cores from the Cleft Segment of the Juan de Fuca Ridge to evaluate the $^{230}Th_{XS}$ and $^{3}He_{ET}$ constant flux proxies in the Northeast Pacific from 45 to 440 ka. While $^{3}He_{ET}$ and $^{230}Th_{XS}$ yield vertical rain rate records of similar amplitude and variability on glacial-interglacial timescales, the helium-based records exhibit suborbital variability that is not found in thorium-based records from the same sediments. The suborbital variability resolved by $^{3}He_{ET}$ may reflect an advantage of this proxy over $^{230}Th_{XS}$ in slowly accumulating (<3 cm/ka) sediments or may

result from unanticipated high frequency variability in the delivery of $^{3}He_{ET}$ to the seafloor and motivates future investigation.

The new $^{3}He_{ET}$ -based record extends constraints on hydrothermal iron and copper deposition on the Cleft Segment to 600 ka and reveals a prolonged period of high hydrothermal deposition between ~530 and ~490 ka that is unlike any other interval in the past 600 ka. Over the past 600 ka, the Cleft Segment sediments exhibit factors of 2 to 4 variations in hydrothermal Fe deposition over timescales of ~10 to 100 ka. If Cleft Segment hydrothermal variability is globally representative, such changes in hydrothermal Fe input to the deep ocean may generate significant variability in the delivery of dissolved Fe into the global oceans.

Pressure fluctuations above mid-ocean ridges associated with glacially-driven changes in sea level have been proposed as a mechanism to generate global variability in hydrothermal output. The long-term records of hydrothermal deposition on the Juan de Fuca Ridge provide interesting observational constraints with which to examine the potential relationship between sea level changes and hydrothermal output on an intermediate-spreading ridge. While statistical comparison of the Cleft Segment hydrothermal records to proxy estimates of sea level variability suggest that the relationship between sea level and hydrothermal deposition may be complex and evolving, significant correlations are observed between high hydrothermal Fe deposition and high sea level over the past 250 ka. Such a result motivates the development of geochemical and geophysical models to examine the mechanisms that may drive enhanced hydrothermal circulation during periods of sea level rise.

4.1. Introduction

Important constraints on the atmospheric and oceanographic responses to changing climatic conditions are provided by depositional records of climate proxies such as carbonate, terrigenous dust, and biogenic opal constructed from marine sedimentary cores (e.g., Anderson et al., 2009; Schoepfer et al., 2015; Winckler et al., 2008; Winckler et al., 2005; Ruddiman, 1997; Haug et al., 1999). Further, the mass accumulation rates of hydrothermal plume precipitates in near-axis sediment cores provide continuous and datable records of hydrothermal deposition that are used to investigate millennial- and orbital-scale variations in submarine hydrothermal activity (Frank et al., 1994; Cherkashev, 1995; Auffret et al., 1996; German et al., 1997; Cave et al., 2002; Middleton et al., 2016; Lund et al., 2016; Costa et al., 2017). Such records of hydrothermal variability are an essential tool in evaluation of the hypothesis that submarine volcanic centers are sensitive to the overlying pressure fluctuations associated with glacially-driven changes in sea level (Huybers and Langmuir, 2009; Crowley et al., 2015; Lund and Asimow, 2011; Tolstoy, 2015; Middleton et al., 2016; Lund et al., 2016; Costa et al., 2017).

Sediment deposition rates that are estimated using traditional mass accumulation rates calculated from sediment core age models can be subject to bias from lateral sediment transport and are limited by age model resolution (Higgins et al., 2002; Marcantonio et al., 1996; Marcantonio et al., 2001b; Suman and Bacon, 1989). In contrast, constant flux proxies, such as extraterrestrial helium-3 ($^{3}He_{ET}$; Takayanagi and Ozima, 1987; Farley and Patterson, 1995; Marcantonio et al., 1995; Farley, 1995; McGee and Mukhopadhyay, 2013) and excess thorium-230 ($^{230}Th_{XS}$; Bacon, 1984; Francois et al., 2004; Suman and Bacon, 1989), can be used to calculate vertical sediment

rain rates that are independent of age model uncertainties and the effects of lateral sediment transport. Consequently, constant flux proxies provide a means to constrain high resolution records of depositional variability of biogenic, lithogenic, and hydrothermal inputs to even complex sedimentary environments (e.g., Higgins et al., 2002; Middleton et al., 2016; Costa and McManus, 2017).

The utility of $^{3}He_{ET}$ and $^{230}Th_{XS}$ as constant flux proxies results from the predictable and well-constrained influx of these nuclides to the seafloor. While ^{4}He is dominantly delivered to marine sediments via terrigenous dust, ^{3}He is primarily delivered to the seafloor via interplanetary dust particles (IDPs; Farley, 1995; Nier and Schlutter, 1993; Takayanagi and Ozima, 1987). Sourced from asteroid and comet debris, IDPs host implanted solar helium with a $^{3}He/^{4}He$ ratio of 2.4 x 10^{-4} (or 170 R_A, where R_A denotes the atmospheric $^{3}He/^{4}He$ value of 1.39 x 10^{-6}; Nier and Schlutter, 1992) that is significantly higher than the values of typical terrigenous sediments of ~2 x 10^{-8} (or 0.01 R_A; Farley and Patterson, 1995; Marcantonio et al., 1998). The presence of IDPs in marine sediments can thus be identified by the high $^{3}He/^{4}He$ ratios measured in sedimentary samples, which are often ~10^{2} to 10^{3} times higher than terrigenous materials (Takayanagi and Ozima, 1987; Farley and Patterson, 1995; Marcantonio et al., 1995). The concentration of IDP-associated $^{3}He_{ET}$ in sedimentary samples is calculated by subtracting the terrigenous component from total ^{3}He (See Section 4.2.2). While the influx of $^{3}He_{ET}$ from space can vary over millions of years (Farley, 1995; Farley and Eltgroth, 2003; Marcantonio et al., 2009; Mukhopadhyay et al., 2001; Farley et al., 2006), a compilation of marine records suggests a consistent influx of IDP $^{3}He_{ET}$ of 8.0 ± 1.2 x10^{-13} cc STP cm^{-2} ka^{-1} throughout the Quaternary (McGee and Mukhopadhyay, 2013). The retention of $^{3}He_{ET}$ in limestones dating to ~480 Ma suggests that

$^{3}He_{ET}$ could be employed to constrain sedimentary fluxes throughout much of the Phanerozoic (Patterson et al., 1998).

In contrast to $^{3}He_{ET}$, $^{230}Th_{XS}$ is generated in seawater through the decay of aqueous ^{234}U and is rapidly scavenged by settling particulate matter to the sediments below (Bacon and Anderson, 1982). Due its long residence time, seawater ^{234}U is well mixed and $^{230}Th_{XS}$ is consequently produced at a uniform rate throughout the water column (Anderson et al., 2010). The flux of $^{230}Th_{XS}$ to the seafloor is thus a function the activity of ^{234}U in seawater and the height of water column overlying the sediments below (Bacon et al., 1984). Sedimentary concentrations of $^{230}Th_{XS}$ are determined by correcting total ^{230}Th for its terrigenous component and for authigenic ingrowth from in situ ^{234}U decay (e.g., Francois et al., 2004). Resulting values are then adjusted for the decay of $^{230}Th_{XS}$ itself using the sediment sample age. Given the 75.7 ka half-life of ^{230}Th, there are increased uncertainties in the determination of $^{230}Th_{XS}$ concentrations in sediments older than ~350 ka, and applications of $^{230}Th_{XS}$ as a constant flux proxy are limited to the past ~500 ka (e.g., Winckler et al., 2008; Costa and McManus, 2017).

Despite the vast paleoceanographic potential of constant flux proxies, studies that directly compare the behavior of $^{230}Th_{XS}$ and $^{3}He_{ET}$ using measurements from the same samples are limited in temporal resolution and only include sediments younger than 325 ka (Marcantonio et al., 1995; Marcantonio et al., 1999; Marcantonio et al., 2001b). Higher resolution (~1 sample per 1 to 2 ka) comparative studies are spatially sparse and exclusively examine the past 25 ka (Marcantonio et al., 2001a; McGee et al., 2010a). Previous comparisons of $^{230}Th_{XS}$ - and $^{3}He_{ET}$ - derived sedimentary fluxes in the Atlantic, Equatorial Pacific, and Equatorial Indian ocean basins

demonstrate relatively good agreement between these proxies on Milankovitch timescales (Marcantonio et al., 1995; 1999; Higgins et al., 2002). However, these studies are of insufficient resolution to evaluate potential variations between the $^{3}He_{ET}$ and $^{230}Th_{XS}$ systems on suborbital timescales. The high resolution (~1 sample per 1 ka) comparative record from the Arabian Sea extends only to the Last Glacial Maximum, and suggests potentially different behaviors between the two constant flux proxies on suborbital-timescales (Marcantonio et al., 2001a). Additional high resolution comparative records are therefore essential to examine potential discrepancies in the behavior of $^{3}He_{ET}$ and $^{230}Th_{XS}$ when applied to studies of high frequency climate variability.

This study presents new records of vertical sediment rain rates spanning the past 600 ka in the Northeast Pacific, constrained using analyses of $^{3}He_{ET}$ in two sediment cores from the Cleft Segment of the Juan de Fuca Ridge. The new helium data include over 130 samples between 50 and 440 ka in which thorium analyses were also performed (Costa and McManus, 2017) and allow for a direct comparison of the performance of $^{3}He_{ET}$ and $^{230}Th_{XS}$ as constant flux proxies in the Northeast Pacific over both Milankovitch and millennial-timescales. The $^{3}He_{ET}$- and $^{230}Th_{XS}$ -based flux records are additionally combined with carbonate, iron, copper, titanium, and terrigenous helium-4 ($^{4}He_{terr}$) concentration data to generate records of carbonate, lithogenic, and hydrothermal sedimentary fluxes to the Juan de Fuca Ridge from Marine Isotope Stage (MIS) 15 through the Last Glacial Maximum. While in-depth evaluation and discussion of the variations in carbonate and lithogenic fluxes to the Juan de Fuca Ridge provide ample material for future work, this study focuses discussion on the recorded variations in hydrothermal deposition over the past 600 ka. Finally, the hydrothermal iron and copper flux records are used to investigate the proposed relationship between glacially-driven changes in sea level and hydrothermal activity on

the intermediate-spreading Juan de Fuca Ridge (e.g., Huybers and Langmuir, 2009; Crowley et al., 2015; Lund and Asimow, 2011; Middleton et al., 2016; Lund et al., 2016; Costa et al., 2017).

4.2. Sampling and Methods

4.2.1 Study Area

The sediment cores examined in this study were recovered from the western flank of the Cleft Segment of the southern Juan de Fuca Ridge in the Northeast Pacific during the SeaVOICE cruise (AT26-19) of the R/V Atlantis in September 2014 (Figure 4.1; Costa et al., 2016). The cores are located ~500 km from the Northwest American coastline and ~50 to 20 km from the neovolcanic zone of the Cleft Segment and its confirmed active hydrothermal fields (Stakes et al., 2006). Sedimentary records from the eastern flank of the Cleft Segment are not available as seafloor conditions east of the ridge axis inhibited successful sediment core recovery (Costa et al., 2017).

Sediment core chronologies were constrained using radiocarbon analyses, as well as benthic oxygen isotope and lithologic stratigraphic correlations (Costa et al., 2016). Vertical sediment rain rates derived using $^{230}Th_{XS}$ demonstrate regionally consistent glacial-interglacial variability over the past ~500 ka, with higher vertical sediment rain rates occurring during glacial periods, when carbonate preservation in the Northeast Pacific is highest (Costa and McManus, 2017). The hydrothermal component of the SeaVOICE sediment cores was constrained using iron and

copper concentrations, with a titanium-based correction for lithogenic input, that were measured using x-ray fluorescence scanning (Costa et al., 2017).

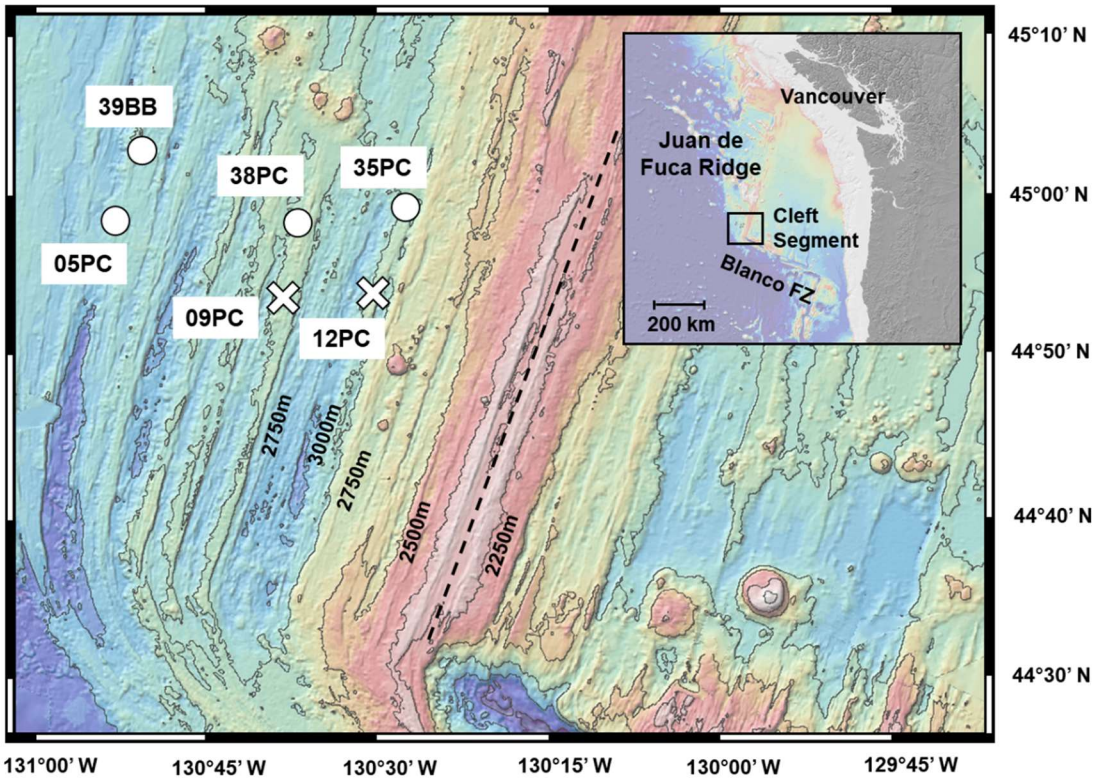

Figure 4.1: Map of select sediment cores (white markers) from cruise AT26-19 on the Cleft Segment of the Juan de Fuca Ridge. Black contours are shown at 250 m depth intervals. Helium isotope data were measured in 09PC and 12PC (white crosses). Dashed line indicates the neovolcanic zone of the Cleft Segment, where axial hydrothermal fields are located (Stakes et al., 2006). Inset shows the location of the Cleft Segment within the broader context of the Juan de Fuca Ridge and the Northeast Pacific Ocean. Both maps were generated using GeoMapApp.

Extensive helium isotope analyses (167 samples) were performed in AT26-19-12PC (44.90°N, 130.50°W, 2689 m water depth, 550 cm core length) due to its temporal coverage, extending >600 ka (Costa et al., 2016), and due to its proximity to the ridge axis (18 km; Figure 4.1). The bottom of the 12PC sedimentary record is terminated by the presence of basalt rock, and conspicuous fragments of basalt glass are observed in 12PC in sediments >545 ka in age

(Ferguson et al., 2017). Helium isotope analyses were additionally performed in 50 samples from AT16-19-09PC (44.89°N, 130.64°W, 2678 m water depth, 766 cm core length) to evaluate the spatial reproducibility of $^3He_{ET}$ -derived vertical sediment rain rates in the Juan de Fuca Ridge sediments.

4.2.2. Helium Isotope Analyses

Helium concentration and isotope ratios were performed on 0.5 g initial aliquots of dry bulk sediment at the UC Davis Noble Gas Laboratory following the methods of Middleton et al. (2016). Each sample reflects the average value of a ~1cm sedimentary interval and typically represents ~600 and ~1200 years of time in 09PC and 12PC, respectively. Mantle-derived helium in mid-ocean basalt is a potential contaminant with respect to the application of $^3He_{ET}$ in near-ridge sediments (Graham, 2002). Thus, most samples were sieved during preparation, with the helium analyses performed in the <64 um fraction to reduce the possibility of helium contamination from coarse fragments of mid-ocean ridge basalt glass. A subset of samples from 12PC, indicated by 'star' in the sample name, were previously homogenized with a mortar and pestle and were thus not sieved. Samples for which both sieved and unsieved helium analyses were performed do not exhibit systematic offsets in $^3He_{ET}$ concentrations (Figure 4.2).

Sample $^3He_{ET}$ and $^4He_{terr}$ concentrations were calculated assuming a two component mixture of IDP helium ($(^3He/^4He)_{ET}$) with a $^3He/^4He$ ratio of 170 R_A and terrigenous input ($(^3He/^4He)_{terr}$) with a $^3He/^4He$ ratio of 0.01 R_A (Farley and Patterson, 1995), as in Middleton et al. (2016). Using these IDP and terrigenous $^3He/^4He$ end-member values, $^3He_{ET}$ represents >92% of total ^3He in all

sediment aliquots measured and ~99% of total ^{3}He on average. Similarly, $^{4}He_{terr}$ represents >90% of total ^{4}He in all aliquots measured and ~99% of total ^{4}He on average. Although the exact $^{3}He/^{4}He$ ratio of terrigenous input into the northeast Pacific is not precisely constrained, most Juan de Fuca Ridge samples are not sensitive to the end-member $^{3}He/^{4}He$ value. For example, assuming an extreme $(^{3}He/^{4}He)_{terr}$ end-member value of 0.10 R_A (Marcantonio et al., 1998), $^{3}He_{ET}$ would represent ~90% of total sedimentary ^{3}He on average. For all but one sample from a known turbidite layer at 272 ka (Costa and McManus, 2017), this would lead to $^{3}He_{ET}$ -derived vertical rain rates that are 10% higher, on average, than the values reported in this study. In comparison, values of $^{4}He_{terr}$ calculating using the extreme $(^{3}He/^{4}He)_{terr}$ end-member would change by less than 0.1%.

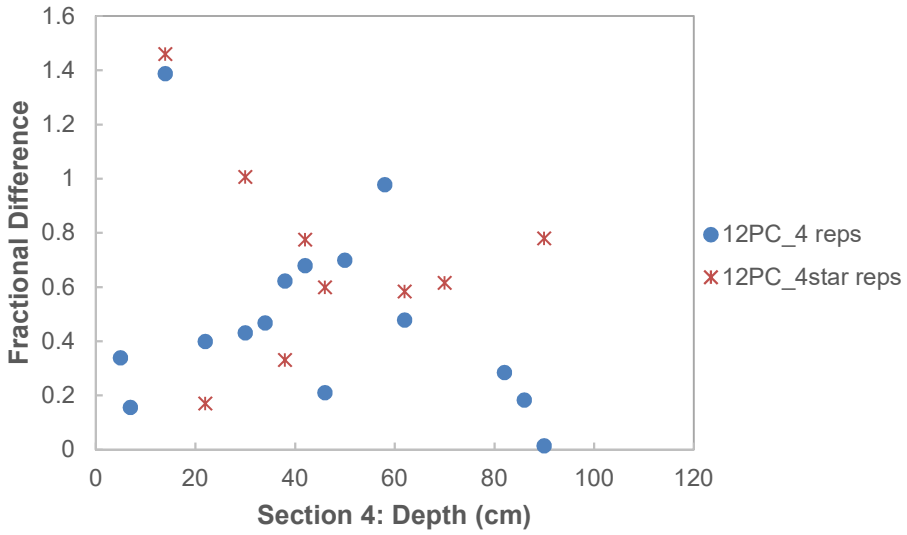

Figure 4.2: Comparison of the fractional difference between replicated sample estimates of $^{3}He_{ET}$ concentrations for sieved (blue circles) and unsieved (red stars) aliquots of sediments from 12PC Section 4. No systematic difference between the reproducibility of sieved and unsieved samples is observed. The full distributions of fractional differences between replicated He measurements are included in Figure 4.3.

Reproducibility in the determination of $^4He_{terr}$ concentrations is comparable to analytical uncertainty and, with the exception of three outliers, replicated samples indicate typical 1σ values of 4% (Figure 4.3). In contrast, reproducibility in the determination of sedimentary concentrations of $^3He_{ET}$ is influenced by the heterogeneous distribution of unusually large, helium-rich IDPs. Large IDPs are rare and consequently are not representatively sampled in typical sediment aliquots. This 'nugget effect' leads to uncertainty in the determination of sediment sample concentrations of $^3He_{ET}$ that is significantly larger than analytical uncertainties associated with the measurement of helium isotopes (Farley et al., 1997). Uncertainties in sediment concentrations of $^3He_{ET}$ were assessed using a suite of 101 replicated samples. The observed distribution of fractional differences in $^3He_{ET}$ concentrations between replicated samples can be reasonably approximated as a Gaussian with 1σ of 39% (Figure 4.3).

The estimated 1σ value of 39% is higher than the $^3He_{ET}$ uncertainties observed in previous sedimentary studies (e.g., 28% in Middleton et al., 2016; 20% in Mukhopadhyay et al., 2001 and Farley et al., 1997). The magnitude of IDP-associated uncertainties in the determination of $^3He_{ET}$ concentrations is a function of the area-time product of the samples measured, with lower area-time products associated with higher uncertainties (Farley et al., 1997). The area-time product is calculated by dividing the sample aliquot mass (in g) by the bulk sediment accumulation rate (in g m^{-2} a^{-1}). A typical area-time product of 0.25 m^2a yields a 1σ uncertainty in sedimentary $^3He_{ET}$ concentrations of ~20% (Farley et al., 1997; Mukhopadhyay et al., 2001). In comparison, the 0.5 g sample aliquots and the average bulk sedimentation rates of the 12PC sediments (including vertical and lateral sediment accumulation) yield an area-time product of ~0.10 m^2a for the helium data of this study. Given the relatively low area-time product of the

Juan de Fuca Ridge samples, a 39% value for 1σ uncertainty in the determination of $^3He_{ET}$ is not unexpected. The 1σ uncertainty in $^3He_{ET}$ concentrations in replicated samples is scaled as $0.39/\sqrt{n}$, where n is the number of aliquots analyzed.

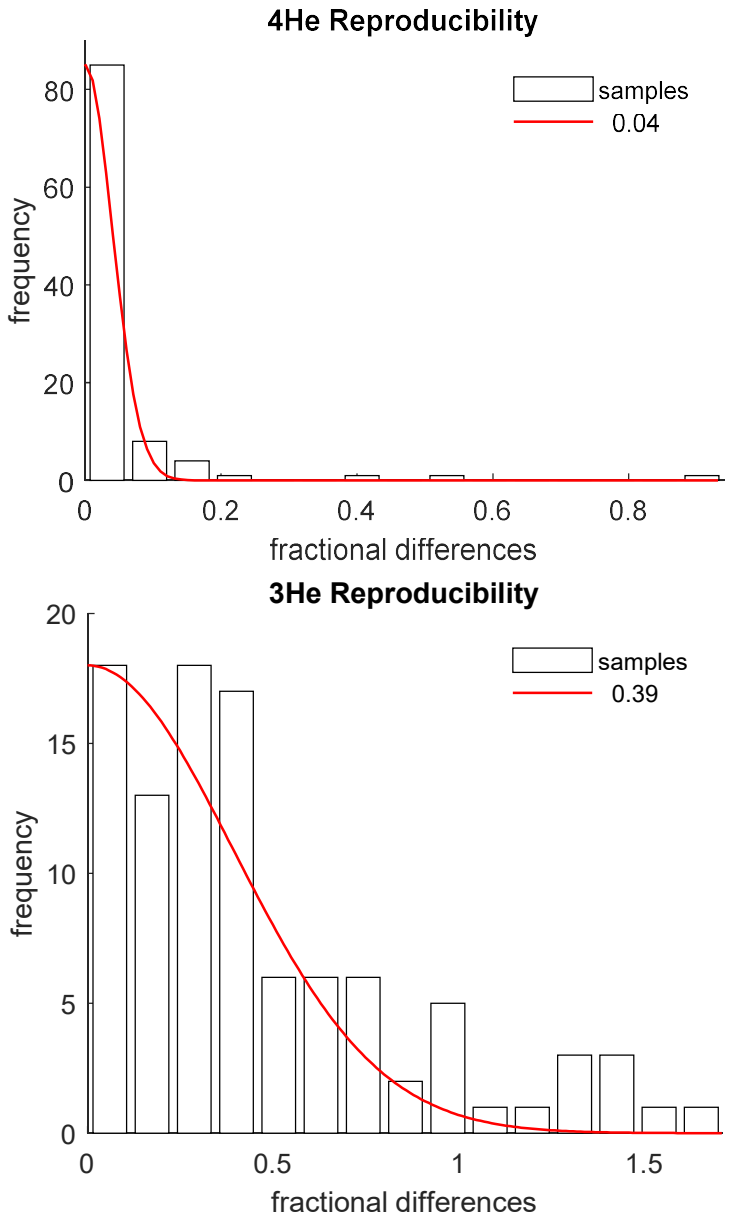

Figure 4.3: Histograms of the fractional difference in the concentrations of helium-4 (upper panel) and helium-3 (lower panel) in 101 replicated sample aliquots. The distributions of fractional differences observed in the Juan de Fuca sediments are best fit by Gaussian distributions with 1σ uncertainties of 4% and 39% for ^4He and ^3He, respectively.

4.2.3. Elemental and Hydrothermal Fluxes

Bulk sediment vertical sediment rain rates (Φ_{sed}) were computed by dividing the $^3He_{ET}$ influx from space (f) by the average $^3He_{ET}$ concentration of each sample [$^3He_{ET}$] using the following equation:

$$\Phi_{sed} = \frac{fR}{[^3He_{ET}]} \quad \text{EQ. 4.1}$$

Where f is 8.0 ± 1.2 x 10^{-13} cm^3 STP cm^{-2} ka^{-1} (McGee and Mukhopadhyay, 2013) and R is the fractional retentivity of He within the sediments (Farley, 1995). The retention of $^3He_{ET}$ in limestones dating to ~480 Ma suggests high $^3He_{ET}$ retention under ambient sedimentary conditions, with negligible variations in R over relatively short geologic timescales (Patterson et al., 1998). Thus, R is assumed to be 1 for the Pleistocene sediments examined here. The $^3He_{ET}$ data from this study is compared with $^{230}Th_{XS}$ data from Costa and McManus (2017).

Component-specific fluxes (Φ_x) were then calculated by multiplying the vertical sediment rain rate by the concentration of the sedimentary component of interest ($[X]_{sed}$) in each sample as follows:

$$\Phi_x = [X]_{sed} * \Phi_{sed} \quad \text{EQ. 4.2}$$

Sedimentary concentrations of $^4He_{terr}$ were determined as described above, while $CaCO_3$, Ti, Fe and Cu data were determined using x-ray fluorescence (XRF) scanning from Costa et al. (2017) and Costa and McManus (2017). In order to compare the constant flux proxy data, measured in 1 cm sediment layers, with the XRF-based elemental concentration records sampled at 2 mm resolution, XRF records were averaged over 1 cm intervals.

The hydrothermal components (X_{HT}) of total Fe and Cu were distinguished from lithogenic contributions following the relationship:

$$X_{HT} = X_{total} - (X/Ti)_{lith} * Ti_{total} \quad \text{EQ. 4.3}$$

where $(X/Ti)_{lith}$ represents the lithogenic ratio of the average upper continental crust (~11.7 wt.%/wt.% and 83 ppm/wt.% for Fe, and Cu, respectively; Taylor and McLennan, 1995). The observed basalt fragments in the oldest 12PC sediments are likely to lower the Fe/Ti ratios (from ~11.7 to ~8.3 wt.%/ wt.%) of the lithogenic sediment contribution below the presumed continental values (Gale et al., 2013) and likely lead to overcorrection for lithogenic Fe in these intervals (See Section 4.4.2).

4.3. Results of $^3He_{ET}$-derived sediment fluxes

Throughout the interval for which helium data is available from both 09PC and 12PC, the magnitudes and patterns of $^3He_{ET}$ -derived bulk sediment rain rate records demonstrate good agreement between cores (Figures 4.4 and 4.5; Appendix D). The $^3He_{ET}$ -derived fluxes of both cores are consistently higher during glacial periods and lower during interglacial periods, consistent with the glacial-interglacial variability observed in $^{230}Th_{XS}$ -derived flux records from the same region (Costa and McManus, 2017). Further, the patterns of variability in the 09PC and 12PC $^3He_{ET}$-derived flux records are well correlated with each other, demonstrating spatial consistency in $^3He_{ET}$-derived sediment rain rates on the Juan de Fuca Ridge (Figure 4.5).

The magnitudes of $^3He_{ET}$-derived bulk sediment flux values for 09PC and 12PC sediments generally agree with those derived using $^{230}Th_{XS}$ (Figure 4.6). In 09PC, $^3He_{ET}$-derived vertical

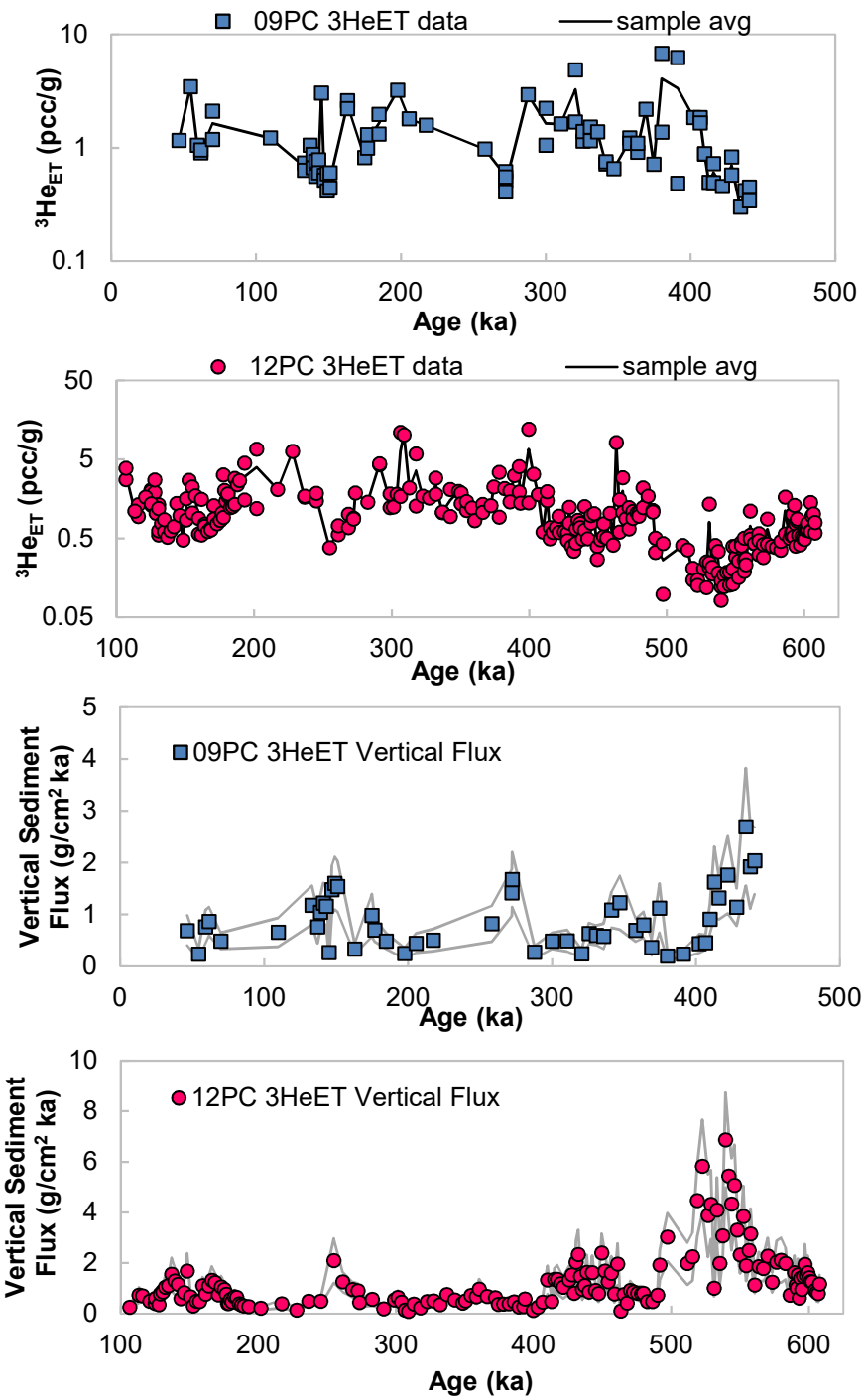

Figure 4.4: Concentrations of extraterrestrial helium-3 ($^3He_{ET}$) and $^3He_{ET}$ -derived bulk sediment vertical rain rates for 09PC and 12PC. The $^3He_{ET}$ concentrations for every aliquot analyzed (markers) are plotted on a log scale for 09PC (A) and 12PC (B). Black lines indicate the average $^3He_{ET}$ concentration for each sample. **(Caption continued on next page.)**

Figure 4.4 caption (continued): $^{3}He_{ET}$ -derived rain rates, calculated using average sample $^{3}He_{ET}$ concentrations, are plotted (markers) for 09PC (C) and 12PC (D) within a 1 σ error envelope (gray lines). $^{3}He_{ET}$ concentrations are reported in units of pcc STP/g, where pcc STP refers to 10^{-12} cm^{3} of gas at standard temperature and pressure (STP) of 273K and 1 atm. Note that 09PC values are plotted on an x-axis scale of 0 to 500 ka, while 12PC values are plotted on an x-axis scale of 100 to 600 ka.

rain rates typically overlap with $^{230}Th_{XS}$ -derived vertical rain rates within the 1 sigma error envelope (Figure 4.6; Costa and McManus, 2017). In 12PC, however, $^{3}He_{ET}$-derived fluxes only overlap within error of $^{230}Th_{XS}$ -derived fluxes in samples younger than 300 ka (Figure 4.6). For 12PC samples older than 300 ka, $^{3}He_{ET}$-derived vertical rain rates are systematically lower than those derived using $^{230}Th_{XS}$ (Figure 4.6). However, the $^{3}He_{ET}$ -derived flux record from 12PC agrees with $^{230}Th_{XS}$ -derived flux records from neighboring sediments cores on the Juan de Fuca Ridge, while the $^{230}Th_{XS}$ -derived fluxes in 12PC sediments >300 ka do not (Figure 4.6; Costa and McManus, 2017). Thus, the offset between $^{3}He_{ET}$ - and $^{230}Th_{XS}$ -derived vertical rain rates in 12PC sediments >300 ka may be caused by unanticipated complexities with the utilization of the $^{230}Th_{XS}$ constant flux proxy in these particular sediments (See Section 4.4.1.1).

In general, the agreement between $^{3}He_{ET}$ - and $^{230}Th_{XS}$ -derived flux data over glacial-interglacial cycles supports the utilization of $^{3}He_{ET}$ to extend the vertical rain rate records of different sedimentary components from the SeaVOICE cores beyond the ~500 ka age limit of $^{230}Th_{XS}$. The 600 ka $^{3}He_{ET}$ -derived flux record of 12PC reveals significantly higher bulk sediment rain rates in sediments older than ~500 ka, than are observed by either $^{3}He_{ET}$ or by $^{230}Th_{XS}$ analyses in younger sediments from the SeaVOICE cores (Figure 4.6). With the exception of a distinct turbidite layer at 272 ka and the anomalously high values from 12PC sediments >300 ka, the suite of $^{230}Th_{XS}$ -derived fluxes determined for the six cores examined varies from 0.26 to 3.2 mg

cm^{-2} ka^{-1} over the past ~500 ka (Costa and McManus, 2017). Over the same time period, $^3He_{ET}$ -derived fluxes in 12PC and 09PC vary from 0.08 to 2.7 mg cm^{-2} ka^{-1}. In comparison, the $^3He_{ET}$ data from 12PC reveal bulk sedimentary fluxes ranging from 0.10 to 6.9 mg cm^{-2} ka^{-1} between 500 ka and the bottom of the core (Figure 4.6). The maximum flux values occur between 500 and 550 ka, coinciding with Marine Isotope Stages (MIS) 13 and 14, and are associated with increased rates of both carbonate and non-carbonate sedimentary deposition (Figure 4.7). The high $^3He_{ET}$ -derived flux values exhibited in older 12PC sediments cannot result from basalt contamination of the helium signal because an overestimation of $^3He_{ET}$ caused by the presence of basalt ^3He would lead to an underestimation of $^3He_{ET}$ -derived fluxes. Rather, the 600 ka flux record determined from $^3He_{ET}$ suggests fundamentally different depositional behavior at 12PC during MIS 13 and 14 than during any of the more recent glacial-interglacial cycles.

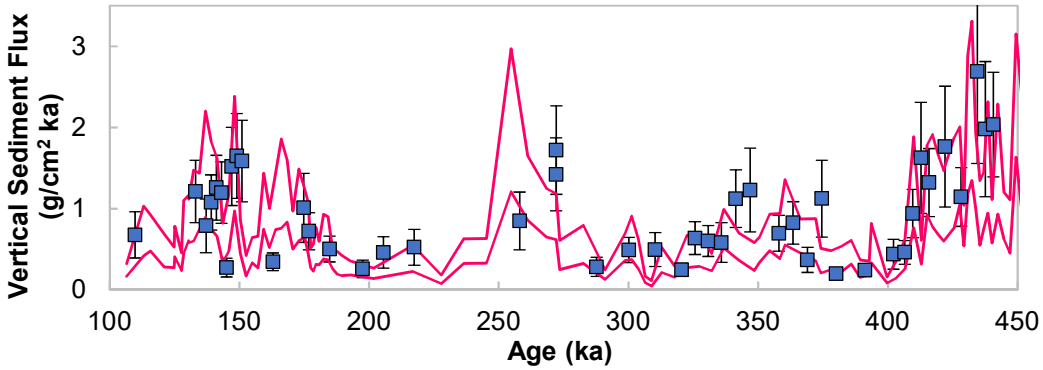

Figure 4.5: Comparison of $^3He_{ET}$ -derived vertical sediment rain rates of 09PC and 12PC for overlapping sedimentary intervals. Rain rates and 1 σ uncertainties for 09PC (blue squares) are plotted within the 1 σ error envelope of estimated rain rates for 12PC (pink lines). Similarity between $^3He_{ET}$ -derived vertical rain rates of 09PC and 12PC demonstrate good spatial consistency in $^3He_{ET}$ -derived values in the Juan de Fuca Ridge sediments.

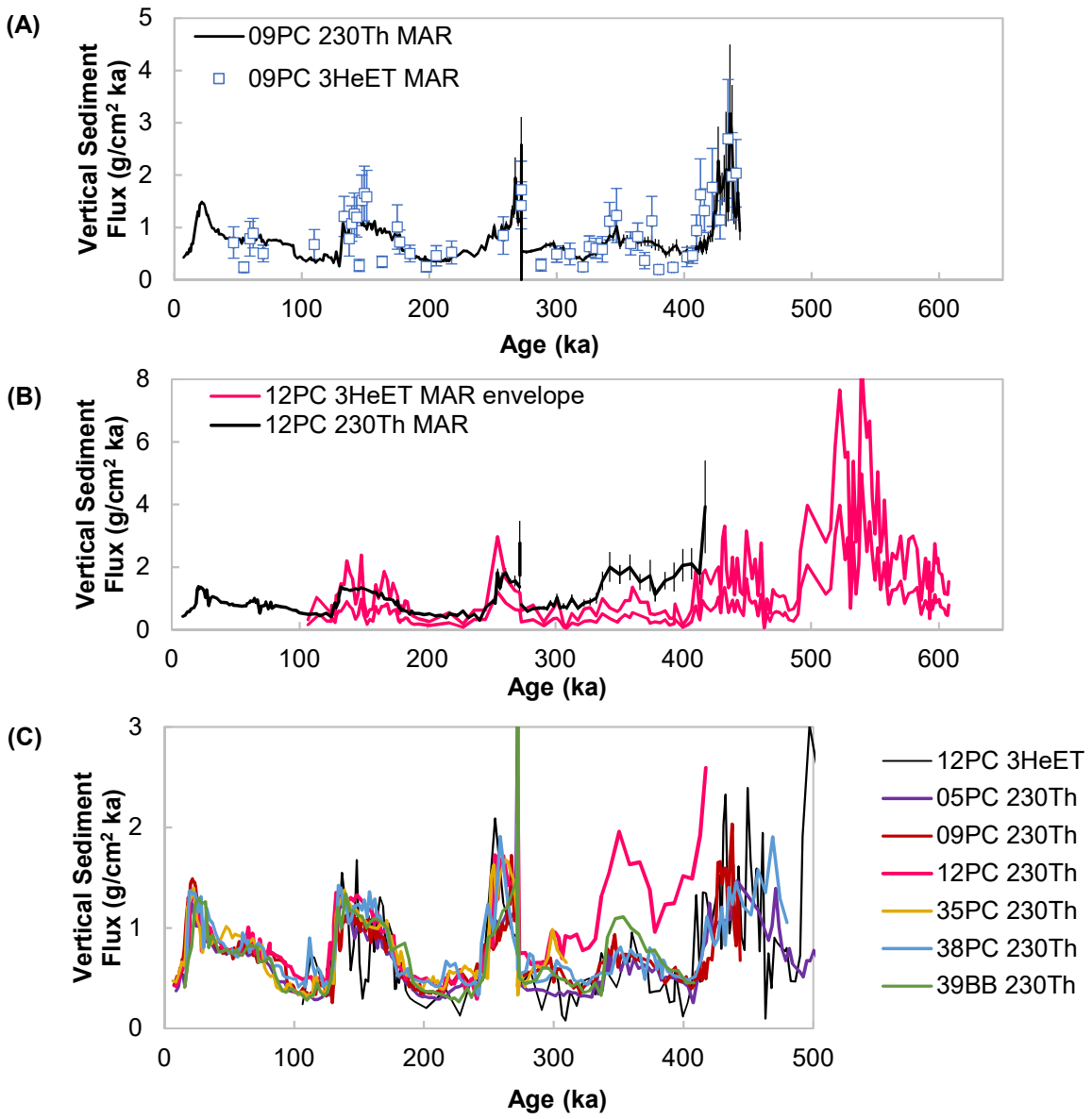

Figure 4.6: Comparison of $^{3}He_{ET}$ -derived (this study) and $^{230}Th_{XS}$-derived (Costa and McManus, 2017) vertical sediment rain rates in the SeaVOICE cores of the Juan de Fuca Ridge. (A) $^{3}He_{ET}$ -derived (blue markers) and $^{230}Th_{XS}$ -derived rain rates (black line) of 09PC. (B) $^{3}He_{ET}$ -derived (pink error envelope) and $^{230}Th_{XS}$ -derived rain rates (black line) of 12PC. (C) The $^{3}He_{ET}$ -derived rain rates of 12PC (thin black line) are compared with $^{230}Th_{XS}$ -derived rain rates (colors) of all six SeaVOICE cores examined by Costa and McManus (2017). The $^{230}Th_{XS}$ -derived record of 12PC (thick pink line) exhibits uniquely high values in sediments >300 ka, relative to the $^{3}He_{ET}$ -derived record and $^{230}Th_{XS}$ -derived records of neighboring cores. Error indicators in (A) and (B) reflect 1 σ uncertainties. Error bars are omitted from (C) for clarity.

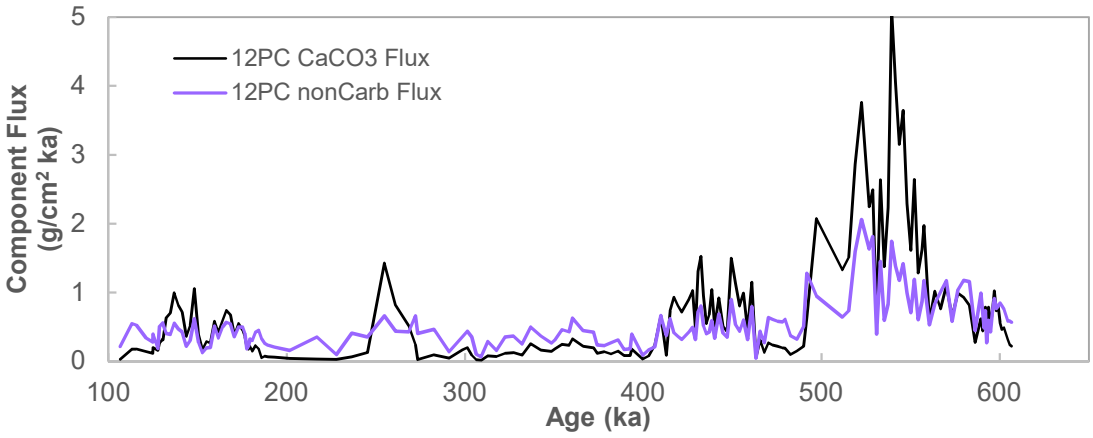

Figure 4.7: $^{3}He_{ET}$ -derived vertical rain rates for the carbonate (black) and non-carbonate (purple) components of 12PC sediments. Both the carbonate and the non-carbonate fluxes are highest during Marine Isotope Stages (MIS) 13 and 14 (~490 to 550 ka), suggestive of a fundamentally different depositional environment at to 12PC at this time.

4.4. Discussion

4.4.1. Differences between $^{3}He_{ET}$- and $^{230}Th_{XS}$-derived fluxes

The good first-order agreement between $^{3}He_{ET}$- and $^{230}Th_{XS}$ -derived vertical rain rates encourages the continued use of both proxies to evaluate climate-driven changes in marine fluxes on Milankovitch timescales. However, examination of intervals where the two constant flux proxies yield differing results improves our understanding of the caveats and benefits of each system and informs decisions regarding the most appropriate analytical approach for future marine sedimentary studies.

4.4.1.1. Comparison to the expected $^{3}He_{ET}/^{230}Th_{XS}$ production ratio

The potential causes driving the differences between $^{3}He_{ET}$- and $^{230}Th_{XS}$ - derived flux are more readily evaluated by examining the concentration ratio of $^{3}He_{ET}$ /$^{230}Th_{XS}$ within the sedimentary records (Figure 4.8). Using a $^{3}He_{ET}$ influx from space of 8.0 ± 1.2 x 10^{-13} cc STP cm^{-2} ka^{-1} (McGee and Mukhopadhyay, 2013) and the 2689 m water depth of 12PC, $^{3}He_{ET}$ and $^{230}Th_{XS}$ are expected to accumulate in the SeaVOICE cores in a $^{3}He_{ET}$ /$^{230}Th_{XS}$ production ratio of 5.4 ± 0.8 x 10^{-3} cc STP g^{-1} (or mcc STP g^{-1}). Samples with $^{3}He_{ET}$ /$^{230}Th_{XS}$ values exceeding the expected production ratio may result from extra accumulation of $^{3}He_{ET}$ or from the preferential loss of $^{230}Th_{XS}$, while the inverse applies to samples with $^{3}He_{ET}$ /$^{230}Th_{XS}$ values lower than the expected production ratio.

With the exception of the oldest sediments in 09PC and sediments older than 300 ka in 12PC, $^{3}He_{ET}/^{230}Th_{XS}$ ratios in the SeaVOICE cores do not appear to deviate systematically from the predicted production ratio (Figure 4.8). Samples from the full length of 09PC contain $^{3}He_{ET}$ /$^{230}Th_{XS}$ ratios varying from 1.9 ± 0.8 to 24 ± 10 mcc STP g^{-1}, with a mean value of 6.4 ± 0.6 mcc STP g^{-1} that falls within the 1 σ uncertainty of the expected production ratio (Figure 4.8). Compared with the full 09PC record, 09PC samples that are older than 410 ka are generally lower than the expected production ratio, with a mean $^{3}He_{ET}$ /$^{230}Th_{XS}$ value of 4.1 ± 0.4 mcc STP g^{-1}. The shift to lower $^{3}He_{ET}$ /$^{230}Th_{XS}$ values in these older sediments may result from unanticipated uncertainties leading to overestimation of $^{230}Th_{XS}$ concentrations as the sediments approach the $^{230}Th_{XS}$ age limit. Samples from 12PC sediments younger than 300 ka behave similarly to 09PC, with $^{3}He_{ET}$ /$^{230}Th_{XS}$ ratios varying from 3.6 ± 1.0 to 25 ± 10 mcc STP g^{-1}.

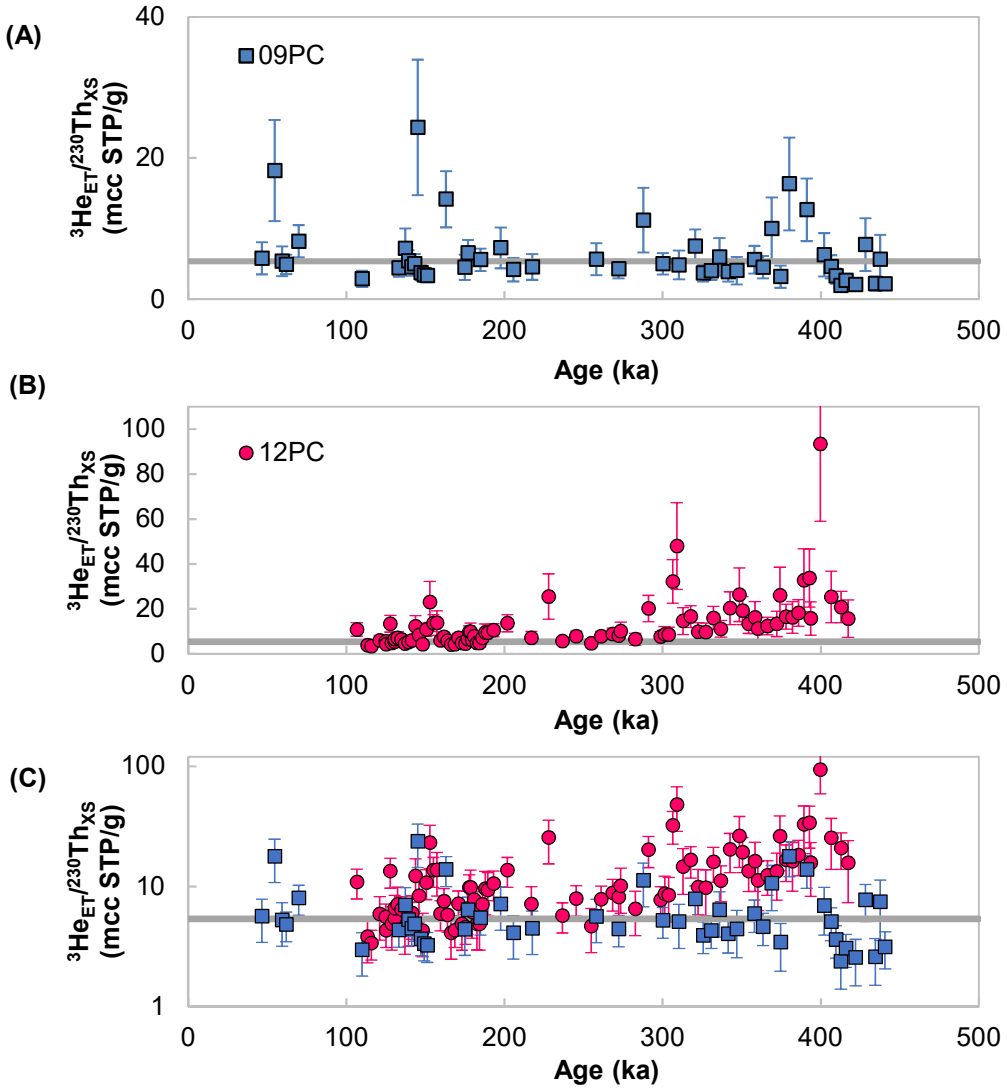

Figure 4.8: Values of $^3He_{ET}$ /$^{230}Th_{XS}$ for samples from 09PC (A), 12PC (B), and both cores plotted on a log scale for clarity (C). Error bars indicate 1 σ uncertainty. Solid line indicates the expected production ratio of 5.4 ± 0.8 x 10^{-3} cc STP g^{-1} (or mcc STP g^{-1}) assuming a 2689 m water depth and a $^3He_{ET}$ influx from space of 8.0 ± 1.2 x 10^{-13} cc STP cm^{-2} ka^{-1} (McGee and Mukhopadhyay, 2013). For clarity, uncertainty in the expected production ratio is not plotted. $^{230}Th_{XS}$ data are from Costa and McManus, 2017.

However, the mean $^{3}He_{ET}$ /$^{230}Th_{XS}$ ratio of 12PC sediments <300 ka is 8.0 ± 0.6 mcc STP g^{-1}, slightly higher than that of 09PC, and only overlaps with the expected production rate within the 2 σ level of uncertainty. Overlap between the average observed $^{3}He_{ET}$ /$^{230}Th_{XS}$ ratios and the predicted $^{3}He_{ET}$ /$^{230}Th_{XS}$ ratio suggest that, on glacial-interglacial timescales, both constant flux proxies are performing as expected in these sediments.

In stark contrast to 09PC and the younger sediments of 12PC, 12PC sediments >300 ka have $^{3}He_{ET}$ /$^{230}Th_{XS}$ ratios that are significantly in excess of the expected production ratio, with a mean value of 20.2 ± 2.8 mcc STP g^{-1} (Figure 4.8). The mean $^{3}He_{ET}$ /$^{230}Th_{XS}$ values exhibited by 12PC sediments >300 ka is ~4-fold higher than the expected production ratio of 5.4 ± 0.8 mcc STP g^{-1}. Given the anomalously high $^{230}Th_{XS}$ -derived sediment rain rates exhibited in 12PC sediments >300 ka (Figure 4.6), the consistently high $^{3}He_{ET}$ /$^{230}Th_{XS}$ from this sedimentary interval are interpreted to result primarily from a deficit in the expected accumulation of $^{230}Th_{XS}$.

A deficit of sedimentary $^{230}Th_{XS}$ may arise if the overlying water column does not deliver $^{230}Th_{XS}$ to the seafloor at the expected production rate. Hydrothermal plumes in both the Atlantic and the Pacific are associated with depleted seawater concentrations of $^{230}Th_{XS}$, likely caused by the $^{230}Th_{XS}$ scavenging onto particulate Fe and Mn (Hayes et al., 2015; Pavia et al., 2017). If the majority of hydrothermally-scavenged $^{230}Th_{XS}$ is deposited locally at the vent site, lateral advection of the $^{230}Th_{XS}$ -depleted buoyant hydrothermal plume could potentially lead to deficit $^{230}Th_{XS}$ deposition to sediments at intermediate distances from the ridge axis. Today, the 12PC sediment core sits at ~18 km from the spreading center of the Juan de Fuca Ridge (Figure 4.1). Assuming a constant half-spreading rate of 30 mm/yr (Govers and Meijer, 2001), the >300 ka

sediments of 12PC were deposited at distances <9 km from the neovolcanic zone of the Cleft Segment, representing the closest samples to the ridge-axis of all the SeaVOICE sediments examined by Costa and McManus (2017). Thus, it is plausible that the >300 ka 12PC sediments exhibit high $^{3}He_{ET}$ /$^{230}Th_{XS}$ ratios due to reduced $^{230}Th_{XS}$ deposition associated with their particular proximity to the ridge-axis.

It is conceivable that the >300 ka 12PC sediment samples could appear to contain too much $^{3}He_{ET}$ if the two-component assumption used to determine the fraction of $^{3}He_{ET}$ out of total ^{3}He measured is invalid. This assumption could be violated if mantle helium comprised a significant component of the total helium measured in a given sample. Due to the relatively high $^{3}He/^{4}He$ ratio of mid-ocean ridge basalts (~8 R_A; Graham, 2002), the presence of basalt-associated ^{3}He would lead to an overestimate of sedimentary concentrations of $^{3}He_{ET}$. This potential effect does not appear to be significant in 12PC, however, as the interval with the highest occurrence of basalt chips (>545 ka, Ferguson et al., 2017) is also the interval yielding some of the lowest concentrations of $^{3}He_{ET}$ (Figure 4.4). Hydrothermal vents also emit mantle helium that can be trapped in hydrothermal precipitates at the vent site itself (Jean-Baptiste and Fouquet, 1996; Stuart et al., 1994). However, this is also unlikely to interfere with the determination of $^{3}He_{ET}$ in the SeaVOICE cores, as previous work on the Mid-Atlantic Ridge observed no correlation between hydrothermal iron and copper deposits and $^{3}He_{ET}$ concentrations in a sediment core collected within 1 km of the closest vent field (Middleton et al., 2016). Future analyses of beryllium-10, which has also been employed as a constant flux proxy (e.g., Frank et al., 1994), could help discern whether the discrepancy between $^{3}He_{ET}$ - and $^{230}Th_{XS}$ -derived fluxes in 12PC sediments are more likely associated with complications in the $^{3}He_{ET}$ or the $^{230}Th_{XS}$ systems.

4.4.1.2. High frequency differences between $^{3}He_{ET}$- and $^{230}Th_{XS}$- derived fluxes

The relatively high helium sampling resolution (~1 sample per 2 ka) for 12PC between 100 and 200 ka allows for the comparison of $^{230}Th_{XS}$ - vs. $^{3}He_{ET}$ -derived sedimentary fluxes on sub-orbital timescales (Figure 4.9). The $^{230}Th_{XS}$ -derived flux records of all 6 SeaVOICE cores generally exhibit a steady increase throughout the glacial period from ~200 to ~135 ka (Figures 4.6 and 4.9). The 12PC $^{3}He_{ET}$ -derived flux record, however, exhibits higher frequency variability across this interval, with a significant flux minimum expressed by three distinct samples between 157 and 152 ka (Figure 4.9). During this $^{3}He_{ET}$ -derived flux minimum, the average $^{3}He_{ET}$ /$^{230}Th_{XS}$ ratios is 16.8 ± 3.2, approximately three times higher than the expected production ratio. The IDP nugget effect may manifest as high frequency variability within $^{3}He_{ET}$ -derived records (Farley, 1995), yet peaks and troughs in the flux record that are defined by multiple samples are unlikely to be caused by the heterogenous distribution of large IDPs. Higher order variability is also expressed in the 12PC $^{3}He_{ET}$ -derived flux record, with flux peaks occurring at ~137, ~148, ~166, and ~185 ka, though these flux peaks are within error of the less variable $^{230}Th_{XS}$ -based records. While the resolution of 09PC $^{3}He_{ET}$ data between 200 to 135 ka is insufficient to establish a regional consistency for all of the variability observed in 12PC, the 09PC data also suggest the presence of a sediment flux peak at ~148 ka (Figure 4.9). The coincidence of 12PC carbonate concentration peaks (Costa and McManus, 2017) with the $^{3}He_{ET}$ -derived flux peaks at ~137, ~148, and ~166 ka further encourages the interpretation of these features as the result of actual changes in the local depositional environment (Figure 4.10).

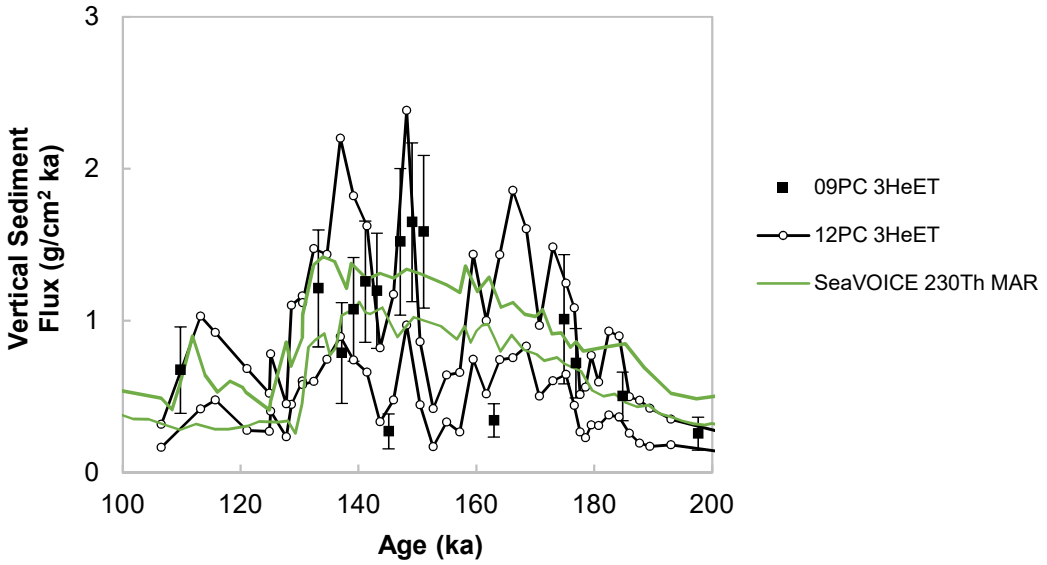

Figure 4.9: Zoomed in comparisons of the vertical sediment rain rates derived from $^{3}He_{ET}$ (this study) and $^{230}Th_{XS}$ (Costa and McManus, 2017) for 100 to 200 ka. The $^{3}He_{ET}$ -based sediment flux records of 12PC (black lines indicate the 1σ error envelope, white dots demark sampling resolution) and 09PC (black squares with 1σ error bars) exhibit suborbital variability that is not exhibited in the $^{230}Th_{XS}$ -based sediment flux records determined in the suite of six SeaVOICE cores (Costa and McManus, 2017). For clarity, the maximum and minimum $^{230}Th_{XS}$ -based sediment flux values of the suite of SeaVOICE cores are plotted (green lines), while the uncertainties associated with the $^{230}Th_{XS}$-based records are omitted.

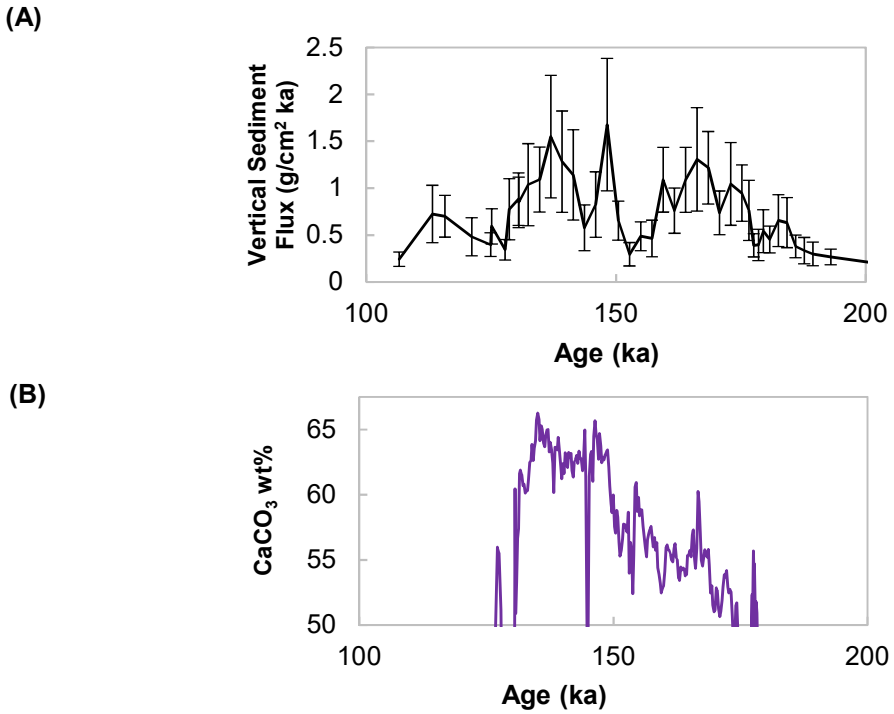

Figure 4.10: Comparison of the 12PC $^{3}He_{ET}$-derived vertical sediment rain rate record (A) with (B) 12PC carbonate content (Costa and McManus, 2017). Carbonate concentrations are plotted on a zoomed in y-axis to highlight suborbital variability. Similarities in the pattern of variability between the $^{3}He_{ET}$-derived record and other parameters within 12PC suggest that the suborbital variability in the $^{3}He_{ET}$-derived data are associated with true changes in the depositional environment at 12PC.

High frequency variability between $^{3}He_{ET}$ - and $^{230}Th_{XS}$ -derived flux records have previously been observed in Arabian Sea sediments spanning the past 23 ka, but the causes of this variability remain poorly understood (Marcantonio et al., 2001a). In the Arabian Sea sediments, $^{3}He_{ET}$ -derived fluxes exhibit abrupt variations in the early Holocene (at 9 ka) and at the Younger Dryas (12.7 ka) that are not recorded in $^{230}Th_{XS}$ -derived fluxes (Marcantonio et al., 2001a). Variations in selective IDP loss associated with changes in lateral sediment transport were proposed as a potential mechanism to explain the abrupt changes observed in the $^{3}He_{ET}$ -derived flux record (Marcantonio et al., 2001a). However, a later comparison of $^{3}He_{ET}$ and $^{230}Th_{XS}$ data

in Atlantic sedimentary deposits subjected to varying degrees of sediment focusing suggests that the two constant flux proxies are not significantly fractionated during lateral transport on the seafloor (McGee et al., 2010a). The variable presence of an unaccounted-for source of ^{3}He in the Arabian Sea sediments, possibly originating from mantle-derived material or from IDPs initially deposited on continents, was proposed as an alternative mechanism to explain the abrupt changes observed in the $^{3}He_{ET}$ -derived flux record (Marcantonio et al., 2001a). However, the potential magnitude of such an effect has not been constrained. Thus, the causes of suborbital variability in $^{3}He_{ET}$ -derived sediment flux records remain an open question.

The suborbital variability observed in the SeaVOICE $^{3}He_{ET}$ -derived sediment flux records may result from either, or a combination of, the following two hypotheses: (1) $^{3}He_{ET}$ is able to record high frequency changes in sediment accumulation on the Juan de Fuca Ridge that are not resolvable using $^{230}Th_{XS}$ in the SeaVOICE cores, or (2) $^{3}He_{ET}$ is not behaving as a constant flux proxy on suborbital timescales due to unanticipated high frequency variations in the transport and deposition of IDPs through the atmosphere and water column associated with changing climatic conditions. The first proposed explanation could result from natural smoothing of $^{230}Th_{XS}$ concentrations within the slowly accumulating (< 3 cm/ka) SeaVOICE cores potentially caused by partial loss and re-absorption of ^{230}Th within the sediment column during carbonate dissolution (e.g., Rowland et al., 2017). Seawater observations suggest that ^{230}Th reversibly exchanges between adsorption onto particles and its dissolved phase such that particulate concentrations of adsorbed ^{230}Th equilibrate with the surroundings on timescales of months (Bacon and Anderson, 1982). In contrast to ^{230}Th, if IDP-bound $^{3}He_{ET}$ were somehow mobilized out of its carrier phase, then it would be expected to diffuse out of the sediment column because

it is light and inert. Independent of long-term diffusional processes within the sediment column, biologic irrigation of the sediment pore fluids leads to a pore fluid mixed layer that is several cm deeper than the corresponding mixed layer depth of the solid sediments (Smethie et al., 1981; Sandnes et al., 2000). Thus, if sedimentary $^{230}Th_{XS}$ is mobilized via carbonate dissolution and pore fluid irrigation associated with changing bottom water conditions, then sedimentary concentrations of $^{230}Th_{XS}$ may be homogenized over greater sediment length-scales, and consequently longer time-scales, than particulate proxies such as IDP-bound $^{3}He_{ET}$.

Alternatively, as suggested in the second hypothesis, the local $^{3}He_{ET}$ -bearing IDP influx to the seafloor may be influenced by high frequency variability in atmospheric and oceanographic conditions. While variations in lateral sediment transport associated with changing oceanographic currents do not seem to fractionate $^{3}He_{ET}$ from $^{230}Th_{XS}$ on the seafloor (McGee et al., 2010a), $^{3}He_{ET}$ may be sensitive to variations in atmospheric circulation that would not affect the marine-based production of $^{230}Th_{XS}$. When IDPs enter the stratosphere, the largest particles are rapidly removed by Stokes settling, while particles <10 um in diameter may follow large scale air mass trajectories before transfer to the troposphere and subsequent wet or dry deposition to the surface of the Earth (Lal and Jull, 2005). The lateral transport of fine grained IDPs in the stratosphere could lead to higher IDP deposition rates beneath mid-latitude (~40 to 45°) storm tracks, where mixing of stratospheric particles into the troposphere is enhanced, relative to the global average (Hayes et al., 2017; Lal and Jull, 2005; Field et al., 2006). However, such a latitudinal effect has not been resolved by the existing suite of marine and ice core records used to constrain the $^{3}He_{ET}$ influx from space (e.g., McGee and Mukhopadhyay, 2013). If storm track positions do affect the local $^{3}He_{ET}$ deposition rate, then climatically-driven shifts in storm track

locations (e.g., Laîné et al., 2009) could potentially lead to high frequency variations in $^{3}He_{ET}$ concentrations in the mid-latitude Juan de Fuca Ridge sediments that preclude its utility as a constant flux proxy in this region on millennial-timescales. Such an effect would be surprising, because climatic variability does not appear to influence $^{3}He_{ET}$ deposition on glacial-interglacial timescales (Figure 4.6; Marcantonio et al., 1995; Marcantonio et al., 1999; Marcantonio et al., 1996; Marcantonio et al., 1998; McGee et al., 2010a). It is also noted that millennial-scale similarities between dust flux records constrained using $^{230}Th_{XS}$ in the high sedimentation rate region of the Northwest African margin (McGee et al., 2013) and downwind Mid-Atlantic dust flux records constrained using $^{3}He_{ET}$ (Middleton et al., *in press*) suggest that the $^{3}He_{ET}$ system is performing well as a constant flux proxy over suborbital timescales in the subtropical Atlantic.

Evaluation of these two hypotheses is essential to understand the appropriate application of constant flux proxies when investigating millennial-scale climate variability. Future work could examine the potential effects of $^{230}Th_{XS}$ homogenization in slowly accumulating depositional environments by comparing $^{230}Th_{XS}$ - derived fluxes in in sediment cores recovered from the same region, such that the expected vertical rain rates are the same, yet representing a range of high and low bulk accumulation rates. The potential atmospheric focusing of IDPs could be examined using a latitudinal transect of high-resolution comparisons $^{3}He_{ET}$ - and $^{230}Th_{XS}$ - derived sediment rain rates over known millennial-scale climate excursions because atmospheric IDP focusing would be expected to increase $^{3}He_{ET}$ deposition in target latitudes while simultaneously decreasing $^{3}He_{ET}$ deposition outside of the storm track belt.

It is noted that potential complications in the utilization of $^{3}He_{ET}$ or $^{230}Th_{XS}$ to constrain high frequency depositional variability in slowly accumulating sediments do not preclude the continued use of these tools on glacial-interglacial timescales, over which the two proxies yield similar results in the Juan de Fuca Ridge sediments.

4.4.2. The 600 ka hydrothermal flux record from 12PC

The new $^{3}He_{ET}$ -derived flux data for 12PC allow for the extension of the hydrothermal flux record from the Cleft Segment of the Juan de Fuca Ridge from ~500 to 600 ka. The $^{3}He_{ET}$ -derived (this study) and $^{230}Th_{XS}$ -derived flux records (Costa and McManus, 2017) for 12PC are combined, with $^{230}Th_{XS}$ -based values filling in gaps in the $^{3}He_{ET}$ -based record, to construct a continuous record of sedimentary fluxes from the Last Glacial Maximum to MIS 15 (~25 to 607 ka) with an average resolution of ~1 sample per 2 ka (Figure 4.11).

The extended 12PC record reveals a broad maximum in hydrothermal flux between ~490 and ~530 ka (MIS 13) that is unlike any other interval of the past 600 ka (Figures 4.11 and 4.12). Across this maximum, Cu_{HT} flux values range from ~195 to 265 μg cm^{-2} ka^{-1}, with a local minimum in Cu_{HT} fluxes occurring at ~512 ka. The average Cu_{HT} flux during this peak of 200 ± 20 μg cm^{-2} ka^{-1} is more than a factor of two higher than the average Cu_{HT} fluxes in either the preceding 70 ka (102 ± 5 μg cm^{-2} ka^{-1}) of the following 90 ka (75 ± 4 μg cm^{-2} ka^{-1}). The MIS 13 hydrothermal maximum is apparent in the Fe_{HT} flux record as well, with Fe_{HT} values ranging from ~21 to 45 mg/cm2 ka, compared with the average values of 10 ± 2 mg cm^{-2} ka^{-1} and 12 ± 1 mg cm^{-2} ka^{-1} for the preceding and following intervals, respectively (Figure 4.11). The increase

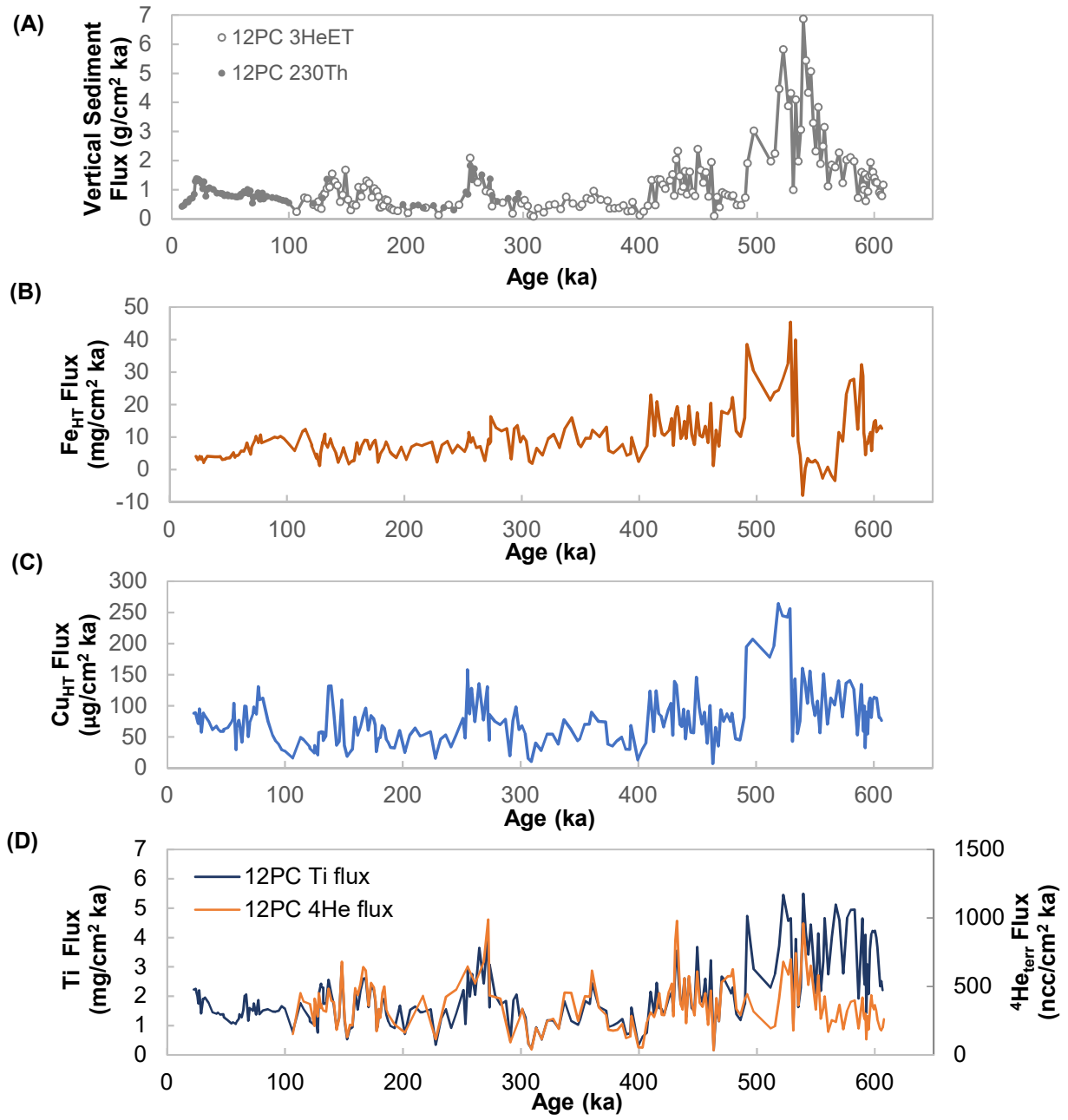

Figure 4.11: The 600 ka combined proxy vertical rain rate record of 12PC. The $^{230}Th_{XS}$-based values (filled markers) of Costa and McManus (2017) fill gaps in the $^{3}He_{ET}$ (open markers) data to produce a combined proxy vertical rain rate record for 12PC (A). The 600 ka vertical rain rate record is combined with trace element concentration data (Costa et al., 2017) to calculate depositional records of hydrothermal Fe (B), hydrothermal Cu (C), and (D) total Ti (blue line) and $^{4}He_{terr}$ (orange line) for 12PC over the past 600 ka. High Ti fluxes, relative to $^{4}He_{terr}$, in the oldest sediments likely reflect increasing concentrations of basalt. **(Caption continued on next page.)**

Figure 4.11 caption (continued): High concentrations of basalt-hosted Ti lead to overestimates of the lithogenic fraction of total Fe, yielding minimum hydrothermal Fe fluxes. Negative hydrothermal Fe fluxes between 540 and 567 ka are attributed to this effect. $^{4}He_{terr}$ fluxes are reported in units of ncc STP cm^{-2} ka^{-1}, where ncc STP refers to 10^{-9} cm^{3} of gas at standard temperature and pressure (STP) of 273K and 1 atm.

in the magnitude of hydrothermal deposition between 600 ka and the intense peak at MIS 13 suggests that the high Cu_{HT} and Fe_{HT} fluxes during MIS 13 are not exclusively caused by increased proximity of 12PC to the ridge-axis at this earlier point in time. Rather, as suggested by Costa et al. (2017), high hydrothermal fluxes in MIS 13 sediments may be related to the enhanced magmatic activity and crustal formation associated with the possible capture of the Cobb Hot Spot by the ridge axis and the development of Axial Volcano. Seismic and magnetic data suggest that the Axial Segment of the Juan de Fuca Ridge, located directly north of the Cleft Segment, initiated around ~0.5 Ma following a 20 km westward jump of the ridge axis that accompanied the possible hot spot capture (Delaney et al., 1981; Tivey and Johnson, 1990). An approximate age of ~570 ka is estimated for this advent of this event based on the extent of a thick crustal plateau across the Axial Segment (Carbotte et al., 2008). The timing of enhanced magmatic activity on the southern Juan de Fuca Ridge is consistent with the MIS 13 hydrothermal peak recorded in 12PC.

The extended hydrothermal record exhibits an additional peak in Fe_{HT} fluxes between ~575 and 590 ka that is not accompanied by an analogous peak in Cu_{HT} fluxes (Figure 4.11). Average Fe_{HT} fluxes across this peak are 25± 3 mg cm^{-2} ka^{-1}. Although the magnitude of hydrothermal deposition across this interval is relatively high, the ~15 ka duration of this Fe_{HT} peak is similar to Fe_{HT} peaks observed elsewhere within the 600 ka record (Figure 4.11). The occurrence of a

Fe_{HT} peak without a coinciding peak in Cu_{HT} is also found at ~94 ka, ~113 ka, and ~475 in 12PC and is not uncommon in the SeaVOICE hydrothermal records (Costa et al., 2017). The relatively Cu-poor peaks in Fe_{HT} deposition may result from spatial variability in the origin of the hydrothermal plume and the short transport radius of hydrothermal Cu relative to hydrothermal Fe (German et al., 1991; Rona et al., 1993). Alternatively, such features may reflect variations in the Cu/Fe ratio of hydrothermal fluids emanating from the ridge that could arise from variations in hydrothermal fluid reaction zone temperatures or redox conditions (Costa et al., 2017; Von Damm et al., 1998).

A caveat of the 600 ka hydrothermal record is that the increasing presence of basalt fragments in the oldest 12PC sediments complicates estimates of hydrothermal Fe made using a Ti-based correction for lithogenic Fe. Due to the difference in Fe/Ti ratios between the average continental crust (~11.7 wt.%/wt.%, Taylor and McLennan, 1995) and mid-ocean ridge basalts (~8.3 wt.%/wt.%, Gale et al., 2013), the increased basalt component of the oldest 12PC sediments invalidates the two-component mixing assumption used to estimate the total fraction of sedimentary Fe that is hydrothermal (see Section 4.2.3). The presence of basalt chips with low Fe/Ti values within a sample leads to an over-correction for lithogenic Fe and results in underestimates of Fe_{HT} concentrations and fluxes. Estimates of Cu_{HT} are less sensitive to the presence of basalt chips because the Cu/Ti ratio of continental crust (83 ppm/wt.%; Taylor and McLennan, 1995) and mid-ocean ridge basalt (80 ppm/wt.%; Gale et al., 2013) are relatively similar.

The influence of basalt-hosted Ti in 12PC sediments can be qualitatively estimated by comparing depositional variability of total Ti to that of an independent proxy for continental dust, such as $^4He_{terr}$. Although mid-ocean ridge basalts can contain mantle-derived helium (Graham, 2002), the low ^3He concentrations observed in the basalt-hosting sedimentary layers of 12PC suggest that mantle-derived helium contributions to these sediments are negligible (Section 4.4.1.1). Depositional similarity between Ti and $^4He_{terr}$ is expected when continental dust is the dominant source of sedimentary Ti (e.g., Middleton et al., *in review*). In 12PC sediments <500 ka, the Ti and $^4He_{terr}$ flux records typically follow similar patterns of variability, suggesting negligible basalt contributions to the total Ti flux (Figure 4.11). In contrast, 12PC sediments >500 ka exhibit higher Ti fluxes relative to $^4He_{terr}$ fluxes, suggesting that basalt-hosted Ti contributes a significant fraction of the total Ti flux in these samples. Unfortunately, the existing $^4He_{terr}$ data are an impractical tool for lithogenic corrections because endmember Fe/^{4}He and Ti/^{4}He ratios in the likely continental inputs to the Northeast Pacific and in mid-ocean ridge basalt are poorly constrained and naturally quite variable (e.g., McGee et al., 2016; Graham, 2002). For now, over-correction for lithogenic Fe in these basalt-bearing sediments leads to increased uncertainties in the 12PC Fe_{HT} flux records >500 ka and is the likeliest explanation for the negative Fe_{HT} flux values calculated between 540 and 567 ka (Figure 4.11). Thus, while the Cu_{HT} flux record is relatively insensitive to the presence of basalt, the >500 ka Fe_{HT} flux record should be interpreted with this known bias in mind. Future work could quantitatively evaluate and correct for the influence of basalt on estimates of Fe_{HT} using measurements of additional lithogenic elements, such as ^{232}Th, that are not themselves concentrated within mid-ocean ridge basalt.

Examined in full, the 600 ka hydrothermal record of 12PC exhibits clear variations in Fe_{HT} flux of a factor of 2 to 4 over ~10 to 100 ka timescales (Figure 4.11). Such variability is notable because hydrothermal Fe represents a significant source of dissolved Fe to the deep ocean (Conway and John, 2014; Fitzsimmons et al., 2014; Resing et al., 2015). Though emitted at depth, ligand-complexation can stabilize dissolved hydrothermal Fe and allow for its long-distance transport to the surface ocean, where hydrothermal Fe may provide a critical nutrient source (Bennett et al., 2008; Toner et al., 2009; Conway and John, 2014; Fitzsimmons et al., 2014; Resing et al., 2015). Biogeochemical models suggest that hydrothermal Fe may account for ~15 to 30% of carbon export in the Southern Ocean today (Tagliabue et al., 2010; Saito et al., 2013; Resing et al., 2015). If the variability in hydrothermal Fe output suggested by the Cleft Segment sediments is representative of a global trend, as would occur if sea level influences hydrothermal activity, then long-term hydrothermal variability could drive significant changes in the marine dissolved Fe budget that are on par with the glacial-interglacial variations in the amount of dissolved Fe delivered to the sea by wind-blown dust (e.g., Middleton et al., 2016).

4.5. Sea level triggers of hydrothermal flux variability

The Cleft Segment hydrothermal flux records allow for evaluation of the potential influence of sea level changes on variations in hydrothermal activity over multiple glacial cycles (Figure 4.12; Costa et al., 2017). Pressure fluctuations associated with glacially-driven changes in sea level may be sufficient to influence the magmatic and hydrothermal output of submarine volcanic centers (Huybers and Langmuir, 2009; Lund and Asimow, 2011; Crowley et al., 2015).

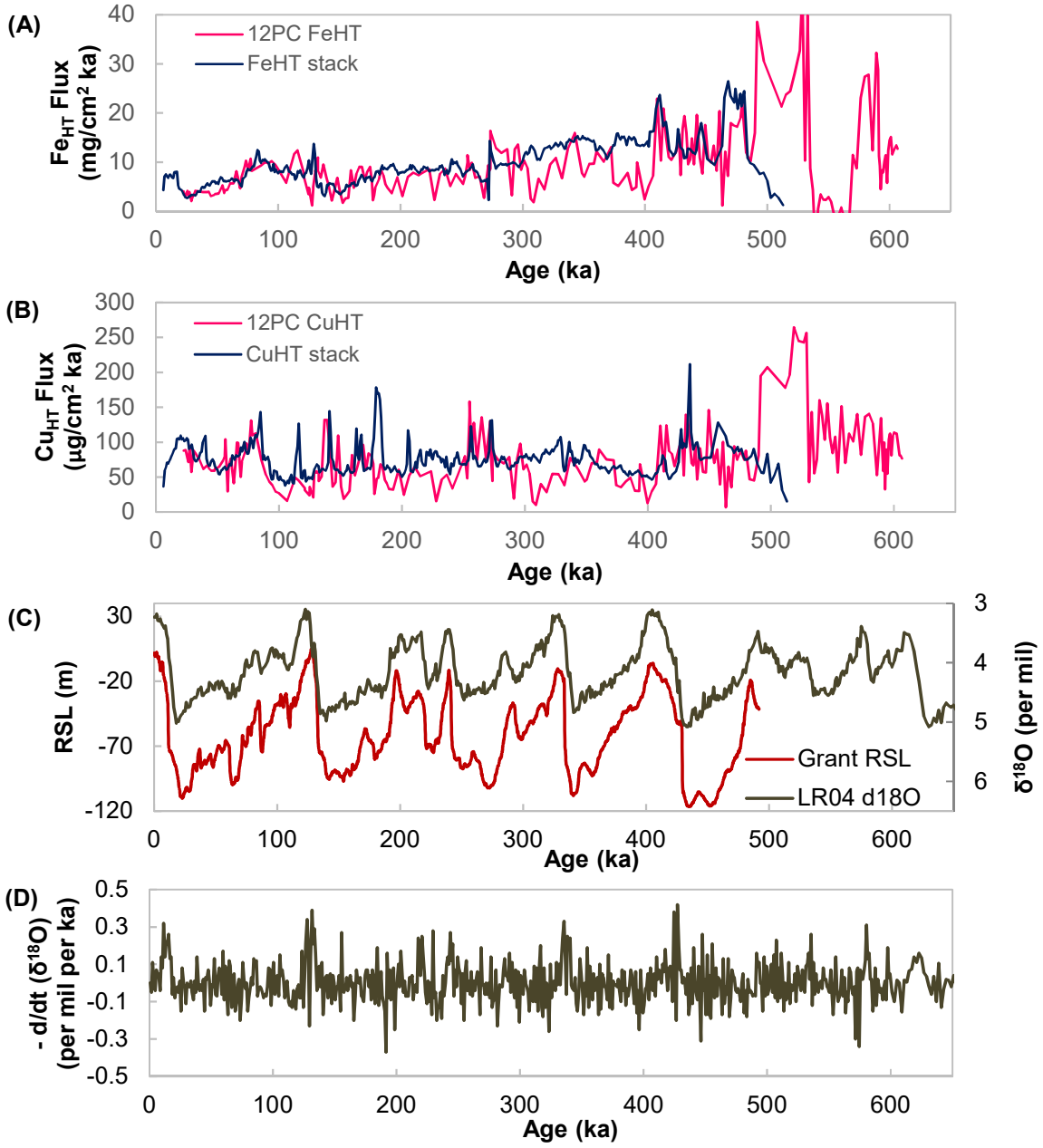

Figure 4.12: Comparison of Juan de Fuca Ridge hydrothermal flux records with glacial cycles and sea level. (A) Hydrothermal Fe flux records from 12PC (pink) and the Cleft Segment stack (blue; Costa et al., 2017). (B) Hydrothermal Cu flux records from 12PC (pink) and the Cleft Segment stack (blue; Costa et al., 2017). (C) LR04 benthic oxygen isotope stack (black; Lisiecki and Raymo, 2005) and relative sea level (red; Grant et al., 2014). (D) The negative of the derivative of the LR04 $\delta^{18}O$ stack. The negative is plotted such that higher values indicate periods of sea level rise. Uncertainty estimates are excluded for clarity. Rapid sea level changes are hypothesized to drive variability in submarine hydrothermal output across glacial cycles (Lund and Asimow, 2011; Lund et al., 2016; Middleton et al., 2016; Costa et al., 2017).

Spectral analysis of seafloor bathymetry from the Australian-Antarctic Ridge (Crowley et al., 2015) and the Southern East Pacific Rise (Tolstoy, 2015) reveal peaks in spectral power density that coincide Milankovitch frequencies of orbital variation, however, interpretation of this bathymetric variability is complicated by the regular tectonic activity and crustal faulting associated with seafloor spreading (e.g., Olive et al., 2015; 2016; Tolstoy, 2016; Huybers et al., 2016). Sedimentary records of hydrothermal deposition provide an important additional means of examining the impact of sea level on mid-ocean ridge activity over Milankovitch timescales (Lund and Asimow, 2011; Lund et al., 2016; Middleton et al., 2016; Costa et al., 2017), yet the precise nature of a hydrothermal response to sea level change remains unclear (e.g., Costa et al., 2017).

Geophysical modelling predicts a lagged response between rapid sea level fall and increased mid-ocean ridge volcanism due to the time required for new melts generated at depth to transit to through the crust (Crowley et al., 2015; Lund and Asimow, 2011). For an intermediate spread-rate ridge, such as the Juan de Fuca Ridge, the delay between sea level change and increased volcanism may be on the order of ~5 to 30 ka (Crowley et al., 2015). Increased magmatic production is expected to increase hydrothermal activity because the hydrothermal plume incidence on mid-ocean ridges appears to scale linearly with magma flux (Baker and German, 2004). As such, previous work has predicted hydrothermal activity to increase following rapid sea level falls (Lund and Asimow, 2011; Lund et al., 2016). Hydrothermal records from the Mid-Atlantic Ridge (Middleton et al., 2016), the Galapagos Microplate (Frank et al., 1994), the East Pacific Rise (Lund et al., 2016), and the Juan de Fuca Ridge (Costa et al., 2017) each reveal

increases in hydrothermal Fe deposition following the Last Glacial Maximum that peak ~10 to 15 ka after a rapid sea level drop of ~14 m/ka at ~30 ka (Grant et al., 2014) and are thus consistent with this hypothesis. However, more recent work suggests that the relationship between sea level and hydrothermal activity on the Mid-Atlantic Ridge may be more complicated than previously understood (See Chapter 2).

Development of the 500 ka hydrothermal records from the Juan de Fuca Ridge SeaVOICE cores led Costa et al. (2017) to suggest that hydrothermal activity may increase during deglaciations as an immediate response to *rising* sea level, rather than as a delayed response to previous sea level falls. Rising sea level could potentially trigger an increase in hydrothermal circulation if the associated increase in pressure above the ridge led to enhanced tectonic activity and fracturing within the crust. A comparison of two segments on the northern East Pacific Rise finds higher hydrothermal plume incidence in the segment hosting weaker magmatic activity due to its increased crustal permeability (Baker et al., 2001). During magmatically poor and tectonically dominated phases of seafloor spreading, deep crustal cracking fronts may develop that allow for increased fluid flow at depth and enhanced hydrothermal circulation (Baker et al., 2001; Delaney et al., 1992; Lister, 1974). A tectonically driven hydrothermal response to sea level rise is not expected to be associated with a significant lag time, as modern observations from the Endeavor Segment of the Juan de Fuca Ridge find an immediate increase in hydrothermal activity following tectonically driven earthquake swarms (Johnson et al., 2000).

Thus, two physical explanations have been suggested as possible triggers for enhanced hydrothermal circulation associated with sea level change: (1) falling sea level drives a delayed

increase in hydrothermal output associated with increases magmatic activity, and (2) rising sea level drives a near-immediate increase in hydrothermal output associated with increases tectonic activity.

4.5.1. A statistical approach to the Cleft Segment records

This study uses the Cleft Segment hydrothermal flux records (from this study and from Costa et al., 2017) and the LR04 benthic foraminifera oxygen isotope ($\delta^{18}O$) stack (Lisiecki and Raymo, 2005) as a proxy record for sea level variability to statistically compare the two mechanisms proposed above regarding glacial drivers of hydrothermal activity. The LR04 $\delta^{18}O$ stack was used to approximate sea level variability in lieu of the explicit 500 ka relative sea level record reported by Grant et al. (2014) in order to evaluate the entire 600 ka hydrothermal record of 12PC. The $\delta^{18}O$ values of benthic foraminifera reflect variations in local salinity and temperature in addition to global ice volume (e.g., Lisiecki and Raymo, 2005). Yet, the pattern of variability exhibited by the LR04 $\delta^{18}O$ stack is very similar to the relative sea level curve estimated by Grant et al. (2014) over the past 500 ka (Figure 4.12). Consequently, the LR04 stack is considered a reasonable proxy for sea level variability for the purposes of this analysis. If rapid sea level fall leads to increased hydrothermal activity as a result of increased magmatic activity, then sedimentary records of hydrothermal deposition would be expected to exhibit a negative correlation with sea level change (and a positive correlation with $\delta^{18}O$) following a temporal offset, or lag, of ~5 to 30 ka. Alternatively, if deglacial sea level rise drives increased in hydrothermal activity potentially associated with increased crustal fracturing, then sedimentary

records of hydrothermal fluxes would be expected to exhibit a positive correlation with sea level change (and a negative correlation with $\delta^{18}O$).

Sea level comparisons with hydrothermal variability were separately evaluated using the 600 ka flux records of 12PC, to provide the longer continuous record, and the 500 ka hydrothermal flux stack generated from the SeaVOICE cores by Costa et al. (2017). The stacked hydrothermal flux records were included in order to minimize the influence of spatial heterogeneity in Cleft Segment hydrothermal deposition on the statistical comparison. Both the 12PC and stacked hydrothermal flux record were additionally evaluated over just the interval from 0 to 250 ka to examine potential changes in the relationship between sea level and hydrothermal deposition over time (e.g., Costa et al., 2017). The Fe_{HT} and Cu_{HT} flux records were also separately evaluated, as the two elements are sensitive to different physiochemical aspects of hydrothermal circulation and do not exhibit the same patterns of variability in the SeaVOICE cores (see Section 4.4.2).

The hydrothermal flux and $\delta^{18}O$ records were first linearly interpolated to a uniform time series approximating the average sampling resolution of the SeaVOICE data (1 data point per 2.5 ka in 12PC and 1 data point per 1 ka in hydrothermal stack). Hydrothermal records were also compared to the derivative of the $\delta^{18}O$ record because the rate of sea level change is expected to exert a larger influence on mid-ocean ridges than absolute sea level (Lund and Asimow, 2011; Crowley et al., 2015). Zero lag correlation coefficients (R_0) were computed between the interpolated hydrothermal and $\delta^{18}O$ time series at zero temporal offset to examine the immediate interaction between rising sea level and increasing hydrothermal activity. The hydrothermal time

series were then temporally shifted to lag the $\delta^{18}O$ time series between 0 to 60 ka and a correlation coefficient was computed between the lagged hydrothermal series and the $\delta^{18}O$ isotope record at each step. Optimized lagged correlation coefficients (R_{lag}) were determined from the temporal offset yielding the maximum correlation between the hydrothermal time series and the negative of sea level (positive $\delta^{18}O$) in order to examine delayed interactions between falling sea level and increasing hydrothermal activity.

In the case of no true relationship between time series, the computed values of R_{lag} are expected to be higher than R_0 due to the increasing degrees of freedom associated with varying the temporal offset between time series. This effect inhibits a direct comparison between lagged and unlagged interactions between sea level change and hydrothermal activity. Consequently, a ΔR value is computed such that $\Delta R = R_0 - R_{lag}$ for each pair of hydrothermal and $\delta^{18}O$ time series. The statistical significance of the observed ΔR value is then determined by comparison to a null distribution of 10,000 ΔR values computed as above using randomized synthetic realizations of hydrothermal activity instead of the observed values. Randomized synthetic hydrothermal time series were generated by phase randomization of the original hydrothermal record (e.g., Theiler et al., 1992). It is noted that the statistical power of this test is may not be sufficient to rule out the physical importance of a given correlation, even if the correlation yields insignificant p-values.

4.5.2. Statistical results and discussion

Statistical comparison of hydrothermal Fe and Cu records from 12PC and the Cleft Segment stack with both the LR04 $\delta^{18}O$ record and its derivative suggest that the lagged response model is not significantly favored over the immediate response model (Table 4.1). It is noted that this result assumes that a consistent characteristic lag time between sea level changes and hydrothermal responses over the course of multiple glacial cycles. This statistical approach should not be used to rule out the possibility of varying lag times associated with different degrees of sea level change or variations in crustal permeability beneath the ridge (e.g., Crowley et al., 2015).

Although the consistent lag model does not appear to be favored over the immediate response model, the R_0 correlations calculated without a time offset between the hydrothermal flux records and sea level, approximated by the negative of the LR04 $\delta^{18}O$ stack, are not necessarily as predicted by the immediate response model (Table 4.2). For example, no significant correlations are observed between hydrothermal deposition and sea level within the full 600 ka record of 12PC. Statistical evaluations of the 12PC Fe_{HT} and Cu_{HT} records were additionally performed using only the flux data from the past 500 ka in order to exclude the sedimentary interval in which interpretations of hydrothermal fluxes are most likely to be complicated by the presence of basalt fragments. Using the 500 ka 12PC records, a weak but significant *negative* correlation ($R_0 = -0.25$, $p = 0.04$) is observed between sea level (negative $\delta^{18}O$) and Cu_{HT} fluxes such that low sea level is correlated with high Cu_{HT} deposition (Figure 4.13). Evaluation of the stacked hydrothermal records of Costa et al. (2017) also reveals a significant negative correlation

Table 4.1: Comparison of lagged and unlagged correlations between hydrothermal flux and sea level

Time Series	Fe_{HT} Flux[a] ΔR[b]	p[c]	Cu_{HT} Flux[a] ΔR[b]	p[c]
12PC (full record)				
vs. - $\delta^{18}O$ [d]	-0.14	0.68	-0.30	0.16
vs. – d/dt ($\delta^{18}O$)[d]	-0.05	0.99	-0.06	0.77
12PC (500 ka)[e]				
vs. - $\delta^{18}O$ [d]	-0.06	0.79	Best lag is no lag	
vs. – d/dt ($\delta^{18}O$)[d]	-0.02	0.94	-0.05	0.89
12PC (250 ka)[f]				
vs. - $\delta^{18}O$ [d]	0.14	0.96	Best lag is no lag	
vs. – d/dt ($\delta^{18}O$)[d]	-0.37	0.12	-0.30	0.33
JdFR Stack[g]				
vs. - $\delta^{18}O$ [d]	0.06	0.82	Best lag is no lag	
vs. – d/dt ($\delta^{18}O$)[d]	-0.14	0.20	-0.06	0.82
JdFR Stack[g] *(250 ka)*[f]				
vs. - $\delta^{18}O$ [d]	0.47	0.80	Best lag is no lag	
vs. – d/dt ($\delta^{18}O$)[d]	-0.23	0.42	-0.07	0.67

[a]Fe_{HT} and Cu_{HT} refer to hydrothermal Fe and hydrothermal Cu, respectively.
[b]$\Delta R = R_0 - R_{lag}$, where R_0 is the correlation between records without a lag and R_{lag} is the maximum correlation between records given a time offset of 0 to 60 ka. More positive ΔR values favor the unlagged model.
[c]Left-sided p-values are calculated from a distribution of 10,000 synthetic ΔR values computed by phase randomization of the original hydrothermal time series (See Section 5). None of the reported ΔR values are significant to favor the lagged response model at the 95% confidence level.
[d]$\delta^{18}O$ values from the LR04 benthic foraminifera oxygen isotope stack (Lisiecki and Raymo, 2005), hydrothermal records are compared with negative $\delta^{18}O$ because decreasing values of $\delta^{18}O$ correspond with increasing sea level.
[e]The 12PC flux records are additionally evaluated exclusively over the past 500 ka, to exclude the interval most likely to be complicated by the presence of basalt fragments.
[f]The 0 to 250 ka interval of both records were separately evaluated to examine temporal variations in observed correlations.
[g]JdFR Stack refers to the stacked Cleft Segment records reported by Costa et al. (2017).

(R_0 = -0.35, $p < 0.01$) between Cu_{HT} fluxes and sea level, again with low sea level correlating with high Cu_{HT} fluxes (Figure 4.13). Negative correlations between Cu_{HT} fluxes and sea level are also observed in the 0 to 250 ka intervals of both 12PC and the stacked flux records (Table 4.2).

Table 4.2: Correlations between hydrothermal flux and sea level with zero temporal offset

Time Series	Fe_{HT} Flux[a]		Cu_{HT} Flux[a]		Ti Flux	
	R_0	p[b]	R_0	p[b]	R_0	p[b]
12PC (full record)						
vs. - $\delta^{18}O$ [c]	0.16	0.16	-0.07	0.28	-0.11	0.16
vs. – d/dt ($\delta^{18}O$)[c]	0.17	0.08	0.09	0.09	0.09	0.08
12PC (500 ka)[d]						
vs. - $\delta^{18}O$ [c]	0.08	0.28	-0.25	0.04**	-0.33	0.02**
vs. – d/dt ($\delta^{18}O$)[c]	0.10	0.15	0.11	0.14	0.12	0.12
12PC (250 ka)[e]						
vs. - $\delta^{18}O$ [c]	0.35	0.14	-0.43	0.03**	-0.34	0.03**
vs. – d/dt ($\delta^{18}O$)[c]	-0.07	0.28	-0.07	0.30	-0.02	0.45
JdFR Stack[f]						
vs. - $\delta^{18}O$ [c]	0.19	0.06*	-0.35	< 0.01**	NA	
vs. – d/dt ($\delta^{18}O$)[c]	-0.03	0.31	-0.02	0.41	NA	
JdFR Stack[f] *(250 ka)*[e]						
vs. - $\delta^{18}O$ [c]	0.64	0.02**	-0.29	0.02**	NA	
vs. – d/dt ($\delta^{18}O$)[c]	0.07	0.36	-0.03	0.38	NA	

[a]Fe_{HT} and Cu_{HT} refer to hydrothermal Fe and hydrothermal Cu, respectively.
[b]P-values are calculated from a distribution of 10,000 synthetic R_0 values computed by phase randomization of both original time series.
[c]$\delta^{18}O$ values from the LR04 benthic foraminifera oxygen isotope stack (Lisiecki and Raymo, 2005), hydrothermal records are compared with negative $\delta^{18}O$ because decreasing values of $\delta^{18}O$ correspond with increasing sea level.
[d]The 12PC flux records are additionally evaluated exclusively over the past 500 ka, to exclude the interval most likely to be complicated by the presence of basalt fragments.
[e]The 0 to 250 ka interval of both records were separately evaluated to examine temporal variations in observed correlations.
[f]JdFR Stack refers to the stacked Cleft Segment records reported by Costa et al. (2017).
**These correlations are significant at the 95% confidence interval.
*These correlations are marginally significant.

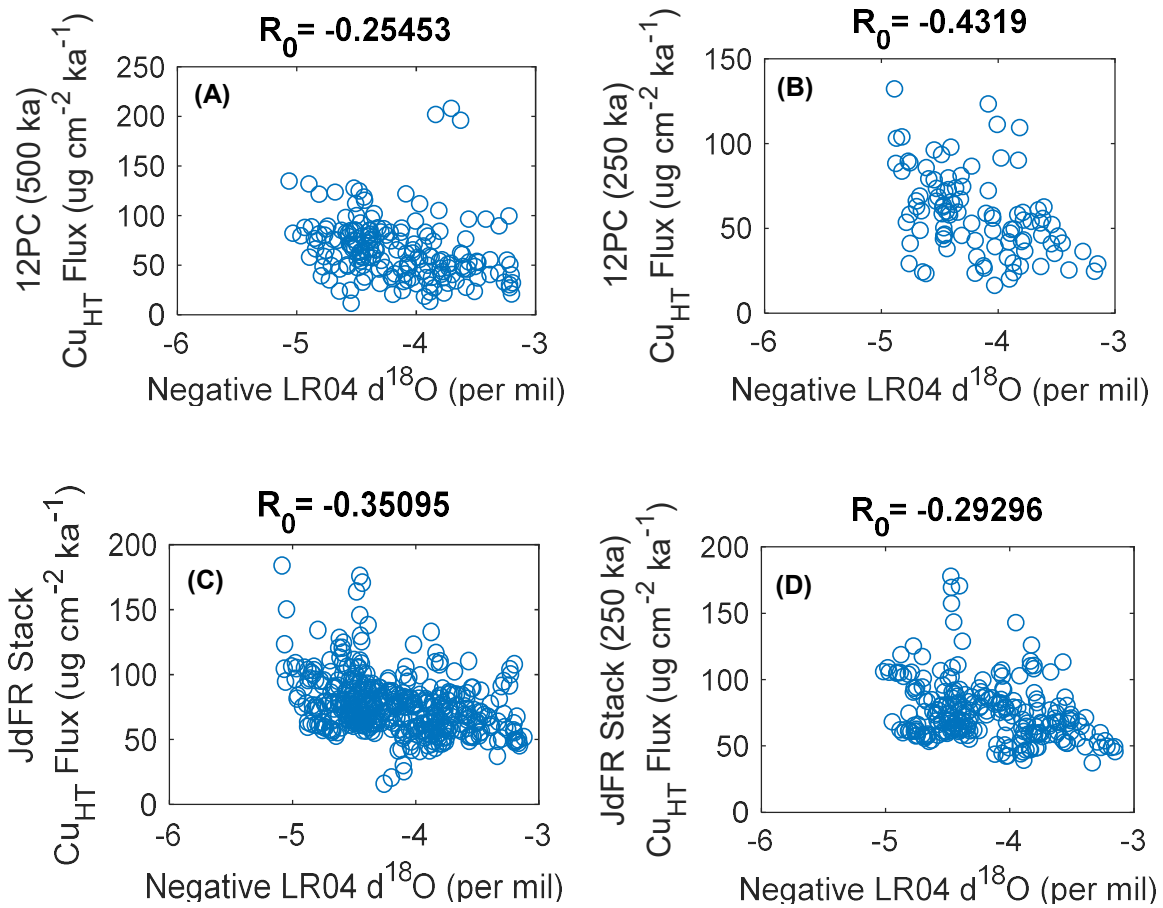

Figure 4.13: Significant correlations with zero temporal offset between hydrothermal Cu (Cu_{HT}) flux records in the (A) 500 ka ($p = 0.04$) and (B) 250 ka ($p = 0.03$) intervals of 12PC as well as (C) the full ~500 ka ($p < 0.01$) and (D) the 250 ka ($p = 0.02$) stacked Cleft Segment record of Costa et al. (2017). Sea level variability is approximated using the negative of the LR04 benthic foraminifera $\delta^{18}O$ stack (Lisiecki and Raymo, 2005) because increasing values of $\delta^{18}O$ correspond with decreasing sea level. Negative correlations between hydrothermal flux and relative sea level are not expected in the immediate response model.

In contrast to Cu_{HT}, the stacked Fe_{HT} records exhibits a marginally significant positive correlation ($R_0 = 0.19$, $p = 0.06$) with sea level (negative $\delta^{18}O$), such that high sea level is somewhat correlated with high Fe_{HT} deposition (Figure 4.14). The positive correlation between Fe_{HT} and sea level is significantly stronger ($R_0 = 0.64$, $p = 0.02$) when only the interval between 0 and 250 ka in the stacked flux record is examined (Figure 4.14b). No significant correlations

are observed between sea level and Fe_{HT} fluxes in the any examined intervals of the 12PC record or between any flux record and the derivative of $\delta^{18}O$ (Table 4.2). However, the high signal to noise ratio in the derivative of the LR04 $\delta^{18}O$ stack likely makes significant correlations between hydrothermal activity and the derivative $\delta^{18}O$ stack may be difficult to detect.

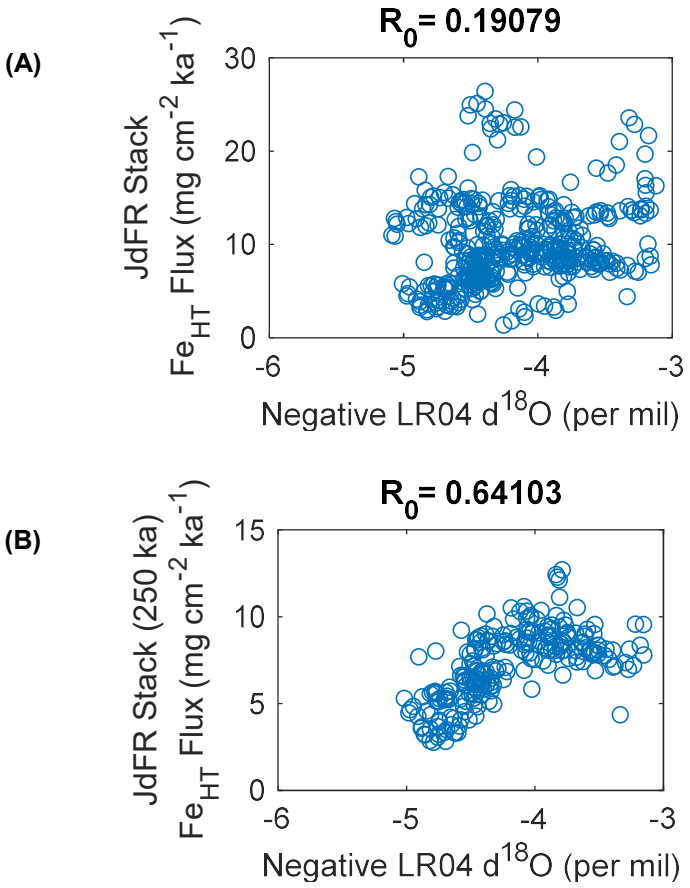

Figure 4.14: Positive correlations with zero temporal offset between hydrothermal Fe (Fe_{HT}) flux records in (A) the full ~500 ka (p = 0.06) and (B) the 250 ka (p = 0.02) stacked Cleft Segment record of Costa et al. (2017). Sea level variability is approximated using the negative of the LR04 benthic foraminifera $\delta^{18}O$ stack (Lisiecki and Raymo, 2005) because increasing values of $\delta^{18}O$ correspond with decreasing sea level. Positive correlations between hydrothermal flux and relative sea level are expected in the immediate response model.

Correlations between the total Ti fluxes in 12PC and the LR04 $\delta^{18}O$ record were also computed in order to evaluate the viability of this approach to detect known relationships between climate and sedimentary deposition on the Juan de Fuca Ridge. Excluding the basalt-bearing sediments in the oldest parts of the 12PC, continental dust likely dominates Ti input to 12PC over the past 500 ka (Section 4.4.2). Consequently, the 500 ka 12PC Ti flux record is expected to exhibit a negative correlation with sea level because wind-blown dust deposition in the Pacific is known to be higher during glacial periods (low sea level) due to increases in wind strength (Winckler et al., 2008; McGee et al., 2010b). Indeed, comparison of the 500 ka 12PC Ti fluxes with the LR04 $\delta^{18}O$ record yields a relatively weak, yet significant negative correlation ($R_0 = -0.33$, $p = 0.02$; Figure 4.15), with high Ti fluxes correlated with low sea level as expected. A similar correlation is observed when just the interval from 0 to 250 ka in 12PC is examined ($R_0 = -0.34$, $p = 0.03$; Figure 4.15b). The relatively low R_0 values computed for the relationship between Ti fluxes and sea level, for which the driving mechanisms are relatively well understood, suggests strong correlations between climatic variability and hydrothermal deposition in marine sedimentary environments may be difficult to detect. Strong correlations between climate and hydrothermal deposition may be especially difficult to detect because hydrothermal circulation is likely to be sensitive to a variety of local magmatic, volcanic, and tectonic influences unrelated to sea level (e.g., German and Seyfried, 2014; Von Damm, 1995; Kelley et al., 2002) that will introduce additional temporal and spatial variability into long-term records of hydrothermal activity. Thus, although weak, the observation of significant correlations between hydrothermal fluxes and sea level in the Cleft Segment sediments should not be discounted.

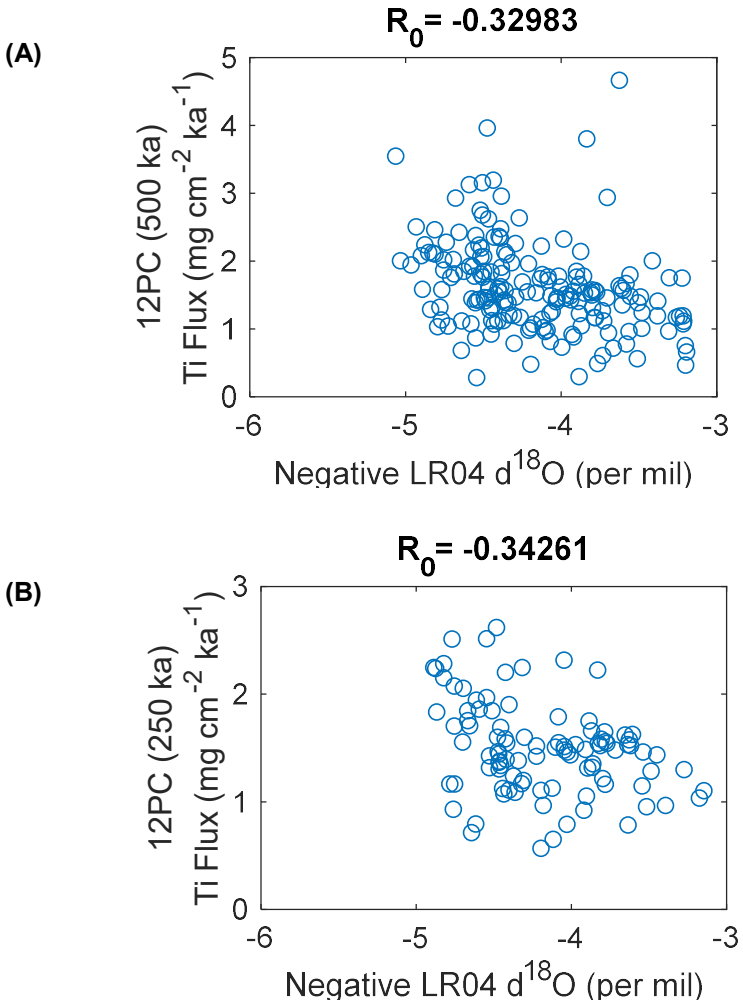

Figure 4.15: Significant correlations with zero temporal offset between hydrothermal Cu (Cu_{HT}) flux records in the (A) 500 ka (p = 0.02) and (B) 250 ka (p = 0.03) records from 12PC. Examination of fluxes in sediments younger than 500 ka excludes complications associated with the presence of basalt fragments in older sediments. Sea level variability is approximated using the negative of the LR04 benthic foraminifera $\delta^{18}O$ stack (Lisiecki and Raymo, 2005) because increasing values of $\delta^{18}O$ correspond with decreasing sea level. Negative correlations are expected between Ti fluxes and sea level (negative $\delta^{18}O$) because wind-blown Ti deposition to the Pacific is higher during glacial periods and lower during interglacial periods (e.g., Winckler et al., 2008). Detection of this expected relationship within the 12PC records demonstrates the viability of the statistical approach used to evaluate relationships between hydrothermal activity and sea level.

The difference in sign of the correlations between Fe_{HT} and Cu_{HT} fluxes with sea level is puzzling and reflects the observation of Costa et al. (2017) that the Fe_{HT} and Cu_{HT} flux records from the Cleft Segment sediments are not significantly correlated with each other. Costa et al. (2017) suggest that the high Cu/Fe peaks in Cu_{HT} flux observed in the Juan de Fuca Ridge sediments during glacial periods may reflect increased temperatures within the hydrothermal fluid reaction zone. In turn, the authors propose that the high hydrothermal reaction temperatures may be associated with increased or shallower magmatic activity caused by decompression melting during the glacial periods (e.g., Huybers and Langmuir, 2009; Lund and Asimow, 2011). However, while high temperature hydrothermal reactions may generate fluids that are rich in Cu relative to Fe, these fluids also contain very high concentrations of Fe (Seewald and Seyfried, 1990). Accordingly, if glacial peaks in Cu_{HT} flux are caused by increased high temperature hydrothermal activity, then these events are expected to also cause detectable increases in Fe_{HT} flux from the vent. Yet several Cu_{HT} flux peaks in the Cleft Segment stack, including those at ~40 ka and ~179 ka occur during intervals in which Fe_{HT} fluxes are declining (Figure 4.12). Rather than evidence of increased hydrothermal activity, the Fe-poor Cu_{HT} flux peaks may result from remobilization of sedimentary Cu_{HT} during early diagenesis (e.g., Pederson et al., 1986). Some Cu_{HT} flux peaks do correlate well with increased in Fe_{HT} flux, most notably during the broad hydrothermal maximum between ~490 and ~530 ka, and are thus very likely to reflect variations in hydrothermal deposition. However, the negative correlations observed between apparent Cu_{HT} flux and sea level in records limited to the past 500 ka may be driven by variable redox conditions at the sediment-water interface associated with changes in ocean circulation over glacial-interglacial cycles.

In contrast, Cleft Segment records of Fe_{HT} fluxes are interpreted to more directly reflect variations in hydrothermal output of the nearby ridge. The positive correlations observed with zero time offset between inferred sea level and Fe_{HT} flux in both the full and in the 0 to 250 ka intervals of the Cleft Segment hydrothermal stack of Costa et al. (2017) are consistent with the immediate response model proposed for sea level influences on hydrothermal activity. The increase in correlation observed between the full ~500 ka Fe_{HT} flux stack and the most recent 250 ka is interesting and may reflect varying sensitivity of Cleft Segment hydrothermal circulation to changes in sea level. The absence of strong correlations to sea level within the 12PC Fe_{HT} flux records is likely to result from enhanced variability in the deposition of hydrothermal material to any single sedimentary location compared with a regionally integrated stacked record. This result motivates the development of additional regionally stacked records of long-term hydrothermal Fe fluxes with which to evaluate the segment-scale relationships between sea level variations and hydrothermal circulation.

Statistical examination of the Cleft Segment hydrothermal flux records highlights the complexities associated with evaluation of interactions between sea level change and submarine hydrothermal activity. Nonetheless, a significant correlation is observed between high sea level and high hydrothermal Fe fluxes on the Juan de Fuca Ridge over the past 250 ka. This result encourages the development of geochemical and geophysical models to examine the mechanistic plausibility of enhanced hydrothermal activity driven by rising sea level. Further, the development of in-depth predictive models focusing on potential hydrothermal responses to sea level variability would provide a valuable tool for interpretation of observed long-term variability in hydrothermal activity. Finally, the statistical approach outlined in this study

provides a basis to build upon in future examinations of the proposed relationships between glacially driven sea level change and submarine hydrothermal circulation.

4.6. Conclusions

This study uses $^{3}He_{ET}$ as a constant flux proxy to constrain vertical sediment rain rates over the past 600 ka in the Northeast Pacific in two sediment cores from the Cleft Segment of the Juan de Fuca Ridge. On glacial-interglacial timescales, the $^{3}He_{ET}$ -derived vertical rain rates typically overlap within 1 σ uncertainty of those derived using $^{230}Th_{XS}$ (Costa and McManus, 2017), demonstrating general reproducibility between the two constant flux proxies within the complex depositional environment of the Juan de Fuca Ridge. On suborbital timescales, however, the $^{3}He_{ET}$ -based fluxes record significantly more variability than is exhibited by $^{230}Th_{XS}$. The difference in variability recorded by $^{3}He_{ET}$ and $^{230}Th_{XS}$ on suborbital timescales may demonstrate the unique utility of the $^{3}He_{ET}$ system in slowly accumulating (< 3 cm/ka) sediments or may result from high frequency variability in the local deposition of $^{3}He_{ET}$ -bearing interplanetary dust particles. Future work is necessary to discern between these two hypotheses in order to inform the application of $^{3}He_{ET}$ and $^{230}Th_{XS}$ to future sedimentary studies of high frequency climate variability.

The $^{3}He_{ET}$ - and $^{230}Th_{XS}$ -based flux records are additionally combined with $^{4}He_{terr}$ concentration data and previous measurements of carbonate, iron, copper, and titanium concentrations (Costa and McManus, 2017; Costa et al., 2017) to evaluate hydrothermal sedimentary fluxes to the Juan de Fuca Ridge beyond the ~500 ka limit of $^{230}Th_{XS}$ (Costa et al., 2017). Extension of the Cleft

Segment record of hydrothermal deposition to 600 ka reveals a sustained maximum in both hydrothermal Fe and Cu fluxes between ~530 and ~490 ka suggestive of a uniquely intense interval of hydrothermal activity. The Cleft Segment hydrothermal records exhibit 2 to 4-fold variations in hydrothermal Fe deposition rates over timescales of ~10 to 100 ka and are suggestive of significant variations in the flux of biologically relevant dissolved hydrothermal Fe from the southern Juan de Fuca Ridge over these timescales.

The Juan de Fuca Ridge hydrothermal records additionally provide the opportunity to statistically examine the proposed relationships between glacially-driven changes in sea level and submarine hydrothermal activity (e.g., Lund and Asimow, 2011; Middleton et al., 2016; Lund et al., 2016; Costa et al., 2017). Although the any relationship between sea level and hydrothermal deposition on the Cleft Segment is likely to be complex, a significant positive correlation is observed between sea level, approximated using the LR04 benthic foraminifera oxygen isotope stack (Lisiecki and Raymo, 2005), and the Cleft Segment hydrothermal Fe flux stack (Costa et al., 2017) over the past 250 ka. This result encourages further investigation into the interactions between sea level and hydrothermal circulation on mid-ocean ridges.

References

Andersen, M., Stirling, C., Zimmermann, B., Halliday, A., 2010. Precise determination of the open ocean $^{234}U/^{238}U$ composition. Geochemistry, Geophysics, Geosystems 11.

Anderson, R., Ali, S., Bradtmiller, L., Nielsen, S., Fleisher, M., Anderson, B., Burckle, L., 2009. Wind-driven upwelling in the Southern Ocean and the deglacial rise in atmospheric CO_2. Science 323, 1443-1448.

Auffret, G., Richter, T., Reyss, J., Organo, C., Deloule, E., Gaillard, J., Dennielou, B., Muller, C., Thomas, B., Watremez, P., 1996. Record of hydrothermal activity in sediments from

the Mid-Atlantic Ridge south of the Azores. Comptes rendus de l'académie des sciences serie II fascicule a-sciences de la terre et des planetes 323, 583-590.

Bacon, M.P., 1984. Glacial to interglacial changes in carbonate and clay sedimentation in the Atlantic Ocean estimated from 230Th measurements. Chemical Geology 46, 97-111.

Bacon, M.P., Anderson, R.F., 1982. Distribution of thorium isotopes between dissolved and particulate forms in the deep sea. Journal of Geophysical Research: Oceans 87, 2045-2056.

Baker, E.T., Cormier, M.H., Langmuir, C.H., Zavala, K., 2001. Hydrothermal plumes along segments of contrasting magmatic influence, 15°20′–18°30′ N, East Pacific Rise: Influence of axial faulting. Geochemistry, Geophysics, Geosystems 2.

Baker, E.T., German, C.R., 2004. On the global distribution of hydrothermal vent fields. Mid-Ocean Ridges, 245-266.

Bennett, S.A., Achterberg, E.P., Connelly, D.P., Statham, P.J., Fones, G.R., German, C.R., 2008. The distribution and stabilisation of dissolved Fe in deep-sea hydrothermal plumes. Earth and Planetary Science Letters 270, 157-167.

Carbotte, S.M., Nedimović, M.R., Canales, J.P., Kent, G.M., Harding, A.J., Marjanović, M., 2008. Variable crustal structure along the Juan de Fuca Ridge: Influence of on-axis hot spots and absolute plate motions. Geochemistry, Geophysics, Geosystems 9.

Cave, R., German, C., Thomson, J., Nesbitt, R., 2002. Fluxes to sediments underlying the Rainbow hydrothermal plume at 36°14′ N on the Mid-Atlantic Ridge. Geochimica et Cosmochimica Acta 66, 1905-1923.

Cherkashev, G., 1995. Hydrothermal input into sediments of the Mid-Atlantic Ridge. Geological Society, London, Special Publications 87, 223-229.

Conway, T.M., John, S.G., 2014. Quantification of dissolved iron sources to the North Atlantic Ocean. Nature 511, 212.

Costa, K., McManus, J., 2017. Efficacy of ^{230}Th normalization in sediments from the Juan de Fuca Ridge, northeast Pacific Ocean. Geochimica et Cosmochimica Acta 197, 215-225.

Costa, K.M., McManus, J.F., Boulahanis, B., Carbotte, S.M., Winckler, G., Huybers, P.J., Langmuir, C.H., 2016. Sedimentation, stratigraphy and physical properties of sediment on the Juan de Fuca Ridge. Marine Geology 380, 163-173.

Costa, K.M., McManus, J.F., Middleton, J.L., Langmuir, C.H., Huybers, P.J., Winckler, G., Mukhopadhyay, S., 2017. Hydrothermal deposition on the Juan de Fuca Ridge over multiple glacial–interglacial cycles. Earth and Planetary Science Letters 479, 120-132.

Crowley, J.W., Katz, R.F., Huybers, P., Langmuir, C.H., Park, S.-H., 2015. Glacial cycles drive variations in the production of oceanic crust. Science 347, 1237-1240.

Delaney, J.R., Johnson, H.P., Karsten, J.L., 1981. The Juan de Fuca Ridge—Hot Spot—Propagating rift system: new tectonic, geochemical, and magnetic data. Journal of Geophysical Research: Solid Earth 86, 11747-11750.

Delaney, J.R., Robigou, V., McDuff, R.E., Tivey, M.K., 1992. Geology of a vigorous hydrothermal system on the Endeavour Segment, Juan de Fuca Ridge. Journal of Geophysical Research: Solid Earth 97, 19663-19682.

Farley, K., 1995. Cenozoic variations in the flux of interplanetary dust recorded by ^{3}He in a deep-sea sediment. Nature 376, 153.

Farley, K., Eltgroth, S., 2003. An alternative age model for the Paleocene–Eocene thermal maximum using extraterrestrial ^{3}He. Earth and Planetary Science Letters 208, 135-148.

Farley, K., Love, S., Patterson, D., 1997. Atmospheric entry heating and helium retentivity of interplanetary dust particles. Geochimica et Cosmochimica Acta 61, 2309-2316.

Farley, K., Patterson, D., 1995. A 100-kyr periodicity in the flux of extraterrestrial ^{3}He to the sea floor. Nature 378, 600.

Farley, K.A., Vokrouhlický, D., Bottke, W.F., Nesvorný, D., 2006. A late Miocene dust shower from the break-up of an asteroid in the main belt. Nature 439, 295-297.

Ferguson, D.J., Li, Y., Langmuir, C.H., Costa, K.M., McManus, J.F., Huybers, P., Carbotte, S.M., 2017. A 65 ky time series from sediment-hosted glasses reveals rapid transitions in ocean ridge magmas. Geology 45, 491-494.

Field, C.V., Schmidt, G.A., Koch, D., Salyk, C., 2006. Modeling production and climate-related impacts on ^{10}Be concentration in ice cores. Journal of Geophysical Research: Atmospheres 111.

Fitzsimmons, J.N., Boyle, E.A., Jenkins, W.J., 2014. Distal transport of dissolved hydrothermal iron in the deep South Pacific Ocean. Proceedings of the National Academy of Sciences 111, 16654-16661.

Francois, R., Frank, M., Rutgers van der Loeff, M.M., Bacon, M.P., 2004. ^{230}Th normalization: An essential tool for interpreting sedimentary fluxes during the late Quaternary. Paleoceanography 19.

Frank, M., Eckhardt, J.D., Eisenhauer, A., Kubik, P.W., Dittrich-Hannen, B., Segl, M., Mangini, A., 1994. Beryllium-10, thorium-230, and protactinium-231 in Galapagos microplate sediments: Implications of hydrothermal activity and paleoproductivity changes during the last 100,000 years. Paleoceanography 9, 559-578.

Gale, A., Dalton, C.A., Langmuir, C.H., Su, Y., Schilling, J.G., 2013. The mean composition of ocean ridge basalts. Geochemistry, Geophysics, Geosystems 14, 489-518.

German, C., Bourles, D., Brown, E., Hergt, J., Colley, S., Higgs, N., Ludford, E., Nelsen, T., Feely, R., Raisbeck, G., 1997. Hydrothermal scavenging on the Juan de Fuca Ridge: $^{230}Th_{XS}$, ^{10}Be, and REEs in ridge-flank sediments. Geochimica et Cosmochimica Acta 61, 4067-4078.

German, C., Campbell, A., Edmond, J., 1991a. Hydrothermal scavenging at the Mid-Atlantic Ridge: modification of trace element dissolved fluxes. Earth and Planetary Science Letters 107, 101-114.

German, C., Fleer, A., Bacon, M., Edmond, J., 1991b. Hydrothermal scavenging at the Mid-Atlantic Ridge: radionuclide distributions. Earth and Planetary Science Letters 105, 170-181.

German, C., Seyfried, W., 2014. Hydrothermal processes. In 'Treatise on Geochemistry.' (Eds H. Holland and K. Turekian.) pp. 191–233. Elsevier: Amsterdam, Netherlands.

Govers, R., Meijer, P.T., 2001. On the dynamics of the Juan de Fuca plate. Earth and Planetary Science Letters 189, 115-131.

Graham, D.W., 2002. Noble gas isotope geochemistry of mid-ocean ridge and ocean island basalts: Characterization of mantle source reservoirs. Reviews in Mineralogy and Geochemistry 47, 247-317.

Grant, K., Rohling, E., Ramsey, C.B., Cheng, H., Edwards, R., Florindo, F., Heslop, D., Marra, F., Roberts, A., Tamisiea, M.E., 2014. Sea-level variability over five glacial cycles. Nature Communications 5, ncomms6076.

Haug, G.H., Sigman, D.M., Tiedemann, R., Pedersen, T.F., Sarnthein, M., 1999. Onset of permanent stratification in the subarctic Pacific Ocean. Nature 401, 779.

Hayes, C.T., Anderson, R.F., Fleisher, M.Q., Huang, K.-F., Robinson, L.F., Lu, Y., Cheng, H., Edwards, R.L., Moran, S.B., 2015. 230 Th and 231 Pa on GEOTRACES GA03, the US GEOTRACES North Atlantic transect, and implications for modern and paleoceanographic chemical fluxes. Deep Sea Research Part II: Topical Studies in Oceanography 116, 29-41.

Hayes, C.T., McGee, D., Mukhopadhyay, S., Boyle, E.A., Maloof, A.C., 2017. Helium and thorium isotope constraints on African dust transport to the Bahamas over recent millennia. Earth and Planetary Science Letters 457, 385-394.

Higgins, S.M., Anderson, R.F., Marcantonio, F., Schlosser, P., Stute, M., 2002. Sediment focusing creates 100-ka cycles in interplanetary dust accumulation on the Ontong Java Plateau. Earth and Planetary Science Letters 203, 383-397.

Huybers, P., Langmuir, C., 2009. Feedback between deglaciation, volcanism, and atmospheric CO_2. Earth and Planetary Science Letters 286, 479-491.

Huybers, P., Langmuir, C., Katz, R.F., Ferguson, D., Proistosescu, C., Carbotte, S., 2016. Comment on “Sensitivity of seafloor bathymetry to climate-driven fluctuations in mid-ocean ridge magma supply”. Science 352, 1405-1405.

Jean-Baptiste, P., Fouquet, Y., 1996. Abundance and isotopic composition of helium in hydrothermal sulfides from the East Pacific Rise at 13°N. Geochimica et Cosmochimica Acta 60, 87-93.

Johnson, H.P., Hutnak, M., Dziak, R.P., Fox, C.G., 2000. Earthquake-induced changes in a hydrothermal system on the Juan de Fuca mid-ocean ridge. Nature 407, 174.

Kelley, D.S., Baross, J.A., Delaney, J.R., 2002. Volcanoes, fluids, and life at mid-ocean ridge spreading centers. Annual Review of Earth and Planetary Sciences 30, 385-491.

Laîné, A., Kageyama, M., Salas-Mélia, D., Voldoire, A., Riviere, G., Ramstein, G., Planton, S., Tyteca, S., Peterschmitt, J., 2009. Northern hemisphere storm tracks during the last glacial maximum in the PMIP2 ocean-atmosphere coupled models: energetic study, seasonal cycle, precipitation. Climate Dynamics 32, 593-614.

Lal, D., Jull, A.J., 2005. On the fluxes and fates of ^{3}He accreted by the Earth with extraterrestrial particles. Earth and Planetary Science Letters 235, 375-390.

Lisiecki, L.E., Raymo, M.E., 2005. A Pliocene-Pleistocene stack of 57 globally distributed benthic δ^{18}O records. Paleoceanography 20.

Lister, C., 1974. On the penetration of water into hot rock. Geophysical Journal International 39, 465-509.

Lund, D., Asimow, P., Farley, K., Rooney, T., Seeley, E., Jackson, E., Durham, Z., 2016. Enhanced East Pacific Rise hydrothermal activity during the last two glacial terminations. Science 351, 478-482.

Lund, D.C., Asimow, P.D., 2011. Does sea level influence mid-ocean ridge magmatism on Milankovitch timescales? Geochemistry, Geophysics, Geosystems 12.

Marcantonio, F., Anderson, R.F., Higgins, S., Fleisher, M.Q., Stute, M., Schlosser, P., 2001a. Abrupt intensification of the SW Indian Ocean monsoon during the last deglaciation: constraints from Th, Pa, and He isotopes. Earth and Planetary Science Letters 184, 505-514.

Marcantonio, F., Anderson, R.F., Higgins, S., Stute, M., Schlosser, P., Kubik, P., 2001b. Sediment focusing in the central equatorial Pacific Ocean. Paleoceanography 16, 260-267.

Marcantonio, F., Anderson, R.F., Stute, M., Kumar, N., 1996. Extraterrestrial ^{3}He as a tracer of marine sediment transport and accumulation. Nature 383, 705.

Marcantonio, F., Higgins, S., Anderson, R.F., Stute, M., Schlosser, P., Rasbury, E.T., 1998. Terrigenous helium in deep-sea sediments. Geochimica et Cosmochimica Acta 62, 1535-1543.

Marcantonio, F., Kumar, N., Stute, M., Anderson, R.F., Seidl, M.A., Schlosser, P., Mix, A., 1995. A comparative study of accumulation rates derived by He and Th isotope analysis of marine sediments. Earth and Planetary Science Letters 133, 549-555.

Marcantonio, F., Thomas, D.J., Woodard, S., McGee, D., Winckler, G., 2009. Extraterrestrial ^{3}He in Paleocene sediments from Shatsky Rise: constraints on sedimentation rate variability. Earth and Planetary Science Letters 287, 24-30.

Marcantonio, F., Turekian, K.K., Higgins, S., Anderson, R.F., Stute, M., Schlosser, P., 1999. The accretion rate of extraterrestrial ^{3}He based on oceanic ^{230}Th flux and the relation to Os isotope variation over the past 200,000 years in an Indian Ocean core. Earth and Planetary Science Letters 170, 157-168.

McGee, D., Broecker, W.S., Winckler, G., 2010a. Gustiness: The driver of glacial dustiness? Quaternary Science Reviews 29, 2340-2350.

McGee, D., Marcantonio, F., McManus, J.F., Winckler, G., 2010b. The response of excess ^{230}Th and extraterrestrial ^{3}He to sediment redistribution at the Blake Ridge, western North Atlantic. Earth and Planetary Science Letters 299, 138-149.

McGee, D., Mukhopadhyay, S., 2013. Extraterrestrial He in sediments: From recorder of asteroid collisions to timekeeper of global environmental changes, The Noble Gases as Geochemical Tracers. Springer, pp. 155-176.

McGee, D., Winckler, G., Borunda, A., Serno, S., Anderson, R.F., Recasens, C., Bory, A., Gaiero, D., Jaccard, S.L., Kaplan, M., 2016. Tracking eolian dust with helium and thorium: Impacts of grain size and provenance. Geochimica et cosmochimica acta 175, 47-67.

McGee, D., Winckler, G., Stuut, J., Bradtmiller, L., 2013. The magnitude, timing and abruptness of changes in North African dust deposition over the last 20,000 yr. Earth and Planetary Science Letters 371, 163-176.

Middleton, J.L., Langmuir, C.H., Mukhopadhyay, S., McManus, J.F., Mitrovica, J.X., 2016. Hydrothermal iron flux variability following rapid sea level changes. Geophysical Research Letters 43, 3848-3856.

Middleton, J.L., Mukhopadhyay, S., Langmuir, C.H., McManus, J.F., Huybers, P.J., in press. Millennial-scale variations in dustiness recorded in Mid-Atlantic sediments from 0 to 70 ka. Earth and Planetary Science Letters.

Mukhopadhyay, S., Farley, K., Montanari, A., 2001. A 35 Myr record of helium in pelagic limestones from Italy: Implications for interplanetary dust accretion from the early Maastrichtian to the middle Eocene. Geochimica et Cosmochimica Acta 65, 653-669.

Nier, A., Schlutter, D., 1992. Extraction of helium from individual interplanetary dust particles by step-heating. Meteoritics & Planetary Science 27, 166-173.

Nier, A., Schlutter, D., 1993. The thermal history of interplanetary dust particles collected in the Earth's stratosphere. Meteoritics & Planetary Science 28, 675-681.

Olive, J.-A., Behn, M.D., Ito, G., Buck, W.R., Escartín, J., Howell, S., 2015. Sensitivity of seafloor bathymetry to climate-driven fluctuations in mid-ocean ridge magma supply. Science 350, 310-313.

Olive, J.-A., Behn, M.D., Ito, G., Buck, W.R., Escartín, J., Howell, S., 2016. Response to Comment on "Sensitivity of seafloor bathymetry to climate-driven fluctuations in mid-ocean ridge magma supply". Science 352, 1405-1405.

Patterson, D., Farley, K., Schmitz, B., 1998. Preservation of extraterrestrial ^{3}He in 480-Ma-old marine limestones. Earth and Planetary Science Letters 163, 315-325.

Pavia, F., Anderson, R., Vivancos, S., Fleisher, M., Lam, P., Lu, Y., Cheng, H., Zhang, P., Edwards, R.L., 2017. Intense hydrothermal scavenging of ^{230}Th and ^{231}Pa in the deep Southeast Pacific. Marine Chemistry.

Pedersen, T.F., Vogel, J.S., Southon, J.R., 1986. Copper and manganese in hemipelagic sediments at 21°N, East Pacific Rise: Diagenetic contrasts. Geochimica et Cosmochimica Acta 50, 2019-2031.

Resing, J.A., Sedwick, P.N., German, C.R., Jenkins, W.J., Moffett, J.W., Sohst, B.M., Tagliabue, A., 2015. Basin-scale transport of hydrothermal dissolved metals across the South Pacific Ocean. Nature 523, 200.

Rona, P.A., Bogdanov, Y.A., Gurvich, E.G., Rimski-Korsakov, N.A., Sagalevitch, A.M., Hannington, M.D., Thompson, G., 1993. Relict hydrothermal zones in the TAG Hydrothermal Field, Mid-Atlantic Ridge 26°N, 45°W. Journal of Geophysical Research: Solid Earth 98, 9715-9730.

Rowland, G.H., Ng, H.C., Robinson, L.F., McManus, J.F., Mohamed, K.J., McGee, D., 2017. Investigating the use of ^{232}Th/^{230}Th as a dust proxy using co-located seawater and sediment samples from the low-latitude North Atlantic. Geochimica et Cosmochimica Acta 214, 143-156.

Ruddiman, W.F., 1997. Tropical Atlantic terrigenous fluxes since 25,000 yrs BP. Marine Geology 136, 189-207.

Saito, M.A., Noble, A.E., Tagliabue, A., Goepfert, T.J., Lamborg, C.H., Jenkins, W.J., 2013. Slow-spreading submarine ridges in the South Atlantic as a significant oceanic iron source. Nature Geoscience 6, 775.

Sandnes, J., Forbes, T., Hansen, R., Sandnes, B., Rygg, B., 2000. Bioturbation and irrigation in natural sediments, described by animal-community parameters. Marine Ecology Progress Series, 169-179.

Schoepfer, S.D., Shen, J., Wei, H., Tyson, R.V., Ingall, E., Algeo, T.J., 2015. Total organic carbon, organic phosphorus, and biogenic barium fluxes as proxies for paleomarine productivity. Earth-Science Reviews 149, 23-52.

Seewald, J.S., Seyfried, W.E., 1990. The effect of temperature on metal mobility in subseafloor hydrothermal systems: constraints from basalt alteration experiments. Earth and Planetary Science Letters 101, 388-403.

Smethie, W., Nittrouer, C., Self, R., 1981. The use of radon-222 as a tracer of sediment irrigation and mixing on the Washington continental shelf. Marine Geology 42, 173-200.

Stakes, D.S., Perfit, M.R., Tivey, M.A., Caress, D.W., Ramirez, T.M., Maher, N., 2006. The Cleft revealed: Geologic, magnetic, and morphologic evidence for construction of upper oceanic crust along the southern Juan de Fuca Ridge. Geochemistry, Geophysics, Geosystems 7.

Stuart, F., Turner, G., Duckworth, R.C., Fallick, A., 1994. Helium isotopes as tracers of trapped hydrothermal fluids in ocean-floor sulfides. Geology 22, 823-826.

Suman, D.O., Bacon, M.P., 1989. Variations in Holocene sedimentation in the North American basin determined from ^{230}Th measurements. Deep Sea Research Part A. Oceanographic Research Papers 36, 869-878.

Tagliabue, A., Bopp, L., Dutay, J.-C., Bowie, A.R., Chever, F., Jean-Baptiste, P., Bucciarelli, E., Lannuzel, D., Remenyi, T., Sarthou, G., 2010. Hydrothermal contribution to the oceanic dissolved iron inventory. Nature Geoscience 3, 252.

Takayanagi, M., Ozima, M., 1987. Temporal variation of ^{3}He/^{4}He ratio recorded in deep-sea sediment cores. Journal of Geophysical Research: Solid Earth 92, 12531-12538.

Taylor, S.R., McLennan, S.M., 1995. The geochemical evolution of the continental crust. Reviews of Geophysics 33, 241-265.

Theiler, J., Eubank, S., Longtin, A., Galdrikian, B., Farmer, J.D., 1992. Testing for nonlinearity in time series: the method of surrogate data. Physica D: Nonlinear Phenomena 58, 77-94.

Tivey, M.A., Johnson, H.P., 1990. The magnetic structure of Axial Seamount, Juan de Fuca Ridge. Journal of Geophysical Research: Solid Earth 95, 12735-12750.

Tolstoy, M., 2015. Mid-ocean ridge eruptions as a climate valve. Geophysical Research Letters 42, 1346-1351.

Tolstoy, M., 2016. Comment on "Sensitivity of seafloor bathymetry to climate-driven fluctuations in mid-ocean ridge magma supply". Science 80, 229b.

Toner, B.M., Fakra, S.C., Manganini, S.J., Santelli, C.M., Marcus, M.A., Moffett, J.W., Rouxel, O., German, C.R., Edwards, K.J., 2009. Preservation of iron (II) by carbon-rich matrices in a hydrothermal plume. Nature Geoscience 2, 197.

Von Damm, K., 1995. Controls on the chemistry and temporal variability of seafloor hydrothermal fluids. Seafloor hydrothermal systems: physical, chemical, biological, and geological interactions, 222-247.

Von Damm, K., Bray, A., Buttermore, L., Oosting, S., 1998. The geochemical controls on vent fluids from the Lucky Strike vent field, Mid-Atlantic Ridge. Earth and Planetary Science Letters 160, 521-536.

Winckler, G., Anderson, R.F., Fleisher, M.Q., McGee, D., Mahowald, N., 2008. Covariant glacial-interglacial dust fluxes in the equatorial Pacific and Antarctica. Science 320, 93-96.

Winckler, G., Anderson, R.F., Schlosser, P., 2005. Equatorial Pacific productivity and dust flux during the mid-Pleistocene climate transition. Paleoceanography 20.

Appendix A

Supplemental material for Chapter 1

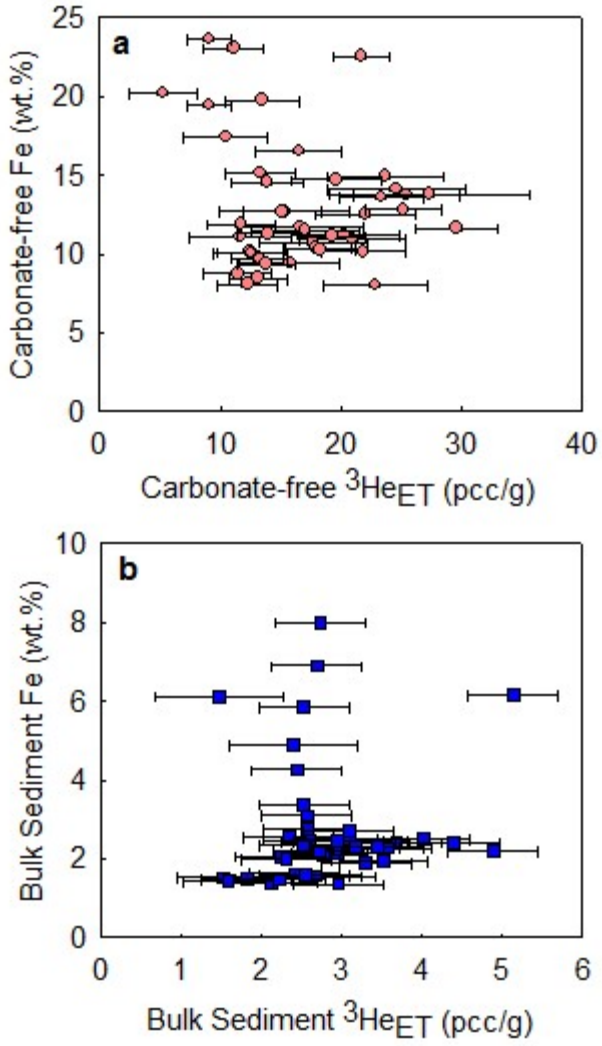

Figure A.1. Mir zone hydrothermal Fe vs. $^3He_{ET}$ for GGC3 carbonate-free sediments (a) and bulk sediments (b). Note that there is no correlation between high Fe contents (indicative of increased hydrothermal contribution) and high $^3He_{ET}$, suggesting no significant vent-fluid ^3He contamination of the $^3He_{ET}$ signal.

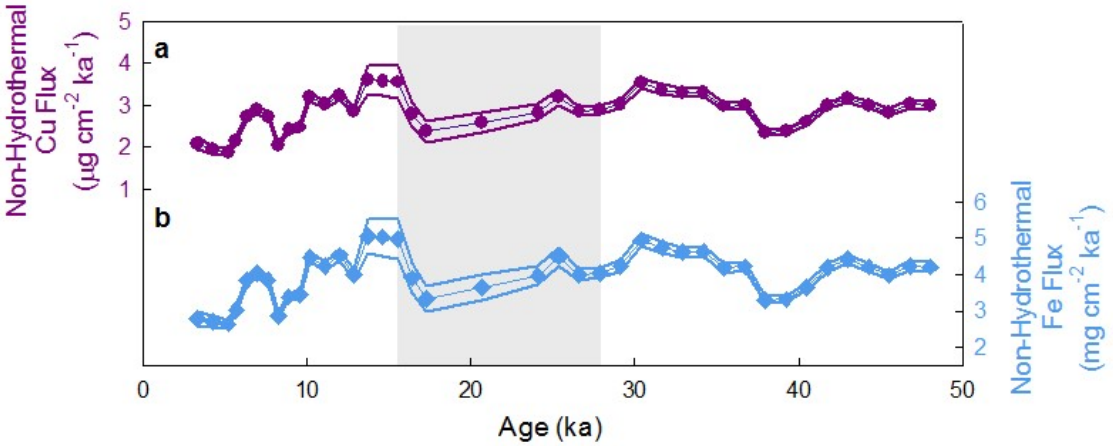

Figure A.2. Mir zone (GGC3) non-hydrothermal fluxes. 3-point running mean fluxes (points) of non-hydrothermal Cu (a) and Fe (b) within 1σ uncertainty envelope (solid lines). Gray bar highlights the interval of the LGM-hydrothermal peak.

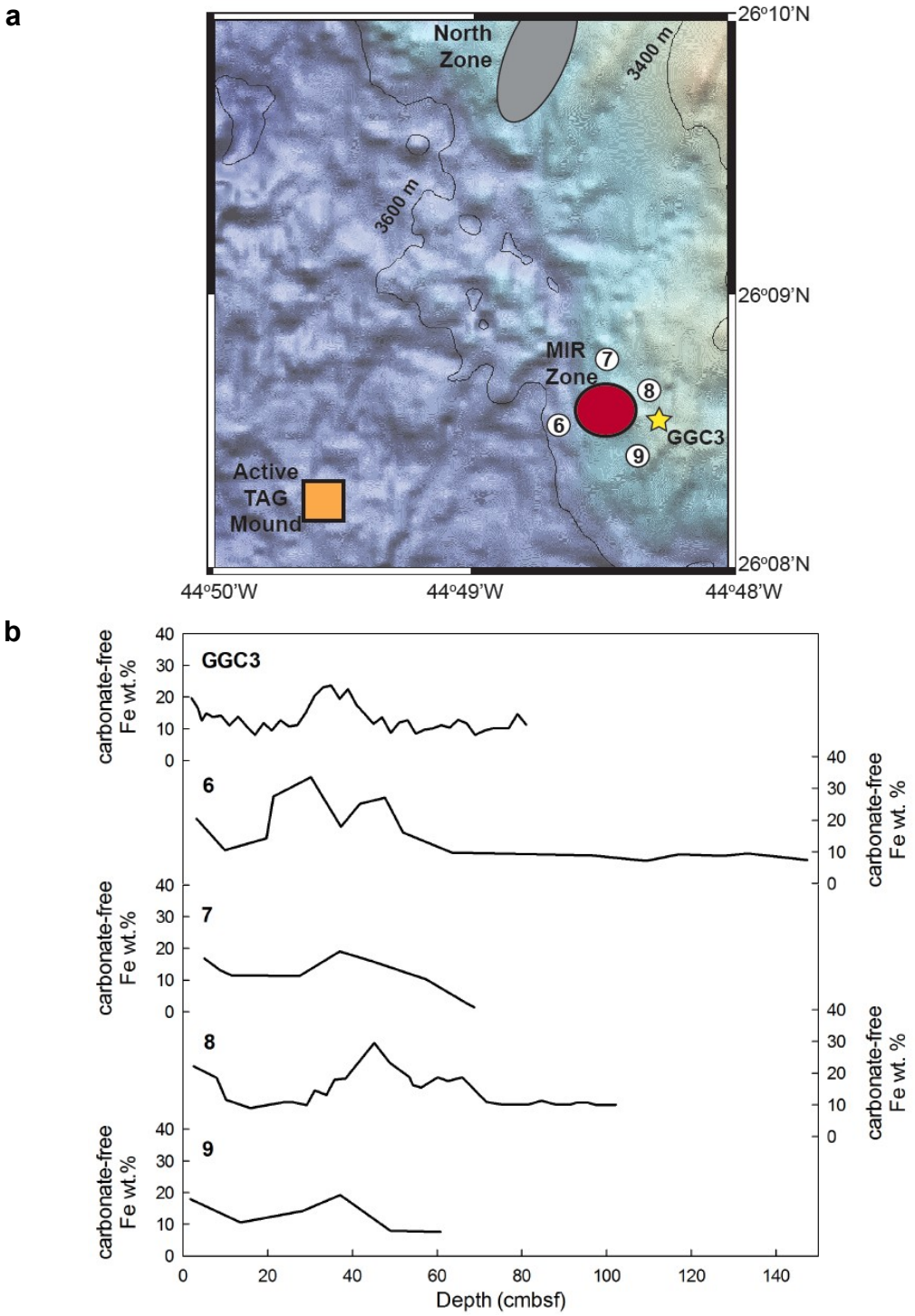

Figure A.3. (a) Location of KN207-2-GGC3 (yellow star) and neighboring Mir zone sediment cores of Cherkashev (1995; numbered circles). (b) Carbonate-free Fe contents of GGC3 and the Cherkashev cores are plotted as a function of depth, due to the lack of age control on the Cherkashev cores. Similarities in Fe deposition between cores from all sides of the Mir zone suggest that the hydrothermal Fe peaks were caused by net increases in hydrothermal plume flux, rather than variations in plume directionality.

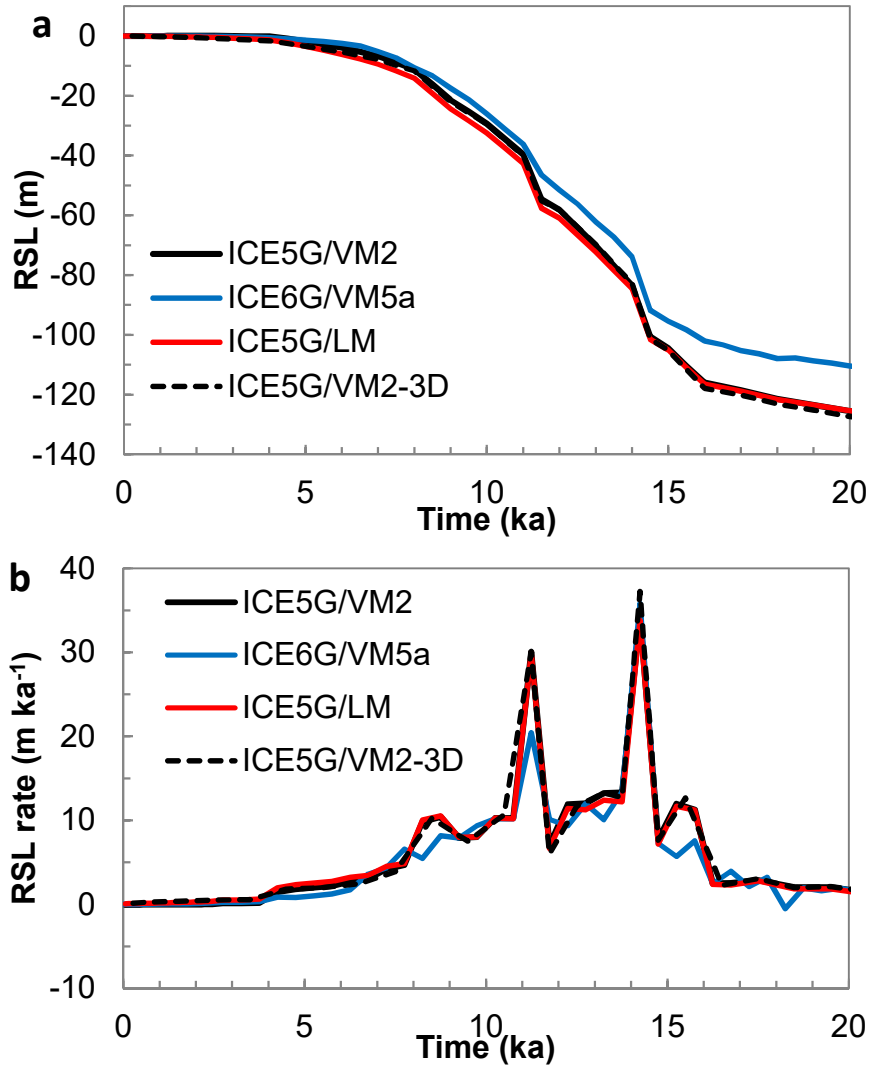

Figure A.4. Relative sea-level prediction sensitivity. a, Predictions of relative sea-level (RSL) change and b, its rate above the TAG vent field on the Mid-Atlantic Ridge since 20 ka. The solid black lines are computed using the ICE-5G ice history and the VM2 mantle viscosity model (Peltier, 2004), as in the bottom frames of main text Figure 1.3. Blue lines, ICE-6G ice history and the VM5a viscosity model (Peltier et al., 2015). Red lines, ICE-5G ice history and a viscosity model (LM) within the class of models favored in a suite of studies (e.g., Nakada and Lambeck, 1989; Mitrovica and Forte, 2004). The LM model is characterized by an elastic lithosphere of thickness 95 km, an upper mantle viscosity of 5 x 10^{20} Pa·s and a lower mantle viscosity of 5 x 10^{21} Pa·s. The dotted black line is the same as the solid black line, except that 3-D variations in mantle viscosity and lithospheric thickness, including plate boundaries, are included in the calculation (e.g., Kendall et al., 2006). This line is indistinguishable from the solid black line in b. The figure demonstrates that the main features of the relative sea-level prediction in Figure 1.3 are insensitive to the details of ice history and Earth structure.

Table A.1: Compiled Isotopic Data and ICP-MS Results

Bulk sediment values

Sample Interval (cm)	Avg. Depth (cm)	Age (ka)[a]	$\delta^{18}O$ (‰)[b]	1σ[b]	$^4He_{terr}$ (ncc/g)[c]	1σ[c]	$^3He_{ET}$ (pcc/g)[c]	1σ[c]	ICP Sample Mass (g)	$CaCO_3$ (wt.%)[d]	1σ
KN207-2-GGC3											
3:1-3	2	1.9	2.49	0.24	461	3	2.45	0.46	0.1442	82	0.8
3:3-4	3.5	3.3	2.73	0.24	458	3	2.58	0.46	0.1603	84	0.8
3:4-5	4.5	4.3	2.64	0.24	439	4	2.95	0.66	0.1751	87	0.9
3:5-6	5.5	5.2	2.59	0.24	424	3	2.78	0.46	0.1836	88	0.9
3:6-8	7	5.7	2.63	0.14	407	3	3.31	0.46	0.2039	87	0.9
3:8-10	9	6.3	-	-	436	3	2.42	0.46	0.2094	90	0.9
3:10-12	11	7.0	2.60	0.24	485	3	1.53	0.46	0.2132	87	0.9
3:12-14	13	7.6	2.60	0.17	530	4	2.60	0.46	0.2113	90	0.9
3:14-16	15	8.3	2.72	0.24	561	4	2.69	0.46	0.1969	87	0.9
3:16-18	17	8.9	3.20	0.24	665	5	2.97	0.46	0.2026	87	0.9
3:18-20	19	9.6	3.58	0.24	689	7	1.83	0.66	0.1821	89	0.9
3:20-22	21	10.2	2.92	0.24	682	5	2.14	0.46	0.1811	87	0.9
3:22-24	23	11.1	3.62	0.24	707	5	1.59	0.46	0.1812	90	0.9
3:24-26	25	12.0	3.76	0.17	729	5	2.24	0.46	0.1754	87	0.9
3:26-28	27	12.9	3.67	0.24	733	5	2.56	0.46	0.1547	88	0.9
3:28-30	29	13.8	3.66	0.24	736	5	2.54	0.46	0.1185	81	0.8
3:30-32	31	14.6	3.82	0.24	754	8	1.46	0.66	0.0800	72	0.7
3:32-34	33	15.5	3.90	0.24	657	5	2.54	0.46	0.0947	77	0.8
3:34-36	35	16.4	4.32	0.17	683	5	2.74	0.46	0.0773	70	0.7
3:36-38	37	17.3	4.15	0.24	619	4	2.70	0.46	0.0778	70	0.7
3:38-40	39	20.7	3.93	0.17	860	6	5.15	0.46	0.0774	76	0.8
3:40-42	41	24.1	3.85	0.24	826	8	2.41	0.66	0.0794	77	0.8
3:42-44	43	25.4	4.16	0.24	836	6	2.58	0.46	0.1089	82	0.8
3:44-46	45	26.6	4.26	0.24	815	6	2.96	0.46	0.1149	82	0.8
3:46-48	47	27.9	4.06	0.17	794	6	3.70	0.46	0.1184	84	0.8
3:48-50	49	29.1	3.94	0.17	776	5	2.26	0.46	0.1231	80	0.8
3:50-52	51	30.4	3.71	0.24	645	5	2.35	0.46	0.1161	80	0.8
3:52-54	53	31.7	3.59	0.24	655	5	2.61	0.46	0.1004	83	0.8
3:54-56	55	32.9	4.01	0.24	643	5	3.10	0.46	0.1198	77	0.8
3:56-58	57	34.2	3.73	0.24	580	4	3.11	0.46	0.1132	77	0.8
3:58-60	59	35.4	3.95	0.17	558	6	2.54	0.66	0.1112	80	0.8
3:60-62	61	36.7	3.98	0.24	511	4	4.03	0.46	0.1251	79	0.8
3:62-64	63	38.0	3.83	0.24	516	4	3.58	0.46	0.1385	80	0.8
3:64-66	65	39.2	3.60	0.24	524	4	4.41	0.46	0.1241	83	0.8
3:66-68	67	40.5	3.96	0.17	589	4	4.90	0.46	0.1336	84	0.8
3:68-70	69	41.7	3.97	0.24	588	4	2.72	0.46	0.1335	78	0.8
3:70-72	71	43.0	3.81	0.24	615	4	3.18	0.46	0.1228	77	0.8
3:72-74	73	44.3	3.75	0.17	646	5	3.53	0.46	0.1347	84	0.8
3:74-76	75	45.5	3.75	0.24	499	4	2.32	0.46	0.1440	82	0.8
3:76-78	77	46.8	3.81	0.17	594	4	3.46	0.46	0.1273	81	0.8
3:78-80	79	48.0	3.70	0.17	677	5	2.96	0.46	0.1136	85	0.9
3:80-82	81	49.3	3.80	0.17	796	6	3.11	0.46	0.0974	78	0.8

Table A.1 (continued): Compiled Isotopic Data and ICP-MS Results

$CaCO_3$ leachate composition[e]									$CaCO_3$-free composition[f]		
Sample Interval (cm)	**Fe (wt. %)**	**1σ**	**Ti (wt. %)**	**1σ**	**Cu (ppm)**	**1σ**	**Th (ppm)**	**1σ**	**$CaCO_3$-free Mass (g)**	**Fe (wt.%)**	**1σ**
KN207-2-GGC3											
3:1-3	0.844	0.009	0.029	0.006	1737	51	0.157	0.009	0.0260	19.8	0.2
3:3-4	0.229	0.002	0.003	0.001	763	23	0.274	0.016	0.0249	16.5	0.2
3:4-5	0.553	0.006	0.017	0.004	410	12	0.164	0.010	0.0233	12.5	0.1
3:5-6	0.395	0.004	0.020	0.004	419	12	0.218	0.013	0.0214	14.9	0.2
3:6-8	0.143	0.001	0.019	0.004	254	8	0.168	0.010	0.0264	13.8	0.1
3:8-10	0.263	0.003	0.030	0.006	161	5	0.174	0.010	0.0205	14.1	0.1
3:10-12	0.084	0.001	0.019	0.004	120	4	0.108	0.006	0.0278	11.1	0.1
3:12-14	0.253	0.003	0.019	0.004	105	3	0.168	0.010	0.0203	13.8	0.1
3:14-16	0.198	0.002	0.019	0.004	106	3	0.275	0.016	0.0251	11.0	0.1
3:16-18	0.369	0.004	0.017	0.003	87	3	0.283	0.016	0.0261	8.0	0.1
3:18-20	0.235	0.002	0.018	0.004	72	2	0.271	0.016	0.0198	11.7	0.1
3:20-22	0.151	0.002	0.004	0.001	83	2	0.548	0.032	0.0244	9.4	0.1
3:22-24	0.138	0.001	0.018	0.004	81	2	0.247	0.014	0.0187	12.7	0.1
3:24-26	0.171	0.002	0.018	0.004	92	3	0.255	0.015	0.0220	10.8	0.1
3:26-28	0.202	0.002	0.040	0.008	138	4	0.392	0.023	0.0193	11.2	0.1
3:28-30	0.632	0.006	0.020	0.004	539	16	0.354	0.021	0.0225	15.1	0.2
3:30-32	0.713	0.007	0.019	0.004	926	27	0.241	0.014	0.0222	20.2	0.2
3:32-34	0.788	0.008	0.029	0.006	1264	37	0.256	0.015	0.0216	23.1	0.2
3:34-36	1.285	0.013	0.029	0.006	2658	79	0.202	0.012	0.0234	23.6	0.2
3:36-38	1.630	0.017	0.018	0.004	2586	77	0.276	0.016	0.0230	19.4	0.2
3:38-40	1.093	0.011	0.019	0.004	2059	61	0.335	0.019	0.0183	22.6	0.2
3:40-42	1.195	0.012	0.017	0.004	1172	35	0.347	0.020	0.0181	17.4	0.2
3:42-44	0.494	0.005	0.019	0.004	590	17	0.428	0.025	0.0201	14.6	0.1
3:44-46	0.496	0.005	0.020	0.004	396	12	0.596	0.035	0.0204	11.5	0.1
3:46-48	0.326	0.003	0.019	0.004	274	8	0.445	0.026	0.0187	13.6	0.1
3:48-50	0.437	0.004	0.021	0.004	216	6	0.584	0.034	0.0241	8.8	0.1
3:50-52	0.243	0.002	0.002	0.000	150	4	0.610	0.035	0.0231	11.9	0.1
3:52-54	0.350	0.004	0.018	0.004	93	3	0.475	0.028	0.0172	12.7	0.1
3:54-56	0.405	0.004	0.020	0.004	99	3	0.571	0.033	0.0281	8.5	0.1
3:56-58	0.256	0.003	0.002	0.000	76	2	0.608	0.035	0.0265	9.7	0.1
3:58-60	0.393	0.004	0.021	0.004	73	2	0.486	0.028	0.0225	10.1	0.1
3:60-62	0.234	0.002	0.003	0.001	66	2	0.539	0.031	0.0260	11.2	0.1
3:62-64	0.274	0.003	0.041	0.009	70	2	0.464	0.027	0.0274	10.4	0.1
3:64-66	0.207	0.002	0.003	0.001	54	2	0.526	0.031	0.0216	12.8	0.1
3:66-68	0.316	0.003	0.031	0.006	53	2	0.458	0.027	0.0220	11.6	0.1
3:68-70	0.524	0.005	0.017	0.004	36	1	0.422	0.025	0.0295	8.1	0.1
3:70-72	0.214	0.002	0.003	0.001	37	1	0.618	0.036	0.0282	9.4	0.1
3:72-74	0.354	0.004	0.027	0.006	41	1	0.279	0.016	0.0216	10.2	0.1
3:74-76	0.174	0.002	0.004	0.001	40	1	0.534	0.031	0.0265	10.1	0.1
3:76-78	0.445	0.005	0.029	0.006	50	1	0.360	0.021	0.0239	10.3	0.1
3:78-80	0.288	0.003	0.019	0.004	35	1	0.220	0.013	0.0170	14.7	0.1
3:80-82	0.234	0.002	0.002	0.000	46	1	0.769	0.045	0.0216	11.3	0.1

Table A.1 (continued): Compiled Isotopic Data and ICP-MS Results

$CaCO_3$-free composition continued[f]

Sample Interval (cm)	Ti (wt.%)	1σ	Cu (ppm)	1σ	Th (ppm)	1σ	Mg/Th[g]	1σ	Mg/Rb[g]	1σ	f_{basalt} (%)[h]
KN207-2-GGC3											
3:1-3	0.41	0.09	4373	130	10.3	0.6	0.14	0.01	0.026	0.001	1.0
3:3-4	0.47	0.10	3171	94	11.7	0.7	0.16	0.01	0.027	0.002	1.1
3:4-5	0.52	0.11	2851	84	12.8	0.7	0.12	0.01	0.020	0.001	0.8
3:5-6	0.63	0.13	2687	80	14.8	0.9	0.13	0.01	0.022	0.001	0.9
3:6-8	0.57	0.12	1856	55	13.0	0.8	0.15	0.01	0.028	0.002	1.1
3:8-10	0.73	0.15	1626	48	17.0	1.0	0.13	0.01	0.024	0.001	0.9
3:10-12	0.57	0.12	1151	34	14.2	0.8	0.13	0.01	0.025	0.001	1.0
3:12-14	0.76	0.16	1323	39	19.6	1.1	0.13	0.01	0.024	0.001	0.9
3:14-16	0.59	0.12	1039	31	16.0	0.9	0.13	0.01	0.022	0.001	0.9
3:16-18	0.51	0.11	955	28	16.1	0.9	0.10	0.01	0.016	0.001	0.6
3:18-20	0.72	0.15	954	28	21.3	1.2	0.11	0.01	0.019	0.001	0.7
3:20-22	0.55	0.12	763	23	15.7	0.9	0.13	0.01	0.019	0.001	0.8
3:22-24	0.77	0.16	1098	33	23.4	1.4	0.11	0.01	0.018	0.001	0.7
3:24-26	0.65	0.14	1052	31	18.9	1.1	0.12	0.01	0.019	0.001	0.8
3:26-28	0.67	0.14	1353	40	19.5	1.1	0.10	0.01	0.016	0.001	0.6
3:28-30	0.49	0.10	3002	89	13.4	0.8	0.12	0.01	0.018	0.001	0.7
3:30-32	0.37	0.08	4668	138	9.4	0.5	0.18	0.01	0.026	0.001	1.0
3:32-34	0.40	0.08	6047	179	11.0	0.6	0.18	0.01	0.026	0.002	1.0
3:34-36	0.31	0.06	7096	210	7.7	0.4	0.21	0.02	0.029	0.002	1.1
3:36-38	0.35	0.07	6336	188	9.3	0.5	0.16	0.01	0.023	0.001	0.9
3:38-40	0.51	0.11	6780	201	12.8	0.7	0.19	0.02	0.025	0.001	1.0
3:40-42	0.49	0.10	5747	170	12.6	0.7	0.17	0.01	0.024	0.001	0.9
3:42-44	0.68	0.14	3563	106	14.2	0.8	0.20	0.02	0.027	0.002	1.1
3:44-46	0.64	0.14	2211	66	14.2	0.8	0.18	0.01	0.024	0.001	0.9
3:46-48	0.73	0.15	2031	60	15.6	0.9	0.22	0.02	0.030	0.002	1.2
3:48-50	0.56	0.12	1099	33	11.5	0.7	0.21	0.02	0.028	0.002	1.1
3:50-52	0.57	0.12	1100	33	10.7	0.6	0.34	0.03	0.047	0.003	1.8
3:52-54	0.82	0.17	971	29	13.0	0.8	0.34	0.03	0.049	0.003	1.9
3:54-56	0.58	0.12	593	18	8.6	0.5	0.40	0.03	0.054	0.003	2.1
3:56-58	0.59	0.12	590	17	8.2	0.5	0.49	0.04	0.065	0.004	2.6
3:58-60	0.68	0.14	614	18	8.4	0.5	0.53	0.04	0.070	0.004	2.8
3:60-62	0.64	0.13	679	20	8.5	0.5	0.51	0.04	0.068	0.004	2.7
3:62-64	0.68	0.14	720	21	8.9	0.5	0.42	0.03	0.058	0.003	2.3
3:64-66	0.75	0.16	784	23	10.9	0.6	0.39	0.03	0.053	0.003	2.1
3:66-68	0.86	0.18	730	22	12.1	0.7	0.28	0.02	0.039	0.002	1.5
3:68-70	0.65	0.14	527	16	9.6	0.6	0.26	0.02	0.036	0.002	1.4
3:70-72	0.66	0.14	490	15	8.9	0.5	0.31	0.03	0.041	0.002	1.6
3:72-74	0.78	0.16	527	16	12.8	0.7	0.24	0.02	0.035	0.002	1.4
3:74-76	0.61	0.13	530	16	9.9	0.6	0.32	0.03	0.044	0.003	1.7
3:76-78	0.63	0.13	630	19	11.9	0.7	0.23	0.02	0.032	0.002	1.3
3:78-80	0.89	0.19	798	24	16.3	0.9	0.26	0.02	0.035	0.002	1.4
3:80-82	0.67	0.14	531	16	12.2	0.7	0.31	0.03	0.040	0.002	1.6

Table A.1 (continued): Compiled Isotopic Data and ICP-MS Results

[a]Age model was calculated using a constant sedimentation rate through radiocarbon tie points (Table A.5)
[b]Reported $\delta^{18}O$ values reflect average of all replicates for each depth, using a 0.24‰ 1σ uncertainty for single analyses based on the reproducibility of replicated samples (Table A.4)
[c]Reported helium values reflect average of all replicates for each depth, 1σ values reflect uncertainty based on the reproducibility of replicated samples (Table A.2), cc's refer to cm^3 of gas at standard temperature and pressure (STP) of 273K and 1 atm.
[d]Carbonate content was calculated from the initial ICP-MS bulk sediment mass and the dry carbonate-free sediment mass following an acetic acid leach
[e]Elemental concentrations reflect ICP-MS values for the acetic acid leachate, 1σ uncertainties are determined from the long-term reproducibility of internal standard K1919
[f]Elemental concentrations reflect ICP-MS values for residual sediment after the acetic acid leach, 1σ uncertainties are determined from the long-term reproducibility of internal standard K1919
[g]Mg/Th and Mg/Rb ratios were calculated from ICP-MS measurements of the residual sediment after the acetic acid leach, units are wt%/ppm
[h]Reported f_{basalt} values were calculated assuming two component mixing between an extreme zero-Mg end-member and mid-ocean ridge basalt with Mg/Rb = 2.54 wt.% / ppm

Table A.2: Sediment Helium Analyses

Sample Interval (cm)[a]	Mass (g)	^{4}He total (ncc/g)[b]	1σ[c]	^{3}He/^{4}He (R_A)[d]	1σ[c]	$^4He_{terr}$ (ncc/g)[b,e]	1σ[f]	$^3He_{ET}$ (pcc/g)[b,e]	1σ[f]
Core: KN207-2-GGC3									
3:01-03	1.51	471	5	3.34	0.07	462	5	2.20	0.04
3:01-03A	1.50	472	5	4.08	0.08	461	5	2.70	0.05
3:03-04	1.51	468	5	3.71	0.07	458	5	2.43	0.05
3:03-04A	1.50	470	5	4.15	0.08	458	5	2.73	0.05
3:04-05	1.50	452	5	4.66	0.09	439	4	2.95	0.06
3:05-06	1.50	437	4	5.57	0.11	423	4	3.41	0.07
3:05-06A	1.50	435	4	3.54	0.07	426	4	2.15	0.04
3:06-08	1.51	414	4	4.07	0.08	404	4	2.36	0.05
3:06-08A	1.50	427	4	7.13	0.14	409	4	4.26	0.09
3:08-10	1.50	449	4	4.06	0.08	438	4	2.55	0.05
3:08-10A	1.50	443	4	3.71	0.07	433	4	2.30	0.05
3:10-12	1.50	498	5	2.41	0.05	491	5	1.68	0.03
3:10-12A	1.51	485	5	2.04	0.04	479	5	1.38	0.03
3:12-14	1.50	536	5	3.52	0.07	525	5	2.64	0.05
3:12-14A	1.50	546	5	3.36	0.07	535	5	2.56	0.05
3:14-16	1.50	516	5	2.27	0.05	509	5	1.64	0.03
3:14-16A	1.51	629	6	4.25	0.09	613	6	3.74	0.07
3:16-18	1.50	676	7	2.78	0.06	665	7	2.63	0.05
3:16-18A	1.51	679	7	3.48	0.07	665	7	3.30	0.07
3:18-20	1.50	696	7	1.87	0.04	689	7	1.83	0.04
3:20-22	1.50	688	7	1.80	0.04	681	7	1.73	0.03
3:20-22A	1.51	695	7	2.62	0.05	684	7	2.55	0.05
3:22-24	1.51	719	7	1.52	0.03	713	7	1.52	0.03
3:22-24A	1.49	707	7	1.68	0.03	700	7	1.67	0.03
3:24-26	1.50	737	7	2.18	0.04	728	7	2.25	0.04
3:24-26A	1.50	739	7	2.16	0.04	730	7	2.23	0.04
3:26-28	1.50	730	7	2.42	0.05	719	7	2.47	0.05
3:26-28A	1.51	757	8	2.49	0.05	746	7	2.64	0.05
3:28-30	1.50	750	7	2.13	0.04	740	7	2.24	0.04
3:28-30A	1.51	743	7	2.73	0.05	732	7	2.84	0.06
3:30-32	1.51	760	8	1.38	0.03	754	8	1.46	0.03
3:32-34	1.51	580	6	2.50	0.05	571	6	2.03	0.04
3:32-34A	1.51	756	8	2.88	0.06	743	7	3.05	0.06
3:34-36	1.51	646	6	3.38	0.07	633	6	3.05	0.06
3:34-36A	1.51	744	7	2.34	0.05	734	7	2.43	0.05
3:36-38	1.51	506	5	4.37	0.09	493	5	3.10	0.06
3:36-38A	1.51	754	8	2.18	0.04	745	7	2.29	0.05
3:38-40	1.50	831	8	2.49	0.05	819	8	2.90	0.06
3:38-40A	1.50	931	9	5.69	0.11	900	9	7.41	0.15
3:40-42	1.50	836	8	2.06	0.04	826	8	2.41	0.05
3:42-44	1.50	851	9	2.19	0.04	840	8	2.60	0.05
3:42-44A	1.50	842	8	2.18	0.04	831	8	2.57	0.05

Table A.2 (continued): Sediment Helium Analyses

Sample Interval (cm)[a]	Mass (g)	^{4}He total (ncc/g)[b]	1σ[c]	^{3}He/^{4}He (R_A)[d]	1σ[c]	$^4He_{terr}$ (ncc/g)[b,e]	1σ[f]	$^3He_{ET}$ (pcc/g)[b,e]	1σ[f]
Core: KN207-2-GGC3 (continued)									
3:44-46	1.50	842	8	2.59	0.05	829	8	3.05	0.06
3:44-46A	1.50	814	8	2.53	0.05	802	8	2.88	0.06
3:46-48	1.50	821	8	3.79	0.08	803	8	4.36	0.09
3:46-48A	1.50	797	8	2.73	0.05	784	8	3.04	0.06
3:48-50	1.49	785	8	2.13	0.04	775	8	2.34	0.05
3:48-50A	1.50	787	8	1.98	0.04	778	8	2.18	0.04
3:50-52	1.50	660	7	2.66	0.05	650	6	2.46	0.05
3:50-52A	1.50	650	7	2.47	0.05	641	6	2.25	0.04
3:52-54	1.50	669	7	2.52	0.05	659	7	2.35	0.05
3:52-54A	1.50	663	7	3.08	0.06	651	7	2.86	0.06
3:54-56	1.50	655	7	4.04	0.08	640	6	3.70	0.07
3:54-56A	1.50	657	7	2.71	0.05	647	6	2.49	0.05
3:56-58	1.51	590	6	3.94	0.08	577	6	3.26	0.07
3:56-58A	1.50	595	6	3.57	0.07	583	6	2.97	0.06
3:58-60	1.50	569	6	3.19	0.06	558	6	2.54	0.05
3:60-62	1.49	524	5	6.05	0.12	506	5	4.44	0.09
3:60-62A	1.50	532	5	4.86	0.10	517	5	3.62	0.07
3:62-64	1.50	517	5	3.12	0.06	508	5	2.26	0.05
3:62-64A	1.51	544	5	6.43	0.13	524	5	4.89	0.10
3:64-66	1.50	542	5	5.70	0.11	524	5	4.32	0.09
3:64-66A	1.51	543	5	5.92	0.12	524	5	4.49	0.09
3:66-68	1.51	612	6	7.04	0.14	587	6	6.04	0.12
3:66-68A	1.51	607	6	4.43	0.09	591	6	3.76	0.08
3:68-70	1.50	599	6	3.09	0.06	588	6	2.59	0.05
3:68-70A	1.50	600	6	3.40	0.07	588	6	2.85	0.06
3:70-72	1.50	637	6	2.88	0.06	627	6	2.56	0.05
3:70-72A	1.49	620	6	4.38	0.09	604	6	3.80	0.08
3:72-74	1.50	629	6	4.16	0.08	614	6	3.66	0.07
3:72-74A	1.51	692	7	3.52	0.07	678	7	3.40	0.07
3:74-76	1.49	503	5	3.10	0.06	494	5	2.18	0.04
3:74-76A	1.49	514	5	3.41	0.07	504	5	2.45	0.05
3:76-78	1.50	619	6	4.71	0.09	602	6	4.08	0.08
3:76-78A	1.50	597	6	3.40	0.07	585	6	2.84	0.06
3:78-80	1.50	686	7	3.83	0.08	671	7	3.67	0.07
3:78-80A	1.50	692	7	2.32	0.05	683	7	2.24	0.04
3:80-82	1.51	813	8	2.96	0.06	799	8	3.36	0.07
3:80-82A	1.50	806	8	2.53	0.05	794	8	2.86	0.06

Table A.2 (continued): Sediment Helium Analyses

Sample Interval (cm)[a]	Mass (g)	^{4}He total (ncc/g)[b]	1σ[c]	^{3}He/^{4}He (R_A)[d]	1σ[c]	$^4He_{terr}$ (ncc/g)[b,e]	1σ[f]	$^3He_{ET}$ (pcc/g)[b,e]	1σ[f]
Core: KN207-2-GGC6									
6:00-02	1.51	427	4	4.33	0.09	417	4	2.59	0.05
6:00-02A	1.51	429	4	2.93	0.06	422	4	1.76	0.04
6:00-02B	1.50	422	4	3.97	0.08	413	4	2.34	0.05
6:00-02C	1.51	343	3	2.58	0.05	338	3	1.24	0.02
6:02-04	1.50	466	5	2.28	0.05	460	5	1.48	0.03
6:02-04A	1.50	468	5	2.27	0.05	462	5	1.48	0.03
6:04-06	1.50	485	5	3.02	0.06	477	5	2.05	0.04
6:04-06A	1.51	484	5	2.49	0.05	477	5	1.68	0.03
6:06-08	1.50	109	1	4.68	0.09	106	1	0.72	0.01
6:06-08A	1.50	112	1	4.43	0.09	109	1	0.70	0.01
6:08-10	1.50	230	2	5.87	0.12	222	2	1.89	0.04
6:08-10A	1.49	223	2	5.77	0.12	216	2	1.80	0.04
6:10-12	1.51	224	2	6.68	0.13	215	2	2.10	0.04
6:10-12A	1.50	230	2	11.44	0.23	215	2	3.68	0.07
6:10-12B	1.50	231	2	6.55	0.13	222	2	2.12	0.04
6:10-12C	1.50	228	2	4.19	0.08	222	2	1.34	0.03
6:12-14	1.51	196	2	6.48	0.13	188	2	1.77	0.04
6:12-14A	1.50	195	2	7.59	0.15	186	2	2.07	0.04
6:14-16	1.50	254	3	7.04	0.14	244	2	2.50	0.05
6:14-16A	1.51	247	2	5.18	0.10	240	2	1.79	0.04
6:14-16B	1.50	247	2	3.77	0.08	242	2	1.30	0.03
6:14-16C	1.51	246	2	4.65	0.09	239	2	1.60	0.03
6:16-18	1.50	318	3	3.04	0.06	313	3	1.35	0.03
6:16-18A	1.50	319	3	3.76	0.08	312	3	1.68	0.03
6:16-18B	1.51	322	3	2.52	0.05	317	3	1.14	0.02
6:16-18C	1.50	321	3	8.69	0.17	305	3	3.91	0.08
6:18-20	1.50	367	4	2.62	0.05	362	4	1.35	0.03
6:18-20A	1.51	371	4	2.07	0.04	367	4	1.08	0.02
6:20-22	1.51	406	4	4.29	0.09	396	4	2.43	0.05
6:20-22A	1.49	417	4	3.46	0.07	408	4	2.01	0.04
6:20-22B	1.51	413	4	4.89	0.10	401	4	2.82	0.06
6:20-22C	1.50	402	4	2.93	0.06	396	4	1.65	0.03
6:22-24	1.51	463	5	2.21	0.04	457	5	1.43	0.03
6:22-24A	1.51	453	5	1.68	0.03	449	4	1.07	0.02
6:22-24B	1.50	447	4	1.71	0.03	443	4	1.07	0.02
6:22-24C	1.50	458	5	1.48	0.03	454	5	0.95	0.02
6:24-26	1.50	539	5	2.14	0.04	533	5	1.61	0.03
6:24-26A	1.50	494	5	1.66	0.03	489	5	1.15	0.02
6:24-26B	1.50	501	5	2.18	0.04	495	5	1.53	0.03
6:24-26C	1.49	492	5	1.41	0.03	488	5	0.97	0.02
6:26-28	1.50	589	6	1.58	0.03	583	6	1.30	0.03
6:26-28A	1.49	583	6	1.41	0.03	579	6	1.15	0.02

Table A.2 (continued): Sediment Helium Analyses

Sample Interval (cm)[a]	Mass (g)	^{4}He total (ncc/g)[b]	1σ[c]	^{3}He/^{4}He (R_A)[d]	1σ[c]	^{4}He$_{terr}$ (ncc/g)[b,e]	1σ[f]	^{3}He$_{ET}$ (pcc/g)[b,e]	1σ[f]
Core: KN207-2-GGC6 (continued)									
6:28-30	1.49	608	6	5.12	0.10	590	6	4.36	0.09
6:28-30A	1.50	606	6	1.61	0.03	600	6	1.37	0.03
6:30-32	1.50	605	6	2.03	0.04	598	6	1.72	0.03
6:30-32A	1.51	606	6	2.65	0.05	596	6	2.25	0.04
6:32-34	1.51	544	5	1.53	0.03	539	5	1.16	0.02
6:32-34A	1.50	553	6	1.68	0.03	548	5	1.30	0.03
6:34-36	1.50	543	5	3.50	0.07	532	5	2.66	0.05
6:34-36A	1.49	550	6	2.36	0.05	543	5	1.81	0.04
6:34-36B	1.51	542	5	1.66	0.03	537	5	1.26	0.03
6:36-38	1.49	686	7	1.95	0.04	678	7	1.87	0.04
6:36-38A	1.51	691	7	1.19	0.02	686	7	1.15	0.02
6:38-40	1.50	717	7	1.68	0.03	710	7	1.69	0.03
6:38-40A	1.51	733	7	2.27	0.05	723	7	2.32	0.05
6:40-42	1.51	769	8	2.39	0.05	759	8	2.57	0.05
6:40-42A	1.50	750	7	1.97	0.04	741	7	2.07	0.04
6:42-44	1.50	749	7	1.57	0.03	742	7	1.65	0.03
6:42-44A	1.50	744	7	3.21	0.06	730	7	3.34	0.07
6:42-44B	1.51	735	7	2.78	0.06	723	7	2.86	0.06
6:42-44C	1.51	752	8	3.09	0.06	739	7	3.25	0.06
6:44-46	1.49	792	8	1.70	0.03	784	8	1.88	0.04
6:44-46A	1.50	754	8	1.91	0.04	746	7	2.02	0.04
6:46-48	1.50	762	8	1.77	0.04	754	8	1.89	0.04
6:46-48A	1.50	767	8	2.45	0.05	756	8	2.63	0.05
6:48-49	1.50	590	6	2.06	0.04	583	6	1.70	0.03
6:48-49A	1.01	591	6	1.86	0.04	585	6	1.54	0.03
6:48-49B	1.50	607	6	4.68	0.09	590	6	3.97	0.08
6:49-50	1.50	374	4	2.20	0.04	369	4	1.15	0.02
6:49-50A	1.52	359	4	2.21	0.04	354	4	1.11	0.02
6:50-52	1.51	765	8	2.07	0.04	755	8	2.22	0.04
6:50-52A	1.51	741	7	2.85	0.06	729	7	2.96	0.06
6:50-52B	1.50	737	7	3.35	0.07	722	7	3.46	0.07
6:50-52C	1.50	776	8	4.66	0.09	755	8	5.05	0.10
6:52-54	1.50	842	8	1.75	0.03	833	8	2.06	0.04
6:52-54A	1.50	883	9	1.75	0.03	874	9	2.16	0.04
6:54-56	1.51	846	8	2.21	0.04	835	8	2.61	0.05
6:54-56A	1.49	843	8	1.93	0.04	833	8	2.27	0.05
6:56-58	1.51	773	8	2.11	0.04	764	8	2.28	0.05
6:56-58A	1.49	774	8	2.02	0.04	765	8	2.19	0.04
6:58-60	1.50	713	7	1.52	0.03	707	7	1.52	0.03
6:58-60A	1.50	707	7	1.45	0.03	701	7	1.43	0.03
6:60-62	1.50	685	7	2.31	0.05	676	7	2.22	0.04
6:60-62A	1.51	663	7	2.80	0.06	652	7	2.59	0.05

Table A.2 (continued): Sediment Helium Analyses

Sample Interval (cm)[a]	Mass (g)	^{4}He total (ncc/g)[b]	1σ[c]	^{3}He/^{4}He (R_A)[d]	1σ[c]	$^4He_{terr}$ (ncc/g)[b,e]	1σ[f]	$^3He_{ET}$ (pcc/g)[b,e]	1σ[f]
Core: KN207-2-GGC6 (continued)									
6:62-64	1.51	614	6	2.05	0.04	607	6	1.76	0.04
6:62-64A	1.50	603	6	3.64	0.07	590	6	3.07	0.06
6:64-66	1.50	576	6	1.56	0.03	571	6	1.26	0.03
6:64-66A	1.50	573	6	2.01	0.04	566	6	1.61	0.03
6:64-66B	1.01	606	6	1.93	0.04	599	6	1.64	0.03
6:64-66C	1.50	581	6	3.04	0.06	570	6	2.47	0.05
6:66-68	1.51	556	6	1.68	0.03	551	6	1.31	0.03
6:66-68A	1.52	540	5	1.34	0.03	536	5	1.01	0.02
6:68-70	1.51	463	5	1.88	0.04	458	5	1.22	0.02
6:68-70A	1.51	448	4	4.69	0.09	436	4	2.94	0.06
6:68-70B	1.50	446	4	1.85	0.04	441	4	1.15	0.02
6:70-71	1.50	396	4	3.74	0.07	388	4	2.07	0.04
6:70-71A	1.00	370	4	1.80	0.04	366	4	0.93	0.02
6:70-71B	1.50	388	4	2.61	0.05	382	4	1.42	0.03
6:70-71C	1.51	407	4	8.10	0.16	388	4	4.62	0.09
6:71-73	1.50	241	2	1.86	0.04	238	2	0.63	0.01
6:71-73A	1.50	229	2	2.11	0.04	227	2	0.68	0.01
6:73-74	1.51	344	3	1.63	0.03	340	3	0.78	0.02
6:74-76	1.50	400	4	2.06	0.04	395	4	1.15	0.02
6:74-76A	1.51	383	4	2.25	0.05	378	4	1.21	0.02
6:76-78	1.50	389	4	2.43	0.05	384	4	1.32	0.03
6:76-78A	1.51	392	4	3.25	0.06	384	4	1.78	0.04
6:78-80	1.50	367	4	2.83	0.06	361	4	1.45	0.03
6:78-80A	1.50	364	4	2.07	0.04	359	4	1.05	0.02
6:80-82	1.50	425	4	3.06	0.06	418	4	1.82	0.04
6:80-82A	1.51	420	4	1.99	0.04	415	4	1.17	0.02
6:80-82B	1.50	424	4	2.74	0.05	417	4	1.63	0.03
6:82-84	1.51	490	5	1.91	0.04	485	5	1.31	0.03
6:82-84A	1.51	484	5	2.90	0.06	476	5	1.96	0.04
6:84-86	1.51	548	5	4.15	0.08	535	5	3.18	0.06
6:84-86A	1.50	533	5	1.67	0.03	528	5	1.24	0.02
6:84-86B	1.50	538	5	2.29	0.05	531	5	1.72	0.03
6:84-86C	1.50	534	5	2.30	0.05	527	5	1.72	0.03
6:86-88	1.51	594	6	1.83	0.04	588	6	1.52	0.03
6:86-88A	1.50	594	6	1.87	0.04	588	6	1.56	0.03
6:88-90	1.49	495	5	1.89	0.04	489	5	1.31	0.03
6:88-90A	1.50	496	5	2.08	0.04	490	5	1.44	0.03
6:90-92	1.48	455	5	2.41	0.05	449	4	1.54	0.03
6:90-92A	1.51	428	4	2.63	0.05	421	4	1.58	0.03
6:92-94	3.01	274	3	2.17	0.04	271	3	0.83	0.02
6:92-94A	3.01	172	2	1.64	0.03	170	2	0.39	0.01
6:92-94B	1.03	458	5	2.77	0.06	450	5	1.77	0.04

Table A.2 (continued): Sediment Helium Analyses

Sample Interval (cm)[a]	Mass (g)	^{4}He total (ncc/g)[b]	1σ[c]	^{3}He/^{4}He (R_A)[d]	1σ[c]	$^4He_{terr}$ (ncc/g)[b,e]	1σ[f]	$^3He_{ET}$ (pcc/g)[b,e]	1σ[f]
Core: KN207-2-GGC6 (continued)									
6:92-94C	1.00	443	4	1.57	0.03	439	4	0.97	0.02
6:94-96	1.56	386	4	8.61	0.17	367	4	4.65	0.09
6:94-96A	1.07	382	4	2.25	0.05	377	4	1.20	0.02
6:94-96B	1.03	375	4	5.73	0.11	362	4	3.01	0.06
6:94-96C	1.49	366	4	2.05	0.04	362	4	1.05	0.02
6:96-98	1.50	420	4	2.08	0.04	415	4	1.22	0.02
6:96-98A	1.50	405	4	2.75	0.06	399	4	1.56	0.03
6:98-100	3.01	227	2	1.80	0.04	225	2	0.57	0.01
6:98-100A	3.01	299	3	2.19	0.04	295	3	0.92	0.02
6:100-102	1.42	594	6	1.55	0.03	588	6	1.29	0.03
6:100-102A	1.54	596	6	2.04	0.04	589	6	1.70	0.03
6:102-104	1.50	492	5	2.44	0.05	485	5	1.68	0.03
6:102-104A	1.01	479	5	1.62	0.03	474	5	1.08	0.02
6:102-104B	1.50	494	5	1.76	0.04	489	5	1.22	0.02
6:102-104C	1.50	511	5	7.68	0.15	488	5	5.49	0.11
6:104-106	1.51	339	3	2.27	0.05	334	3	1.07	0.02
6:104-106A	1.50	314	3	2.55	0.05	310	3	1.12	0.02
6:106-108	3.00	176	2	3.26	0.07	172	2	0.80	0.02
6:106-108A	3.00	118	1	4.04	0.08	115	1	0.67	0.01
6:106-108B	1.47	311	3	3.48	0.07	305	3	1.52	0.03
6:106-108C	1.52	301	3	7.66	0.15	288	3	3.22	0.06
6:108-110	1.47	286	3	4.08	0.08	279	3	1.63	0.03
6:108-110A	1.50	288	3	3.26	0.07	282	3	1.31	0.03
6:110-112	1.51	327	3	3.16	0.06	321	3	1.44	0.03
6:110-112A	1.50	412	4	2.09	0.04	407	4	1.20	0.02
6:112-114	3.00	292	3	4.55	0.09	284	3	1.86	0.04
6:112-114A	3.00	119	1	5.40	0.11	116	1	0.90	0.02
6:112-114B	1.47	413	4	8.81	0.18	392	4	5.08	0.10
6:112-114C	1.51	455	5	2.20	0.04	450	4	1.40	0.03
6:114-116	1.50	437	4	3.44	0.07	428	4	2.10	0.04
6:114-116A	1.49	429	4	4.00	0.08	419	4	2.40	0.05
6:116-118	1.50	478	5	2.12	0.04	473	5	1.42	0.03
6:116-118A	1.50	564	6	2.35	0.05	557	6	1.86	0.04
6:118-120	1.50	431	4	2.41	0.05	425	4	1.45	0.03
6:118-120A	1.49	393	4	2.38	0.05	387	4	1.31	0.03
6:120-122	1.52	454	5	9.13	0.18	429	4	5.79	0.12
6:120-122A	1.51	420	4	2.56	0.05	414	4	1.50	0.03
6:122-124	1.51	774	8	1.76	0.04	766	8	1.91	0.04
6:122-124A	1.50	528	5	2.22	0.04	521	5	1.63	0.03
6:124-126	1.51	654	7	2.35	0.05	645	6	2.15	0.04
6:124-126A	1.52	623	6	2.18	0.04	615	6	1.90	0.04

Table A.2 (continued): Sediment Helium Analyses

Sample Interval (cm)[a]	Mass (g)	^{4}He total (ncc/g)[b]	1σ[c]	^{3}He/^{4}He (R_A)[d]	1σ[c]	^{4}He$_{terr}$ (ncc/g)[b,e]	1σ[f]	^{3}He$_{ET}$ (pcc/g)[b,e]	1σ[f]
Core: KN207-2-GGC6 (continued)									
6:126-128	1.52	690	7	2.09	0.04	681	7	2.01	0.04
6:126-128A	1.52	661	7	2.74	0.05	651	7	2.53	0.05
6:128-130	1.48	770	8	3.03	0.06	757	8	3.27	0.07
6:128-130A	1.48	800	8	2.37	0.05	789	8	2.65	0.05
6:128-130B	1.52	795	8	2.59	0.05	783	8	2.88	0.06
6:128-130C	1.50	783	8	2.04	0.04	773	8	2.23	0.04
6:130-132	1.51	814	8	2.61	0.05	802	8	2.98	0.06
6:132-134	1.47	777	8	2.42	0.05	766	8	2.63	0.05
6:132-134A	1.53	887	9	2.25	0.04	876	9	2.79	0.06
6:134-136	1.49	830	8	2.75	0.05	816	8	3.19	0.06
6:134-136A	1.51	822	8	2.41	0.05	811	8	2.77	0.06
6:136-138	1.53	838	8	1.63	0.03	830	8	1.91	0.04
6:136-138A	1.51	857	9	4.65	0.09	834	8	5.57	0.11
6:136-138B	1.50	811	8	2.47	0.05	799	8	2.80	0.06
6:136-138C	1.51	808	8	2.71	0.05	795	8	3.06	0.06
6:138-140	1.50	838	8	3.46	0.07	821	8	4.06	0.08
6:138-140A	1.48	837	8	4.64	0.09	815	8	5.43	0.11
6:138-140B	1.50	823	8	2.98	0.06	809	8	3.43	0.07
6:138-140C	1.50	827	8	1.81	0.04	819	8	2.09	0.04
6:140-142	1.52	803	8	2.88	0.06	790	8	3.24	0.06
6:140-142A	1.49	825	8	3.39	0.07	809	8	3.92	0.08
6:142-144	1.50	817	8	2.30	0.05	807	8	2.63	0.05
6:144-147	1.50	707	7	1.53	0.03	701	7	1.52	0.03
6:144-147A	1.47	743	7	2.60	0.05	731	7	2.70	0.05
6:144-147B	1.54	731	7	2.34	0.05	721	7	2.39	0.05
6:144-147C	1.51	701	7	2.59	0.05	691	7	2.54	0.05

[a]Sample intervals tagged A, B, or C indicate replicate analyses using additional aliquots of the same depth interval

[b]cc's refer to cm^3 of gas at standard temperature and pressure (STP) of 273K and 1 atm.

[c]1σ values reflect analytical uncertainty derived from the reproducibility of an 8.81 R_A internal standard

[d]R_A is the ratio normalized to the atmospheric ^{3}He/^{4}He value of 1.39×10^{-6}

[e, ^{4}He$_{terr}$ and ^{3}He$_{ET}$ were calculated assuming two component mixing of IDP He (^{3}He/^{4}He = 170 R_A) and terrigenous He (^{3}He/^{4}He = 0.01 R_A)

[f]1σ values reflect propagated analytical uncertainties for each individual sample

Table A.3: MORB Helium Analyses

Sample Name	Grain Size	Mass (g)	^{4}He total (ncc/g)[a]	1σ[b]	^{3}He/^{4}He (R_A)[c]	1σ[b]
KN207-2:						
D4-1	<64 μm	0.04	228	2	6.80	0.14
D4-1	>200 μm	0.43	224	2	8.94	0.18
D42-4	<64 μm	0.18	2249	22	8.17	0.16
D42-4	64-200 μm	0.36	4803	48	8.25	0.16
D57-1	<64 μm	0.39	2667	27	8.50	0.17
D57-1	64-200 μm	0.21	4721	47	8.50	0.17

[a] cc's refer to cm^3 of gas at standard temperature and pressure (STP) of 273K and 1 atm.
[b] 1σ values reflect analytical uncertainty derived from the reproducibility of an 8.81 R_A internal standard

[c] R_A is the ratio normalized to the atmospheric ^{3}He/^{4}He value of 1.39×10^{-6}

Table A.4: Benthic Oxygen Isotope Analyses

Sample Interval (cm)[a]	Mass (µg)[b]	$\delta^{18}O$ (‰)	1σ[c]
Core: KN207-2-GGC3			
3:01-03	40	2.49	0.06
3:03-04	69	2.73	0.06
3:04-05	68	2.64	0.06
3:05-06	63	2.59	0.06
3:06-08	99	2.66	0.06
3:06-08A	67	2.65	0.06
3:06-08B	51	2.59	0.06
3:08-10	NA	-	-
3:10-12	45	2.60	0.06
3:12-14	59	2.66	0.06
3:12-14A	58	2.53	0.06
3:14-16	76	2.72	0.06
3:16-18	78	3.20	0.06
3:18-20	44	3.58	0.06
3:20-22	87	2.92	0.06
3:22-24	69	3.62	0.06
3:24-26	65	3.47	0.06
3:24-26A	88	4.05	0.06
3:26-28	93	3.67	0.06
3:28-30	62	3.66	0.06
3:30-32	48	3.82	0.06
3:32-34	79	3.90	0.06
3:34-36	78	4.29	0.06
3:34-36A	72	4.36	0.06
3:36-38	62	4.15	0.06
3:38-40	59	4.06	0.06
3:38-40A	20	3.79	0.06
3:40-42	59	3.85	0.06
3:42-44	67	4.16	0.06
3:44-46	130	4.26	0.06
3:46-48	72	3.98	0.06
3:46-48A	78	4.14	0.06
3:48-50	91	3.96	0.06
3:48-50A	77	3.91	0.06
3:50-52	57	3.71	0.06
3:52-54	50	3.59	0.06
3:54-56	71	4.01	0.06
3:56-58	58	3.73	0.06
3:58-60	76	3.88	0.06
3:58-60A	66	4.01	0.06
3:60-62	76	3.98	0.06
3:62-64	55	3.83	0.06
3:64-66	75	3.60	0.06

Table A.4 (continued): Benthic Oxygen Isotope Analyses

Sample Interval (cm)[a]	Mass (µg)[b]	δ18O (‰)	1σ[c]
Core: KN207-2-GGC3			
3:66-68	72	4.02	0.06
3:66-68A	70	3.89	0.06
3:68-70	83	3.97	0.06
3:70-72	51	3.81	0.06
3:72-74	74	3.84	0.06
3:72-74A	72	3.66	0.06
3:74-76	21	3.75	0.06
3:76-78	95	3.79	0.06
3:76-78A	92	3.83	0.06
3:78-80	60	3.72	0.06
3:78-80A	58	3.69	0.06
3:80-82	55	4.02	0.06
3:80-82A	71	3.58	0.06

[a]Sample intervals tagged A or B indicate replicate analyses using additional aliquots of the same depth interval

[b]Total mass of *C. wuellerstorfi* tests analysed for each sample. Depth intervals with no available *C. wuellerstorfi* are listed as NA.

[c]1σ uncertanies reflect the 0.06‰ long-term standard devitiation of the NBS-19 international standard

Table A.5: Radiocarbon Measurements

Sample Interval (cm)	Avg. Depth (cm)	NOSAMS Accession #	^{14}C Age (yr)	1σ (yr)[a]	Sample Age (ka)	1σ (ka)[a]
KN207-2-GGC3						
3:05-06	5.5	OS-118321	5,610	20	5.2	0.02
3:20-22	21	OS-118320	10,600	30	10.2	0.03
3:36-38	37	OS-118323	17,650	50	17.3	0.05
3:40-42	41	OS-118326	24,500	75	24.1	0.08
3:50-52	51	OS-118325	30,800	110	30.4	0.11
3:64-66[b]	65	OS-118324	38,700	220	38.3	0.22

[a]1σ values reflect ^{14}C age uncertainties reported by NOSAMS

[b]Ages exceeding 35ka were not included in determination of the sediment core age-model

Appendix B

Supplemental material for Chapter 2

Table B.1: Uncertainty in ICP-MS analyses

Element[a]	K1919	1σ	Percent Uncertainty[b]
Na_2O (wt.%)	2.29	0.03	1.2%
MgO (wt.%)	7.23	0.41	5.7%
Al_2O_3 (wt.%)	13.5	0.9	6.9%
K_2O (wt.%)	0.513	0.008	1.6%
CaO (wt.%)	11.4	0.2	1.5%
Fe_2O_3 (wt.%)	12.2	0.1	1.0%
Li	4.77	0.11	2.3%
P_2O_5 (wt.%)	0.278	0.013	4.5%
Sc	29.9	3.0	10%
TiO_2 (wt.%)	2.76	0.05	1.9%
V	307	17	5.6%
Cr	302	9	2.9%
MnO	0.16	0.003	2.0%
Co	44.3	0.6	1.3%
Ni	115	2	1.9%
Cu	140	4	3.0%
Zn	109	2	1.9%
Rb	9.22	0.11	1.2%
Sr	391	5	1.4%
Y	27.1	0.6	2.1%
Zr	181	4	2.0%
Cs	0.108	0.004	3.8%
Ba	132	2	1.2%
La	15.5	0.3	1.6%
Ce	37.8	0.7	1.8%
Pr	5.36	0.11	2.0%
Nd	24.5	0.4	1.7%
Sm	6.10	0.09	1.5%
Eu	1.96	0.03	1.5%
Gd	6.22	0.12	1.9%
Tb	0.954	0.015	1.5%
Dy	5.31	0.08	1.5%
Ho	0.977	0.014	1.4%
Er	2.50	0.04	1.8%
Yb	2.03	0.03	1.4%
Lu	0.291	0.004	1.4%
Hf	4.47	0.10	2.1%
Ta	1.03	0.32	31%
Pb	1.49	0.12	8.2%
Th	1.18	0.07	5.8%
U	0.409	0.008	1.9%

[a]Units of concentration are ppm, unless otherwise noted.

[b]Percent uncertainty reflects the fractional 1σ uncertainty determined from the reproducibility of the internal basalt standard K1919.

Table B.2: GGC3 ICP-MS Results of carbonate-free component

Sample Interval (cm)	Avg. Depth (cm)	Age (ka)	ICP Bulk Sample Mass (g)	$CaCO_3$ (wt%)	Na_2O (wt%)	MgO (wt%)	Al_2O_3 (wt%)	K_2O (wt%)	CaO (wt%)	Fe_2O_3 (wt%)	Li	P_2O_5 (wt%)	Sc
KN207-2-GGC3				**Carbonate-free component (concentrations reported as ppm unless otherwise stated)**									
3:1-3	2	2.2	0.144	82	0.51	2.48	10.53	1.38	1.56	28.2	34.1	1.35	12.9
3:3-4	3.5	3.8	0.160	84	0.24	3.06	12.05	0.81	2.28	23.6	38.8	1.22	15.0
3:4-5	4.5	4.9	0.175	87	0.56	2.50	9.75	1.31	2.10	17.9	46.3	1.11	18.3
3:5-6	5.5	6.0	0.184	88	0.86	3.13	12.84	1.66	2.29	21.4	51.1	1.25	20.6
3:6-8	7	6.6	0.204	87	0.76	3.26	13.11	1.65	2.54	19.7	45.1	1.00	20.2
3:8-10	9	7.3	0.209	90	0.99	3.61	15.26	1.96	2.79	20.2	55.7	1.17	23.0
3:10-12	11	8.1	0.213	87	0.78	3.13	12.81	1.68	2.49	15.8	46.1	0.84	18.3
3:12-14	13	8.9	0.211	90	1.16	4.32	18.95	2.60	3.47	19.7	66.4	1.04	26.5
3:14-16	15	9.6	0.197	87	0.91	3.41	16.06	2.22	2.48	15.7	55.4	0.74	19.0
3:16-18	17	10.4	0.203	87	0.76	2.61	12.29	1.88	2.25	11.5	56.6	0.56	19.3
3:18-20	19	11.1	0.182	89	1.10	3.93	20.18	2.98	2.67	16.8	71.0	0.77	23.8
3:20-22	21	11.9	0.181	87	0.34	3.31	16.29	1.36	2.63	13.5	55.0	0.63	16.1
3:22-24	23	13.0	0.181	90	1.20	4.21	21.84	3.22	2.95	18.2	77.1	0.84	25.1
3:24-26	25	14.1	0.175	87	1.09	3.80	18.52	2.82	2.55	15.4	66.5	0.70	22.9
3:26-28	27	15.2	0.155	88	1.13	3.38	17.78	2.73	2.28	16.0	68.4	0.73	22.0
3:28-30	29	16.4	0.119	81	0.72	2.64	12.26	1.90	1.70	21.6	45.0	0.78	15.2
3:30-32	31	17.5	0.080	72	0.50	2.74	9.83	1.53	1.47	28.9	34.4	0.79	13.0
3:32-34	33	18.6	0.095	77	0.59	3.20	11.45	1.83	1.80	33.0	37.3	0.94	14.8
3:34-36	35	19.7	0.077	70	0.42	2.64	8.41	1.42	1.40	33.8	26.6	0.93	11.0
3:36-38	37	20.8	0.078	70	0.47	2.51	9.00	1.56	1.47	27.8	33.1	0.80	11.4
3:38-40	39	24.5	0.077	76	0.75	3.96	13.93	2.31	2.10	32.3	48.7	0.85	18.0
3:40-42	41	28.1	0.079	77	0.71	3.65	13.15	2.16	2.37	24.9	45.2	0.70	16.7
3:42-44	43	29.4	0.109	82	0.99	4.74	17.72	2.57	2.74	20.8	59.6	0.60	23.0
3:44-46	45	30.6	0.115	82	1.02	4.12	16.32	2.30	2.48	16.5	60.6	0.55	20.6
3:46-48	47	31.9	0.118	84	1.15	5.62	19.53	2.70	3.31	19.5	66.6	0.58	24.0
3:48-50	49	33.1	0.123	80	0.92	3.97	13.86	1.86	2.40	12.5	50.9	0.41	18.2
3:50-52	51	34.4	0.116	80	0.34	6.06	15.79	1.08	3.31	17.0	53.2	0.48	17.9

Table B.2 (continued): GGC3 ICP-MS Results of carbonate-free component

TiO_2 (wt%)	V	Cr	MnO (wt%)	Co	Ni	Cu	Zn	Rb	Sr	Y	Zr	Cs
Carbonate-free component (concentrations reported as ppm unless otherwise stated)												
0.68	771	91	0.80	66.3	54.7	4373	569	58.5	120	33.5	117	3.39
0.78	564	92	1.00	85.9	67.8	3171	480	68.5	165	35.6	132	4.03
0.86	562	106	1.32	121.7	100.2	2851	541	74.5	206	41.8	145	4.11
1.04	576	118	1.21	130.2	88.3	2687	542	84.1	207	45.2	177	4.80
0.95	431	107	1.23	123.6	91.5	1856	420	70.5	198	48.9	148	4.13
1.23	476	145	1.31	149.8	98.1	1626	410	92.1	222	48.9	196	5.06
0.95	328	109	1.04	118.1	89.2	1151	293	74.4	185	54.3	154	3.94
1.27	385	137	1.36	161.9	118.6	1323	361	109.1	280	65.1	207	6.12
0.99	287	111	1.16	118.8	91.1	1039	281	94.3	220	47.9	166	5.19
0.85	263	103	0.93	113.3	94.7	955	283	99.3	240	40.4	154	5.30
1.20	281	133	1.09	137.9	103.2	954	289	127.8	271	57.4	207	7.33
0.92	209	103	0.82	102.9	74.3	763	237	102.6	225	35.9	165	5.69
1.29	286	141	1.16	144.0	108.1	1098	336	139.1	302	63.5	223	7.90
1.09	246	121	0.97	119.5	92.6	1052	300	119.2	252	53.1	190	7.01
1.11	269	122	0.94	122.4	81.7	1353	365	127.5	269	42.5	198	7.21
0.81	331	92	0.72	86.6	54.2	3002	513	88.6	191	25.3	149	5.05
0.62	392	81	0.64	65.5	54.3	4668	691	64.2	139	26.1	111	3.37
0.68	464	90	0.76	84.4	59.9	6047	804	73.5	158	30.8	126	4.12
0.51	491	76	0.64	79.8	47.7	7096	905	54.7	113	29.0	96	2.97
0.59	441	75	0.65	88.7	50.7	6336	908	67.0	140	28.9	105	3.35
0.85	510	107	0.81	123.2	67.9	6780	1104	95.9	187	35.8	146	4.97
0.81	381	101	0.73	114.2	70.9	5747	934	93.3	196	32.8	138	4.65
1.13	304	132	0.89	115.0	87.4	3563	689	104.9	216	36.2	168	5.59
1.07	274	126	0.83	102.7	82.9	2211	496	105.5	214	30.6	171	5.88
1.23	297	151	0.99	121.1	105.7	2031	489	112.6	243	41.7	187	6.03
0.93	214	118	0.75	90.9	79.1	1099	324	85.3	183	25.7	141	4.72
0.96	220	130	0.85	91.3	109.4	1100	338	78.3	189	29.1	138	4.37

Table B.2 (continued): GGC3 ICP-MS Results of carbonate-free component

Ba	La	Ce	Pr	Nd	Sm	Eu	Gd	Tb	Dy	Ho	Er	Yb
Carbonate-free component (concentrations reported as ppm unless otherwise stated)												
241	35.9	85	8.4	31.3	6.31	1.52	5.86	0.96	5.62	1.17	3.39	3.33
280	40.1	110	9.5	35.4	6.87	1.64	6.68	1.08	6.24	1.26	3.71	3.53
318	44.0	126	10.2	37.7	7.12	1.63	6.68	1.06	6.50	1.34	3.96	3.85
362	49.5	143	11.6	43.2	8.12	1.87	7.61	1.23	7.21	1.47	4.31	4.26
325	49.4	132	11.4	42.4	8.39	1.92	8.07	1.29	7.57	1.51	4.41	4.22
479	55.1	163	12.8	46.9	8.91	2.03	8.32	1.34	7.84	1.56	4.57	4.45
435	53.1	137	12.2	45.8	9.03	2.06	8.86	1.39	8.10	1.62	4.67	4.34
1007	69.0	191	16.0	59.3	11.62	2.66	11.01	1.72	10.03	1.95	5.68	5.26
1297	53.9	150	12.4	46.1	8.97	2.13	8.33	1.31	7.48	1.49	4.25	3.96
1469	49.2	149	10.9	39.8	7.48	1.81	6.81	1.06	6.22	1.25	3.63	3.44
2223	68.2	192	15.7	58.0	11.13	2.67	10.19	1.60	9.03	1.78	5.02	4.70
1844	48.0	155	11.1	40.5	7.70	2.06	7.00	1.10	6.08	1.19	3.46	3.22
2873	75.2	207	17.4	64.1	12.31	3.05	11.21	1.78	9.93	1.97	5.58	5.11
2394	62.3	171	14.5	53.3	10.31	2.52	9.36	1.47	8.41	1.62	4.61	4.36
2844	58.5	177	13.4	48.4	8.88	2.32	7.82	1.24	7.02	1.39	4.03	3.90
2196	34.9	109	8.0	30.0	5.33	1.57	4.82	0.79	4.49	0.91	2.65	2.63
1536	30.9	82	7.2	26.8	5.17	1.63	5.03	0.81	4.54	0.93	2.83	2.85
1720	34.8	92	8.4	31.2	6.28	1.81	5.83	0.95	5.50	1.11	3.18	3.18
1072	28.8	66	7.0	26.9	5.70	1.67	5.42	0.87	5.15	1.05	2.96	2.96
1318	33.1	80	7.9	29.0	5.62	1.70	5.35	0.88	5.07	1.03	3.07	3.01
1589	44.3	113	10.2	37.9	7.32	2.04	6.97	1.12	6.28	1.27	3.86	3.76
1543	40.5	111	9.7	34.3	6.58	1.74	5.98	0.98	5.75	1.17	3.44	3.42
1731	45.7	138	10.6	38.8	7.44	1.94	6.77	1.09	6.27	1.25	3.66	3.56
1874	41.3	135	9.4	34.5	6.41	1.69	5.77	0.93	5.34	1.08	3.15	3.12
1918	51.5	156	12.0	43.6	8.32	2.13	7.61	1.22	7.02	1.39	4.06	3.94
1485	34.1	112	7.8	28.2	5.26	1.39	4.79	0.77	4.49	0.91	2.61	2.58
1184	34.2	107	8.0	29.7	5.83	1.57	5.53	0.89	5.14	1.02	2.98	2.84

Table B.2 (continued): GGC3 ICP-MS Results of carbonate-free component

Lu	Hf	Ta	Pb	Th	U
Carbonate-free component (concentrations reported as ppm unless otherwise stated)					
0.484	2.80	0.82	228	10.35	2.04
0.516	3.40	1.00	168	11.73	1.97
0.557	3.19	0.57	126	12.79	2.25
0.617	4.09	0.94	127	14.81	2.56
0.612	3.57	1.01	106	13.02	2.00
0.648	4.61	1.18	105	17.03	2.32
0.636	3.61	1.00	77	14.17	1.85
0.774	5.07	1.51	97	19.58	2.42
0.581	4.03	1.25	81	15.96	2.17
0.504	3.48	0.27	62	16.13	2.01
0.690	5.05	1.72	81	21.27	2.58
0.474	4.20	1.35	63	15.72	2.05
0.748	5.52	1.80	85	23.38	2.85
0.640	4.65	1.49	69	18.88	2.40
0.569	4.87	1.23	62	19.47	2.63
0.385	3.49	0.86	72	13.43	2.71
0.405	2.66	0.76	98	9.42	2.83
0.449	2.91	0.91	126	11.00	3.04
0.419	2.14	0.63	146	7.73	2.46
0.435	2.54	0.73	136	9.34	2.01
0.548	3.64	1.06	180	12.81	2.05
0.498	3.31	0.91	113	12.61	1.87
0.514	4.26	1.18	92	14.22	1.99
0.456	4.12	0.93	63	14.16	1.98
0.580	4.72	1.31	75	15.60	2.11
0.379	3.49	0.78	45	11.51	1.60
0.421	3.53	0.95	54	10.66	1.64

Table B.2 (continued): GGC3 ICP-MS Results of carbonate-free component

Sample Interval (cm)	Avg. Depth (cm)	Age (ka)	ICP Bulk Sample Mass (g)	$CaCO_3$ (wt%)	Na_2O (wt%)	MgO (wt%)	Al_2O_3 (wt%)	K_2O (wt%)	CaO (wt%)	Fe_2O_3 (wt%)	Li	P_2O_5 (wt%)	Sc
KN207-2-GGC3 (continued)				**Carbonate-free component (concentrations reported as ppm unless otherwise stated)**									
3:52-54	53	35.0	0.100	83	1.15	7.45	19.50	2.21	4.00	18.2	72.5	0.55	26.4
3:54-56	55	35.6	0.120	77	0.88	5.62	14.18	1.56	2.92	12.1	48.4	0.35	18.7
3:56-58	57	36.2	0.113	77	0.30	6.64	14.97	0.79	3.53	13.9	50.4	0.39	18.0
3:58-60	59	36.7	0.111	80	1.11	7.40	16.71	1.58	4.00	14.5	55.6	0.43	24.2
3:60-62	61	37.3	0.125	79	0.32	7.19	15.90	0.82	3.85	15.9	54.3	0.46	20.3
3:62-64	63	37.9	0.139	80	1.03	6.24	15.32	1.58	3.62	14.8	50.7	0.48	23.6
3:64-66	65	39.2	0.124	83	0.35	7.08	18.60	1.02	4.28	18.3	64.2	0.56	22.4
3:66-68	67	40.5	0.134	84	1.12	5.71	19.01	2.14	3.81	16.7	65.5	0.54	24.9
3:68-70	69	41.8	0.134	78	0.84	4.10	13.71	1.56	3.22	11.5	49.9	0.39	19.9
3:70-72	71	43.0	0.123	77	0.34	4.62	15.49	0.94	3.79	13.4	47.8	0.40	19.3
3:72-74	73	44.3	0.135	84	1.09	4.99	18.67	2.10	3.49	14.5	57.6	0.54	25.2
3:74-76	75	45.6	0.144	82	0.30	5.22	15.70	0.85	3.60	14.4	50.5	0.52	27.9
3:76-78	77	46.9	0.127	81	0.94	4.56	15.82	1.99	3.04	14.7	54.1	0.48	21.6
3:78-80	79	48.2	0.114	85	1.38	7.03	22.71	2.87	4.23	21.0	78.5	0.55	28.1
3:80-82	81	49.5	0.097	78	0.41	6.24	18.91	1.27	3.73	16.2	64.1	0.42	23.6

Table B.2 (continued): GGC3 ICP-MS Results of carbonate-free component

TiO_2 (wt%)	V	Cr	MnO (wt%)	Co	Ni	Cu	Zn	Rb	Sr	Y	Zr	Cs
Carbonate-free component (concentrations reported as ppm unless otherwise stated)												
1.36	278	176	1.06	121.3	148.1	971	317	91.7	230	40.7	177	5.35
0.96	191	142	0.68	80.6	103.8	593	207	63.2	161	24.1	122	3.54
0.99	193	137	0.82	80.0	117.0	590	214	61.7	166	26.0	124	3.40
1.13	243	162	0.86	92.8	131.8	614	233	63.5	173	26.4	143	3.62
1.06	220	143	0.86	88.1	129.0	679	226	64.1	177	29.0	134	3.60
1.13	247	152	0.94	92.6	129.1	720	242	64.7	175	29.9	145	3.61
1.25	248	162	1.03	98.8	143.7	784	253	80.1	218	37.4	159	4.46
1.44	267	171	0.97	102.1	127.4	730	246	87.8	218	35.5	175	4.87
1.08	192	125	0.72	78.7	102.7	527	180	67.9	196	28.6	132	3.86
1.10	184	133	0.71	73.5	97.7	490	173	68.4	189	28.2	131	3.71
1.29	248	149	0.89	95.7	98.5	527	198	85.7	189	31.5	173	4.75
1.02	214	134	1.01	91.6	111.8	530	179	71.6	185	31.6	138	4.20
1.04	261	135	0.94	92.8	99.4	630	197	85.2	180	28.7	158	4.97
1.48	348	200	1.31	123.5	139.3	798	251	119.8	242	46.9	215	6.26
1.13	243	156	0.96	87.3	107.5	531	187	94.8	193	31.7	164	5.53

Table B.2 (continued): GGC3 ICP-MS Results of carbonate-free component

Ba	La	Ce	Pr	Nd	Sm	Eu	Gd	Tb	Dy	Ho	Er	Yb
Carbonate-free component (concentrations reported as ppm unless otherwise stated)												
1417	43.0	136	10.2	38.0	7.58	1.92	7.15	1.18	6.85	1.38	3.95	3.78
955	27.3	88	6.4	23.6	4.67	1.21	4.36	0.71	4.17	0.84	2.41	2.37
732	27.3	88	6.5	24.3	4.91	1.29	4.81	0.79	4.60	0.93	2.69	2.58
754	26.7	88	6.3	23.5	4.76	1.25	4.66	0.77	4.58	0.93	2.72	2.70
661	29.4	94	7.0	26.4	5.37	1.39	5.33	0.87	5.12	1.03	2.99	2.87
668	30.5	97	7.3	27.1	5.42	1.38	5.25	0.86	5.07	1.03	2.98	2.92
764	38.7	120	9.2	34.8	7.09	1.76	6.90	1.12	6.53	1.32	3.77	3.58
978	40.1	129	9.3	34.5	6.84	1.70	6.45	1.04	6.14	1.20	3.54	3.44
820	31.1	103	7.2	26.6	5.32	1.34	5.10	0.82	4.86	0.98	2.85	2.79
793	30.8	100	7.3	27.2	5.49	1.42	5.34	0.86	5.00	1.00	2.88	2.75
982	37.3	121	8.7	31.6	6.08	1.53	5.71	0.93	5.45	1.09	3.18	3.13
720	34.0	112	8.2	30.5	6.11	1.53	5.98	0.96	5.57	1.12	3.24	3.08
861	34.7	116	8.0	29.2	5.61	1.40	5.23	0.84	4.97	1.00	2.95	2.90
1407	54.3	169	12.6	46.5	8.96	2.22	8.46	1.36	7.90	1.58	4.63	4.49
1211	38.7	125	9.0	33.1	6.46	1.69	6.09	0.99	5.68	1.14	3.28	3.19

Table B.2 (continued): GGC3 ICP-MS Results of carbonate-free component

Lu	Hf	Ta	Pb	Th	U
Carbonate-free component (concentrations reported as ppm unless otherwise stated)					
0.561	4.40	1.15	55	13.02	1.87
0.346	3.09	0.79	34	8.57	1.20
0.384	3.20	0.78	36	8.19	1.26
0.387	3.34	0.82	35	8.42	1.24
0.425	3.48	0.84	43	8.49	1.38
0.418	3.43	0.85	41	8.91	1.33
0.530	4.16	1.04	51	10.88	1.76
0.511	4.46	1.11	50	12.14	1.82
0.411	3.32	0.78	31	9.61	1.45
0.407	3.48	0.87	36	8.93	1.38
0.447	4.17	1.10	45	12.79	1.68
0.455	3.58	0.89	45	9.92	1.56
0.418	3.68	0.99	42	11.92	1.74
0.671	5.32	1.42	61	16.27	2.44
0.470	4.20	1.19	49	12.19	1.84

Table B.3: GGC3 ICP-MS Results of carbonate component

Sample Interval (cm)	Na_2O (wt%)	MgO (wt%)	Al_2O_3 (wt%)	K_2O (wt%)	CaO (wt%)	Fe_2O_3 (wt%)	Li	P_2O_5 (wt%)	Sc	TiO_2 (wt%)	V	Cr
KN207-2-GGC3												
3:1-3	2.16	0.76	0.23	0.13	54.3	1.21	2.20	0.029	1.04	0.05	2.94	10.23
3:3-4	1.85	0.70	0.36	0.11	56.4	0.33	2.12	0.028	1.40	0.01	2.75	9.61
3:4-5	1.59	0.52	0.27	0.11	59.7	0.79	1.96	0.027	1.30	0.03	1.91	9.09
3:5-6	1.57	0.59	0.06	0.12	54.6	0.56	2.21	0.029	1.04	0.03	1.03	8.73
3:6-8	1.82	0.64	0.57	0.10	59.8	0.20	2.25	0.025	1.31	0.03	0.00	8.77
3:8-10	1.54	0.62	0.15	0.11	54.7	0.38	2.42	0.022	0.78	0.05	1.21	8.64
3:10-12	1.64	0.60	0.38	0.09	59.3	0.12	2.16	0.024	1.48	0.03	0.00	8.32
3:12-14	1.40	0.56	0.75	0.12	70.1	0.36	2.11	0.029	1.37	0.03	0.00	8.01
3:14-16	1.80	0.59	0.21	0.11	55.9	0.28	2.19	0.027	1.20	0.03	0.43	7.42
3:16-18	1.99	0.49	0.26	0.13	56.9	0.53	1.96	0.027	1.25	0.03	1.50	8.68
3:18-20	1.52	0.55	0.41	0.11	59.4	0.34	1.90	0.030	1.63	0.03	0.36	7.57
3:20-22	1.57	0.62	0.36	0.10	55.7	0.22	2.25	0.034	1.65	0.01	2.29	10.52
3:22-24	1.87	0.55	0.32	0.11	54.4	0.20	2.00	0.029	1.36	0.03	0.22	8.20
3:24-26	1.51	0.53	0.28	0.10	55.1	0.25	1.94	0.031	1.71	0.03	0.30	8.04
3:26-28	1.64	0.60	0.23	0.12	54.4	0.29	2.05	0.021	-0.23	0.07	1.50	10.03
3:28-30	1.82	0.68	0.11	0.17	51.3	0.90	2.96	0.019	1.09	0.03	0.67	13.53
3:30-32	2.55	0.85	0.74	0.19	39.8	1.02	2.75	0.031	2.41	0.03	0.00	14.31
3:32-34	2.83	0.90	0.25	0.20	47.9	1.13	2.54	0.021	1.84	0.05	1.56	10.92
3:34-36	3.21	1.03	0.27	0.24	46.6	1.84	2.72	0.029	2.40	0.05	2.23	14.01
3:36-38	3.34	0.93	0.40	0.26	56.1	2.33	2.71	0.051	3.54	0.03	1.31	20.85
3:38-40	2.98	0.91	0.48	0.24	53.0	1.56	3.14	0.057	3.51	0.03	0.00	19.37
3:40-42	2.82	0.76	0.36	0.23	55.4	1.71	2.36	0.029	2.21	0.03	2.10	14.05
3:42-44	2.20	0.70	0.56	0.19	64.0	0.71	3.02	0.044	2.69	0.03	0.00	12.81
3:44-46	2.07	0.62	0.13	0.19	49.8	0.71	3.16	0.036	2.03	0.03	0.77	13.56
3:46-48	2.14	0.62	0.48	0.18	60.0	0.47	2.92	0.041	2.47	0.03	0.00	12.60
3:48-50	2.17	0.63	0.14	0.18	53.4	0.62	3.38	0.030	1.14	0.03	0.82	12.38
3:50-52	2.64	0.75	0.45	0.19	60.1	0.35	3.43	0.032	2.21	0.00	2.35	11.81

Table B.3 (continued): GGC3 ICP-MS Results of carbonate component

MnO (wt%)	Co	Ni	Cu	Zn	Rb	Sr	Y	Zr	Cs	Ba	La	Ce	Pr	Nd
0.09	6.08	18.4	1737	185.0	0.530	2223	15.7	0.94	0.030	11.4	8.9	5.49	2.20	9.4
0.05	3.45	15.5	763	122.2	0.511	2378	17.0	1.29	0.023	10.0	10.2	4.92	2.44	10.5
0.02	0.52	16.7	410	78.8	0.386	2273	16.4	2.07	0.026	7.9	9.1	3.53	2.18	9.5
0.04	1.74	16.8	419	84.5	0.362	2547	16.2	0.67	0.024	9.5	9.2	4.14	2.34	9.7
0.03	1.18	18.5	254	57.5	0.346	2485	14.9	1.36	0.020	9.6	8.4	3.18	2.02	9.6
0.04	1.50	17.7	161	42.1	0.380	2463	15.8	0.70	0.025	13.7	9.2	4.19	2.30	9.8
0.03	1.43	18.4	120	30.4	0.439	2463	14.7	1.29	0.021	19.4	8.7	3.42	2.07	9.8
0.02	0.86	16.9	105	24.8	0.349	2331	15.2	1.34	0.024	10.4	9.1	3.52	2.40	10.3
0.03	0.92	16.8	106	26.2	0.378	2295	16.6	0.92	0.024	16.0	10.1	4.11	2.57	11.2
0.02	0.33	14.5	87	20.9	0.430	1976	18.1	2.03	0.027	11.5	11.0	4.30	2.71	11.8
0.02	0.70	16.7	72	21.7	0.399	2182	17.3	1.15	0.026	18.5	10.6	4.21	2.85	12.0
0.03	1.71	16.7	83	25.3	0.503	2179	19.4	1.32	0.023	27.7	12.9	5.74	3.22	13.7
0.02	0.81	17.2	81	23.4	0.399	2105	17.0	1.21	0.023	22.5	10.4	4.03	2.66	12.0
0.02	0.87	17.6	92	25.2	0.424	2173	17.7	1.13	0.025	28.1	10.8	4.25	2.80	12.4
0.03	1.22	18.2	138	32.4	0.377	2179	19.8	0.80	0.026	30.1	12.6	5.57	3.22	13.9
0.05	2.64	20.5	539	83.3	0.579	2138	22.5	0.55	0.026	81.7	14.6	7.91	3.85	15.9
0.04	2.09	19.4	926	117.4	0.497	1467	16.9	1.29	0.020	63.4	10.2	4.49	2.46	12.0
0.04	1.94	17.8	1264	133.9	0.497	1890	19.4	0.79	0.027	48.4	12.2	5.44	3.15	13.4
0.04	2.92	17.3	2658	231.9	0.608	1691	19.3	0.85	0.030	74.3	11.7	4.98	2.96	12.7
0.04	2.77	17.2	2586	203.4	0.604	1697	23.4	1.69	0.028	51.0	14.3	5.90	3.61	15.8
0.04	3.92	18.6	2059	176.2	0.578	1779	23.1	1.42	0.023	45.3	14.7	5.78	3.78	17.2
0.03	1.28	13.5	1172	121.6	0.504	1789	23.8	2.02	0.028	25.9	15.3	5.51	3.75	16.2
0.03	1.92	17.3	590	73.7	0.558	2169	23.6	1.36	0.026	35.8	15.0	5.15	4.05	17.5
0.04	2.23	17.8	396	70.7	0.516	2187	23.7	0.62	0.025	34.1	15.5	6.83	4.12	17.2
0.03	1.41	18.4	274	51.0	0.515	2208	21.9	1.35	0.023	27.2	13.7	4.95	3.58	16.2
0.04	1.81	19.8	216	53.9	0.531	2244	22.5	0.67	0.025	33.1	14.8	6.68	3.93	16.5
0.03	1.90	17.7	150	45.5	0.724	2239	22.0	1.10	0.023	40.9	14.5	5.95	3.66	15.7

Table B.3 (continued): GGC3 ICP-MS Results of carbonate component

Sm	Eu	Gd	Tb	Dy	Ho	Er	Yb	Lu	Hf	Ta	Pb	Th	U
2.15	0.57	2.47	0.36	2.04	0.42	1.11	0.87	0.14	0.00	0.016	2.10	0.157	0.722
2.34	0.58	2.61	0.38	2.22	0.45	1.19	0.96	0.15	0.00	0.000	1.14	0.274	0.557
2.13	0.53	2.48	0.37	2.08	0.42	1.11	0.94	0.13	0.01	0.000	0.61	0.164	0.458
2.25	0.55	2.53	0.37	2.14	0.47	1.14	0.91	0.14	0.00	0.046	0.93	0.218	0.468
2.10	0.50	2.35	0.35	1.99	0.41	1.06	0.92	0.14	0.00	0.005	0.28	0.168	0.431
2.18	0.52	2.46	0.36	2.10	0.45	1.13	0.90	0.14	0.00	0.040	0.73	0.174	0.393
2.12	0.49	2.32	0.35	1.97	0.40	1.04	0.91	0.14	0.00	0.006	0.14	0.108	0.365
2.24	0.51	2.45	0.36	2.06	0.42	1.09	0.86	0.13	0.00	0.000	0.16	0.168	0.337
2.49	0.57	2.72	0.40	2.27	0.47	1.19	0.98	0.15	0.00	0.017	0.39	0.275	0.314
2.59	0.60	2.89	0.43	2.41	0.48	1.27	1.10	0.15	0.02	0.000	0.38	0.283	0.285
2.69	0.60	2.90	0.43	2.40	0.48	1.26	1.00	0.16	0.00	0.000	0.23	0.271	0.277
3.00	0.67	3.19	0.47	2.69	0.53	1.41	1.13	0.17	0.00	0.000	0.53	0.548	0.300
2.65	0.60	2.86	0.42	2.37	0.47	1.24	1.05	0.16	0.00	0.004	0.21	0.247	0.264
2.78	0.62	2.97	0.44	2.45	0.49	1.28	1.06	0.17	0.00	0.003	0.23	0.255	0.265
3.05	0.70	3.33	0.49	2.73	0.54	1.42	1.14	0.17	0.00	0.033	0.71	0.392	0.295
3.63	0.88	3.89	0.58	3.21	0.66	1.68	1.37	0.20	0.00	0.045	1.23	0.354	0.505
2.67	0.69	2.96	0.43	2.42	0.48	1.23	0.98	0.15	0.00	0.002	0.65	0.241	0.567
3.06	0.77	3.36	0.49	2.71	0.53	1.39	1.12	0.17	0.00	0.015	1.04	0.256	0.698
2.96	0.82	3.30	0.47	2.63	0.52	1.35	1.09	0.17	0.00	0.013	1.71	0.202	1.064
3.54	0.98	3.96	0.57	3.17	0.62	1.62	1.28	0.20	0.01	0.000	2.02	0.276	0.923
3.86	0.99	4.13	0.60	3.30	0.64	1.68	1.35	0.20	0.00	0.001	1.74	0.335	0.750
3.63	0.92	4.09	0.60	3.30	0.64	1.69	1.32	0.20	0.02	0.000	1.07	0.347	0.553
3.90	0.92	4.19	0.61	3.43	0.67	1.76	1.40	0.21	0.00	0.000	0.36	0.428	0.364
3.92	0.91	4.14	0.61	3.44	0.70	1.77	1.43	0.21	0.00	0.044	0.80	0.596	0.323
3.58	0.82	3.83	0.56	3.14	0.62	1.62	1.33	0.20	0.00	0.003	0.20	0.445	0.292
3.74	0.86	3.97	0.58	3.26	0.67	1.70	1.39	0.20	0.00	0.044	0.74	0.584	0.286
3.51	0.81	3.75	0.55	3.14	0.62	1.64	1.34	0.20	0.00	0.000	0.39	0.610	0.284

Table B.3 (continued): GGC3 ICP-MS Results of carbonate component

Sample Interval (cm)	Na_2O (wt%)	MgO (wt%)	Al_2O_3 (wt%)	K_2O (wt%)	CaO (wt%)	Fe_2O_3 (wt%)	Li	P_2O_5 (wt%)	Sc	TiO_2 (wt%)	V	Cr
KN207-2-GGC3 (continued)												
3:52-54	2.25	0.65	0.39	0.19	56.6	0.50	3.28	0.038	3.09	0.03	0.49	10.81
3:54-56	2.15	0.63	0.22	0.22	54.6	0.58	3.95	0.035	2.47	0.03	0.81	13.62
3:56-58	2.60	0.78	0.53	0.23	60.8	0.37	4.20	0.032	3.02	0.00	2.25	14.31
3:58-60	2.07	0.63	0.21	0.21	49.4	0.56	4.27	0.035	2.22	0.03	0.94	14.23
3:60-62	2.35	0.73	0.48	0.21	58.1	0.33	3.91	0.030	2.53	0.00	2.34	11.51
3:62-64	2.14	0.68	0.39	0.20	53.4	0.39	4.01	0.030	2.13	0.07	1.88	12.08
3:64-66	2.49	0.71	0.49	0.21	57.0	0.30	3.87	0.027	2.59	0.00	2.19	10.80
3:66-68	2.11	0.62	0.33	0.21	50.9	0.45	3.75	0.024	1.83	0.05	1.24	11.73
3:68-70	2.57	0.61	0.49	0.24	60.0	0.75	3.49	0.034	3.45	0.03	1.54	12.35
3:70-72	2.76	0.76	0.57	0.25	59.8	0.31	3.93	0.028	2.97	0.00	2.27	11.85
3:72-74	2.23	0.70	0.36	0.20	52.5	0.51	3.85	0.021	1.85	0.05	1.00	11.88
3:74-76	2.16	0.69	0.45	0.17	58.6	0.25	3.48	0.034	2.23	0.01	2.41	10.06
3:76-78	2.20	0.69	0.38	0.19	56.6	0.64	3.33	0.022	1.65	0.05	1.74	12.37
3:78-80	1.32	0.55	0.97	0.16	41.4	0.41	3.04	0.029	2.01	0.03	0.00	9.98
3:80-82	2.97	0.95	0.50	0.23	59.3	0.33	4.84	0.029	2.25	0.00	2.57	13.57

Table B.3 (continued): GGC3 ICP-MS Results of carbonate component

MnO (wt%)	Co	Ni	Cu	Zn	Rb	Sr	Y	Zr	Cs	Ba	La	Ce	Pr	Nd
0.02	0.94	18.9	93	32.5	0.655	2049	20.8	1.10	0.027	30.9	12.4	4.35	3.41	14.4
0.04	1.72	21.1	99	36.8	0.668	2217	22.9	0.60	0.025	33.9	13.7	5.88	3.76	15.6
0.03	1.86	20.0	76	33.0	0.843	2279	23.5	1.08	0.023	38.6	14.2	5.78	3.62	15.7
0.04	1.72	23.6	73	31.6	0.651	1950	20.4	0.68	0.026	28.2	11.7	5.52	3.20	13.3
0.03	1.60	18.6	66	28.9	0.762	2162	21.0	1.10	0.023	32.0	12.2	4.97	3.08	13.4
0.03	1.24	22.2	70	28.4	0.610	2042	20.7	0.78	0.027	23.9	11.6	4.62	3.01	13.1
0.02	1.25	15.9	54	23.9	0.750	2188	20.2	1.10	0.022	28.4	12.0	4.48	3.04	13.2
0.03	1.18	17.0	53	22.5	0.638	2088	20.5	0.70	0.026	24.7	11.8	4.67	3.10	13.3
0.02	0.41	14.4	36	15.3	0.706	2165	22.1	1.92	0.026	16.5	12.8	4.00	3.26	14.1
0.02	1.25	13.4	37	17.2	0.901	2390	21.7	1.10	0.023	36.4	13.5	4.76	3.44	14.9
0.04	1.95	20.4	41	17.5	0.699	2104	20.0	0.67	0.026	36.1	11.7	6.02	3.04	13.2
0.02	1.12	17.4	40	16.2	0.661	2274	21.5	1.14	0.022	29.8	12.7	4.69	3.19	13.8
0.04	1.27	20.8	50	15.7	0.619	2057	21.9	1.36	0.028	32.0	13.4	5.76	3.36	14.5
0.03	0.73	17.6	35	10.2	0.472	1386	15.5	1.30	0.024	25.8	9.4	3.45	2.59	11.2
0.05	2.45	22.1	46	14.6	0.833	2023	26.8	1.10	0.024	49.0	18.3	7.40	4.70	20.2

Table B.3 (continued): GGC3 ICP-MS Results of carbonate component

Sm	Eu	Gd	Tb	Dy	Ho	Er	Yb	Lu	Hf	Ta	Pb	Th	U
3.30	0.75	3.56	0.53	2.95	0.59	1.55	1.26	0.19	0.00	0.000	0.14	0.475	0.236
3.63	0.85	3.91	0.58	3.29	0.68	1.71	1.39	0.20	0.00	0.044	0.56	0.571	0.251
3.59	0.84	3.91	0.58	3.33	0.66	1.77	1.47	0.22	0.00	0.000	0.28	0.608	0.268
3.10	0.74	3.44	0.51	2.91	0.60	1.55	1.29	0.19	0.00	0.044	0.57	0.486	0.246
3.05	0.72	3.36	0.50	2.87	0.58	1.54	1.29	0.20	0.00	0.000	0.27	0.539	0.265
2.95	0.70	3.29	0.49	2.80	0.56	1.50	1.23	0.19	0.00	0.034	0.57	0.464	0.261
2.98	0.70	3.28	0.49	2.81	0.56	1.49	1.23	0.19	0.00	0.000	0.25	0.526	0.253
3.05	0.72	3.36	0.50	2.86	0.59	1.52	1.24	0.18	0.00	0.038	0.55	0.458	0.239
3.21	0.76	3.62	0.54	3.04	0.60	1.60	1.37	0.19	0.02	0.000	0.25	0.422	0.222
3.39	0.78	3.67	0.55	3.15	0.62	1.64	1.35	0.20	0.00	0.000	0.22	0.618	0.249
3.00	0.71	3.31	0.50	2.80	0.59	1.49	1.22	0.18	0.00	0.041	0.57	0.279	0.247
3.10	0.72	3.41	0.51	2.94	0.59	1.55	1.28	0.19	0.00	0.000	0.22	0.534	0.289
3.24	0.77	3.63	0.54	3.03	0.60	1.60	1.32	0.19	0.01	0.016	0.45	0.360	0.290
2.49	0.58	2.74	0.40	2.25	0.45	1.17	0.95	0.14	0.00	0.000	0.02	0.220	0.212
4.51	1.02	4.78	0.70	4.00	0.78	2.06	1.67	0.25	0.00	0.000	0.38	0.769	0.317

Table B.4: GGC6 ICP-MS Results of carbonate-free component

Sample Interval (cm)	Avg. Depth (cm)	Age (ka)	ICP Bulk Sample Mass (g)	$CaCO_3$ (wt%)	Na_2O (wt%)	MgO (wt%)	Al_2O_3 (wt%)	K_2O (wt%)	CaO (wt%)	Fe_2O_3 (wt%)	Li	P_2O_5 (wt%)	Sc
KN207-2-GGC6				**Carbonate-free component (concentrations reported as ppm unless otherwise stated)**									
6:0-2	1	0.5	0.272	93	0.38	3.61	21.84	1.63	4.45	13.9	76.0	1.12	27.8
6:2-4	3	1.4	0.263	91	0.91	2.77	17.36	2.51	2.78	11.6	64.4	0.88	23.6
6:4-6	5	2.4	0.449	90	0.22	2.63	16.02	0.95	3.05	9.9	53.0	0.92	21.0
6:6-8	7	3.3	0.893	95	1.03	2.69	18.22	2.08	5.03	11.2	53.4	0.89	18.7
6:8-10	9	4.3	0.388	93	0.67	2.10	12.57	1.61	3.05	9.4	49.2	1.00	19.3
6:10-12	11	5.2	0.380	94	0.91	2.50	14.09	1.81	2.98	11.7	57.6	1.30	23.7
6:12-14	13	6.2	0.439	94	0.63	1.72	10.03	1.21	3.10	9.8	47.7	1.32	21.3
6:14-16	15	7.3	0.429	94	1.00	2.38	13.64	1.72	3.66	13.7	50.3	1.54	23.0
6:16-18	17	8.3	0.352	94	1.24	2.99	17.73	2.43	4.31	15.5	60.6	1.55	27.3
6:18-20	19	9.4	0.384	93	0.28	2.86	16.62	1.06	4.33	12.8	55.1	1.32	19.6
6:20-22	21	10.4	0.373	92	0.94	2.27	13.22	1.99	3.36	10.1	54.3	1.08	22.5
6:22-24	23	11.5	0.263	93	1.16	3.00	18.69	2.69	3.49	11.5	65.4	0.94	23.7
6:24-26	25	12.5	0.294	92	0.80	3.19	20.34	2.29	3.73	12.2	69.6	0.98	23.1
6:26-28	27	13.4	0.202	91	1.15	3.15	20.51	3.22	3.18	10.3	70.8	0.69	23.9
6:28-30	29	14.2	0.235	88	0.84	2.04	14.15	2.20	2.03	7.9	59.0	0.54	19.0
6:30-32	31	15.1	0.178	89	1.03	2.75	18.52	2.65	2.58	9.4	62.0	0.56	20.7
6:32-34	33	16.0	0.257	88	0.86	2.20	15.61	2.25	2.38	8.3	48.9	0.61	18.9
6:34-36	35	16.8	0.201	90	0.96	2.73	18.48	2.79	2.90	9.4	64.5	0.64	21.2
6:36-38	37	17.7	0.196	86	0.85	2.29	17.60	2.40	2.34	8.8	55.4	0.50	19.3
6:38-40	39	18.5	0.190	87	0.86	2.41	19.55	2.66	2.22	10.1	70.3	0.51	20.0
6:40-42	41	19.4	0.141	87	0.97	2.84	21.38	3.10	2.74	9.3	75.8	0.45	21.7
6:42-44	43	20.3	0.173	85	0.86	2.19	17.85	2.50	2.33	8.6	63.5	0.42	17.4
6:44-46	45	21.1	0.138	87	1.07	2.86	21.43	2.87	2.77	10.4	71.9	0.43	20.8
6:46-48	47	22.0	0.152	91	1.50	4.18	30.05	4.27	3.73	16.3	101.5	0.78	31.3
6:48-49	48.5	22.6	0.220	87	0.40	2.47	18.40	1.49	3.22	9.0	58.5	0.56	16.5
6:49-50	49.5	23.1	0.292	92	1.08	2.98	22.44	2.59	4.29	12.3	67.5	0.65	20.4
6:50-52	51	23.7	0.136	86	1.06	2.92	21.08	2.51	3.81	10.7	61.0	0.43	19.6

Table B.4 (continued): GGC6 ICP-MS Results of carbonate-free component

TiO_2 (wt%)	V	Cr	MnO (wt%)	Co	Ni	Cu	Zn	Rb	Sr	Y	Zr	Cs	Ba	La	Ce	Pr
Carbonate-free component (concentrations reported as ppm unless otherwise stated)																
1.26	334	129	1.20	161.3	89.9	274	156	134.0	332	57.2	221	8.00	1123	69.1	214	15.2
1.10	282	102	1.10	143.2	87.2	258	143	112.7	276	55.9	188	6.88	1825	64.0	183	14.3
0.89	228	84	0.84	107.4	69.6	192	115	104.2	287	50.4	161	6.33	1994	62.6	159	13.3
1.03	265	111	1.02	196.0	85.4	224	128	90.0	231	54.8	166	5.85	1423	54.0	165	12.0
0.93	297	94	0.98	128.7	58.3	210	117	82.8	223	42.6	149	4.78	504	48.0	143	10.4
1.11	353	105	1.34	163.5	87.5	288	146	94.6	269	65.5	180	5.29	725	62.5	182	14.1
0.92	379	90	1.45	175.0	66.2	284	138	75.7	284	54.5	151	4.50	570	57.6	169	12.3
1.07	392	106	1.76	210.2	102.4	353	158	85.3	332	84.7	195	4.75	562	81.7	222	18.1
1.22	387	110	1.71	229.4	119.2	381	177	108.0	355	84.0	220	6.38	890	88.2	248	19.4
1.00	271	96	1.15	155.3	83.1	259	135	99.6	324	72.6	181	5.87	1158	79.2	206	17.5
0.93	261	94	1.18	153.9	96.4	284	145	95.7	308	67.9	176	5.42	1508	71.2	192	15.6
1.20	254	102	1.09	164.0	99.7	300	162	116.8	304	57.3	196	6.81	2276	68.9	219	15.5
1.08	262	112	1.00	136.1	98.9	293	163	123.8	323	65.5	211	7.25	2974	73.7	207	17.1
1.19	241	108	0.87	134.9	93.8	287	153	127.0	328	46.5	205	7.57	4175	62.1	206	14.2
0.96	201	88	0.63	97.5	54.9	209	131	107.3	271	31.1	171	6.13	3649	45.1	147	9.8
1.02	211	91	0.75	114.1	77.4	240	137	112.9	280	36.8	178	6.53	3306	51.3	151	11.6
0.82	201	85	0.65	88.5	51.5	195	123	93.9	238	30.8	165	5.82	3294	42.0	139	9.6
1.08	214	95	0.82	129.4	80.3	242	141	113.0	302	40.8	181	6.92	4216	54.8	186	12.5
0.87	211	92	0.63	91.9	54.3	217	132	100.8	260	24.9	175	6.40	4732	38.9	140	8.5
1.01	207	101	0.75	117.8	69.1	222	137	114.4	288	33.9	191	6.99	5348	50.0	169	11.3
1.11	211	101	0.80	128.7	84.9	240	168	126.2	316	31.9	192	7.60	5489	50.5	178	11.0
0.99	193	92	0.61	100.7	52.4	195	126	111.9	241	23.3	174	6.53	3618	37.9	141	8.3
1.17	211	103	0.99	169.2	82.3	235	154	126.7	273	28.6	181	7.72	3499	46.9	192	10.6
1.57	300	150	1.23	190.5	113.0	334	206	177.3	391	66.3	269	9.49	5098	85.6	261	19.6
0.91	165	90	0.58	93.9	58.5	182	117	99.9	224	34.2	155	5.84	2527	46.6	143	10.5
1.15	220	110	1.09	211.6	89.9	254	151	109.9	214	46.2	188	6.57	1324	61.2	211	13.4
1.11	199	102	0.64	112.2	71.4	273	151	107.2	260	26.2	166	6.15	3107	41.0	141	9.3

Table B.4 (continued): GGC6 ICP-MS Results of carbonate-free component

Nd	Sm	Eu	Gd	Tb	Dy	Ho	Er	Yb	Lu	Hf	Ta	Pb	Th	U
Carbonate-free component (concentrations reported as ppm unless otherwise stated)														
55.9	10.68	2.40	9.89	1.53	8.68	1.72	5.02	4.71	0.695	5.58	1.90	106	21.78	2.68
52.3	10.01	2.35	9.20	1.43	8.44	1.63	4.76	4.53	0.659	4.57	1.50	70	19.24	2.19
49.3	9.47	2.40	8.91	1.37	7.78	1.54	4.43	4.01	0.588	4.05	1.42	65	18.00	1.97
45.8	9.05	2.12	8.89	1.35	7.97	1.57	4.40	3.97	0.602	4.17	1.38	73	13.70	1.76
37.8	7.16	1.57	6.69	1.03	6.17	1.25	3.63	3.39	0.495	3.34	0.90	61	14.83	1.67
51.3	10.27	2.30	9.90	1.57	9.24	1.88	5.42	5.04	0.750	4.17	1.08	69	17.42	1.99
44.7	8.63	1.92	8.32	1.25	7.62	1.54	4.43	3.98	0.586	3.07	0.68	80	17.23	1.69
66.3	12.88	2.84	12.55	1.98	11.56	2.32	6.68	6.16	0.909	4.34	1.25	87	21.77	2.01
72.6	13.98	3.12	13.43	2.01	12.20	2.42	6.95	6.37	0.908	5.14	1.84	98	25.47	2.24
66.3	12.86	2.87	12.17	1.88	10.57	2.09	5.93	5.24	0.764	4.47	1.63	87	23.46	1.97
57.7	10.90	2.57	10.55	1.61	9.44	1.87	5.35	4.80	0.680	3.84	1.22	68	20.92	1.86
58.4	11.24	2.70	10.36	1.49	9.12	1.79	5.10	4.73	0.683	5.14	1.73	72	22.06	2.15
63.7	11.96	3.06	11.11	1.71	9.68	1.89	5.40	4.92	0.713	4.95	1.48	73	23.94	2.32
51.9	9.87	2.65	8.76	1.28	7.76	1.53	4.37	4.23	0.609	5.38	1.93	65	21.10	2.28
34.9	6.39	1.96	5.54	0.85	4.94	0.98	2.86	2.70	0.399	4.05	0.96	47	17.74	1.88
42.6	8.05	2.23	7.01	1.03	6.25	1.23	3.56	3.50	0.513	4.69	1.60	53	17.64	2.02
34.3	5.99	1.81	5.30	0.85	4.82	0.95	2.77	2.71	0.387	3.66	0.94	47	15.45	1.71
46.0	8.68	2.40	7.65	1.12	6.83	1.35	3.87	3.72	0.542	4.78	1.49	56	18.38	2.10
30.4	5.22	1.89	4.50	0.72	4.08	0.82	2.43	2.46	0.356	3.91	0.90	49	15.31	1.92
40.1	7.30	2.45	6.29	1.00	5.54	1.11	3.22	3.09	0.449	4.57	1.58	58	17.04	2.24
39.7	7.28	2.26	6.24	0.93	5.62	1.13	3.28	3.28	0.492	5.17	1.70	59	17.61	2.46
29.3	5.24	1.69	4.47	0.70	3.97	0.80	2.37	2.39	0.355	4.22	1.29	46	15.93	2.12
38.1	6.91	1.89	5.80	0.84	5.21	1.05	3.06	3.10	0.463	4.90	1.52	67	17.61	2.41
71.0	13.14	3.64	11.87	1.85	10.51	2.04	5.95	5.68	0.852	6.92	2.23	85	27.04	3.43
38.3	7.14	2.06	6.42	1.00	5.50	1.08	3.13	2.93	0.434	3.96	1.25	49	15.13	1.91
48.7	9.00	2.02	8.18	1.29	7.16	1.43	4.03	3.75	0.562	4.67	1.43	84	17.37	2.13
33.3	6.14	1.74	5.24	0.79	4.75	0.95	2.78	2.80	0.415	4.31	1.29	48	14.20	2.10

Table B.4: GGC6 ICP-MS Results of carbonate-free component

Sample Interval (cm)	Avg. Depth (cm)	Age (ka)	ICP Bulk Sample Mass (g)	$CaCO_3$ (wt%)	Na_2O (wt%)	MgO (wt%)	Al_2O_3 (wt%)	K_2O (wt%)	CaO (wt%)	Fe_2O_3 (wt%)	Li	P_2O_5 (wt%)	Sc
KN207-2-GGC6 (continued)				**Carbonate-free component (concentrations reported as ppm unless otherwise stated)**									
6:52-54	53	24.6	0.170	88	1.16	3.13	23.63	3.36	2.66	11.8	79.4	0.59	24.0
6:54-56	55	25.4	0.140	86	1.00	2.83	20.90	3.00	2.50	9.0	69.5	0.39	21.0
6:56-58	57	26.3	0.178	87	1.07	3.00	23.56	3.00	3.24	10.9	74.1	0.56	21.9
6:58-60	59	27.1	0.189	87	0.89	2.38	17.87	2.62	2.31	8.7	61.6	0.45	18.0
6:60-62	61	28.0	0.157	88	1.08	3.09	21.36	3.04	2.97	10.2	71.9	0.51	22.0
6:62-64	63	29.1	0.215	91	1.28	3.46	25.79	3.67	3.36	13.4	88.0	0.73	26.3
6:64-66	65	30.1	0.183	89	0.97	2.78	19.08	2.69	2.89	9.0	64.6	0.48	20.1
6:66-68	67	31.2	0.235	91	1.06	2.82	20.51	3.02	2.88	10.2	71.3	0.58	21.6
6:68-70	69	32.2	0.276	90	0.98	2.48	17.27	2.55	3.02	9.9	61.0	0.65	18.6
6:70-71	70.5	33.0	0.246	92	1.03	2.96	19.77	2.64	3.82	10.0	62.7	0.67	21.8
6:71-73	72	33.8	0.494	93	0.73	1.85	13.13	1.71	3.41	7.8	51.6	0.70	16.5
6:73-74	73.5	34.6	0.348	95	1.64	4.58	30.11	4.47	4.83	16.9	106.4	1.31	35.0
6:74-76	75	35.4	0.253	92	0.95	2.89	18.72	2.98	3.06	8.9	65.3	0.73	21.3
6:76-78	77	36.4	0.319	94	1.16	3.26	24.00	3.36	3.47	12.8	81.9	0.95	23.9
6:78-80	79	37.4	0.374	93	1.05	2.33	16.20	2.46	3.09	9.0	61.7	0.67	21.3
6:80-82	81	38.4	0.260	92	0.95	2.85	18.89	2.82	2.89	9.5	65.3	0.68	21.7
6:82-84	83	39.5	0.290	92	1.05	2.92	19.60	2.89	3.05	11.2	69.0	0.75	20.9
6:84-86	85	40.5	0.265	91	0.41	3.07	20.98	1.79	3.25	10.8	72.5	0.79	20.1
6:86-88	87	41.5	0.201	91	1.07	3.03	20.98	3.11	3.01	10.0	72.2	0.64	23.1
6:88-90	89	42.5	0.279	92	1.13	3.03	20.78	3.11	2.89	11.7	75.2	0.82	24.1
6:90-92	91	43.6	0.287	93	0.34	3.67	23.50	1.64	4.38	12.6	81.9	0.89	21.2
6:92-94	93	44.6	0.287	92	0.97	2.72	19.34	2.79	2.87	11.5	69.0	0.80	20.5
6:94-96	95	45.6	0.338	92	0.87	2.36	15.96	2.29	2.97	9.7	58.0	0.82	19.1
6:96-98	97	46.6	0.321	93	0.97	2.96	19.67	2.78	2.80	12.1	67.5	0.85	21.6
6:98-100	99	47.6	0.270	91	0.80	2.14	15.26	2.28	2.08	8.6	66.7	0.66	20.1
6:100-102	101	48.6	0.249	92	0.97	2.80	21.20	3.08	2.57	12.1	79.7	0.76	22.5
6:102-104	103	49.5	0.278	92	1.15	3.27	22.46	3.28	2.85	12.7	82.2	0.81	25.5
6:104-106	105	50.5	0.376	93	1.05	3.10	19.36	2.84	2.97	12.2	70.9	0.92	23.1

Table B.4 (continued): GGC6 ICP-MS Results of carbonate-free component

TiO_2 (wt%)	V	Cr	MnO (wt%)	Co	Ni	Cu	Zn	Rb	Sr	Y	Zr	Cs	Ba	La	Ce	Pr
Carbonate-free component (concentrations reported as ppm unless otherwise stated)																
1.18	233	120	0.87	141.6	76.5	232	159	144.6	314	46.5	221	8.28	4638	65.9	203	14.9
1.04	198	100	0.70	120.0	71.2	211	137	129.0	281	31.2	180	7.61	3579	50.3	155	11.0
1.09	200	114	0.81	113.1	77.2	232	142	129.2	297	53.7	188	7.68	4091	65.7	184	14.9
0.95	177	92	0.56	87.0	51.6	200	126	117.5	245	27.0	167	6.97	3583	41.3	144	9.2
1.15	197	104	0.74	114.8	81.7	250	150	130.0	294	36.8	179	8.00	4193	53.2	183	12.3
1.34	245	132	1.02	144.3	89.6	279	169	158.9	355	56.7	229	9.19	4893	74.5	222	17.0
1.11	180	94	0.68	105.4	72.1	219	148	116.8	278	33.7	159	7.05	3485	47.9	147	11.0
1.14	209	108	0.71	107.2	61.2	231	148	136.3	299	33.5	195	8.24	4306	50.5	172	11.3
1.02	184	99	0.84	103.5	78.1	218	129	107.0	258	48.5	167	6.87	3058	55.5	155	12.7
1.09	201	105	0.89	116.5	88.5	251	137	110.6	280	45.9	171	6.72	2721	56.2	167	12.7
0.89	189	89	0.91	142.3	63.1	197	123	90.4	228	40.1	147	5.49	1610	50.8	158	10.8
1.64	321	160	1.58	180.2	146.1	369	225	189.6	470	95.3	288	11.88	5320	102.7	279	23.2
1.03	191	101	0.88	105.0	83.0	227	140	118.8	296	50.6	169	7.36	3306	62.5	184	14.2
1.21	233	117	1.17	130.4	89.8	267	167	144.8	364	69.8	221	8.85	4370	78.5	221	18.0
0.92	207	97	0.89	104.8	62.2	218	147	122.7	310	51.2	167	6.64	3206	61.6	181	14.1
0.99	193	99	0.97	118.6	84.1	252	130	118.1	286	51.3	178	7.26	3577	61.3	214	14.0
1.08	209	108	1.01	122.5	78.8	242	140	124.1	316	60.6	197	6.91	3788	68.3	202	15.9
1.06	197	105	0.81	102.7	73.1	229	142	132.1	332	59.5	200	7.83	4232	72.1	198	16.1
1.10	214	105	0.90	120.0	83.1	251	150	131.3	329	47.9	189	7.81	3850	63.7	180	14.4
1.18	226	114	0.99	121.5	84.5	254	155	133.4	320	65.1	203	8.03	4115	72.6	199	16.8
1.18	234	118	1.25	135.4	95.1	257	160	146.4	388	59.2	210	8.78	4214	71.5	224	16.2
1.09	214	105	1.07	111.0	75.8	235	140	121.3	288	58.9	187	7.08	2976	66.9	190	15.3
0.99	203	91	0.93	104.4	56.3	213	132	108.5	264	47.2	169	6.33	2582	57.3	176	13.0
1.10	220	106	1.12	121.1	80.4	243	146	121.6	276	62.8	190	7.47	2739	69.6	198	15.8
1.03	208	98	0.82	102.8	55.9	215	140	118.6	254	39.5	179	6.88	2426	55.4	173	11.8
1.19	226	114	0.99	120.4	79.5	256	151	139.6	308	60.5	213	8.44	3299	75.4	211	17.1
1.26	241	125	1.07	125.0	85.4	274	166	142.6	314	65.2	219	9.03	3271	75.1	211	17.0
1.12	229	107	1.12	124.1	84.9	252	149	121.4	291	68.0	183	7.41	2961	67.1	190	15.4

Table B.4 (continued): GGC6 ICP-MS Results of carbonate-free component

Nd	Sm	Eu	Gd	Tb	Dy	Ho	Er	Yb	Lu	Hf	Ta	Pb	Th	U
Carbonate-free component (concentrations reported as ppm unless otherwise stated)														
53.4	9.72	2.82	8.56	1.34	7.47	1.46	4.25	4.08	0.591	5.35	1.87	63	20.91	2.70
39.8	7.29	2.07	6.15	0.91	5.55	1.10	3.20	3.22	0.477	4.87	1.67	52	17.09	2.36
54.8	10.44	2.88	9.43	1.49	8.25	1.63	4.67	4.21	0.615	4.73	1.59	58	19.77	2.47
32.3	5.84	1.78	5.03	0.79	4.47	0.90	2.64	2.65	0.392	4.12	1.24	41	16.62	2.12
44.6	8.27	2.29	7.24	1.05	6.39	1.28	3.66	3.60	0.529	4.84	1.54	55	17.72	2.37
61.5	11.50	3.21	10.19	1.59	8.83	1.75	5.00	4.62	0.682	5.79	1.86	71	24.75	2.89
40.5	7.55	2.12	6.59	0.96	5.81	1.15	3.31	3.22	0.471	4.30	0.99	48	16.01	2.06
39.8	7.24	2.21	6.26	0.97	5.48	1.09	3.17	3.17	0.460	4.82	1.44	49	19.59	2.37
47.3	9.29	2.45	8.41	1.29	7.43	1.40	4.02	3.66	0.543	4.23	1.30	50	16.98	1.90
47.6	9.16	2.34	8.37	1.22	7.38	1.46	4.11	3.86	0.571	4.55	1.40	54	16.78	2.02
39.8	7.33	1.78	6.83	1.02	5.85	1.16	3.29	3.01	0.452	3.58	0.85	54	13.51	1.62
86.9	17.05	4.41	15.81	2.39	13.84	2.61	7.53	6.73	1.009	7.25	2.21	93	30.36	3.33
52.9	10.23	2.61	9.38	1.34	8.06	1.57	4.43	4.06	0.597	4.51	1.48	54	20.96	2.18
67.1	12.85	3.44	11.86	1.85	10.20	2.03	5.74	4.92	0.735	5.56	1.84	75	25.38	2.67
49.5	9.81	2.57	8.70	1.33	7.40	1.44	4.13	3.79	0.556	4.00	0.67	49	19.04	2.15
52.2	10.07	2.56	9.21	1.34	8.10	1.59	4.51	4.20	0.630	4.73	1.61	60	19.70	2.20
58.9	11.14	3.02	10.58	1.61	8.95	1.76	4.96	4.47	0.675	4.89	1.59	65	21.03	2.26
60.7	11.71	3.40	10.81	1.65	9.07	1.76	5.02	4.49	0.658	5.13	1.67	64	22.79	2.42
53.1	10.16	2.71	9.01	1.30	7.86	1.53	4.39	4.12	0.606	5.13	1.63	61	21.07	2.36
62.5	12.25	3.20	11.05	1.69	9.81	1.83	5.20	4.63	0.677	5.09	1.76	64	20.95	2.28
61.4	11.95	3.44	10.99	1.67	9.19	1.79	5.10	4.56	0.674	5.53	1.80	77	21.58	2.71
57.0	10.92	2.79	10.19	1.57	8.74	1.71	4.85	4.28	0.642	4.71	1.52	62	20.58	2.26
47.2	9.00	2.28	8.28	1.25	7.09	1.38	3.92	3.60	0.528	4.08	1.22	51	17.94	1.97
58.8	11.24	2.74	10.50	1.63	9.06	1.81	5.02	4.48	0.659	4.68	1.54	70	21.64	2.31
42.0	7.72	1.97	6.81	1.03	6.06	1.19	3.45	3.16	0.462	4.26	0.99	52	18.98	2.12
62.8	11.81	3.00	10.76	1.66	9.19	1.80	5.11	4.57	0.664	5.29	1.86	71	23.44	2.61
63.1	12.30	3.07	11.24	1.72	9.83	1.86	5.34	4.76	0.706	5.47	1.78	67	23.16	2.56
58.4	11.42	2.75	11.19	1.68	9.58	1.91	5.15	4.67	0.694	4.48	1.52	70	20.80	2.22

Table B.4: GGC6 ICP-MS Results of carbonate-free component

Sample Interval (cm)	Avg. Depth (cm)	Age (ka)	ICP Bulk Sample Mass (g)	$CaCO_3$ (wt%)	Na_2O (wt%)	MgO (wt%)	Al_2O_3 (wt%)	K_2O (wt%)	CaO (wt%)	Fe_2O_3 (wt%)	Li	P_2O_5 (wt%)	Sc
KN207-2-GGC6 (continued)				**Carbonate-free component (concentrations reported as ppm unless otherwise stated)**									
6:106-108	107	51.5	0.381	95	1.23	2.90	18.63	2.69	3.52	12.7	74.1	1.32	25.6
6:108-110	109	52.5	0.400	94	1.13	3.23	19.75	2.69	4.47	13.6	65.6	1.10	24.1
6:110-112	111	53.5	0.353	93	0.30	3.11	19.81	1.25	4.50	12.2	62.9	1.08	19.4
6:112-114	113	54.5	0.276	92	1.09	3.17	20.29	2.74	3.62	12.1	66.8	0.76	20.8
6:114-116	115	55.4	0.249	90	1.08	2.74	17.75	2.39	3.04	10.2	67.0	0.66	21.1
6:116-118	117	56.4	0.225	88	0.81	2.07	14.77	2.06	2.53	8.1	56.5	0.49	17.8
6:118-120	119	57.4	0.254	90	1.07	2.76	19.01	2.54	3.27	10.3	65.0	0.62	20.8
6:120-122	121	58.3	0.240	92	1.33	3.53	26.21	3.18	4.79	14.0	79.1	0.74	25.4
6:122-124	123	59.1	0.195	91	0.68	4.17	30.86	2.39	5.88	15.0	88.6	0.75	24.9
6:124-126	125	60.0	0.161	88	1.56	3.72	27.82	3.24	5.65	13.1	78.5	0.53	25.0
6:126-128	127	60.8	0.137	83	0.58	2.76	21.71	1.75	4.31	9.1	56.3	0.35	15.5
6:128-130	129	61.7	0.098	78	1.21	2.88	21.64	2.24	4.85	9.7	50.3	0.29	17.6
6:130-132	131	62.6	0.120	82	0.74	3.25	24.51	1.88	5.88	10.0	58.2	0.32	17.2
6:132-134	133	63.4	0.122	82	1.38	3.54	26.23	2.60	5.71	11.4	56.7	0.35	22.5
6:134-136	135	64.3	0.120	78	0.57	2.76	20.93	1.60	4.62	9.4	52.3	0.32	16.2
6:136-138	137	65.1	0.119	84	1.45	3.50	25.72	2.79	5.61	12.7	66.2	0.41	23.3
6:138-140	139	66.0	0.141	83	0.45	2.65	20.35	1.65	3.13	9.9	59.8	0.37	15.5
6:140-142	141	66.9	0.141	85	1.20	3.12	23.05	2.90	3.62	12.2	70.9	0.45	21.9
6:142-144	143	67.7	0.158	86	0.49	2.97	22.44	1.86	3.18	11.8	69.6	0.50	19.6
6:144-147	145.5	68.8	0.146	88	1.01	2.77	22.04	2.91	2.92	13.0	81.6	0.58	24.4

Table B.4 (continued): GGC6 ICP-MS Results of carbonate-free component

TiO_2 (wt%)	V	Cr	MnO (wt%)	Co	Ni	Cu	Zn	Rb	Sr	Y	Zr	Cs	Ba	La	Ce	Pr
Carbonate-free component (concentrations reported as ppm unless otherwise stated)																
1.26	267	117	1.34	139.8	92.8	305	179	131.1	357	82.6	211	7.65	3083	79.3	221	18.3
1.18	249	110	1.34	132.4	103.1	305	163	114.1	363	81.8	188	6.23	2838	71.3	207	16.6
1.06	211	101	1.07	113.3	85.5	264	146	109.1	325	66.5	171	6.60	2553	64.2	188	15.0
1.16	214	109	1.03	115.7	88.5	274	149	113.1	280	55.9	180	6.37	2430	60.4	184	13.8
1.12	194	108	0.85	101.3	83.2	261	149	110.2	258	49.1	170	6.40	2266	55.3	164	12.7
1.02	177	90	0.63	78.2	50.8	207	127	98.2	213	25.9	145	5.64	2023	36.8	128	7.8
1.10	191	105	0.83	99.8	77.3	237	141	110.3	250	46.8	172	6.74	2324	53.1	158	12.1
1.40	243	143	1.02	124.8	98.3	303	172	134.0	316	59.2	220	7.83	2954	67.5	201	15.5
1.56	255	154	0.89	120.0	96.3	310	201	153.3	335	51.4	242	9.07	3265	65.6	215	15.2
1.36	223	150	0.80	103.8	97.9	286	161	133.9	314	53.8	213	7.39	3050	63.5	183	14.6
1.00	158	101	0.54	71.6	60.9	203	120	100.7	224	25.2	155	5.82	2531	36.6	133	8.3
0.97	153	104	0.54	67.7	65.3	209	108	90.1	220	25.6	145	4.84	2197	35.8	124	8.0
1.09	173	124	0.53	67.5	66.4	219	124	105.1	256	25.3	161	6.06	2573	36.4	132	8.2
1.16	184	129	0.66	81.4	82.9	245	133	105.5	271	35.7	171	6.10	2554	46.3	148	10.4
0.97	154	105	0.50	63.2	58.8	197	117	93.3	208	22.9	146	5.42	1852	33.7	126	7.5
1.25	206	129	0.71	88.1	85.4	271	140	116.0	262	38.6	185	6.37	2300	51.0	163	11.4
0.99	170	97	0.60	74.6	63.1	212	130	107.3	193	26.8	165	6.32	1808	40.4	151	8.9
1.17	212	117	0.81	94.3	85.7	264	143	123.4	248	46.6	192	6.75	2293	60.6	181	13.6
1.10	205	114	0.72	86.3	68.6	244	143	123.1	218	33.6	190	7.37	1976	50.6	174	11.1
1.25	239	122	0.90	104.5	85.8	282	155	130.6	246	52.9	211	8.08	2092	67.1	196	15.2

Table B.4 (continued): GGC6 ICP-MS Results of carbonate-free component

Nd	Sm	Eu	Gd	Tb	Dy	Ho	Er	Yb	Lu	Hf	Ta	Pb	Th	U
Carbonate-free component (concentrations reported as ppm unless otherwise stated)														
68.5	13.75	3.45	13.29	2.02	11.54	2.29	6.43	5.60	0.827	5.15	1.29	63	24.09	2.42
63.9	12.57	3.26	12.80	1.94	11.22	2.23	6.31	5.51	0.837	4.69	1.44	70	21.19	2.20
58.1	11.61	3.03	11.27	1.72	9.69	1.92	5.40	4.70	0.689	4.42	1.34	68	20.00	2.01
51.6	10.04	2.54	9.66	1.48	8.37	1.65	4.66	4.20	0.628	4.56	1.24	59	18.24	2.06
47.0	9.23	2.33	8.60	1.32	7.53	1.48	4.18	3.82	0.565	4.24	1.00	43	15.84	2.02
28.2	5.17	1.40	4.54	0.72	4.13	0.83	2.43	2.31	0.337	3.54	0.76	39	13.94	1.71
45.2	8.75	2.23	8.16	1.25	7.24	1.39	4.01	3.66	0.541	4.36	1.19	46	16.07	2.00
57.4	11.01	2.85	10.36	1.61	9.11	1.80	5.12	4.64	0.687	5.54	1.66	64	20.31	2.50
55.4	10.61	2.97	9.60	1.51	8.44	1.66	4.80	4.52	0.661	6.30	1.90	68	22.11	2.84
53.8	10.27	2.73	9.68	1.49	8.51	1.68	4.81	4.47	0.677	5.44	1.57	54	17.75	2.50
29.6	5.46	1.76	4.93	0.79	4.37	0.87	2.56	2.49	0.370	4.00	1.24	43	13.32	1.85
29.1	5.36	1.54	4.89	0.79	4.45	0.89	2.59	2.54	0.386	3.75	1.08	37	11.49	1.66
29.6	5.49	1.81	4.99	0.80	4.44	0.89	2.61	2.55	0.377	4.15	1.28	43	13.18	1.89
38.0	7.19	1.98	6.53	1.06	5.99	1.20	3.45	3.21	0.478	4.29	1.31	45	14.01	1.97
26.8	4.93	1.50	4.49	0.72	4.02	0.81	2.37	2.31	0.344	3.74	1.14	40	12.33	1.72
41.4	7.80	2.05	7.17	1.14	6.50	1.30	3.73	3.63	0.533	4.73	1.42	48	15.34	2.17
31.8	5.78	1.60	5.18	0.83	4.59	0.92	2.71	2.67	0.392	4.18	1.33	47	14.39	2.00
49.6	9.16	2.31	8.50	1.32	7.48	1.48	4.26	4.04	0.605	4.88	1.53	53	16.84	2.33
39.6	7.25	1.91	6.45	1.03	5.69	1.13	3.34	3.24	0.477	4.87	1.56	56	17.31	2.33
55.4	10.44	2.49	9.40	1.49	8.32	1.65	4.76	4.35	0.640	5.20	1.76	61	19.78	2.58

Table B.5: GGC6 ICP-MS Results of carbonate component

Sample Interval (cm)	Na_2O (wt%)	MgO (wt%)	Al_2O_3 (wt%)	K_2O (wt%)	CaO (wt%)	Fe_2O_3 (wt%)	Li	P_2O_5 (wt%)	Sc	TiO_2 (wt%)	V	Cr
KN207-2-GGC6												
6:0-2	1.29	0.59	0.35	0.08	50.1	0.19	1.81	0.035	1.39	0.01	2.86	9.56
6:2-4	1.40	0.49	0.16	0.11	55.7	0.36	1.90	0.031	1.01	0.03	1.11	7.76
6:4-6	1.17	0.52	0.32	0.08	46.6	0.11	2.08	0.020	1.14	0.01	2.20	6.74
6:6-8	0.93	0.32	0.15	0.06	46.8	0.08	1.74	0.023	1.02	0.05	1.30	6.91
6:8-10	1.14	0.37	0.25	0.08	56.9	0.41	1.93	0.025	1.32	0.03	1.70	9.12
6:10-12	1.33	0.50	0.03	0.10	58.2	0.27	1.81	0.029	0.81	0.03	0.63	7.30
6:12-14	1.27	0.43	0.25	0.08	56.0	0.39	2.10	0.024	1.35	0.03	1.66	8.68
6:14-16	1.17	0.54	0.03	0.09	62.8	0.24	1.62	0.020	0.69	0.03	0.46	6.03
6:16-18	1.21	0.44	0.24	0.07	48.9	0.12	1.51	0.030	0.36	0.02	0.48	6.92
6:18-20	1.39	0.53	0.31	0.08	47.3	0.10	1.86	0.018	0.84	0.01	2.14	5.77
6:20-22	1.19	0.41	0.13	0.09	58.8	0.29	1.68	0.026	0.79	0.03	0.89	6.46
6:22-24	1.26	0.37	0.29	0.07	48.3	0.16	1.87	0.042	0.76	0.00	0.00	8.39
6:24-26	1.12	0.43	0.29	0.08	53.5	0.26	2.10	0.027	1.17	0.02	1.90	7.72
6:26-28	1.33	0.39	0.30	0.08	47.1	0.17	2.28	0.045	1.01	0.00	0.00	9.76
6:28-30	1.35	0.43	0.30	0.11	59.8	0.52	2.89	0.039	1.97	0.03	1.74	12.67
6:30-32	1.42	0.41	0.31	0.09	49.6	0.22	2.48	0.046	1.15	0.00	0.00	10.84
6:32-34	1.40	0.44	0.30	0.11	60.1	0.51	2.85	0.039	1.95	0.03	1.66	12.11
6:34-36	1.37	0.42	0.31	0.08	47.3	0.18	2.54	0.045	1.15	0.00	0.00	10.20
6:36-38	1.43	0.53	0.36	0.13	61.7	0.60	4.00	0.036	2.22	0.03	1.73	13.10
6:38-40	1.56	0.59	0.20	0.12	53.8	0.26	3.53	0.027	0.82	0.05	1.21	9.47
6:40-42	1.50	0.50	0.35	0.10	49.6	0.25	3.60	0.045	1.80	0.00	0.00	13.10
6:42-44	1.90	0.62	0.41	0.15	60.6	0.65	4.68	0.041	2.98	0.03	1.78	16.68
6:44-46	1.86	0.62	0.37	0.12	50.8	0.27	3.68	0.051	2.08	0.00	0.00	13.28
6:46-48	1.45	0.65	0.52	0.13	64.7	0.37	2.86	0.038	2.03	0.03	0.00	10.31
6:48-49	1.39	0.64	0.38	0.10	53.7	0.17	3.10	0.025	1.77	0.01	2.29	9.10
6:49-50	1.63	0.47	0.34	0.10	58.0	0.24	2.30	0.022	1.63	0.03	0.31	7.11
6:50-52	1.90	0.59	0.36	0.13	48.3	0.29	3.22	0.044	2.15	0.00	0.00	14.42

Table B.5 (continued): GGC6 ICP-MS Results of carbonate component

MnO (wt%)	Co	Ni	Cu	Zn	Rb	Sr	Y	Zr	Cs	Ba	La	Ce	Pr	Nd
0.04	1.58	13.5	22	6.7	0.373	2281	16.7	1.37	0.022	10.0	10.0	5.72	2.40	10.2
0.03	0.89	14.2	14	5.5	0.350	2322	16.6	1.30	0.025	13.3	9.6	4.94	2.35	10.0
0.04	1.66	12.9	16	5.7	0.422	2295	17.1	1.15	0.021	26.0	10.0	5.89	2.39	10.2
0.02	0.73	13.5	4	3.9	0.273	1846	7.0	0.82	0.027	14.1	4.7	2.30	1.15	5.0
0.04	2.35	17.3	15	3.7	0.388	2207	12.8	2.02	0.026	10.4	6.8	4.16	1.59	6.9
0.03	0.96	13.2	14	4.9	0.269	2493	11.7	0.57	0.024	9.5	6.4	3.25	1.60	6.7
0.04	2.19	18.3	21	5.5	0.392	2358	14.1	2.04	0.026	9.6	7.1	4.20	1.66	7.2
0.03	0.61	14.5	15	5.1	0.265	2471	12.2	0.46	0.024	10.6	6.8	3.05	1.65	6.8
0.03	0.83	13.7	14	5.6	0.501	2036	13.5	1.73	0.036	16.7	8.2	3.93	1.92	8.3
0.04	2.04	13.2	18	5.7	0.435	2062	14.1	1.12	0.022	19.2	8.6	4.53	2.01	8.5
0.02	0.55	14.1	14	4.6	0.312	2111	14.5	1.19	0.025	14.5	8.8	3.84	2.10	8.9
0.03	0.71	12.4	13	5.7	0.595	1789	15.8	2.39	0.040	21.9	9.8	4.68	2.37	10.2
0.03	1.32	13.8	15	5.2	0.428	1954	16.5	1.60	0.025	26.2	10.2	4.64	2.45	10.5
0.03	0.62	12.6	12	5.4	0.622	1706	17.7	2.50	0.040	24.2	11.2	5.20	2.75	11.9
0.04	2.22	20.6	19	6.0	0.545	2054	21.5	2.09	0.026	37.3	13.3	6.82	3.28	14.0
0.03	0.83	14.1	13	7.2	0.665	1865	19.6	2.51	0.040	29.8	12.0	5.58	2.98	12.8
0.04	3.02	19.6	17	5.9	0.546	2073	20.5	2.03	0.027	39.3	12.4	6.68	2.99	12.8
0.03	1.15	12.9	12	5.8	0.674	1878	18.9	2.41	0.042	37.6	11.3	5.28	2.77	12.0
0.05	4.14	20.0	17	6.4	0.626	2163	24.2	2.05	0.027	70.1	15.7	8.06	3.82	16.4
0.03	1.24	15.8	12	6.6	0.392	2125	20.8	0.80	0.026	36.2	13.6	5.37	3.44	14.7
0.03	1.18	13.8	10	6.4	0.694	2161	22.4	2.42	0.041	34.9	14.4	6.24	3.56	15.3
0.06	4.38	21.6	17	7.0	0.725	2178	23.9	2.04	0.027	58.6	15.5	8.71	3.79	16.1
0.03	1.61	16.7	13	7.3	0.782	2354	23.6	2.44	0.041	38.5	15.4	6.75	3.71	15.9
0.02	0.97	16.3	12	7.6	0.421	2239	21.0	1.48	0.025	30.7	12.8	5.06	3.28	14.2
0.04	2.79	13.3	13	6.6	0.598	2088	19.8	1.22	0.025	52.9	13.4	6.18	3.15	13.6
0.02	0.93	12.6	5	4.9	0.377	1751	11.2	1.13	0.027	17.4	10.1	2.93	2.40	10.1
0.03	1.77	11.8	9	6.3	0.698	2133	21.0	2.40	0.040	37.6	13.9	5.80	3.37	14.5

Table B.5 (continued): GGC6 ICP-MS Results of carbonate component

Sm	Eu	Gd	Tb	Dy	Ho	Er	Yb	Lu	Hf	Ta	Pb	Th	U
2.25	0.50	2.44	0.37	2.12	0.43	1.15	0.92	0.14	0.00	0.000	0.70	0.394	0.316
2.24	0.52	2.54	0.38	2.13	0.46	1.14	0.97	0.14	0.01	0.024	0.53	0.211	0.311
2.23	0.50	2.43	0.37	2.07	0.42	1.11	0.89	0.14	0.00	0.000	0.47	0.206	0.322
0.96	0.22	1.01	0.16	0.85	0.18	0.45	0.36	0.07	0.00	0.018	0.56	0.167	0.220
1.49	0.36	1.77	0.27	1.52	0.32	0.83	0.83	0.10	0.01	0.000	0.41	0.178	0.348
1.50	0.35	1.72	0.26	1.45	0.35	0.79	0.63	0.10	0.00	0.048	0.61	0.134	0.351
1.57	0.38	1.89	0.29	1.65	0.35	0.91	0.92	0.11	0.01	0.000	0.37	0.174	0.395
1.53	0.36	1.78	0.26	1.49	0.36	0.81	0.64	0.10	0.00	0.048	0.56	0.037	0.357
1.71	0.40	1.97	0.29	1.84	0.34	0.93	0.79	0.12	0.00	0.012	0.32	0.114	0.290
1.83	0.41	2.00	0.30	1.72	0.35	0.92	0.74	0.11	0.00	0.000	0.38	0.126	0.305
1.93	0.44	2.17	0.32	1.82	0.40	0.97	0.85	0.11	0.01	0.024	0.47	0.096	0.289
2.14	0.48	2.41	0.35	2.29	0.40	1.11	0.97	0.15	0.01	0.000	0.23	0.287	0.243
2.27	0.52	2.53	0.38	2.13	0.43	1.14	0.99	0.14	0.01	0.000	0.56	0.218	0.277
2.53	0.57	2.83	0.41	2.59	0.46	1.25	1.09	0.16	0.01	0.000	0.26	0.420	0.229
3.07	0.71	3.42	0.51	2.85	0.57	1.51	1.36	0.18	0.02	0.000	0.74	0.529	0.286
2.74	0.61	3.05	0.43	2.79	0.50	1.36	1.17	0.17	0.01	0.000	0.26	0.478	0.251
2.81	0.66	3.19	0.48	2.69	0.54	1.42	1.29	0.17	0.02	0.000	0.64	0.425	0.305
2.57	0.59	2.87	0.41	2.68	0.48	1.30	1.13	0.17	0.01	0.000	0.31	0.387	0.249
3.53	0.80	3.84	0.57	3.19	0.63	1.67	1.47	0.20	0.02	0.000	0.81	0.591	0.322
3.22	0.72	3.46	0.51	2.85	0.59	1.48	1.18	0.17	0.00	0.040	0.77	0.583	0.284
3.29	0.73	3.59	0.51	3.18	0.57	1.55	1.32	0.19	0.01	0.000	0.32	0.724	0.264
3.52	0.81	3.88	0.58	3.21	0.63	1.66	1.44	0.20	0.02	0.000	0.97	0.648	0.332
3.41	0.74	3.71	0.52	3.32	0.59	1.62	1.37	0.20	0.01	0.000	0.39	0.765	0.309
3.15	0.71	3.47	0.51	2.86	0.57	1.50	1.20	0.18	0.00	0.000	0.23	0.348	0.299
2.89	0.65	3.12	0.46	2.61	0.52	1.39	1.13	0.17	0.00	0.000	0.71	0.476	0.322
1.83	0.40	1.87	0.27	1.48	0.30	0.79	0.64	0.11	0.00	0.000	0.25	0.233	0.346
3.06	0.67	3.35	0.47	3.00	0.54	1.47	1.26	0.19	0.01	0.000	0.16	0.669	0.284

Table B.5 (continued): GGC6 ICP-MS Results of carbonate component

Sample Interval (cm)	Na_2O (wt%)	MgO (wt%)	Al_2O_3 (wt%)	K_2O (wt%)	CaO (wt%)	Fe_2O_3 (wt%)	Li	P_2O_5 (wt%)	Sc	TiO_2 (wt%)	V	Cr
KN207-2-GGC6 (continued)												
6:52-54	1.66	0.66	0.36	0.14	61.5	0.36	2.92	0.034	1.43	0.03	0.30	9.56
6:54-56	1.61	0.53	0.35	0.11	50.4	0.26	3.16	0.045	1.56	0.00	0.00	13.26
6:56-58	1.12	0.51	0.85	0.12	52.6	0.32	2.24	0.025	1.20	0.03	0.00	7.36
6:58-60	1.61	0.54	0.36	0.13	61.4	0.59	3.27	0.038	2.26	0.03	1.55	13.23
6:60-62	1.51	0.45	0.33	0.10	50.6	0.24	2.63	0.043	1.57	0.00	0.00	12.26
6:62-64	1.33	0.50	0.53	0.11	62.3	0.22	2.46	0.033	1.89	0.03	0.00	10.88
6:64-66	1.63	0.42	0.32	0.10	49.6	0.21	2.45	0.043	1.35	0.00	0.00	10.86
6:66-68	1.41	0.43	0.32	0.12	58.7	0.51	2.80	0.039	2.27	0.03	1.50	12.86
6:68-70	1.27	0.48	0.28	0.11	71.1	0.31	2.04	0.036	1.91	0.03	0.00	9.43
6:70-71	1.38	0.36	0.30	0.08	47.5	0.16	2.00	0.039	1.09	0.00	0.00	8.84
6:71-73	1.09	0.27	0.24	0.08	57.2	0.34	2.12	0.021	1.47	0.03	1.32	8.46
6:73-74	1.60	0.45	0.37	0.08	56.5	0.03	1.76	0.030	1.08	0.03	0.00	8.01
6:74-76	1.28	0.35	0.30	0.08	46.8	0.15	1.80	0.034	0.87	0.00	0.00	8.08
6:76-78	1.18	0.44	0.46	0.10	69.1	0.29	1.72	0.033	1.32	0.03	0.00	8.43
6:78-80	1.30	0.33	0.26	0.10	57.2	0.38	2.03	0.026	1.55	0.03	1.34	8.90
6:80-82	1.14	0.30	0.30	0.07	48.3	0.15	1.76	0.041	0.93	0.00	0.00	8.50
6:82-84	1.58	0.45	0.39	0.08	58.2	0.06	1.99	0.032	1.36	0.03	0.00	9.21
6:84-86	1.16	0.47	0.35	0.09	50.0	0.14	2.22	0.021	1.41	0.01	2.21	7.59
6:86-88	1.34	0.34	0.32	0.09	48.0	0.20	2.16	0.037	1.10	0.00	0.00	9.90
6:88-90	1.39	0.43	0.05	0.12	57.3	0.29	1.89	0.031	1.11	0.03	0.40	7.93
6:90-92	1.40	0.49	0.35	0.09	49.3	0.15	1.87	0.031	1.54	0.01	2.14	9.14
6:92-94	1.57	0.48	0.40	0.12	65.6	0.30	2.06	0.033	1.45	0.03	0.30	8.78
6:94-96	1.42	0.35	0.27	0.10	57.5	0.43	2.04	0.029	1.75	0.03	1.43	9.71
6:96-98	1.56	0.46	0.28	0.08	53.3	0.13	1.87	0.033	1.65	0.03	0.39	8.34
6:98-100	1.35	0.37	0.29	0.11	58.3	0.45	2.62	0.035	1.93	0.03	1.49	11.22
6:100-102	1.33	0.48	0.21	0.10	52.3	0.15	2.20	0.030	0.44	0.07	1.51	7.39
6:102-104	1.46	0.43	0.35	0.08	56.9	0.05	2.11	0.033	1.45	0.03	0.00	9.37
6:104-106	1.30	0.43	0.17	0.08	48.5	0.15	1.63	0.031	1.70	0.03	0.69	5.83

Table B.5 (continued): GGC6 ICP-MS Results of carbonate component

MnO (wt%)	Co	Ni	Cu	Zn	Rb	Sr	Y	Zr	Cs	Ba	La	Ce	Pr	Nd
0.03	1.29	16.5	12	6.7	0.446	2234	21.6	1.04	0.025	30.6	14.0	5.60	3.59	15.4
0.03	1.31	14.5	10	7.2	0.771	2283	23.8	2.42	0.042	40.0	16.2	7.20	3.94	16.9
0.02	0.56	12.3	9	4.5	0.357	1745	14.9	1.32	0.024	31.2	9.7	3.65	2.50	10.9
0.05	2.87	19.5	14	5.3	0.664	2167	24.0	1.97	0.027	55.9	15.9	8.49	3.84	16.4
0.03	0.91	12.7	9	5.2	0.701	2116	20.9	2.33	0.041	38.4	14.1	6.56	3.43	14.8
0.02	0.97	17.1	13	5.8	0.462	2235	19.0	1.35	0.023	43.2	12.1	5.37	3.03	13.6
0.02	0.67	11.8	9	5.8	0.686	1878	18.7	2.28	0.040	29.6	12.7	6.08	3.10	13.4
0.04	2.19	17.9	13	8.4	0.590	2047	20.0	1.93	0.027	45.0	13.1	7.32	3.19	13.6
0.02	0.62	15.8	13	5.6	0.435	2337	16.9	1.36	0.024	28.2	10.3	4.95	2.64	11.4
0.02	0.53	11.2	8	5.6	0.643	1744	15.3	2.24	0.041	26.1	10.0	4.97	2.36	10.2
0.02	0.93	16.9	11	3.6	0.375	1753	11.1	1.98	0.026	15.2	8.5	3.74	1.93	8.2
0.02	0.56	15.0	9	5.0	0.352	1962	12.9	1.31	0.020	20.2	8.4	4.35	1.97	9.2
0.02	0.73	11.3	8	5.1	0.749	1738	14.4	2.26	0.041	50.7	9.2	5.51	2.23	9.7
0.02	0.58	14.1	11	5.5	0.387	2212	13.7	1.30	0.024	22.4	8.9	4.50	2.31	9.9
0.03	0.91	15.8	11	4.1	0.432	1975	15.2	1.94	0.025	16.5	9.1	5.02	2.18	9.5
0.02	0.51	10.9	8	5.1	0.635	1842	15.2	2.24	0.040	33.6	9.7	4.91	2.33	10.1
0.02	0.81	15.1	11	5.2	0.395	2078	15.5	1.34	0.021	30.5	9.9	4.58	2.35	11.0
0.03	1.56	12.9	14	5.7	0.559	2034	16.7	1.19	0.024	54.5	11.3	6.16	2.73	11.7
0.02	0.67	12.4	10	6.1	0.711	1796	17.4	2.29	0.042	41.9	11.9	5.99	2.90	12.5
0.02	0.34	13.9	11	5.7	0.323	2263	15.7	0.54	0.024	24.2	10.3	5.18	2.60	10.8
0.02	0.47	12.8	17	6.2	0.389	2052	16.4	1.23	0.021	14.6	10.8	5.36	2.61	11.1
0.02	0.53	14.3	13	6.0	0.417	2294	15.6	0.94	0.025	24.0	9.6	4.77	2.46	10.5
0.03	1.23	15.8	13	4.7	0.456	2014	16.8	1.96	0.026	17.8	9.6	5.29	2.29	10.0
0.02	0.63	14.7	9	6.2	0.400	2062	14.6	1.10	0.026	23.2	9.0	4.52	2.18	9.7
0.03	1.56	17.7	14	5.1	0.506	2074	18.5	1.95	0.026	26.5	11.4	6.53	2.74	11.8
0.02	0.58	14.7	10	5.4	0.327	2217	15.4	0.74	0.026	20.1	10.1	5.38	2.45	10.6
0.02	0.78	16.1	11	5.3	0.374	2216	14.8	1.33	0.020	26.8	9.2	5.06	2.22	10.3
0.02	0.48	13.1	6	6.6	0.386	2107	13.1	0.84	0.030	24.4	7.9	4.56	1.96	8.3

Table B.5 (continued): GGC6 ICP-MS Results of carbonate component

Sm	Eu	Gd	Tb	Dy	Ho	Er	Yb	Lu	Hf	Ta	Pb	Th	U
3.34	0.74	3.59	0.53	2.95	0.61	1.54	1.24	0.18	0.00	0.024	0.57	0.460	0.286
3.56	0.77	3.87	0.53	3.39	0.60	1.67	1.40	0.21	0.01	0.000	0.42	0.752	0.248
2.34	0.54	2.57	0.38	2.09	0.41	1.08	0.86	0.13	0.00	0.000	0.11	0.211	0.208
3.54	0.80	3.84	0.57	3.15	0.62	1.65	1.44	0.19	0.02	0.000	0.78	0.594	0.268
3.10	0.68	3.37	0.47	2.99	0.53	1.46	1.23	0.18	0.01	0.000	0.28	0.640	0.223
2.93	0.66	3.15	0.46	2.57	0.51	1.34	1.13	0.17	0.00	0.003	0.35	0.350	0.241
2.83	0.62	3.07	0.43	2.74	0.48	1.33	1.14	0.17	0.01	0.000	0.24	0.594	0.204
2.96	0.68	3.27	0.48	2.69	0.53	1.38	1.25	0.16	0.02	0.000	0.74	0.547	0.236
2.48	0.57	2.71	0.40	2.24	0.45	1.17	0.93	0.14	0.00	0.000	0.25	0.295	0.245
2.15	0.49	2.40	0.35	2.23	0.40	1.09	0.95	0.14	0.01	0.000	0.23	0.382	0.207
1.54	0.35	1.68	0.25	1.36	0.28	0.72	0.74	0.09	0.01	0.000	0.46	0.266	0.251
1.93	0.44	2.07	0.31	1.69	0.34	0.88	0.83	0.13	0.00	0.006	0.20	0.237	0.220
2.06	0.48	2.32	0.34	2.12	0.38	1.02	0.88	0.13	0.01	0.000	0.40	0.216	0.190
2.10	0.48	2.28	0.34	1.86	0.37	0.96	0.76	0.11	0.00	0.000	0.25	0.223	0.225
2.06	0.48	2.32	0.35	1.91	0.39	1.01	0.97	0.12	0.01	0.000	0.45	0.339	0.217
2.14	0.49	2.39	0.35	2.25	0.39	1.07	0.95	0.14	0.01	0.000	0.19	0.328	0.187
2.34	0.53	2.52	0.38	2.10	0.42	1.09	1.00	0.15	0.00	0.006	0.28	0.280	0.227
2.55	0.57	2.71	0.40	2.26	0.45	1.17	0.94	0.14	0.00	0.000	0.81	0.352	0.227
2.64	0.59	2.87	0.41	2.59	0.46	1.25	1.07	0.16	0.01	0.000	0.42	0.447	0.194
2.41	0.55	2.62	0.39	2.16	0.48	1.12	0.89	0.13	0.00	0.048	0.72	0.379	0.221
2.43	0.54	2.61	0.39	2.19	0.44	1.14	0.92	0.14	0.00	0.000	0.47	0.579	0.225
2.32	0.53	2.56	0.38	2.12	0.45	1.10	0.87	0.13	0.00	0.024	0.44	0.299	0.234
2.19	0.51	2.49	0.37	2.10	0.42	1.11	1.07	0.13	0.02	0.000	0.41	0.324	0.238
2.14	0.48	2.35	0.35	1.96	0.39	1.03	0.89	0.15	0.00	0.003	0.28	0.239	0.220
2.58	0.59	2.90	0.43	2.41	0.48	1.26	1.17	0.15	0.02	0.000	0.63	0.457	0.247
2.29	0.52	2.54	0.38	2.10	0.42	1.11	0.88	0.13	0.00	0.035	0.69	0.373	0.236
2.22	0.50	2.42	0.36	2.02	0.41	1.05	0.98	0.15	0.00	0.006	0.26	0.254	0.237
1.88	0.43	2.07	0.31	1.75	0.35	0.93	0.74	0.14	0.00	0.000	0.29	0.242	0.200

Table B.5 (continued): GGC6 ICP-MS Results of carbonate component

Sample Interval (cm)	Na_2O (wt%)	MgO (wt%)	Al_2O_3 (wt%)	K_2O (wt%)	CaO (wt%)	Fe_2O_3 (wt%)	Li	P_2O_5 (wt%)	Sc	TiO_2 (wt%)	V	Cr
KN207-2-GGC6 (continued)												
6:106-108	1.38	0.41	0.04	0.11	61.3	0.28	1.78	0.030	1.07	0.03	0.44	7.55
6:108-110	1.59	0.40	0.39	0.08	58.2	0.03	1.59	0.032	1.20	0.03	0.00	7.60
6:110-112	1.24	0.44	0.33	0.09	47.7	0.12	2.02	0.022	1.48	0.01	2.06	7.61
6:112-114	1.63	0.45	0.42	0.09	59.2	0.08	2.31	0.032	1.73	0.03	0.00	9.42
6:114-116	1.28	0.42	0.08	0.12	58.0	0.31	2.31	0.030	1.39	0.03	0.47	7.60
6:116-118	1.40	0.42	0.35	0.13	61.4	0.58	2.93	0.035	2.79	0.03	1.49	13.85
6:118-120	1.48	0.45	0.33	0.10	54.8	0.13	2.31	0.032	1.58	0.05	0.77	9.77
6:120-122	1.67	0.47	0.43	0.12	61.8	0.21	2.56	0.032	2.07	0.03	0.00	10.20
6:122-124	1.65	0.55	0.42	0.13	50.1	0.18	2.92	0.023	2.20	0.01	2.20	9.92
6:124-126	1.68	0.53	1.18	0.16	64.2	0.37	2.75	0.033	2.49	0.03	0.00	9.40
6:126-128	2.03	0.67	0.55	0.18	57.5	0.23	3.35	0.032	3.30	0.00	2.12	13.43
6:128-130	2.30	0.64	0.94	0.25	59.2	0.26	3.62	0.039	3.88	0.03	0.00	13.73
6:130-132	2.60	0.75	0.68	0.24	54.2	0.27	3.61	0.031	3.63	0.00	2.20	14.29
6:132-134	2.39	0.59	0.64	0.23	56.5	0.18	3.19	0.042	3.81	0.03	0.00	12.40
6:134-136	2.19	0.74	0.70	0.23	58.1	0.29	3.85	0.026	3.76	0.00	2.23	14.91
6:136-138	1.75	0.57	0.50	0.20	62.5	0.43	3.18	0.036	3.02	0.03	0.00	11.49
6:138-140	1.75	0.61	0.51	0.15	58.0	0.23	3.55	0.031	2.96	0.00	2.21	12.75
6:140-142	1.53	0.51	0.47	0.16	65.6	0.38	2.80	0.035	2.37	0.03	0.00	10.33
6:142-144	1.61	0.56	0.46	0.14	55.0	0.21	3.32	0.027	2.27	0.01	2.32	11.60
6:144-147	1.47	0.47	0.36	0.14	65.3	0.38	2.66	0.035	2.21	0.03	0.00	10.14

Table B.5 (continued): GGC6 ICP-MS Results of carbonate component

MnO (wt%)	Co	Ni	Cu	Zn	Rb	Sr	Y	Zr	Cs	Ba	La	Ce	Pr	Nd
0.02	0.75	11.9	10	5.7	0.355	2310	12.9	0.50	0.025	33.4	7.2	4.29	1.78	7.6
0.01	0.61	13.1	8	4.6	0.289	2197	12.9	1.26	0.018	14.0	7.2	3.75	1.72	8.1
0.02	1.19	10.4	12	5.2	0.417	2074	13.8	1.14	0.021	24.6	8.0	4.45	1.91	8.2
0.01	0.78	13.6	9	4.9	0.383	2198	14.8	1.31	0.020	24.6	8.7	4.00	2.08	9.7
0.02	0.54	11.0	8	5.2	0.334	2279	15.2	0.52	0.024	21.2	9.1	4.16	2.28	9.7
0.04	2.25	16.8	13	6.4	0.567	2114	19.1	1.92	0.026	32.3	11.4	6.40	2.79	12.0
0.02	0.84	13.9	8	5.1	0.394	2141	16.1	1.00	0.022	25.4	9.3	4.37	2.27	10.3
0.02	0.85	13.9	8	5.3	0.479	2107	17.1	1.30	0.023	31.1	9.9	4.01	2.47	11.2
0.03	2.10	11.8	11	5.4	0.697	1919	19.2	1.15	0.025	50.8	12.2	5.54	2.96	12.7
0.02	0.72	12.9	7	4.3	0.567	2036	19.5	1.31	0.026	35.1	12.1	3.94	3.17	13.7
0.03	2.54	13.3	12	5.8	0.908	2184	25.2	1.08	0.024	77.0	17.5	6.88	4.28	18.3
0.02	1.35	15.3	9	5.1	0.957	2158	26.8	1.42	0.024	70.3	17.3	5.05	4.21	20.4
0.04	2.67	13.4	12	5.8	1.170	2019	26.4	1.10	0.026	78.7	18.7	7.48	4.63	19.7
0.02	0.84	14.0	7	4.3	0.770	2022	25.5	1.35	0.021	40.9	16.0	4.18	3.88	18.5
0.04	3.01	14.8	13	6.2	1.145	2169	30.1	1.10	0.026	92.8	21.0	8.41	5.16	22.0
0.02	0.88	14.4	10	4.4	0.784	1965	25.6	1.42	0.028	54.0	16.8	4.96	4.36	18.7
0.04	2.07	16.6	14	5.8	0.839	2105	28.0	1.09	0.025	76.1	20.1	7.99	4.83	20.6
0.02	0.52	15.5	9	4.0	0.544	1977	23.7	1.32	0.025	27.9	15.9	4.95	4.06	17.5
0.04	1.97	15.3	14	5.6	0.745	2027	25.6	1.14	0.025	62.0	18.0	7.75	4.35	18.6
0.02	0.60	16.0	11	4.3	0.486	2006	20.7	1.28	0.025	30.1	13.5	4.96	3.50	15.0

Table B.5 (continued): GGC6 ICP-MS Results of carbonate component

Sm	Eu	Gd	Tb	Dy	Ho	Er	Yb	Lu	Hf	Ta	Pb	Th	U
1.71	0.40	1.95	0.29	1.63	0.39	0.88	0.71	0.10	0.00	0.048	0.65	0.163	0.230
1.76	0.41	1.96	0.30	1.64	0.33	0.87	0.84	0.13	0.00	0.006	0.04	0.179	0.234
1.82	0.41	2.00	0.30	1.72	0.35	0.92	0.75	0.11	0.00	0.000	0.26	0.200	0.226
2.11	0.49	2.33	0.35	1.98	0.40	1.04	0.96	0.15	0.00	0.006	0.11	0.272	0.225
2.20	0.51	2.46	0.37	2.07	0.46	1.09	0.88	0.13	0.00	0.047	0.56	0.378	0.215
2.66	0.63	3.01	0.45	2.54	0.51	1.33	1.20	0.16	0.02	0.000	0.46	0.513	0.228
2.25	0.52	2.50	0.38	2.12	0.43	1.13	0.96	0.14	0.00	0.020	0.37	0.349	0.207
2.44	0.56	2.70	0.40	2.27	0.45	1.20	1.04	0.15	0.00	0.003	0.15	0.287	0.211
2.79	0.63	3.05	0.45	2.59	0.52	1.37	1.11	0.17	0.00	0.000	0.59	0.459	0.209
2.98	0.68	3.25	0.48	2.70	0.53	1.40	1.13	0.17	0.00	0.000	0.10	0.364	0.192
3.96	0.90	4.26	0.63	3.56	0.70	1.85	1.50	0.22	0.00	0.000	0.55	0.738	0.205
4.42	0.99	4.71	0.69	3.84	0.75	1.99	1.64	0.24	0.01	0.005	0.15	0.661	0.201
4.31	0.97	4.60	0.68	3.82	0.75	1.98	1.60	0.23	0.00	0.000	0.54	0.843	0.203
4.04	0.91	4.31	0.63	3.57	0.70	1.86	1.56	0.23	0.00	0.006	0.07	0.614	0.189
4.82	1.08	5.15	0.76	4.30	0.84	2.23	1.81	0.26	0.01	0.000	0.63	0.848	0.233
4.07	0.92	4.41	0.65	3.65	0.72	1.88	1.52	0.22	0.00	0.000	0.10	0.491	0.213
4.41	0.98	4.75	0.69	3.95	0.77	2.06	1.66	0.24	0.00	0.000	0.67	0.782	0.239
3.74	0.83	4.05	0.60	3.35	0.66	1.73	1.39	0.20	0.00	0.000	0.12	0.463	0.235
3.99	0.89	4.28	0.63	3.57	0.70	1.86	1.50	0.22	0.00	0.000	0.72	0.637	0.245
3.18	0.72	3.50	0.51	2.90	0.58	1.50	1.21	0.18	0.00	0.000	0.14	0.318	0.233

Table B.6: XRF Results for GGC3

Depth in GGC3 (cm)	Age (ka)	Ti	V	Fe	Cu	Zn	Pb
		Concentrations reported in counts per second (cps)					
2.0	2.2	96	71	39237	3599	457	154
2.4	2.6	110	64	24689	2071	590	192
2.8	3.1	138	50	24932	1971	696	102
3.2	3.5	104	46	19060	1260	259	150
3.6	3.9	124	50	19429	1246	415	175
4.0	4.4	77	69	26830	1536	333	135
4.4	4.8	63	35	16534	905	493	19
4.8	5.3	101	70	17299	894	313	126
5.2	5.7	117	60	30764	1755	849	177
5.6	6.1	109	83	18212	926	249	90
6.0	6.3	123	68	18158	805	333	123
6.4	6.4	105	61	14605	623	336	72
6.8	6.5	95	59	17335	654	189	89
7.2	6.6	73	75	17685	835	314	168
7.6	6.8	96	56	14069	485	431	0
8.0	7.0	95	30	11489	342	207	93
8.4	7.1	56	45	10283	221	128	189
8.8	7.3	84	30	13279	425	399	248
9.2	7.4	69	47	10706	280	66	204
9.6	7.6	83	41	9734	246	187	215
10.0	7.7	102	37	11463	258	150	193
10.4	7.9	93	42	12530	325	314	139
10.8	8.0	60	56	11317	287	316	103
11.2	8.2	127	28	10804	174	186	115
11.6	8.3	102	36	12552	265	285	79
12.0	8.5	98	39	13301	350	211	154
12.4	8.6	103	40	11637	328	253	210
12.8	8.8	94	81	13246	452	393	246
13.2	8.9	95	69	9662	195	320	186
13.6	9.1	91	64	9303	182	252	378
14.0	9.2	84	52	11554	176	234	268
14.4	9.4	86	59	11599	163	265	189
14.8	9.5	101	34	9899	188	445	70
15.2	9.7	104	21	10084	188	237	192
15.6	9.8	139	27	11446	218	256	249
16.0	10.0	115	66	11149	132	74	72
16.4	10.1	106	61	10904	158	0	88
16.8	10.3	119	41	11685	205	399	336
17.2	10.5	105	46	12646	202	153	144
17.6	10.6	106	67	10846	205	95	182
18.0	10.8	143	39	12428	267	151	66
18.4	10.9	109	101	18428	475	329	210
18.8	11.1	134	55	14395	253	126	209
19.2	11.2	110	64	11832	153	343	148

Table B.6 (continued): XRF Results for GGC3

Depth in GGC3 (cm)	Age (ka)	Ti	V	Fe	Cu	Zn	Pb
		Concentrations reported in counts per second (cps)					
19.6	11.4	121	50	12846	228	77	218
20.0	11.5	119	46	13986	314	308	268
20.4	11.6	113	63	13758	272	252	403
20.8	11.8	123	63	13256	279	148	188
21.2	12.0	111	62	12262	145	357	295
21.6	12.2	121	81	11912	180	366	305
22.0	12.4	135	66	11937	163	228	187
22.4	12.7	95	73	12925	266	299	272
22.8	12.9	144	75	14402	272	275	251
23.2	13.1	155	70	16908	406	289	181
23.6	13.3	116	66	14418	347	23	256
24.0	13.6	154	69	13247	357	395	196
24.4	13.8	141	84	15606	371	224	256
24.8	14.0	166	47	18703	442	257	136
25.2	14.2	124	62	17442	525	289	105
25.6	14.5	124	50	16452	528	11	232
26.0	14.7	151	44	16219	440	262	172
26.4	14.9	128	70	19122	731	465	180
26.8	15.1	159	27	23025	949	365	182
27.2	15.3	183	57	35267	1607	267	177
27.6	15.6	114	71	31832	1399	452	166
28.0	15.8	219	66	46434	2356	467	183
28.4	16.0	230	82	58398	3237	583	144
28.8	16.2	150	77	66924	3351	680	95
29.2	16.5	146	36	33656	1851	456	246
29.6	16.7	185	69	48659	2984	628	175
30.0	16.9	181	79	52623	3095	689	190
30.4	17.1	211	71	63129	3998	901	210
30.8	17.4	219	62	62053	4094	655	128
31.2	17.6	190	44	38662	2632	556	184
31.6	17.8	191	63	61304	3721	669	256
32.0	18.0	189	29	38493	2528	495	215
32.4	18.2	221	64	61212	4678	516	219
32.8	18.5	272	52	81629	5846	863	137
33.2	18.7	193	58	77753	6065	873	213
33.6	18.9	186	67	80805	6250	885	145
34.0	19.1	274	79	99887	7949	1248	162
34.4	19.4	218	57	93580	7760	1071	207
34.8	19.6	234	58	89492	6977	1036	190
35.2	19.8	224	88	65289	5684	895	265
35.6	19.9	197	58	74084	6971	943	124
36.0	20.1	209	98	80640	7516	1029	195
36.4	20.3	217	98	75431	6969	1071	126
36.8	20.6	251	41	64841	5944	1060	235

Table B.6 (continued): XRF Results for GGC3

Depth in GGC3 (cm)	Age (ka)	Ti	V	Fe	Cu	Zn	Pb
		Concentrations reported in counts per second (cps)					
37.2	21.1	253	81	58569	5346	1036	252
37.6	21.7	236	4	54572	5037	1057	293
38.0	22.5	246	67	60191	5415	875	233
38.4	23.3	223	71	60030	5390	860	136
38.8	24.1	233	79	65367	5820	872	184
39.2	24.8	189	73	67111	5870	1090	234
39.6	25.6	176	77	70155	6025	937	277
40.0	26.4	260	58	79734	6622	965	167
40.4	27.2	228	50	99729	8301	1367	229
40.8	27.8	179	81	72160	6110	1385	211
41.2	28.3	226	44	50084	3993	908	213
41.6	28.7	197	59	23031	1434	286	201
42.0	28.9	228	49	24184	1543	565	196
42.4	29.1	233	60	36661	2629	787	174
42.8	29.2	204	37	20795	1119	437	231
43.2	29.5	200	108	19008	801	202	222
43.6	29.7	250	60	26517	1396	356	280
44.0	30.0	225	59	34565	2604	974	248
44.4	30.2	259	47	32568	1991	448	153
44.8	30.5	154	82	20221	910	381	166
45.2	30.7	200	58	17956	687	303	231
45.6	31.0	195	34	30558	1912	679	291
46.0	31.3	153	66	19967	898	501	193
46.4	31.5	197	28	18071	642	276	293
46.8	31.8	207	55	19409	646	241	294
47.2	32.0	205	90	19871	613	266	122
47.6	32.3	175	77	18853	585	353	225
48.0	32.5	176	69	18045	565	356	157
48.4	32.8	152	60	20196	625	574	201
48.8	33.0	205	71	20883	572	470	211
49.2	33.3	238	99	30916	1053	360	60
49.6	33.5	202	68	20479	486	522	249
50.0	33.8	163	75	19080	345	459	368
50.4	34.1	170	59	17516	440	282	98
50.8	34.3	206	64	20776	542	356	148
51.2	34.5	207	57	19515	324	157	261
51.6	34.6	174	63	17892	268	264	223
52.0	34.7	211	60	20279	340	7	200
52.4	34.8	240	102	22527	640	235	197
52.8	34.9	280	55	21650	334	113	191
53.2	35.0	255	94	22962	386	280	201
53.6	35.2	196	90	23047	383	370	242
54.0	35.3	204	61	23321	338	395	248
54.4	35.4	218	65	19020	233	207	176

Table B.6 (continued): XRF Results for GGC3

Depth in GGC3 (cm)	Age (ka)	Ti	V	Fe	Cu	Zn	Pb
		Concentrations reported in counts per second (cps)					
54.8	35.5	253	48	23517	282	218	240
55.2	35.6	191	51	20311	332	251	140
55.6	35.7	259	49	21915	326	373	250
56.0	35.9	194	93	20921	238	235	260
56.4	36.0	349	79	29854	534	377	246
56.8	36.1	298	48	27581	479	135	84
57.2	36.2	315	69	24449	327	247	170
57.6	36.3	255	47	23333	286	462	219
58.0	36.4	188	43	19918	151	411	229
58.4	36.6	207	64	21556	260	288	262
58.8	36.7	266	56	20648	125	133	227
59.2	36.8	254	69	23838	207	248	70
59.6	36.9	268	64	25094	283	227	136
60.0	37.0	208	45	21660	252	252	254
60.4	37.1	242	50	29265	541	209	205
60.8	37.3	237	57	22328	226	441	114
61.2	37.4	248	96	22918	248	313	129
61.6	37.5	247	99	28477	345	60	195
62.0	37.6	253	65	26404	363	145	156
62.4	37.7	239	80	25573	386	117	274
62.8	37.8	228	34	23688	340	364	96
63.2	38.0	166	89	24091	320	324	299
63.6	38.2	186	55	23759	388	305	152
64.0	38.5	180	123	24710	379	331	213
64.4	38.8	215	97	22698	285	457	76
64.8	39.1	192	80	21592	316	103	340
65.2	39.3	205	47	21255	245	510	186
65.6	39.6	201	69	21498	239	322	348
66.0	39.8	259	59	23085	230	347	206
66.4	40.1	236	57	22338	238	318	175
66.8	40.3	226	71	23898	303	0	199
67.2	40.6	232	59	22899	196	8	234
67.6	40.9	278	51	20131	254	116	220
68.0	41.1	264	58	20987	203	172	198
68.4	41.4	250	75	21314	177	117	196
68.8	41.6	238	65	20416	198	40	203
69.2	41.9	266	69	20748	265	239	275
69.6	42.1	232	74	20444	136	168	196
70.0	42.4	239	68	19017	149	233	226
70.4	42.6	229	62	19093	174	245	125
70.8	42.9	240	94	21217	164	443	286
71.2	43.2	242	73	19789	181	392	257
71.6	43.4	249	82	18632	176	138	176
72.0	43.7	294	51	24130	232	191	147

Table B.6 (continued): XRF Results for GGC3

Depth in GGC3 (cm)	Age (ka)	Ti	V	Fe	Cu	Zn	Pb
		Concentrations reported in counts per second (cps)					
72.4	43.9	223	85	18238	120	140	260
72.8	44.2	242	68	19438	131	186	214
73.2	44.4	250	72	20444	166	118	303
73.6	44.7	214	70	20699	137	219	163
74.0	45.0	230	52	20003	126	216	193
74.4	45.2	230	78	20523	104	289	278
74.8	45.5	191	63	20496	169	0	220
75.2	45.7	162	78	20235	148	458	302
75.6	46.0	190	84	19682	181	239	337
76.0	46.2	171	36	17045	171	252	345
76.4	46.5	215	82	19305	235	72	345
76.8	46.8	157	46	16443	118	174	150
77.2	47.0	141	61	17287	133	267	268
77.6	47.3	164	62	16772	179	118	223
78.0	47.5	117	76	18384	122	43	192
78.4	47.8	178	67	20244	155	100	103
78.8	48.0	181	70	20813	169	219	300
79.2	48.3	148	26	13985	124	93	131
79.6	48.6	88	38	15833	91	216	191
80.0	48.8	144	49	14524	81	273	147
80.4	49.1	177	38	14026	39	138	74
80.8	49.3	160	31	19293	74	262	195

Table B.7: XRF Results for GGC6

Depth in GGC6 (cm)	Age (ka)	Ti	V	Fe	Cu	Zn	Pb
		Concentrations reported in counts per second (cps)					
0.4	0.2	0	14	690	0	47	272
0.8	0.4	55	117	7882	0	0	301
1.2	0.6	52	107	8230	0	260	413
1.6	0.8	53	49	7355	0	240	179
2.0	0.9	58	65	7538	0	79	208
2.4	1.1	80	68	7802	0	229	300
2.8	1.3	84	50	6710	0	455	361
3.2	1.5	94	47	7881	0	330	285
3.6	1.7	107	66	8155	0	254	232
4.0	1.9	70	75	8140	0	153	147
4.4	2.1	64	68	8061	0	24	350
4.8	2.3	59	88	7883	0	300	364
5.2	2.5	75	58	8194	0	175	325
5.6	2.6	80	82	8877	0	184	384
6.0	2.8	38	41	4095	0	64	149
6.4	3.0	20	40	2557	0	71	126
6.8	3.2	18	79	4415	0	260	142
7.2	3.4	59	61	4882	0	30	131
7.6	3.6	16	55	3517	0	89	319
8.0	3.8	48	68	6016	0	0	189
8.4	4.0	68	74	6913	0	0	431
8.8	4.2	71	45	6496	0	232	161
9.2	4.3	72	56	6601	0	132	201
9.6	4.5	47	54	6453	0	201	308
10.0	4.7	55	54	6431	0	214	199
10.4	4.9	53	51	6869	0	0	192
10.8	5.1	61	48	6745	0	154	130
11.2	5.3	76	52	7881	0	330	179
11.6	5.5	47	73	6244	0	93	263
12.0	5.7	65	41	6486	0	15	224
12.4	5.9	47	60	6472	0	343	256
12.8	6.1	19	85	6367	0	403	314
13.2	6.3	36	80	6229	0	0	288
13.6	6.6	44	76	6434	0	157	214
14.0	6.8	32	57	6629	0	112	251
14.4	7.0	49	56	6253	0	250	304
14.8	7.2	28	77	6173	0	120	257
15.2	7.4	52	63	5918	0	24	117
15.6	7.6	32	62	5974	0	360	229
16.0	7.8	35	65	5680	0	378	275
16.4	8.0	43	79	5935	0	63	270
16.8	8.2	29	51	5404	0	350	216
17.2	8.4	59	40	5460	0	104	201
17.6	8.6	33	72	5193	0	17	243

Table B.7 (continued): XRF Results for GGC6

Depth in GGC6 (cm)	Age (ka)	Ti	V	Fe	Cu	Zn	Pb
		Concentrations reported in counts per second (cps)					
18.0	8.9	55	35	6425	0	141	196
18.4	9.1	99	45	7722	0	122	245
18.8	9.3	58	50	5848	0	0	241
19.2	9.5	47	64	5806	0	85	192
19.6	9.7	55	85	6134	0	137	139
20.0	9.9	65	55	5878	0	181	321
20.4	10.1	51	67	5811	0	177	248
20.8	10.3	87	45	5663	0	202	310
21.2	10.5	88	78	6772	0	0	145
21.6	10.7	68	60	6258	13	221	187
22.0	10.9	91	39	6224	0	15	203
22.4	11.1	74	67	6655	0	211	227
22.8	11.4	95	59	6661	0	99	262
23.2	11.6	81	61	6517	0	210	326
23.6	11.8	74	82	6709	0	254	236
24.0	12.0	91	57	6834	0	133	190
24.4	12.2	65	57	7043	39	192	214
24.8	12.4	86	49	6869	0	155	303
25.2	12.6	101	45	6790	0	104	255
25.6	12.8	84	55	7067	0	300	257
26.0	12.9	85	66	7286	0	159	186
26.4	13.1	72	53	7603	0	211	217
26.8	13.3	100	58	7578	0	135	211
27.2	13.5	50	69	7647	0	245	169
27.6	13.6	88	63	7750	0	40	177
28.0	13.8	107	43	8388	0	263	183
28.4	14.0	117	66	7964	0	104	183
28.8	14.1	102	70	7830	0	47	198
29.2	14.3	81	55	8184	0	202	336
29.6	14.5	82	57	8079	27	384	177
30.0	14.7	112	57	8426	0	318	177
30.4	14.8	136	56	8588	24	32	331
30.8	15.0	75	55	7826	0	236	307
31.2	15.2	88	46	8433	0	177	326
31.6	15.4	110	41	7638	29	240	133
32.0	15.5	100	80	8118	0	0	218
32.4	15.7	83	43	8055	0	132	306
32.8	15.9	92	63	8142	19	43	205
33.2	16.0	82	54	7411	0	218	182
33.6	16.2	101	63	7674	0	244	244
34.0	16.4	124	52	7842	0	158	61
34.4	16.6	104	63	7794	0	471	263
34.8	16.7	101	59	8061	0	226	142
35.2	16.9	84	59	7814	0	115	254

Table B.7 (continued): XRF Results for GGC6

Depth in GGC6 (cm)	Age (ka)	Ti	V	Fe	Cu	Zn	Pb
		Concentrations reported in counts per second (cps)					
35.6	17.1	81	54	7868	0	261	265
36.0	17.3	141	26	9858	0	155	185
36.4	17.4	146	56	9316	0	252	281
36.8	17.6	97	62	9390	0	222	254
37.2	17.8	144	55	9074	0	61	221
37.6	17.9	177	41	10646	0	292	225
38.0	18.1	140	57	10337	0	295	211
38.4	18.3	135	50	9861	0	234	240
38.8	18.5	123	52	9464	0	0	273
39.2	18.6	132	52	9795	0	237	268
39.6	18.8	141	85	10253	0	243	285
40.0	19.0	125	61	10343	20	50	353
40.4	19.2	153	75	10651	26	22	315
40.8	19.3	157	72	10646	0	54	197
41.2	19.5	153	72	10311	0	221	246
41.6	19.7	86	63	10882	0	367	203
42.0	19.8	151	54	10749	0	251	195
42.4	20.0	133	70	10337	0	46	236
42.8	20.2	139	42	10368	0	0	181
43.2	20.4	120	52	9770	0	290	194
43.6	20.5	119	72	9151	0	240	209
44.0	20.7	130	52	8806	0	92	168
44.4	20.9	111	46	7116	0	0	204
44.8	21.1	117	65	9228	0	0	310
45.2	21.2	126	64	9988	0	184	185
45.6	21.4	125	96	10934	0	347	330
46.0	21.6	147	72	10672	0	0	182
46.4	21.7	160	56	10512	0	373	261
46.8	21.9	140	56	10309	0	234	194
47.2	22.1	128	41	9988	0	194	263
47.6	22.3	125	56	9603	0	201	325
48.0	22.4	119	56	8644	0	282	141
48.4	22.6	108	56	8036	0	0	185
48.8	22.8	109	51	6469	8	0	83
49.2	22.9	30	63	4696	0	229	178
49.6	23.1	123	87	8445	0	136	233
50.0	23.3	90	37	6001	0	122	216
50.4	23.5	138	66	10283	0	54	181
50.8	23.6	137	48	12778	0	200	222
51.2	23.8	146	69	11295	0	138	147
51.6	24.0	132	58	9982	0	189	147
52.0	24.1	149	55	10015	0	344	234
52.4	24.3	147	60	11022	0	207	155
52.8	24.5	138	77	10538	0	119	273

Table B.7 (continued): XRF Results for GGC6

Depth in GGC6 (cm)	Age (ka)	Ti	V	Fe	Cu	Zn	Pb
		Concentrations reported in counts per second (cps)					
53.2	24.7	172	80	10360	0	254	371
53.6	24.8	146	59	10269	0	13	210
54.0	25.0	169	57	10485	0	126	225
54.4	25.2	129	89	11101	30	272	221
54.8	25.3	152	83	10314	0	230	197
55.2	25.5	126	63	10332	0	195	224
55.6	25.7	121	64	10437	0	212	234
56.0	25.9	154	83	10161	0	302	285
56.4	26.0	175	41	10535	0	322	292
56.8	26.2	137	58	10438	0	380	341
57.2	26.4	109	69	9586	0	231	267
57.6	26.5	121	78	9503	0	122	205
58.0	26.7	111	49	8293	0	41	191
58.4	26.9	114	43	8646	0	317	270
58.8	27.1	91	70	9580	0	237	179
59.2	27.2	83	102	8716	0	203	267
59.6	27.4	143	62	9488	0	248	324
60.0	27.6	132	53	8777	0	262	313
60.4	27.7	135	54	9006	0	264	240
60.8	27.9	95	61	9132	0	107	168
61.2	28.1	110	69	9822	0	172	272
61.6	28.3	95	65	8266	0	320	265
62.0	28.5	114	51	8154	29	240	187
62.4	28.7	113	58	8751	0	20	335
62.8	29.0	83	60	8005	0	246	339
63.2	29.2	87	66	8851	0	77	209
63.6	29.4	82	65	9066	0	47	156
64.0	29.6	77	51	8387	0	348	295
64.4	29.8	121	73	8260	0	0	292
64.8	30.0	82	53	7835	0	361	163
65.2	30.2	100	80	7829	0	189	206
65.6	30.4	118	65	7882	0	98	142
66.0	30.6	117	24	8179	0	65	167
66.4	30.9	89	30	7529	0	163	220
66.8	31.1	145	74	8430	0	179	222
67.2	31.3	102	65	8701	42	311	193
67.6	31.5	139	56	8506	0	86	191
68.0	31.7	77	35	6801	0	103	253
68.4	31.9	84	52	6806	0	155	247
68.8	32.1	86	46	6549	0	231	226
69.2	32.3	81	50	6764	0	271	276
69.6	32.5	93	95	6761	0	86	242
70.0	32.8	99	33	6491	0	211	324
70.4	33.0	78	50	7056	0	0	193

Table B.7 (continued): XRF Results for GGC6

Depth in GGC6 (cm)	Age (ka)	Ti	V	Fe	Cu	Zn	Pb
		Concentrations reported in counts per second (cps)					
70.8	33.2	83	63	6357	0	346	219
71.2	33.4	107	44	6403	0	438	293
71.6	33.6	123	63	8829	0	215	208
72.0	33.8	100	45	7319	0	140	177
72.4	34.0	67	63	6122	0	264	246
72.8	34.2	90	48	5714	0	181	251
73.2	34.4	50	51	4852	0	0	272
73.6	34.7	101	45	5564	19	340	245
74.0	34.9	74	49	5748	0	31	210
74.4	35.1	64	77	5749	0	0	268
74.8	35.3	100	34	5678	0	238	321
75.2	35.5	70	65	5925	0	242	200
75.6	35.7	65	52	5778	0	158	265
76.0	35.9	17	54	5718	0	242	188
76.4	36.1	27	73	5528	0	130	300
76.8	36.3	71	29	5426	0	173	235
77.2	36.5	82	45	5923	0	12	209
77.6	36.7	71	47	5775	0	235	110
78.0	36.9	31	45	6181	0	152	279
78.4	37.1	64	44	5847	0	181	170
78.8	37.3	78	32	5812	0	0	199
79.2	37.5	92	13	5641	0	360	311
79.6	37.7	84	63	5962	0	141	310
80.0	37.9	66	45	6316	0	256	277
80.4	38.1	65	64	6154	0	234	245
80.8	38.3	66	55	6079	0	151	296
81.2	38.5	38	41	5807	0	245	305
81.6	38.7	37	56	5727	0	206	334
82.0	38.9	54	52	5644	0	356	373
82.4	39.2	46	50	5676	0	192	178
82.8	39.4	86	57	6177	0	435	319
83.2	39.6	97	75	6786	0	331	319
83.6	39.8	82	56	6277	0	243	199
84.0	40.0	53	75	6620	0	0	245
84.4	40.2	88	54	7053	0	225	245
84.8	40.4	90	63	7078	0	412	239
85.2	40.6	67	69	7596	0	375	270
85.6	40.8	108	34	7276	0	256	129
86.0	41.0	78	43	6571	0	20	372
86.4	41.2	67	81	7146	0	0	206
86.8	41.4	103	84	7947	0	262	338
87.2	41.6	69	27	6861	0	81	264
87.6	41.8	84	79	7573	0	96	246
88.0	42.0	100	78	7925	0	242	359

Table B.7 (continued): XRF Results for GGC6

Depth in GGC6 (cm)	Age (ka)	Ti	V	Fe	Cu	Zn	Pb
		Concentrations reported in counts per second (cps)					
88.4	42.2	112	57	7254	0	115	321
88.8	42.4	92	65	6976	0	0	247
89.2	42.6	58	52	5970	0	259	300
89.6	42.8	67	60	6457	0	214	231
90.0	43.0	49	71	6823	0	223	279
90.4	43.2	55	66	6588	0	245	239
90.8	43.5	100	59	7165	0	176	276
91.2	43.7	70	68	7720	0	97	221
91.6	43.9	61	59	6911	0	294	224
92.0	44.1	76	55	7170	0	149	342
92.4	44.3	65	70	7284	0	187	191
92.8	44.5	99	57	7154	0	47	375
93.2	44.7	108	67	7564	0	248	315
93.6	44.9	129	35	7144	0	250	313
94.0	45.1	86	66	6937	0	33	162
94.4	45.3	48	73	7111	0	166	223
94.8	45.5	49	59	7000	0	132	224
95.2	45.7	63	71	7418	0	74	334
95.6	45.9	75	71	7492	0	358	380
96.0	46.1	63	38	6769	0	316	283
96.4	46.3	91	82	6711	0	315	309
96.8	46.5	59	47	6369	0	132	310
97.2	46.7	71	58	6535	0	182	277
97.6	46.9	78	47	6864	0	270	267
98.0	47.1	61	73	6612	0	127	248
98.4	47.3	40	63	6927	0	281	268
98.8	47.5	43	49	6894	0	54	323
99.2	47.7	79	50	8027	0	107	335
99.6	47.9	71	65	6932	0	366	366
100.0	48.1	95	81	8150	0	369	312
100.4	48.3	77	61	7122	0	0	320
100.8	48.5	86	58	7440	0	23	292
101.2	48.6	75	62	7476	0	112	355
101.6	48.8	97	72	7697	0	442	267
102.0	49.0	91	49	8209	0	47	289
102.4	49.2	85	61	7794	0	404	389
102.8	49.4	77	69	7694	0	8	332
103.2	49.6	108	29	7482	0	157	275
103.6	49.8	75	54	7151	0	317	381
104.0	50.0	109	59	7203	0	320	303
104.4	50.2	98	73	7603	0	35	222
104.8	50.4	91	47	6671	0	163	277
105.2	50.6	104	47	6087	0	263	331

Table B.7 (continued): XRF Results for GGC6

Depth in GGC6 (cm)	Age (ka)	Ti	V	Fe	Cu	Zn	Pb
		Concentrations reported in counts per second (cps)					
105.6	50.8	6	62	5841	0	186	344
106.0	51.0	80	54	5833	0	138	300
106.4	51.2	62	68	5666	0	239	403
106.8	51.4	65	38	5561	0	204	346
107.2	51.6	53	59	5712	0	303	436
107.6	51.8	43	53	6381	0	204	295
108.0	52.0	55	40	5780	0	111	289
108.4	52.2	92	45	5857	0	117	374
108.8	52.4	73	34	5821	0	233	231
109.2	52.6	51	36	5942	0	368	265
109.6	52.8	27	51	5850	0	0	309
110.0	53.0	37	60	5732	0	119	244
110.4	53.2	62	80	5951	0	46	205
110.8	53.4	37	75	5603	0	245	293
111.2	53.6	48	58	6340	0	227	116
111.6	53.8	69	39	6263	0	150	297
112.0	54.0	46	66	6663	0	299	238
112.4	54.2	33	70	6405	0	90	312
112.8	54.4	94	57	6081	0	0	261
113.2	54.5	71	67	7261	0	121	342
113.6	54.7	79	83	7750	0	420	412
114.0	54.9	103	71	9026	0	147	230
114.4	55.1	86	82	8257	0	0	275
114.8	55.3	79	60	8453	0	155	247
115.2	55.5	109	87	7930	0	243	361
115.6	55.7	134	59	7960	0	70	147
116.0	55.9	58	72	7978	0	336	244
116.4	56.1	99	63	8621	0	168	232
116.8	56.3	101	66	7825	0	278	304
117.2	56.5	114	55	8114	0	209	187
117.6	56.7	123	71	8370	0	58	316
118.0	56.9	101	53	8326	0	0	120
118.4	57.1	144	71	8601	0	154	203
118.8	57.3	86	63	7649	0	118	237
119.2	57.5	71	58	7366	0	184	460
119.6	57.7	94	72	6937	0	256	302
120.0	57.8	77	74	7094	0	108	102
120.4	58.0	83	28	7156	0	200	392
120.8	58.2	134	47	8722	0	370	301
121.2	58.3	111	64	9971	0	231	439
121.6	58.5	150	44	11188	0	0	240
122.0	58.7	139	74	11925	0	258	403
122.4	58.9	126	66	11881	0	0	176
122.8	59.0	167	66	11772	0	185	238

Table B.7 (continued): XRF Results for GGC6

Depth in GGC6 (cm)	Age (ka)	Ti	V	Fe	Cu	Zn	Pb
		Concentrations reported in counts per second (cps)					
123.2	59.2	110	71	9475	0	77	280
123.6	59.4	175	57	10714	0	0	250
124.0	59.6	177	51	11628	0	78	249
124.4	59.7	129	52	10977	0	264	338
124.8	59.9	184	34	11553	0	304	194
125.2	60.1	169	50	11513	8	207	165
125.6	60.2	177	60	11189	0	97	238
126.0	60.4	153	73	12190	0	0	247
126.4	60.6	124	82	11824	0	96	329
126.8	60.8	208	47	11810	16	119	107
127.2	60.9	180	64	10311	0	231	190
127.6	61.1	193	47	11361	0	150	265
128.0	61.3	144	60	11086	0	361	317
128.4	61.4	133	59	10531	0	35	323
128.8	61.6	217	67	13183	0	195	228
129.2	61.8	165	80	15282	0	169	333
129.6	62.0	156	68	13914	0	232	262
130.0	62.1	170	81	11580	0	186	243
130.4	62.3	246	83	14061	0	220	385
130.8	62.5	217	47	15323	0	308	257
131.2	62.6	227	42	14296	0	70	200
131.6	62.8	182	78	14490	49	439	191
132.0	63.0	197	38	13923	0	180	219
132.4	63.2	199	48	14623	0	118	243
132.8	63.3	168	26	9892	0	104	182
133.2	63.5	179	71	14905	0	185	259
133.6	63.7	207	60	15707	0	175	286
134.0	63.9	217	53	16238	0	45	176
134.4	64.0	249	26	15860	0	211	255
134.8	64.2	216	43	14448	0	212	247
135.2	64.4	161	67	13256	0	51	292
135.6	64.5	170	54	14765	0	52	106
136.0	64.7	243	56	14340	0	22	299
136.4	64.9	186	59	14332	0	84	285
136.8	65.1	211	59	15709	0	241	266
137.2	65.2	176	73	14538	0	89	126
137.6	65.4	213	41	14430	0	36	0
138.0	65.6	188	54	13921	0	11	59
138.4	65.7	172	34	14586	0	183	327
138.8	65.9	160	41	14325	0	39	133
139.2	66.1	206	64	13823	9	217	230
139.6	66.3	111	70	13148	0	66	45
140.0	66.4	114	58	10813	0	303	208
140.4	66.6	124	87	12068	0	231	186

Table B.7 (continued): XRF Results for GGC6

Depth in GGC6 (cm)	Age (ka)	Ti	V	Fe	Cu	Zn	Pb
		Concentrations reported in counts per second (cps)					
140.8	66.8	173	56	12133	0	178	171
141.2	66.9	207	39	13527	0	82	94
141.6	67.1	125	76	12467	0	46	137
142.0	67.3	164	61	12938	0	248	169
142.4	67.5	114	57	12629	7	187	47
142.8	67.6	187	51	11726	0	0	168
143.2	67.8	167	56	11752	0	0	184
143.6	68.0	200	86	12659	0	520	177
144.0	68.2	134	47	12106	7	221	219
144.4	68.3	162	87	11672	0	260	87
144.8	68.5	137	63	11132	0	415	234
145.2	68.7	151	72	10805	0	433	179
145.6	68.8	162	57	10854	0	268	16
146.0	69.0	134	38	8628	0	310	155
146.4	69.2	137	41	9626	0	394	49
146.8	69.4	0	34	333	0	281	380

Appendix C

Supplemental material for Chapter 3

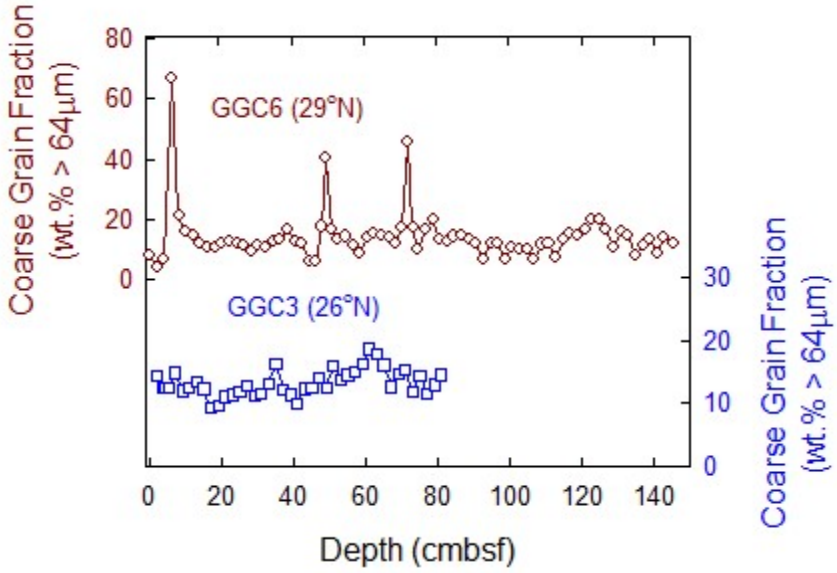

Figure C.1. Coarse grain (> 64 µm) fraction in GGC3 and GGC6 as a function of depth. Note change in y-axis scale. Anomalous coarse layers in GGC6 are carbonate-rich and correspond to ages of 3.3, 23.0, and 33.8 ka.

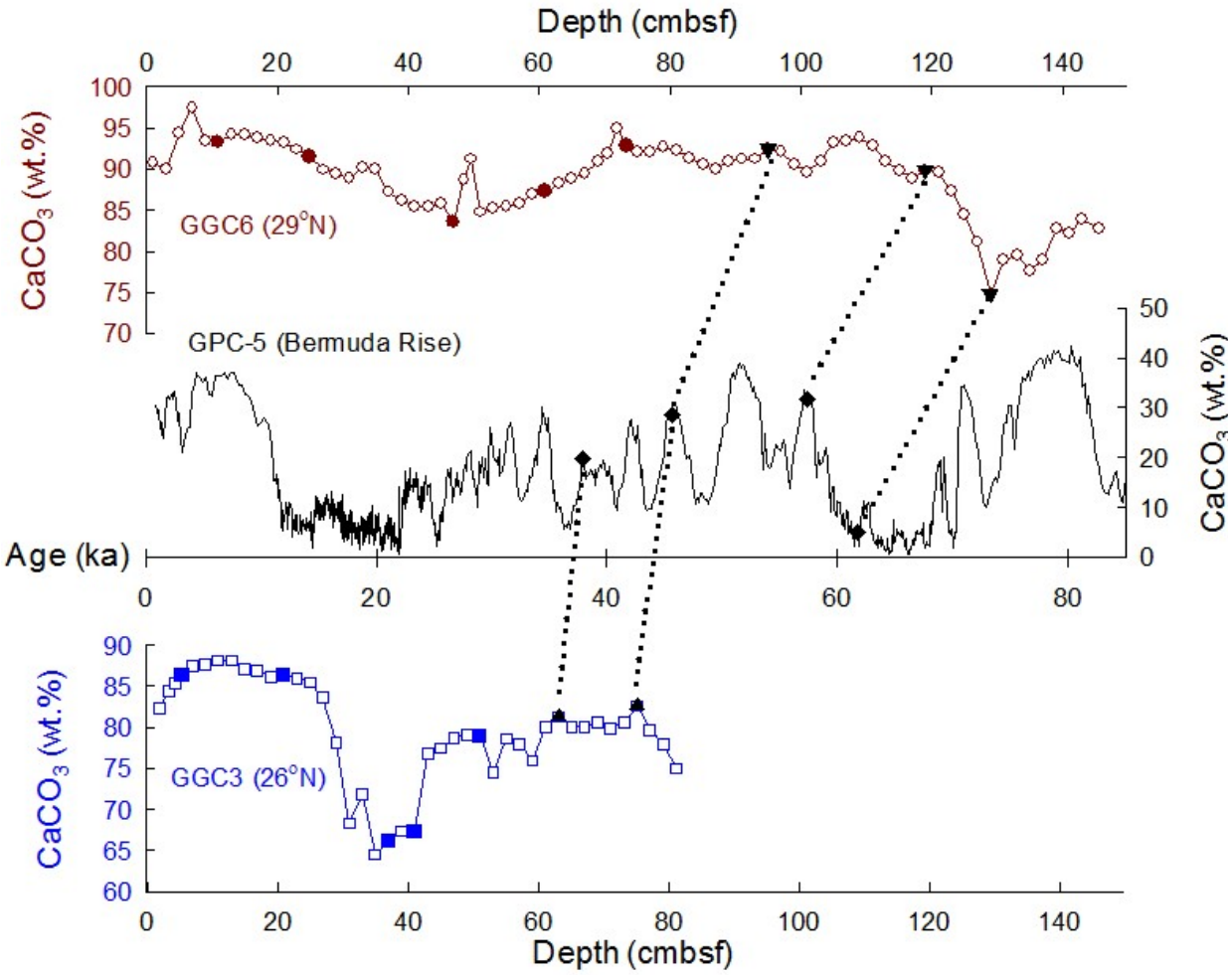

Figure C.2. Stratigraphic carbonate comparison. Bulk carbonate contents for GGC3 (blue, squares) and GGC6 (red, circles) plotted against depth in comparison to the high resolution reference core GPC-5 (solid black) from the northeast Bermuda Rise plotted against age (Keigwin and Jones, 1994). Solid points indicate ages with radiocarbon dates, while black points indicate carbonate maxima or minima used to constrain sediment core chronology beyond the limit of radiocarbon data.

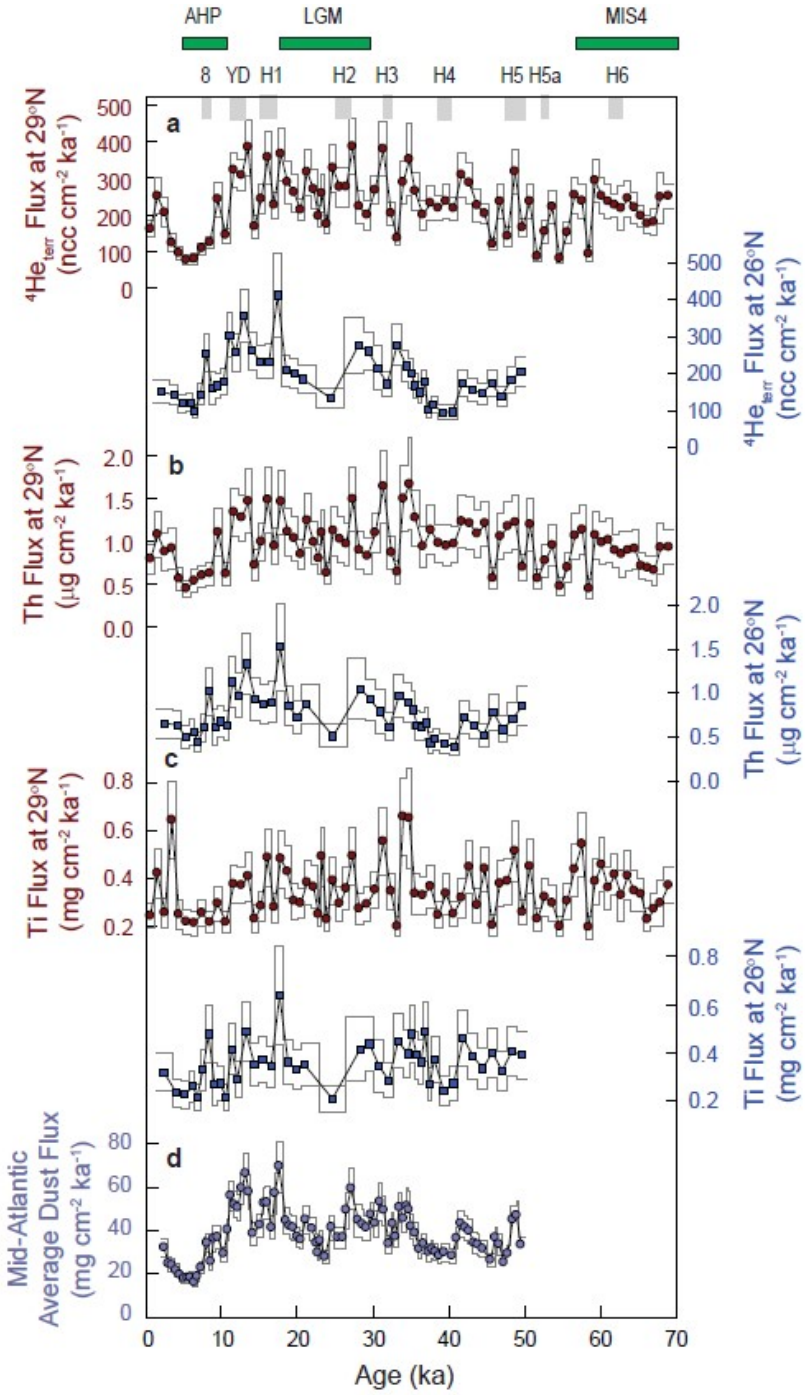

Figure C.3. Unaveraged $^3He_{ET}$-derived dust proxy fluxes and the spatially averaged Mid-Atlantic dust flux stack. (a) $^4He_{terr}$, (b) Th, and (c) Ti fluxes for 26°N (GGC3, blue squares) and for 29°N (GGC6, brown circles) as a function of time. (d) Spatially averaged $^4He_{terr}$-based Mid-Atlantic dust flux record. Flux values indicate sedimentary intervals spanning ~1 ka (data points) within a 1σ error envelope (solid lines). Known climatic events are highlighted as in Figure 3 (main text). GGC3 flux data (Middleton et al., 2016) are presented on a revised age-model.

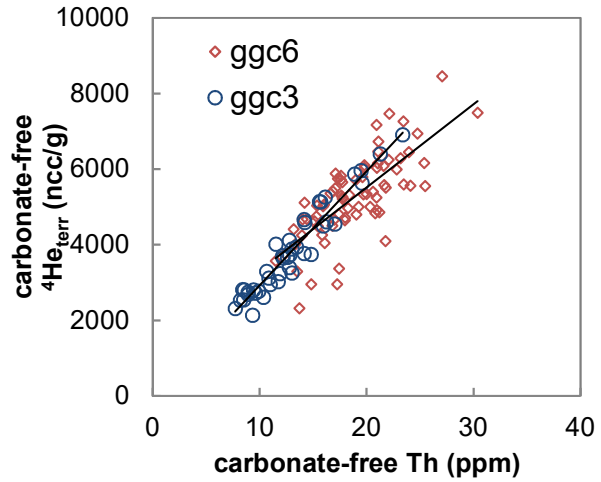

GGC6: R = 0.74, p < 0.01
GGC3: R = 0.96, p < 0.01

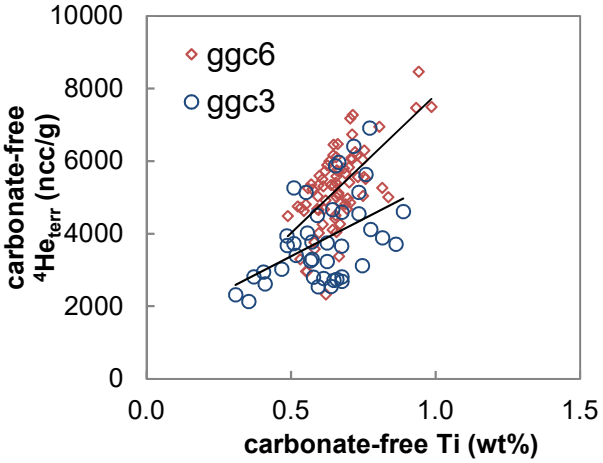

GGC6: R = 0.64, p < 0.01
GGC3: R = 0.46, p = 0.03

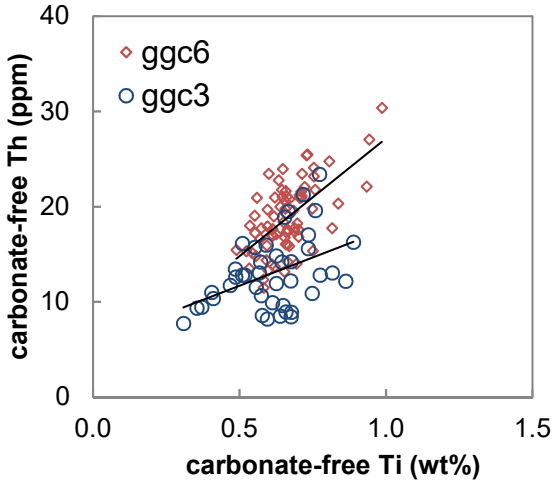

GGC6: R = 0.61, p < 0.01
GGC3: R = 0.42, p = 0.05

Figure C.4. Correlation plots between the concentrations of $^4He_{terr}$, Th, and Ti in the carbonate-free sedimentary components of GGC6 (29°N, red diamonds) and GGC3 (26°N, blue circles). Variance in elemental ratios may be associated with variable dust province to the Mid-Atlantic and, or, with non-dust sedimentary components of Th and Ti. R and p-values for elemental correlations are indicated.

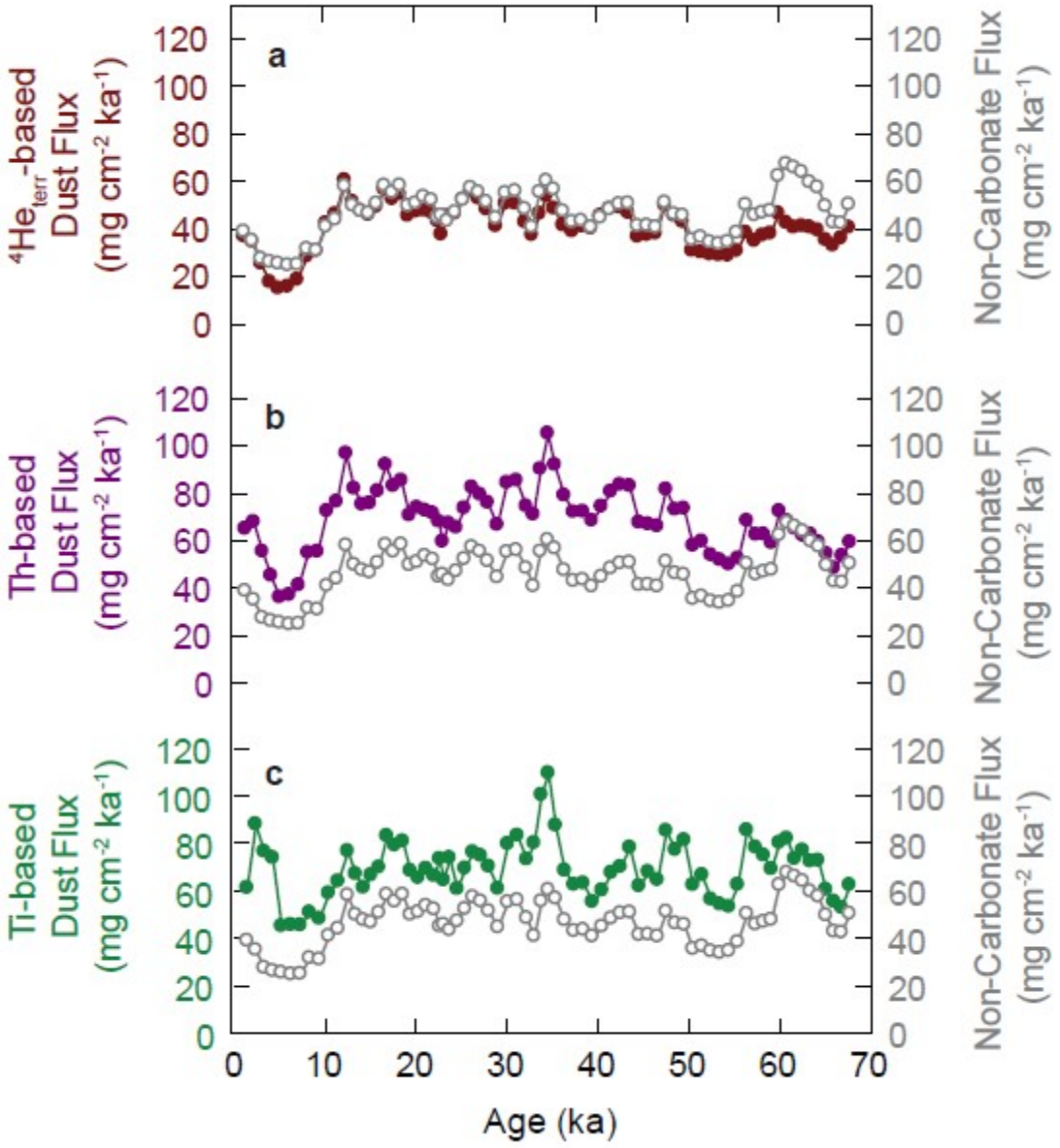

Figure C.5. Alternative dust flux calculations for GGC6 (29°N). Total non-carbonate sediment flux (right axes, open gray points) and absolute dust flux values (left axes, solid points) calculated from (a) $^4He_{terr}$, (b) Th, and (c) Ti. Dust flux values are calculated assuming typical endmember dust concentrations of 5600 ncc g^{-1}, 14 ppm, and 0.5 wt% for $^4He_{terr}$, Th, and Ti, respectively. Both Th and Ti-based dust fluxes exceed the total non-carbonate flux at 29°N, suggesting that the Th and Ti concentrations estimated for Northwest African dust are too low and, or, the presence of non-dust sedimentary components of Th and Ti in the Mid-Atlantic sediments.

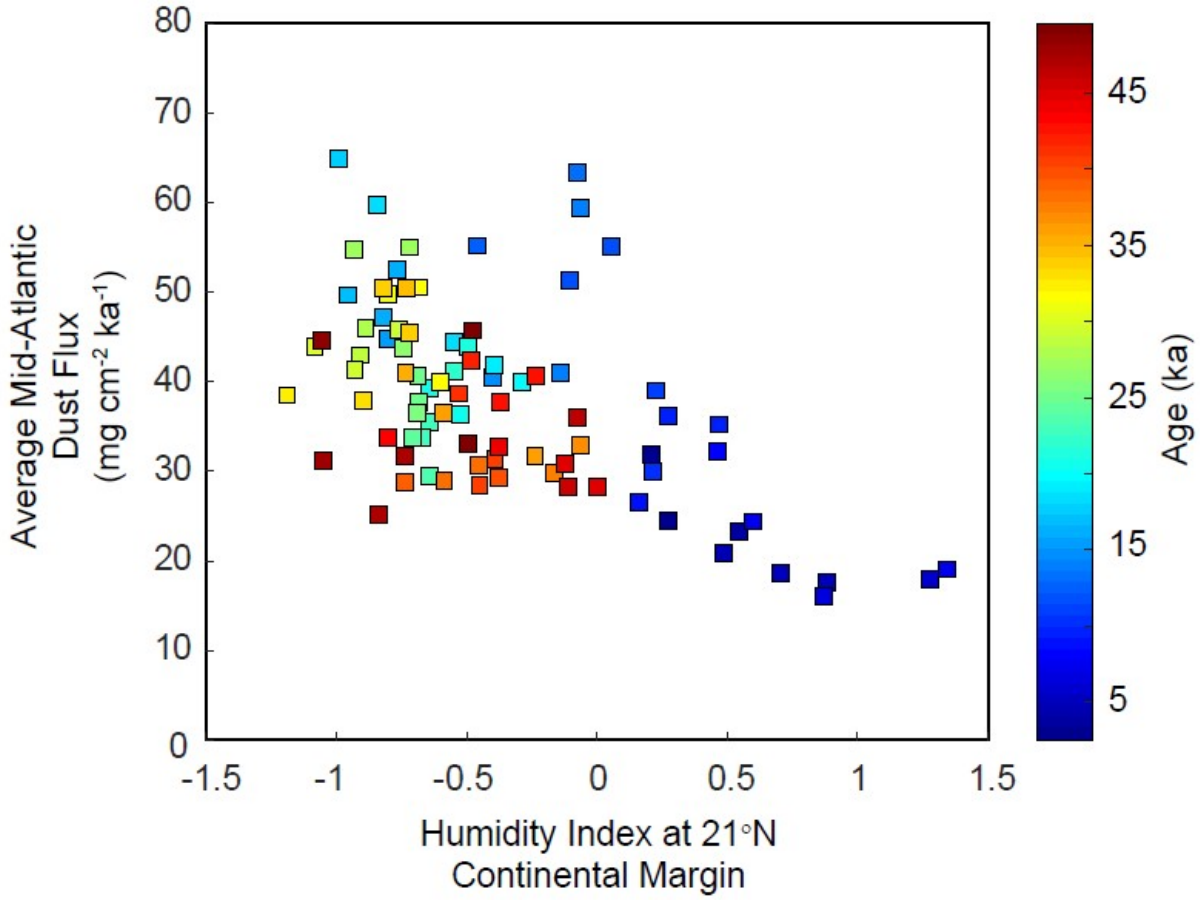

Figure C.6. Comparison of the Mid-Atlantic dust flux stack the North African humidity index calculated from grain size analysis of sediment from 21°N on the Northwest African margin (GeoB7920-2; Tjallingi et al. 2008). The cross-core comparison is made after linear interpolation of each data set to a uniform time series. Correlation between the records is weaker when data points associated with the African Humid Period (5 to 11 ka) are excluded. For the full interval of overlap, R = -0.57, p = 0.03.

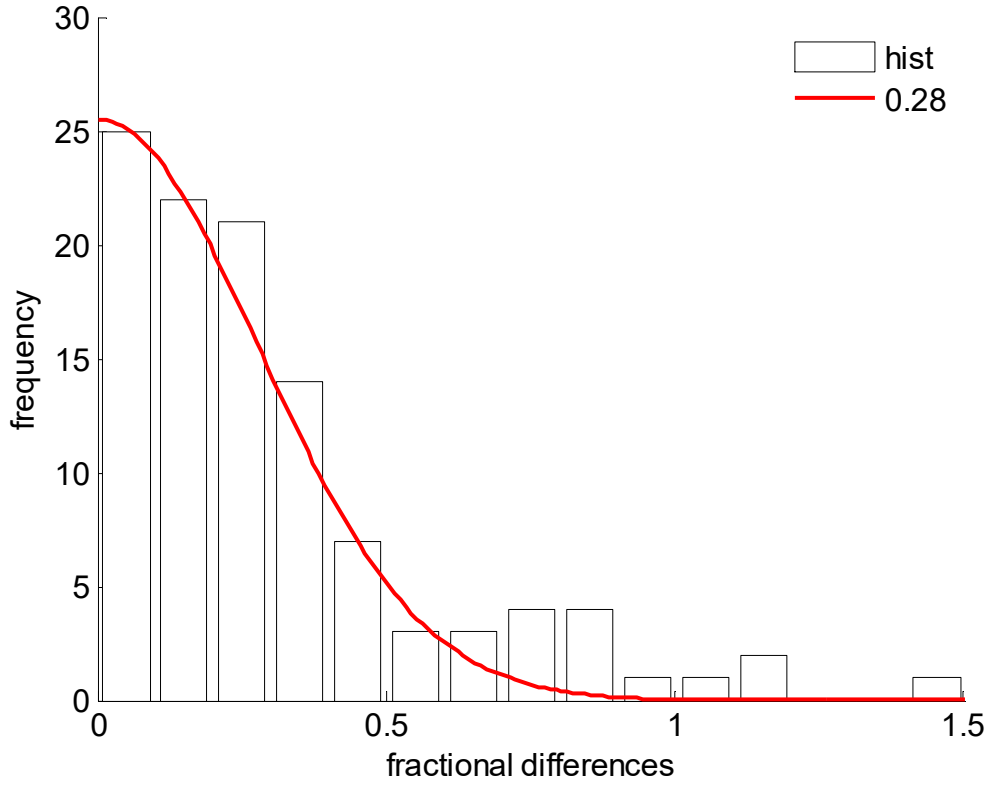

Figure C.7. A histogram of the fractional difference in the extraterrestrial helium-3 concentration of replicated sediment sample aliquots. The distribution of fractional differences observed in the Mid-Atlantic sediments is best fit by a Gaussian distribution with 1σ uncertainty of 28%.

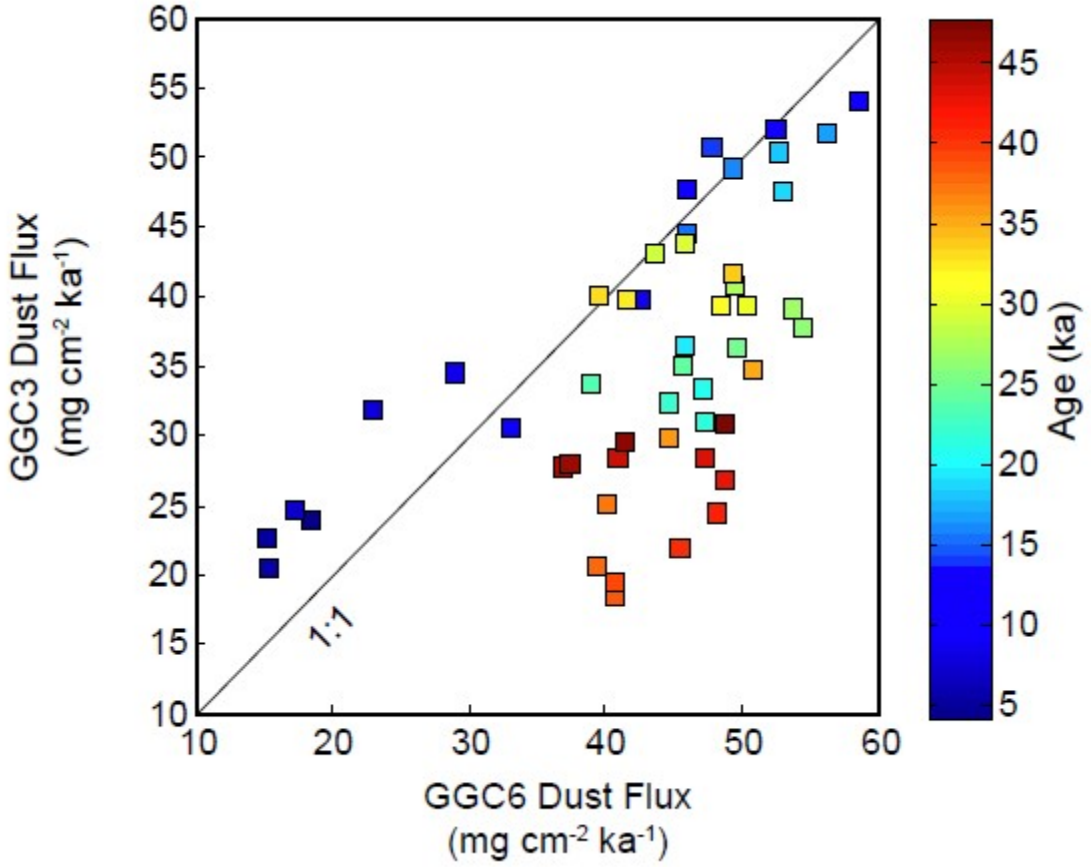

Figure C.8. Comparison of linearly interpolated dust flux records from 26°N (GGC3) and 29°N (GGC6) on the Mid-Atlantic Ridge. Correlations are highest between the cores within the most recent 20 ka. The 1:1 line is indicated for ease of comparison. R = 0.59, p = 0.04.

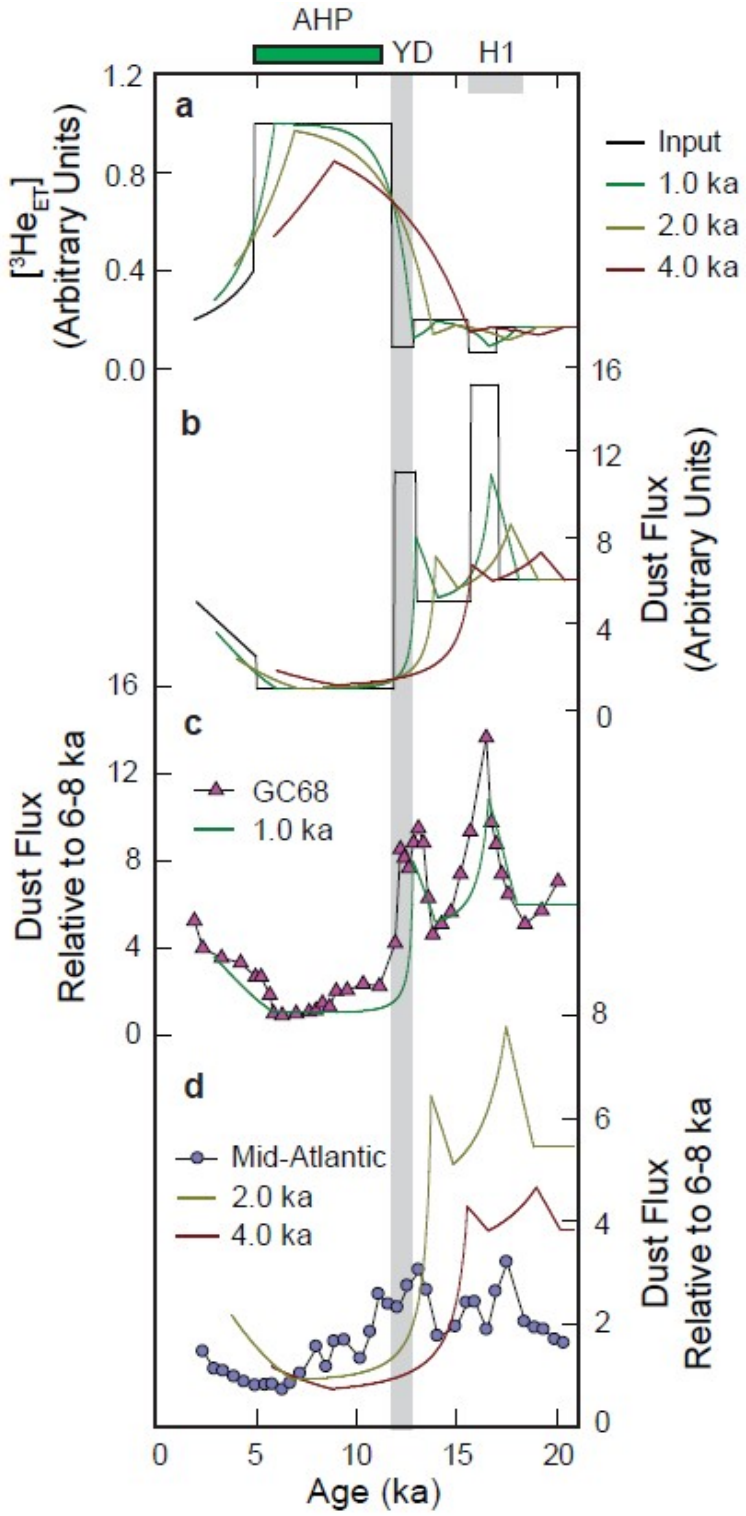

Figure C.9. Results of a bioturbation model in which an input signal of [$^3He_{ET}$], rather than dust flux itself, is linearly homogenized in the sediment column mixed layer. (a) Input $^3He_{ET}$ signal (black) and bioturbation model outputs for mixed layer depths equivalent to 1 ka (green), 2 ka (yellow), and 4 ka (red) of smoothing. **(Caption continues on the next page.)**

Figure C.9 caption (continued): (b) Dust flux records computed as $1/[^3He_{ET}]$ using the $[^3He_{ET}]$ patterns of (a). (c) Comparison of the high-resolution OC437-7-GC68 dust flux record (triangles) from 19°N on the Northwest African continental margin (McGee et al., 2013) with the bioturbation model output for 1 ka of smoothing (green line). (d) Comparison of the Mid-Atlantic dust flux stack (circles) with bioturbation model outputs for 2 ka (yellow line) and 4 ka (red line) of smoothing. Dust fluxes in (b) and (c) are plotted relative to their 6-8 ka average. Known climatic events are highlighted as in Figure 3.3 (main text).

Table C.1: Radiocarbon Measurements

Sample Interval (cm)	Avg. Depth (cm)	NOSAMS Accession #	^{14}C Age (yr)	1σ (yr)[a]	Sample Age (ka)[b]	1σ (ka)[b]
Core: KN207-2-GGC3[c]						
3:05-06	5.5	OS-118321	5,610	20	6.0	0.04
3:20-22	21	OS-118320	10,600	30	11.9	0.08
3:36-38	37	OS-118323	17,650	50	20.8	0.09
3:40-42	41	OS-118326	24,500	75	28.1	0.13
3:50-52	51	OS-118325	30,800	110	34.4	0.15
3:64-66[d]	65	OS-118324	38,700	220	42.5	0.22
Core: KN207-2-GGC6						
6:10-12	11	OS-118473	4,870	20	5.2	0.07
6:24-26	25	OS-118474	10,950	25	12.5	0.05
6:46-48	47	OS-118472	18,550	55	22.0	0.11
6:60-62	61	OS-118475	24,400	70	28.0	0.12
6:73-74	73.5	OS-118431	31,000	140	34.6	0.15
6:106-108[d]	107	OS-118471	39,300	340	42.8	0.34

[a]1σ values reflect ^{14}C age uncertanties reported by NOSAMS

[b]Ages and uncertanties reflect years before 1950 are computed using Calib 7.1 Marine 2013 (Stuvier and Reimer, 1993; Reimer et al., 2013)

[c]Values reflect revised sample ages computed from NOSAMS values reported in Middleton et al. (2016)

[d]Ages exceeding 38ka were not included in determination of the sediment core age-model

Table C.2: Age Models and Compiled Helium Data

Sample Interval (cm)	Avg. Depth (cm)	Age (ka)[a]	Number He Replicates[b]	$^4He_{terr}$ (ncc g^{-1})[c]	1σ[c]	$^3He_{ET}$ (pcc g^{-1})[c]	1σ[c]	Vertical Sed. Rain Rate[c] (g cm^{-2} ka^{-1})	1σ[c]
Core: KN207-2-GGC3									
3:1-3	2	2.2	2	461	3	2.45	0.49	0.33	0.08
3:3-4	3.5	3.8	2	458	3	2.58	0.51	0.31	0.08
3:4-5	4.5	4.9	2	439	4	2.95	0.58	0.27	0.07
3:5-6[d]	5.5	6.0	2	424	3	2.78	0.55	0.29	0.07
3:6-8	7	6.6	2	407	3	3.31	0.66	0.24	0.06
3:8-10	9	7.3	2	436	3	2.42	0.48	0.33	0.08
3:10-12	11	8.1	2	485	3	1.53	0.30	0.53	0.13
3:12-14	13	8.9	1	530	4	2.60	0.73	0.30	0.10
3:14-16	15	9.6	2	561	4	2.69	0.53	0.30	0.08
3:16-18	17	10.4	2	665	5	2.97	0.59	0.27	0.07
3:18-20	19	11.1	2	689	7	1.83	0.36	0.44	0.11
3:20-22[d]	21	11.9	2	682	5	2.14	0.42	0.38	0.09
3:22-24	23	13.0	2	707	5	1.59	0.32	0.51	0.13
3:24-26	25	14.1	2	729	5	2.24	0.44	0.36	0.09
3:26-28	27	15.2	2	733	5	2.56	0.51	0.32	0.08
3:28-30	29	16.4	2	736	5	2.54	0.50	0.32	0.08
3:30-32	31	17.5	1	754	8	1.46	0.41	0.55	0.18
3:32-34	33	18.6	2	657	5	2.54	0.50	0.32	0.08
3:34-36	35	19.7	2	683	5	2.74	0.54	0.29	0.07
3:36-38[d]	37	20.8	2	619	4	2.70	0.53	0.30	0.07
3:38-40	39	24.5	2	860	6	5.15	1.02	0.16	0.04
3:40-42[d]	41	28.1	1	826	8	2.41	0.67	0.34	0.11
3:42-44	43	29.4	2	836	6	2.58	0.51	0.31	0.08
3:44-46	45	30.6	1	815	6	2.96	0.83	0.26	0.08
3:46-48	47	31.9	2	794	6	3.70	0.73	0.22	0.05
3:48-50	49	33.1	2	776	5	2.26	0.45	0.36	0.09
3:50-52[d]	51	34.4	2	645	5	2.35	0.47	0.34	0.09
3:52-54	53	35.0	2	655	5	2.61	0.52	0.31	0.08
3:54-56	55	35.6	2	643	5	3.10	0.61	0.26	0.07
3:56-58	57	36.2	2	580	4	3.11	0.62	0.26	0.06
3:58-60	59	36.7	2	558	6	2.54	0.50	0.32	0.08
3:60-62	61	37.3	2	511	4	4.03	0.80	0.20	0.05
3:62-64[e]	63	37.9	2	516	4	3.58	0.71	0.22	0.06
3:64-66	65	39.2	2	524	4	4.41	0.87	0.18	0.05
3:66-68	67	40.5	2	589	4	4.90	0.97	0.16	0.04
3:68-70	69	41.8	2	588	4	2.72	0.54	0.30	0.07
3:70-72	71	43.0	2	615	4	3.18	0.63	0.25	0.06
3:72-74	73	44.3	2	646	5	3.53	0.70	0.23	0.06
3:74-76[e]	75	45.6	2	499	4	2.32	0.46	0.35	0.09

Table C.2 (continued): Age Models and Compiled Helium Data

Sample Interval (cm)	Avg. Depth (cm)	Age (ka)[a]	Number He Replicates[b]	$^4He_{terr}$ (ncc g^{-1})[c]	1σ[c]	$^3He_{ET}$ (pcc g^{-1})[c]	1σ[c]	Vertical Sed. Rain Rate[c] (g cm^{-2} ka^{-1})	1σ[c]
Core: KN207-2-GGC3 (continued)									
3:76-78	77	46.9	2	594	4	3.46	0.69	0.23	0.06
3:78-80	79	48.2	2	677	5	2.96	0.59	0.27	0.07
3:80-82	81	49.5	2	796	6	3.11	0.62	0.26	0.07
Core: KN207-2-GGC6									
6:0-2	1	0.5	4	397	2	1.98	0.28	0.41	0.08
6:2-4	3	1.4	2	461	3	1.48	0.29	0.54	0.14
6:4-6	5	2.4	2	477	3	1.87	0.37	0.43	0.11
6:6-8	7	3.3	2	108	1	0.71	0.14	1.14	0.29
6:8-10	9	4.3	2	219	2	1.85	0.37	0.44	0.11
6:10-12[d]	11	5.2	3	219	1	2.31	0.37	0.35	0.08
6:12-14	13	6.2	2	187	1	1.92	0.38	0.42	0.10
6:14-16	15	7.3	4	241	1	1.80	0.25	0.45	0.09
6:16-18	17	8.3	4	312	2	2.02	0.28	0.40	0.08
6:18-20	19	9.4	2	364	3	1.21	0.24	0.67	0.17
6:20-22	21	10.4	4	400	2	2.23	0.31	0.36	0.08
6:22-24	23	11.5	4	451	2	1.13	0.16	0.72	0.15
6:24-26[d]	25	12.5	4	501	3	1.32	0.18	0.61	0.13
6:26-28	27	13.4	2	581	4	1.22	0.24	0.66	0.17
6:28-30	29	14.2	2	595	4	2.86	0.57	0.28	0.07
6:30-32	31	15.1	3	597	4	1.98	0.32	0.41	0.09
6:32-34	33	16.0	2	544	4	1.23	0.24	0.66	0.16
6:34-36	35	16.8	3	537	3	1.91	0.31	0.42	0.09
6:36-38	37	17.7	2	682	5	1.51	0.30	0.54	0.13
6:38-40	39	18.5	2	717	5	2.01	0.40	0.40	0.10
6:40-42	41	19.4	2	750	5	2.32	0.46	0.35	0.09
6:42-44	43	20.3	4	734	4	2.77	0.39	0.29	0.06
6:44-46	45	21.1	2	765	5	1.95	0.39	0.41	0.10
6:46-48[d]	47	22.0	2	755	5	2.26	0.45	0.36	0.09
6:48-49	48.5	22.6	4	586	3	2.40	0.34	0.34	0.07
6:49-50	49.5	23.1	2	362	3	1.13	0.22	0.71	0.18
6:50-52	51	23.7	4	740	4	3.42	0.48	0.24	0.05
6:52-54	53	24.6	2	854	6	2.11	0.42	0.38	0.10
6:54-56	55	25.4	2	834	6	2.44	0.48	0.33	0.08
6:56-58	57	26.3	2	764	5	2.24	0.44	0.36	0.09
6:58-60	59	27.1	2	704	5	1.47	0.29	0.55	0.14
6:60-62[d]	61	28.0	2	664	5	2.40	0.48	0.34	0.08
6:62-64	63	29.1	2	598	4	2.42	0.48	0.33	0.08
6:64-66	65	30.1	4	577	3	1.74	0.24	0.46	0.10

Table C.2 (continued): Age Models and Compiled Helium Data

Sample Interval (cm)	Avg. Depth (cm)	Age (ka)[a]	Number He Replicates[b]	$^4He_{terr}$ (ncc g^{-1})[c]	1σ[c]	$^3He_{ET}$ (pcc g^{-1})[c]	1σ[c]	Vertical Sed. Rain Rate[c] (g cm^{-2} ka^{-1})	1σ[c]
Core: KN207-2-GGC6 (continued)									
6:66-68	67	31.2	2	543	4	1.16	0.23	0.70	0.18
6:68-70	69	32.2	3	447	3	1.77	0.29	0.46	0.10
6:70-71	70.5	33.0	4	381	2	2.26	0.32	0.36	0.07
6:71-73	72	33.8	2	232	2	0.65	0.13	1.24	0.31
6:73-74[d]	73.5	34.6	1	340	3	0.78	0.22	1.03	0.33
6:74-76	75	35.4	2	387	3	1.18	0.23	0.68	0.17
6:76-78	77	36.4	2	384	3	1.55	0.31	0.52	0.13
6:78-80	79	37.4	2	360	3	1.25	0.25	0.64	0.16
6:80-82	81	38.4	3	417	2	1.54	0.25	0.52	0.12
6:82-84	83	39.5	2	480	3	1.64	0.32	0.49	0.12
6:84-86	85	40.5	4	530	3	1.97	0.28	0.41	0.09
6:86-88	87	41.5	2	588	4	1.54	0.30	0.53	0.13
6:88-90	89	42.5	2	489	3	1.38	0.27	0.59	0.15
6:90-92	91	43.6	2	435	3	1.56	0.31	0.52	0.13
6:92-94	93	44.6	4	332	2	0.99	0.14	0.61	0.13
6:94-96[e]	95	45.6	4	367	2	2.48	0.35	0.32	0.07
6:96-98	97	46.6	2	407	3	1.39	0.28	0.58	0.15
6:98-100	99	47.6	2	260	2	0.74	0.15	0.54	0.14
6:100-102	101	48.6	2	588	4	1.50	0.30	0.54	0.14
6:102-104	103	49.5	4	484	2	2.37	0.33	0.34	0.07
6:104-106	105	50.5	2	322	2	1.10	0.22	0.73	0.18
6:106-108	107	51.5	4	220	1	1.55	0.22	0.39	0.08
6:108-110	109	52.5	2	281	2	1.47	0.29	0.55	0.14
6:110-112	111	53.5	2	364	3	1.32	0.26	0.61	0.15
6:112-114	113	54.5	4	310	2	2.31	0.32	0.26	0.05
6:114-116	115	55.4	2	424	3	2.25	0.45	0.36	0.09
6:116-118	117	56.4	2	515	4	1.64	0.32	0.49	0.12
6:118-120[e]	119	57.4	2	406	3	1.38	0.27	0.58	0.15
6:120-122	121	58.3	2	422	3	3.65	0.72	0.22	0.06
6:122-124	123	59.1	2	644	5	1.77	0.35	0.46	0.11
6:124-126	125	60.0	2	630	4	2.03	0.40	0.40	0.10
6:126-128	127	60.8	2	666	5	2.27	0.45	0.35	0.09
6:128-130[e]	129	61.7	4	776	4	2.76	0.39	0.29	0.06
6:130-132	131	62.6	1	802	8	2.98	0.83	0.27	0.09
6:132-134	133	63.4	2	821	6	2.71	0.54	0.30	0.07
6:134-136	135	64.3	2	814	6	2.98	0.59	0.27	0.07
6:136-138	137	65.1	4	815	4	3.33	0.47	0.24	0.05
6:138-140	139	66.0	4	816	4	3.75	0.53	0.21	0.04

Table C.2 (continued): Age Models and Compiled Helium Data

Sample Interval (cm)	Avg. Depth (cm)	Age (ka) [a]	Number He Replicates[b]	$^4He_{terr}$ (ncc g^{-1})[c]	1σ [c]	$^3He_{ET}$ (pcc g^{-1})[c]	1σ[c]	Vertical Sed. Rain Rate[c] (g cm^{-2} ka^{-1})	1σ[c]
Core: KN207-2-GGC6 (continued)									
6:140-142	141	66.9	2	800	6	3.58	0.71	0.23	0.06
6:142-144	143	67.7	1	807	8	2.63	0.74	0.31	0.10
6:144-147	145.5	68.8	4	711	4	2.29	0.32	0.35	0.07

[a]Age model was calculated using a constant sedimentation rate between tie points- GGC3 sediment core age model is revised from Middleton et al. (2016)
[b]Average aliquot size is 1.5 g of bulk sediment.
[c]Reported values reflect average of all helium replicates for each depth, 1σ values reflect uncertainty based on the reproducibility of replicated samples (replicate data available in Table S2 of Middleton et al. 2016), cc's refer to cm^3 of gas at standard temperature and pressure (STP) of 273K and 1 atm.
[d]Sediment depths represent age model tie points constrained using radiocarbon analyses
[e]Sediment depths represent age model tie points constrained using carbonate content stratigraphy (Section 3.3)

Table C.3: ICP-MS Results

Bulk sediment values				Carbonate leachate composition[c]				Carbonate-free sediment composition[d]				
Sample Interval (cm)[a]	**ICP Bulk Sample Mass (g)**	**$CaCO_3$ (wt.%)[b]**	**1σ**	**Ti (wt. %)**	**1σ**	**Th (ppm)**	**1σ**	**$CaCO_3$-free Mass (g)**	**Ti (wt.%)**	**1σ**	**Th (ppm)**	**1σ**
Core: KN207-2-GGC6												
6:0-2	0.2718	93	0.9	0.0052	0.0001	0.394	0.023	0.0196	0.758	0.015	21.8	1.3
6:2-4	0.2633	91	0.9	0.0183	0.0004	0.211	0.012	0.0244	0.657	0.013	19.2	1.1
6:4-6	0.4490	90	0.9	0.0054	0.0001	0.206	0.012	0.0454	0.534	0.010	18.0	1.0
6:6-8	0.8932	95	1.0	0.0288	0.0006	0.167	0.010	0.0413	0.620	0.012	13.7	0.8
6:8-10	0.3875	93	0.9	0.0167	0.0003	0.178	0.010	0.0287	0.556	0.011	14.8	0.9
6:10-12	0.3804	94	0.9	0.0200	0.0004	0.134	0.008	0.0247	0.666	0.013	17.4	1.0
6:12-14	0.4389	94	0.9	0.0165	0.0003	0.174	0.010	0.0278	0.552	0.011	17.2	1.0
6:14-16	0.4294	94	0.9	0.0200	0.0004	0.037	0.002	0.0253	0.644	0.012	21.8	1.3
6:16-18	0.3518	94	0.9	0.0134	0.0003	0.114	0.007	0.0198	0.731	0.014	25.5	1.5
6:18-20	0.3837	93	0.9	0.0052	0.0001	0.126	0.007	0.0250	0.599	0.012	23.5	1.4
6:20-22	0.3727	92	0.9	0.0182	0.0004	0.096	0.006	0.0284	0.559	0.011	20.9	1.2
6:22-24	0.2632	93	0.9	0.0000	0.0000	0.287	0.017	0.0190	0.721	0.014	22.1	1.3
6:24-26	0.2938	92	0.9	0.0106	0.0002	0.218	0.013	0.0228	0.647	0.012	23.9	1.4
6:26-28	0.2016	91	0.9	0.0000	0.0000	0.420	0.024	0.0174	0.711	0.014	21.1	1.2
6:28-30	0.2351	88	0.9	0.0165	0.0003	0.529	0.031	0.0272	0.574	0.011	17.7	1.0
6:30-32	0.1779	89	0.9	0.0000	0.0000	0.478	0.028	0.0201	0.612	0.012	17.6	1.0
6:32-34	0.2573	88	0.9	0.0165	0.0003	0.425	0.025	0.0312	0.489	0.009	15.5	0.9
6:34-36	0.2007	90	0.9	0.0000	0.0000	0.387	0.022	0.0203	0.649	0.012	18.4	1.1
6:36-38	0.1964	86	0.9	0.0169	0.0003	0.591	0.034	0.0282	0.523	0.010	15.3	0.9
6:38-40	0.1898	87	0.9	0.0304	0.0006	0.583	0.034	0.0247	0.608	0.012	17.0	1.0
6:40-42	0.1413	87	0.9	0.0000	0.0000	0.724	0.042	0.0186	0.664	0.013	17.6	1.0
6:42-44	0.1730	85	0.9	0.0168	0.0003	0.648	0.038	0.0253	0.592	0.011	15.9	0.9
6:44-46	0.1378	87	0.9	0.0000	0.0000	0.765	0.044	0.0181	0.700	0.013	17.6	1.0
6:46-48	0.1524	91	0.9	0.0189	0.0004	0.348	0.020	0.0136	0.942	0.018	27.0	1.6
6:48-49	0.2202	87	0.9	0.0048	0.0001	0.476	0.028	0.0282	0.544	0.010	15.1	0.9
6:49-50	0.2916	92	0.9	0.0182	0.0004	0.233	0.014	0.0219	0.688	0.013	17.4	1.0

Table C.3 (continued): ICP-MS Results

Bulk sediment values				Carbonate leachate composition[c]				Carbonate-free sediment composition[d]				
Sample Interval (cm)[a]	**ICP Bulk Sample Mass (g)**	**$CaCO_3$ (wt.%)[b]**	**1σ**	**Ti (wt. %)**	**1σ**	**Th (ppm)**	**1σ**	**$CaCO_3$-free Mass (g)**	**Ti (wt.%)**	**1σ**	**Th (ppm)**	**1σ**
Core: KN207-2-GGC6 (continued)												
6:50-52	0.1365	86	0.9	0.0000	0.0000	0.669	0.039	0.0198	0.664	0.013	14.2	0.8
6:52-54	0.1701	88	0.9	0.0196	0.0004	0.460	0.027	0.0203	0.705	0.014	20.9	1.2
6:54-56	0.1396	86	0.9	0.0000	0.0000	0.752	0.044	0.0198	0.625	0.012	17.1	1.0
6:56-58	0.1782	87	0.9	0.0188	0.0004	0.211	0.012	0.0223	0.656	0.013	19.8	1.1
6:58-60	0.1894	87	0.9	0.0168	0.0003	0.594	0.035	0.0249	0.569	0.011	16.6	1.0
6:60-62	0.1568	88	0.9	0.0000	0.0000	0.640	0.037	0.0184	0.688	0.013	17.7	1.0
6:62-64	0.2152	91	0.9	0.0189	0.0004	0.350	0.020	0.0185	0.805	0.015	24.7	1.4
6:64-66	0.1826	89	0.9	0.0000	0.0000	0.594	0.035	0.0208	0.663	0.013	16.0	0.9
6:66-68	0.2346	91	0.9	0.0166	0.0003	0.547	0.032	0.0220	0.683	0.013	19.6	1.1
6:68-70	0.2757	90	0.9	0.0188	0.0004	0.295	0.017	0.0263	0.613	0.012	17.0	1.0
6:70-71	0.2464	92	0.9	0.0000	0.0000	0.382	0.022	0.0209	0.654	0.013	16.8	1.0
6:71-73	0.4944	93	0.9	0.0165	0.0003	0.266	0.015	0.0348	0.532	0.010	13.5	0.8
6:73-74	0.3476	95	1.0	0.0190	0.0004	0.237	0.014	0.0158	0.986	0.019	30.4	1.8
6:74-76	0.2529	92	0.9	0.0000	0.0000	0.216	0.013	0.0199	0.620	0.012	21.0	1.2
6:76-78	0.3192	94	0.9	0.0187	0.0004	0.223	0.013	0.0199	0.728	0.014	25.4	1.5
6:78-80	0.3735	93	0.9	0.0165	0.0003	0.339	0.020	0.0280	0.551	0.011	19.0	1.1
6:80-82	0.2602	92	0.9	0.0000	0.0000	0.328	0.019	0.0204	0.595	0.011	19.7	1.1
6:82-84	0.2895	92	0.9	0.0188	0.0004	0.280	0.016	0.0226	0.646	0.012	21.0	1.2
6:84-86	0.2655	91	0.9	0.0050	0.0001	0.352	0.020	0.0235	0.633	0.012	22.8	1.3
6:86-88	0.2012	91	0.9	0.0000	0.0000	0.447	0.026	0.0183	0.661	0.013	21.1	1.2
6:88-90	0.2788	92	0.9	0.0200	0.0004	0.379	0.022	0.0226	0.710	0.014	20.9	1.2
6:90-92	0.2868	93	0.9	0.0049	0.0001	0.579	0.034	0.0205	0.710	0.014	21.6	1.3

6:92-94	0.2869	92	0.9	0.0195	0.0004	0.299	0.017	0.0236	0.655	0.013	20.6	1.2
6:94-96	0.3380	92	0.9	0.0166	0.0003	0.324	0.019	0.0267	0.595	0.011	17.9	1.0
6:96-98	0.3207	93	0.9	0.0182	0.0004	0.239	0.014	0.0234	0.657	0.013	21.6	1.3
6:98-100	0.2701	91	0.9	0.0165	0.0003	0.457	0.027	0.0246	0.617	0.012	19.0	1.1
6:100-102	0.2494	92	0.9	0.0403	0.0008	0.373	0.022	0.0202	0.713	0.014	23.4	1.4

Table C.3 (continued): ICP-MS Results

Bulk sediment values				Carbonate leachate composition[c]				Carbonate-free sediment composition[d]				
Sample Interval (cm)[a]	**ICP Bulk Sample Mass (g)**	**$CaCO_3$ (wt.%)[b]**	**1σ**	**Ti (wt. %)**	**1σ**	**Th (ppm)**	**1σ**	**$CaCO_3$-free Mass (g)**	**Ti (wt.%)**	**1σ**	**Th (ppm)**	**1σ**
Core: KN207-2-GGC6 (continued)												
6:102-104	0.2781	92	0.9	0.0188	0.0004	0.254	0.015	0.0214	0.753	0.014	23.2	1.3
6:104-106	0.3758	93	0.9	0.0175	0.0003	0.242	0.014	0.0250	0.669	0.013	20.8	1.2
6:106-108	0.3808	95	0.9	0.0200	0.0004	0.163	0.009	0.0201	0.753	0.014	24.1	1.4
6:108-110	0.3999	94	0.9	0.0189	0.0004	0.179	0.010	0.0231	0.704	0.014	21.2	1.2
6:110-112	0.3535	93	0.9	0.0051	0.0001	0.200	0.012	0.0241	0.638	0.012	20.0	1.2
6:112-114	0.2762	92	0.9	0.0189	0.0004	0.272	0.016	0.0230	0.696	0.013	18.2	1.1
6:114-116	0.2493	90	0.9	0.0202	0.0004	0.378	0.022	0.0248	0.669	0.013	15.8	0.9
6:116-118	0.2247	88	0.9	0.0166	0.0003	0.513	0.030	0.0272	0.610	0.012	13.9	0.8
6:118-120	0.2535	90	0.9	0.0296	0.0006	0.349	0.020	0.0255	0.657	0.013	16.1	0.9
6:120-122	0.2401	92	0.9	0.0189	0.0004	0.287	0.017	0.0203	0.836	0.016	20.3	1.2
6:122-124	0.1949	91	0.9	0.0045	0.0001	0.459	0.027	0.0168	0.933	0.018	22.1	1.3
6:124-126	0.1610	88	0.9	0.0188	0.0004	0.364	0.021	0.0193	0.815	0.016	17.7	1.0
6:126-128	0.1367	83	0.8	0.0026	0.0000	0.738	0.043	0.0227	0.597	0.011	13.3	0.8
6:128-130	0.0985	78	0.8	0.0192	0.0004	0.661	0.038	0.0214	0.582	0.011	11.5	0.7
6:130-132	0.1204	82	0.8	0.0023	0.0000	0.843	0.049	0.0219	0.653	0.013	13.2	0.8
6:132-134	0.1224	82	0.8	0.0189	0.0004	0.614	0.036	0.0215	0.694	0.013	14.0	0.8
6:134-136	0.1198	78	0.8	0.0026	0.0001	0.848	0.049	0.0259	0.581	0.011	12.3	0.7
6:136-138	0.1193	84	0.8	0.0194	0.0004	0.491	0.029	0.0193	0.749	0.014	15.3	0.9
6:138-140	0.1410	83	0.8	0.0028	0.0001	0.782	0.045	0.0246	0.591	0.011	14.4	0.8
6:140-142	0.1413	85	0.9	0.0187	0.0004	0.463	0.027	0.0209	0.701	0.013	16.8	1.0
6:142-144	0.1578	86	0.9	0.0038	0.0001	0.637	0.037	0.0222	0.659	0.013	17.3	1.0
6:144-147	0.1460	88	0.9	0.0186	0.0004	0.318	0.018	0.0172	0.748	0.014	19.8	1.2

Table C.3 (continued): ICP-MS Results

[a]ICP-MS results for GGC3 are available in Supplementary Table S1 of Middleton et al. (2016)

[b]Carbonate content was calculated from the initial ICP-MS bulk sediment mass and the dry carbonate-free sediment mass following an acetic acid leach

[c]Elemental concentrations reflect ICP-MS values for the acetic acid leachate, 1σ uncertainties are determined from the long-term reproducibility of internal standard K1919

[d]Elemental concentrations reflect ICP-MS values for residual sediment after the acetic acid leach, 1σ uncertainties are determined from the long-term reproducibility of internal standard K1919

Table C.4: Benthic Carbon and Oxygen Isotope Analyses

Sample Interval (cm)[a]	Mass (µg)[b]	$\delta^{13}C$ (‰)	1σ[c]	$\delta^{18}O$ (‰)	1σ[c]
Core: KN207-2-GGC6					
6:00-02	70	0.78	0.04	4.19	0.06
6:02-04	71	1.25	0.04	2.63	0.06
6:04-06	65	1.33	0.04	2.80	0.06
6:04-06A	73	0.89	0.04	2.57	0.06
6:06-08	85	0.75	0.04	3.51	0.06
6:08-10	80	1.26	0.04	2.45	0.06
6:08-10A	89	1.14	0.04	3.75	0.06
6:10-12	81	1.33	0.04	2.61	0.06
6:12-14	126	1.18	0.04	4.13	0.06
6:14-16	NA	-	-	-	-
6:16-18	67	1.12	0.04	2.72	0.06
6:18-20	55	1.26	0.04	2.78	0.06
6:18-20A	34	0.56	0.04	4.27	0.06
6:20-22	70	1.05	0.04	2.70	0.06
6:22-24	50	0.56	0.04	3.77	0.06
6:24-26	74	0.62	0.04	3.27	0.06
6:26-28	115	0.75	0.04	4.26	0.06
6:28-30	81	0.92	0.04	3.51	0.06
6:28-30A	20	0.27	0.04	3.69	0.06
6:30-32	71	0.93	0.04	3.19	0.06
6:32-34	76	0.58	0.04	3.87	0.06
6:34-36	80	0.60	0.04	3.79	0.06
6:36-38	58	0.37	0.04	4.06	0.06
6:38-40	82	0.33	0.04	4.20	0.06
6:40-42	104	0.21	0.04	3.82	0.06
6:42-44	63	0.58	0.04	4.43	0.06
6:42-44A	81	0.88	0.04	4.31	0.06
6:44-46	82	0.72	0.04	4.46	0.06
6:46-48	70	0.57	0.04	4.41	0.06
6:48-59	54	0.54	0.04	4.35	0.06
6:49-50	83	0.25	0.04	3.90	0.06
6:50-52	68	0.54	0.04	4.43	0.06
6:50-52A	66	0.62	0.04	4.40	0.06
6:52-54	77	0.59	0.04	4.30	0.06
6:52-54A	72	0.73	0.04	4.27	0.06
6:52-54B	117	0.41	0.04	3.88	0.06
6:54-56	81	0.89	0.04	4.25	0.06
6:56-58	59	0.55	0.04	4.24	0.06
6:58-60	64	0.73	0.04	4.00	0.06
6:60-62	99	0.62	0.04	4.05	0.06
6:62-64	58	0.81	0.04	4.05	0.06
6:62-64A	118	0.97	0.04	4.15	0.06
6:64-66	51	0.67	0.04	4.05	0.06

Table C.4 (continued): Benthic Carbon and Oxygen Isotope Analyses

Sample Interval (cm)[a]	Mass (µg)[b]	$\delta^{13}C$ (‰)	1σ[c]	$\delta^{18}O$ (‰)	1σ[c]
Core: KN207-2-GGC6 (continued)					
6:66-68	69	0.62	0.04	4.01	0.06
6:66-68A	70	0.83	0.04	3.96	0.06
6:68-70	82	0.84	0.04	3.90	0.06
6:70-71	72	1.01	0.04	3.91	0.06
6:71-73	70	0.25	0.04	3.74	0.06
6:73-74	73	0.68	0.04	3.86	0.06
6:74-76	83	0.82	0.04	3.64	0.06
6:76-78	75	0.94	0.04	3.86	0.06
6:78-80	55	1.06	0.04	3.89	0.06
6:80-82	105	0.99	0.04	3.64	0.06
6:80-82A	74	0.54	0.04	3.81	0.06
6:82-84	74	1.13	0.04	3.74	0.06
6:82-84A	83	1.15	0.04	3.81	0.06
6:82-84B	63	0.67	0.04	3.93	0.06
6:84-86	83	0.67	0.04	3.88	0.06
6:86-88	57	0.61	0.04	4.06	0.06
6:88-90	99	1.19	0.04	4.00	0.06
6:90-92	61	0.63	0.04	3.83	0.06
6:92-94	98	1.11	0.04	3.98	0.06
6:94-96	70	1.09	0.04	3.80	0.06
6:96-98	63	1.10	0.04	3.83	0.06
6:96-98A	85	1.12	0.04	3.94	0.06
6:96-98B	76	1.18	0.04	3.98	0.06
6:96-98C	123	0.60	0.04	3.15	0.06
6:98-100	67	0.67	0.04	3.87	0.06
6:98-100A	92	0.65	0.04	3.86	0.06
6:98-100B	79	0.64	0.04	3.78	0.06
6:100-102	52	0.98	0.04	3.97	0.06
6:102-104	57	1.19	0.04	4.04	0.06
6:104-106	52	1.07	0.04	3.79	0.06
6:106-108	55	1.12	0.04	3.87	0.06
6:108-110	56	0.90	0.04	3.64	0.06
6:110-112	52	0.41	0.04	3.72	0.06
6:112-114	66	0.87	0.04	3.67	0.06
6:114-116	66	0.83	0.04	3.74	0.06
6:116-118	NA	-	-	-	-
6:118-120	75	0.47	0.04	3.95	0.06
6:120-122	62	0.44	0.04	3.74	0.06
6:122-124	72	0.26	0.04	4.03	0.06
6:122-124A	65	0.76	0.04	3.85	0.06
6:124-126	70	0.05	0.04	3.67	0.06
6:124-126A	70	0.54	0.04	3.48	0.06
6:126-128	74	0.15	0.04	3.77	0.06

Table C.4 (continued): Benthic Carbon and Oxygen Isotope Analyses

Sample Interval (cm)[a]	Mass (µg)[b]	$\delta^{13}C$ (‰)	1σ[c]	$\delta^{18}O$ (‰)	1σ[c]
Core: KN207-2-GGC6 (continued)					
6:128-130	67	0.18	0.04	4.01	0.06
6:130-132	63	1.21	0.04	3.06	0.06
6:132-134	73	0.09	0.04	4.01	0.06
6:134-136	76	0.09	0.04	3.90	0.06
6:136-138	55	0.54	0.04	3.91	0.06
6:136-138A	70	0.73	0.04	3.31	0.06
6:138-140	95	0.17	0.04	3.47	0.06
6:140-142	65	0.26	0.04	4.06	0.06
6:142-144	89	0.73	0.04	3.78	0.06
6:144-147	67	0.77	0.04	3.92	0.06
6:144-147A	81	0.51	0.04	3.72	0.06
Core: KN207-2-GGC3[d]					
3:01-03	40	0.87	0.04		
3:03-04	69	1.18	0.04		
3:04-05	68	1.14	0.04		
3:05-06	63	1.11	0.04		
3:06-08	99	0.49	0.04		
3:06-08A	67	1.20	0.04		
3:06-08B	51	1.00	0.04		
3:08-10	NA	-	-		
3:10-12	45	1.07	0.04		
3:12-14	59	0.94	0.04		
3:12-14A	58	0.59	0.04		
3:14-16	76	0.86	0.04		
3:16-18	78	0.80	0.04		
3:18-20	44	0.92	0.04		
3:20-22	87	0.66	0.04		
3:22-24	69	0.82	0.04		
3:24-26	65	0.68	0.04		
3:24-26A	88	0.42	0.04		
3:26-28	93	0.79	0.04		
3:28-30	62	0.31	0.04		
3:30-32	48	0.26	0.04		
3:32-34	79	0.30	0.04		
3:34-36	78	0.84	0.04		
3:34-36A	72	0.54	0.04		
3:36-38	62	0.60	0.04		
3:38-40	59	0.37	0.04		
3:38-40A	20	1.05	0.04		
3:40-42	59	0.90	0.04		
3:42-44	67	0.72	0.04		
3:44-46	130	0.59	0.04		

Table C.4 (continued): Benthic Carbon and Oxygen Isotope Analyses

Sample Interval (cm)[a]	Mass (µg)[b]	$\delta^{13}C$ (‰)	1σ[c]	$\delta^{18}O$ (‰)	1σ[c]
Core: KN207-2-GGC3[d] (continued)					
3:46-48	72	0.69	0.04		
3:46-48A	78	0.70	0.04		
3:48-50	91	0.37	0.04		
3:48-50A	77	0.63	0.04		
3:50-52	57	0.24	0.04		
3:52-54	50	0.58	0.04		
3:54-56	71	0.52	0.04		
3:56-58	58	0.48	0.04		
3:58-60	76	0.76	0.04		
3:58-60A	66	0.63	0.04		
3:60-62	76	0.90	0.04		
3:62-64	55	0.89	0.04		
3:64-66	75	0.34	0.04		
3:66-68	72	1.14	0.04		
3:66-68A	70	1.05	0.04		
3:68-70	83	0.59	0.04		
3:70-72	51	0.78	0.04		
3:72-74	74	0.48	0.04		
3:72-74A	72	0.95	0.04		
3:74-76	21	0.75	0.04		
3:76-78	95	0.79	0.04		
3:76-78A	92	0.96	0.04		
3:78-80	60	0.59	0.04		
3:78-80A	58	0.61	0.04		
3:80-82	55	0.65	0.04		
3:80-82A	71	0.63	0.04		

[a]Sample intervals tagged A, B, or C indicate replicate analyses using additional aliquots of the same depth interval

[b]Total mass of *C. wuellerstorfi* tests analysed for each sample. Depth intervals with no available *C. wuellerstorfi* are listed as NA.

[c]1σ uncertanies reflect the long-term standard devitiation of the NBS-19 international standard (see Section 3.3)

[d]Oxygen isotope data for GGC3 are available in Supplementary Table S4 in Middleton et al. (2016)

Appendix D

Supplemental material for Chapter 4

Table D.1: Helium analyses of individual sediment aliquots

Sample Interval (section:depths)[a]			Mass (g)	^{4}He total (ncc/g)[b]	1σ[c]	^{3}He/^{4}He (R_A)[d]	1σ[c]	^{4}He$_{terr}$ (ncc/g)[b,e]	1σ[f]	^{3}He$_{ET}$ (pcc/g)[b,e]	1σ[f]
Core: AT26-19-09PC											
2	25	26cmA	1.035	374	4	2.17	0.09	369	15	1.13	0.44
2	45	46cmA	1.069	354	4	6.76	0.27	340	14	3.34	1.30
2	57	58cmA	0.630	299	3	2.45	0.10	295	12	1.02	0.40
2	69	70cmB	0.467	403	4	1.56	0.06	399	16	0.87	0.34
2	69	70cmA	0.556	410	4	1.63	0.07	406	16	0.93	0.36
2	93	94cmB	0.554	614	6	2.39	0.10	605	24	2.04	0.80
2	93	94cmA	0.502	692	7	1.20	0.05	688	28	1.14	0.45
3	99	100cmB	0.500	864	9	1.00	0.04	859	34	1.19	0.46
4	29	30cmB	0.446	476	5	1.08	0.04	473	19	0.71	0.28
4	29	30cmA	0.578	492	5	0.91	0.04	490	20	0.61	0.24
4	37	38cmA	1.026	467	5	1.57	0.06	463	19	1.02	0.40
4	41	42cmB	0.514	405	4	1.15	0.05	402	16	0.64	0.25
4	41	42cmA	0.583	444	4	1.38	0.06	441	18	0.85	0.33
4	45	46cmB	0.468	374	4	1.05	0.04	372	15	0.54	0.21
4	45	46cmA	0.542	382	4	1.39	0.06	379	15	0.73	0.29
4	49	50cmB	0.464	347	3	1.57	0.06	344	14	0.76	0.30
4	49	50cmA	0.573	398	4	1.06	0.04	396	16	0.58	0.23
4	53	54cmA	1.049	339	3	6.23	0.25	327	13	2.95	1.15
4	57	58cmB	0.558	306	3	1.31	0.05	303	12	0.55	0.22
4	57	58cmA	0.455	331	3	1.10	0.04	329	13	0.50	0.20
4	61	62cmB	0.468	306	3	1.35	0.05	304	12	0.57	0.22
4	61	62cmA	0.548	324	3	0.90	0.04	322	13	0.40	0.16
4	65	66cmB	0.496	326	3	0.95	0.04	325	13	0.43	0.17
4	65	66cmA	0.512	373	4	1.13	0.05	370	15	0.58	0.23
4	89	90cmB	0.442	355	4	5.09	0.20	345	14	2.52	0.98
4	89	90cmA	0.628	381	4	4.03	0.16	372	15	2.14	0.83
4	113	114cmA	1.094	422	4	1.36	0.05	419	17	0.79	0.31
4	117	118cmB	0.492	394	4	1.76	0.07	390	16	0.96	0.38
4	117	118cmA	0.509	410	4	2.22	0.09	404	16	1.26	0.49
4	133	134cmA	0.503	883	9	1.05	0.04	877	35	1.28	0.50
4	133	134cmB	0.523	977	10	1.41	0.06	969	39	1.91	0.75

Table D.1 (continued): Helium analyses of individual sediment aliquots

Sample Interval (section:depths)[a]			Mass (g)	^{4}He total (ncc/g)[b]	1σ[c]	^{3}He/^{4}He (R_A)[d]	1σ[c]	^{4}He$_{terr}$ (ncc/g)[b,e]	1σ[f]	^{3}He$_{ET}$ (pcc/g)[b,e]	1σ[f]
Core: AT26-19-09PC (continued)											
5	7	8cmA	0.575	1177	12	1.91	0.08	1164	47	3.12	1.22
5	23	24cmA	0.508	1181	12	1.07	0.04	1174	47	1.75	0.68
5	47	48cmA	0.569	1072	11	1.04	0.04	1066	43	1.53	0.60
5	87	88cmA	1.003	391	4	1.75	0.07	387	15	0.95	0.37
5	111	112cmA	0.509	987	10	0.39	0.02	985	39	0.51	0.20
5	111	112cmB	0.498	927	9	0.49	0.02	925	37	0.62	0.24
5	127	128cmB	0.537	1619	16	0.25	0.01	1617	65	0.54	0.21
5	127	128cmA	0.539	1741	17	0.18	0.01	1739	70	0.40	0.15
6	1	2cmA	0.509	603	6	3.39	0.14	591	24	2.85	1.11
6	9	10cmB	0.525	552	6	1.38	0.06	548	22	1.05	0.41
6	9	10cmA	0.511	553	6	2.88	0.12	544	22	2.22	0.87
6	17	18cmA	0.403	698	7	1.68	0.07	691	28	1.62	0.63
6	25	26cmA	0.459	721	7	1.69	0.07	714	29	1.69	0.66
6	25	26cmB	0.453	764	8	4.54	0.18	744	30	4.84	1.89
6	29	30cmA	0.484	678	7	1.22	0.05	673	27	1.14	0.44
6	29	30cmB	0.495	671	7	1.49	0.06	665	27	1.39	0.54
6	33	34cmA	0.489	605	6	1.37	0.05	600	24	1.15	0.45
6	33	34cmB	0.522	641	6	1.71	0.07	635	25	1.52	0.59
6	37	38cmA	0.510	648	6	1.54	0.06	642	26	1.38	0.54
6	41	42cmA	0.532	668	7	0.76	0.03	665	27	0.70	0.27
6	41	42cmB	0.533	631	6	0.84	0.03	628	25	0.73	0.29
6	45	46cmA	0.493	551	6	0.86	0.03	548	22	0.65	0.25
6	53	54cmA	0.521	731	7	1.20	0.05	726	29	1.21	0.47
6	53	54cmB	0.521	719	7	1.10	0.04	715	29	1.09	0.43
6	57	58cmB	0.506	696	7	0.92	0.04	693	28	0.89	0.35
6	57	58cmA	0.514	696	7	1.10	0.04	692	28	1.06	0.41
6	61	62cmA	0.517	583	6	2.68	0.11	574	23	2.18	0.85
6	65	66cmA	0.493	551	6	0.94	0.04	548	22	0.71	0.28
6	69	70cmA	0.500	492	5	2.01	0.08	486	19	1.37	0.54
6	69	70cmB	0.502	580	6	8.34	0.33	552	22	6.75	2.63
6	77	78cmA	0.499	621	6	7.19	0.29	595	24	6.23	2.43
6	77	78cmB	0.510	217	2	1.61	0.06	215	9	0.49	0.19
6	85	86cmA	0.496	511	5	2.58	0.10	503	20	1.84	0.72
6	89	90cmA	0.497	450	5	2.93	0.12	443	18	1.84	0.72
6	89	90cmB	0.495	479	5	2.48	0.10	472	19	1.65	0.64
6	93	94cmA	0.510	280	3	2.19	0.09	277	11	0.85	0.33
6	93	94cmB	0.515	231	2	2.67	0.11	227	9	0.86	0.33
6	97	98cmA	0.499	166	2	2.14	0.09	164	7	0.49	0.19

Table D.1 (continued): Helium analyses of individual sediment aliquots

Sample Interval (section:depths)[a]			Mass (g)	^{4}He total (ncc/g)[b]	1σ[c]	^{3}He/^{4}He (R_A)[d]	1σ[c]	^{4}He$_{terr}$ (ncc/g)[b,e]	1σ[f]	^{3}He$_{ET}$ (pcc/g)[b,e]	1σ[f]
Core: AT26-19-09PC (continued)											
6	101	102cmA	0.517	197	2	2.63	0.11	194	8	0.72	0.28
6	101	102cmB	0.508	204	2	1.74	0.07	202	8	0.49	0.19
6	109	110cmA	0.513	237	2	1.39	0.06	235	9	0.45	0.18
6	117	118cmB	0.504	390	4	1.53	0.06	386	15	0.83	0.32
6	117	118cmA	0.517	381	4	1.09	0.04	379	15	0.57	0.22
6	125	126cmA	0.509	403	4	0.54	0.02	402	16	0.30	0.12
6	129	130cmA	1.046	435	4	0.68	0.03	433	17	0.41	0.16
6	133	134cmB	0.526	391	4	0.83	0.03	389	16	0.45	0.17
6	133	134cmA	0.527	376	4	0.66	0.03	375	15	0.34	0.13
Core: AT26-19-12TC											
2	52	53cmA	0.414	641	6	3.10	0.12	630	25	2.77	1.08
2	52	53cmB	0.504	651	7	4.25	0.17	635	25	3.86	1.50
2	56	57cmA	0.503	564	6	1.22	0.05	560	22	0.95	0.37
2	56	57cmB	0.507	561	6	1.72	0.07	556	22	1.34	0.52
2	60	61cmA	0.504	537	5	2.77	0.11	528	21	2.07	0.81
2	60	61cmB	0.503	546	5	2.60	0.10	538	22	1.97	0.77
2	64	65cmA	0.505	819	8	1.68	0.07	811	32	1.91	0.75
2	64	65cmB	0.502	831	8	2.38	0.10	819	33	2.75	1.07
2	68	69cmA	0.509	434	4	0.93	0.04	431	17	0.55	0.22
2	68	69cmB	0.505	444	4	2.17	0.09	438	18	1.34	0.52
Core: AT26-19-12PC											
1	43	44cmA	0.507	627	6	1.28	0.05	622	25	1.11	0.43
1	45	46cmA	0.503	781	8	1.54	0.06	774	31	1.67	0.65
1	47	48cmA	0.494	690	7	1.39	0.06	684	27	1.33	0.52
1	47	48cmB	0.503	704	7	1.41	0.06	698	28	1.38	0.54
1	49	50cmB	0.503	587	6	1.28	0.05	582	23	1.04	0.40
1	51	52cmA	0.505	393	4	2.18	0.09	388	16	1.19	0.46
1	51	52cmB	0.506	387	4	1.17	0.05	385	15	0.63	0.24
1	53	54cmA	0.503	315	3	1.77	0.07	311	12	0.77	0.30
1	55	56cmA	0.505	294	3	1.49	0.06	291	12	0.61	0.24
1	55	56cmB	0.506	291	3	2.14	0.09	287	11	0.86	0.34
1	57	58cmA	0.510	314	3	1.19	0.05	312	12	0.52	0.20
1	59	60cmB	0.506	312	3	1.45	0.06	310	12	0.63	0.24
1	61	62cmA	0.502	341	3	1.49	0.06	338	14	0.70	0.27
1	63	64cmB	0.504	323	3	3.09	0.12	317	13	1.39	0.54
1	65	66cmA	0.497	326	3	2.14	0.09	322	13	0.97	0.38
1	67	68cmA	0.505	408	4	0.85	0.03	406	16	0.48	0.19

Table D.1 (continued): Helium analyses of individual sediment aliquots

Sample Interval (section:depths)[a]			Mass (g)	^{4}He total (ncc/g)[b]	1σ[c]	^{3}He/^{4}He (R_A)[d]	1σ[c]	^{4}He$_{terr}$ (ncc/g)[b,e]	1σ[f]	^{3}He$_{ET}$ (pcc/g)[b,e]	1σ[f]
Core: AT26-19-12PC (continued)											
1	69	70cmA	0.502	401	4	1.55	0.06	397	16	0.86	0.34
1	69	70cmB	0.510	410	4	2.79	0.11	403	16	1.59	0.62
1	71	72cmA	0.507	453	5	4.30	0.17	441	18	2.71	1.06
1	73	74cmA	0.503	457	5	1.65	0.07	452	18	1.05	0.41
1	73	74cmB	0.503	464	5	3.48	0.14	454	18	2.25	0.88
1	75	76cmA	0.507	473	5	2.63	0.11	465	19	1.73	0.68
1	77	78cmA	0.502	453	5	0.92	0.04	451	18	0.57	0.22
1	77	78cmB	0.507	449	4	1.45	0.06	445	18	0.90	0.35
1	79	80cmA	0.506	461	5	0.87	0.03	459	18	0.55	0.22
1	79	80cmB	0.502	697	7	1.61	0.06	690	28	1.56	0.61
1	81	82cmA	0.507	490	5	1.12	0.04	487	19	0.76	0.30
1	81	82cmB	0.502	465	5	1.11	0.04	462	18	0.71	0.28
1	83	84cmA	0.508	493	5	0.90	0.04	490	20	0.61	0.24
1	85	86cmA	0.501	509	5	0.96	0.04	506	20	0.67	0.26
1	85	86cmB	0.504	509	5	0.92	0.04	506	20	0.64	0.25
1	87	88cmA	0.503	501	5	1.87	0.07	496	20	1.30	0.51
1	87	88cmB	0.509	486	5	1.31	0.05	482	19	0.88	0.34
1	89	90cmB	0.506	506	5	1.10	0.04	503	20	0.77	0.30
1	91	92cmA	0.508	532	5	1.15	0.05	528	21	0.85	0.33
1	91	92cmB	0.508	517	5	1.18	0.05	514	21	0.85	0.33
1	93	94cmA	0.506	525	5	1.45	0.06	521	21	1.05	0.41
1	95	96cmA	0.507	449	4	1.48	0.06	445	18	0.92	0.36
1	95	96cmB	0.509	451	5	5.06	0.20	438	18	3.18	1.24
1	95	96cmA	0.507	449	4	1.48	0.06	445	18	0.92	0.36
1	97	98cmA	0.501	538	5	2.71	0.11	530	21	2.03	0.79
1	99	100cmA	0.497	626	6	1.70	0.07	620	25	1.48	0.58
1	101	102cmA	0.503	600	6	2.06	0.08	593	24	1.72	0.67
1	101	102cmB	0.509	612	6	2.14	0.09	604	24	1.82	0.71
1	103	104cmB	0.506	693	7	1.28	0.05	688	28	1.23	0.48
1	105	106cmA	0.503	794	8	1.16	0.05	789	32	1.27	0.49
1	107	108cmA	0.506	877	9	1.11	0.04	871	35	1.35	0.53
1	107	108cmB	0.505	898	9	2.31	0.09	886	35	2.89	1.13
1	109	110cmA	0.497	884	9	1.95	0.08	874	35	2.40	0.94
1	111	112cmA	0.503	919	9	2.11	0.08	908	36	2.69	1.05
1	113	114cmA	0.504	862	9	3.73	0.15	844	34	4.48	1.75
1	113	114cmB	0.505	827	8	1.34	0.05	821	33	1.53	0.60
1	115	116cmA	0.502	810	8	1.09	0.04	805	32	1.22	0.48
1	117	118cmA	0.504	872	9	5.57	0.22	844	34	6.78	2.65
1	117	118cmB	0.503	793	8	1.09	0.04	788	32	1.20	0.47
1	124	125cmA	0.508	1125	11	1.34	0.05	1116	45	2.08	0.81

Table D.1 (continued): Helium analyses of individual sediment aliquots

Sample Interval (section:depths)[a]			Mass (g)	^{4}He total (ncc/g)[b]	1σ[c]	^{3}He/^{4}He (R_A)[d]	1σ[c]	^{4}He$_{terr}$ (ncc/g)[b,e]	1σ[f]	^{3}He$_{ET}$ (pcc/g)[b,e]	1σ[f]
Core: AT26-19-12PC (continued)											
1	129	130cmA	0.506	936	9	4.85	0.19	910	36	6.33	2.47
1	133	134cmA	0.501	895	9	1.34	0.05	889	36	1.67	0.65
1	133	134cmB	0.503	905	9	1.36	0.05	897	36	1.71	0.67
1	137	138cmA	0.507	993	10	1.09	0.04	986	39	1.49	0.58
1	137	138cmB	0.508	1016	10	1.33	0.05	1008	40	1.87	0.73
1	145	146cmA	0.501	310	3	0.90	0.04	309	12	0.38	0.15
2	1	2cmA	0.505	406	4	1.00	0.04	404	16	0.56	0.22
2	1	2cmB	0.507	432	4	1.21	0.05	429	17	0.72	0.28
2	9	10cmA	0.498	716	7	1.02	0.04	712	28	1.01	0.39
2	9	10cmB	0.501	726	7	0.69	0.03	723	29	0.69	0.27
2	17	18cmA	0.505	1100	11	0.60	0.02	1096	44	0.90	0.35
2	17	18cmB	0.502	1105	11	0.58	0.02	1102	44	0.88	0.34
2	61	62cmA	0.496	1018	10	1.33	0.05	1010	40	1.88	0.73
2	69	70cmA	0.508	741	7	1.40	0.06	735	29	1.44	0.56
2	77	78cmA	0.504	524	5	5.85	0.23	506	20	4.28	1.67
2	77	78cmB	0.502	510	5	6.19	0.25	492	20	4.40	1.72
2	89	90cmA	0.501	516	5	2.54	0.10	508	20	1.83	0.71
2	89	90cmB	0.506	518	5	1.71	0.07	513	21	1.23	0.48
2	93	94cmA	0.508	531	5	1.71	0.07	526	21	1.26	0.49
2	97	98cmB	0.505	577	6	2.27	0.09	569	23	1.82	0.71
2	101	102cmA	0.501	731	7	10.80	0.43	685	27	11.03	4.30
2	101	102cmB	0.505	666	7	1.83	0.07	658	26	1.69	0.66
2	105	106cmA	0.503	544	5	13.53	0.54	501	20	10.29	4.01
2	109	110cmA	0.507	550	6	2.86	0.11	541	22	2.19	0.85
2	113	114cmA	0.504	508	5	1.83	0.07	503	20	1.29	0.50
2	113	114cmB	0.507	541	5	7.78	0.31	517	21	5.88	2.29
2	117	118cmA	0.509	536	5	2.29	0.09	529	21	1.71	0.67
2	121	122cmA	0.507	538	5	2.16	0.09	531	21	1.62	0.63
2	125	126cmA	0.507	564	6	2.31	0.09	556	22	1.81	0.71
2	125	126cmB	0.503	574	6	3.65	0.15	562	22	2.92	1.14
2	129	130cmA	0.502	605	6	1.27	0.05	600	24	1.06	0.41
2	129	130cmB	0.506	619	6	1.26	0.05	614	25	1.08	0.42
2	133	134cmA	0.501	645	6	1.07	0.04	641	26	0.95	0.37
2	133	134cmB	0.505	1081	11	1.39	0.06	1073	43	2.08	0.81
2	136	137cmA	0.505	617	6	2.29	0.09	609	24	1.96	0.77
2	137	138cmA	0.504	646	6	2.10	0.08	638	26	1.89	0.74
2	137	138cmB	0.509	635	6	1.56	0.06	629	25	1.37	0.54
2	139	140cmA	0.506	612	6	1.34	0.05	608	24	1.14	0.44
2	139	140cmB	0.510	630	6	1.67	0.07	624	25	1.46	0.57

Table D.1 (continued): Helium analyses of individual sediment aliquots

Sample Interval (section:depths)[a]			Mass (g)	^{4}He total (ncc/g)[b]	1σ[c]	^{3}He/^{4}He (R_A)[d]	1σ[c]	^{4}He$_{terr}$ (ncc/g)[b,e]	1σ[f]	^{3}He$_{ET}$ (pcc/g)[b,e]	1σ[f]
Core: AT26-19-12PC (continued)											
2	141	142cmA	0.503	648	6	1.35	0.05	643	26	1.21	0.47
2	142	143cmA	0.505	648	6	0.94	0.04	645	26	0.84	0.33
2	145	146cmA	0.503	526	5	1.85	0.07	520	21	1.35	0.53
2	145	146cmB	0.504	521	5	1.48	0.06	516	21	1.07	0.42
2	148	149cmA	0.501	478	5	1.96	0.08	473	19	1.30	0.51
2	149	150cmA	0.505	526	5	3.07	0.12	516	21	2.25	0.88
3	1	2cmA	0.503	484	5	1.39	0.06	481	19	0.93	0.36
3	1	2cmB	0.508	497	5	4.96	0.20	483	19	3.44	1.34
3	3	4cmA	0.510	499	5	3.08	0.12	490	20	2.14	0.83
3	5	6cmA	0.505	478	5	3.03	0.12	470	19	2.02	0.79
3	5	6cmB	0.507	513	5	2.04	0.08	507	20	1.46	0.57
3	7	8cmA	0.504	490	5	4.57	0.18	477	19	3.12	1.22
3	9	10cmA	0.504	511	5	5.69	0.23	494	20	4.06	1.58
3	9	10cmB	0.501	514	5	2.70	0.11	506	20	1.93	0.75
3	11	12cmA	0.501	502	5	2.00	0.08	496	20	1.40	0.54
3	13	14cmA	0.502	523	5	16.63	0.67	472	19	12.14	4.74
3	13	14cmB	0.505	466	5	2.17	0.09	460	18	1.41	0.55
3	15	16cmA	0.496	229	2	10.17	0.41	215	9	3.25	1.27
3	17	18cmA	0.505	535	5	2.41	0.10	528	21	1.80	0.70
3	19	20cmA	0.501	238	2	1.83	0.07	235	9	0.60	0.24
3	21	22cmA	0.491	603	6	1.81	0.07	597	24	1.51	0.59
3	21	22cmB	0.492	607	6	2.30	0.09	599	24	1.95	0.76
3	23	24cmA	0.501	254	3	1.95	0.08	251	10	0.69	0.27
3	23	24cmB	0.502	247	2	1.45	0.06	245	10	0.50	0.19
3	25	26cmA	0.501	338	3	1.27	0.05	336	13	0.60	0.23
3	27	28cmA	0.506	252	3	1.95	0.08	250	10	0.69	0.27
3	29	30cmA	0.504	288	3	2.39	0.10	284	11	0.96	0.37
3	29	30cmB	0.498	284	3	1.52	0.06	281	11	0.60	0.23
3	33	34cmA	0.501	354	4	1.24	0.05	351	14	0.61	0.24
3	37	38cmA	0.502	342	3	1.23	0.05	340	14	0.58	0.23
3	37	38cmB	0.506	346	3	0.98	0.04	344	14	0.47	0.18
3	41	42cmA	0.507	368	4	2.43	0.10	363	15	1.24	0.48
3	41	42cmB	0.503	357	4	1.58	0.06	354	14	0.78	0.31
3	45	46cmA	0.506	411	4	0.70	0.03	409	16	0.40	0.15
3	49	50cmA	0.509	422	4	0.60	0.02	420	17	0.34	0.13
3	53	54cmA	0.503	432	4	0.73	0.03	431	17	0.43	0.17
3	53	54cmB	0.501	433	4	1.11	0.04	430	17	0.66	0.26
3	57	58cmA	0.507	392	4	1.56	0.06	389	16	0.85	0.33

Table D.1 (continued): Helium analyses of individual sediment aliquots

Sample Interval (section:depths)[a]			Mass (g)	^{4}He total (ncc/g)[b]	1σ[c]	^{3}He/^{4}He (R_A)[d]	1σ[c]	^{4}He$_{terr}$ (ncc/g)[b,e]	1σ[f]	^{3}He$_{ET}$ (pcc/g)[b,e]	1σ[f]
Core: AT26-19-12PC (continued)											
3	61	62cmA	0.508	304	3	1.83	0.07	301	12	0.77	0.30
3	61	62cmB	0.505	305	3	1.61	0.06	302	12	0.68	0.27
3	65	66cmA	0.508	344	3	1.04	0.04	342	14	0.49	0.19
3	69	70cmA	0.504	279	3	1.65	0.07	277	11	0.64	0.25
3	69	70cmB	0.503	280	3	3.23	0.13	275	11	1.26	0.49
3	73	74cmA	0.504	359	4	1.01	0.04	357	14	0.50	0.19
3	77	78cmA	0.508	413	4	1.37	0.05	410	16	0.78	0.31
3	77	78cmB	0.508	419	4	1.68	0.07	415	17	0.98	0.38
3	81	82cmA	0.507	376	4	1.97	0.08	372	15	1.03	0.40
3	85	86cmA	0.504	259	3	1.11	0.04	257	10	0.40	0.16
3	85	86cmB	0.503	253	3	0.79	0.03	252	10	0.27	0.11
3	89	90cmA	0.506	229	2	1.51	0.06	227	9	0.48	0.19
3	93	94cmA	0.505	289	3	1.32	0.05	287	11	0.53	0.21
3	93	94cmB	0.508	284	3	1.94	0.08	281	11	0.76	0.30
3	97	98cmA	0.501	285	3	1.28	0.05	283	11	0.50	0.20
3	101	102cmA	0.508	290	3	2.59	0.10	286	11	1.04	0.41
3	105	106cmA	0.503	243	2	1.23	0.05	241	10	0.41	0.16
3	109	110cmA	0.508	398	4	14.72	0.59	364	15	8.19	3.19
3	113	114cmA	0.503	566	6	0.77	0.03	563	23	0.60	0.23
3	113	114cmB	0.502	551	6	2.02	0.08	545	22	1.55	0.60
3	117	118cmA	0.502	623	6	1.24	0.05	618	25	1.07	0.42
3	117	118cmB	0.510	630	6	3.34	0.13	617	25	2.93	1.14
3	121	122cmA	0.501	594	6	1.08	0.04	590	24	0.89	0.35
3	125	126cmA	0.503	645	6	0.75	0.03	642	26	0.66	0.26
3	125	126cmB	0.508	655	7	1.36	0.05	650	26	1.23	0.48
3	129	130cmA	0.502	735	7	1.09	0.04	730	29	1.10	0.43
3	129	130cmB	0.502	709	7	0.92	0.04	705	28	0.90	0.35
3	133	134cmA	0.511	753	8	1.01	0.04	748	30	1.05	0.41
3	135	136cmA	0.504	788	8	0.96	0.04	783	31	1.04	0.41
3	135	136cmB	0.501	780	8	0.89	0.04	776	31	0.96	0.37
3	137	138cmA	0.508	716	7	2.19	0.09	706	28	2.18	0.85
3	137	138cmB	0.507	723	7	1.23	0.05	718	29	1.23	0.48
3	139	140cmA	0.503	632	6	1.96	0.08	625	25	1.72	0.67
3	141	142cmA	0.507	558	6	1.46	0.06	553	22	1.13	0.44
3	141	142cmB	0.503	584	6	1.34	0.05	579	23	1.08	0.42
3	143	144cmA	0.507	247	2	0.98	0.04	246	10	0.33	0.13
3	143	144cmB	0.504	221	2	1.65	0.07	219	9	0.51	0.20
3	145	146cmA	0.503	107	1	2.90	0.12	105	4	0.43	0.17
3	145	146cmB	0.506	103	1	0.69	0.03	103	4	0.10	0.04
3	147	148cmA	0.509	103	1	0.49	0.02	102	4	0.07	0.03

Table D.1 (continued): Helium analyses of individual sediment aliquots

Sample Interval (section:depths)[a]			Mass (g)	^{4}He total (ncc/g)[b]	1σ[c]	^{3}He/^{4}He (R_A)[d]	1σ[c]	^{4}He$_{terr}$ (ncc/g)[b,e]	1σ[f]	^{3}He$_{ET}$ (pcc/g)[b,e]	1σ[f]
Core: AT26-19-12PC (continued)											
3	149	150cmA	0.504	96	1	0.59	0.02	96	4	0.08	0.03
4	1	2cmA	0.507	100	1	2.92	0.12	98	4	0.41	0.16
4	3	4cmA	0.508	95	1	2.72	0.11	93	4	0.36	0.14
4	5	6cmA	0.503	96	1	1.13	0.05	95	4	0.15	0.06
4	5	6cmB	0.509	91	1	1.66	0.07	90	4	0.21	0.08
4	7	8cmA	0.507	119	1	0.90	0.04	119	5	0.15	0.06
4	7	8cmB	0.507	115	1	0.80	0.03	115	5	0.13	0.05
4	10	11cmA	0.506	152	2	0.99	0.04	152	6	0.21	0.08
4star	12	13cmA	0.507	162	2	0.54	0.02	162	6	0.12	0.05
4star	12	13cmB	0.506	164	2	1.12	0.04	163	7	0.25	0.10
4	14	15cmA	0.506	181	2	5.39	0.22	175	7	1.36	0.53
4	14	15cmB	0.506	186	2	0.96	0.04	185	7	0.25	0.10
4star	14	15cmA	0.501	174	2	0.89	0.04	173	7	0.21	0.08
4star	16	17cmA	0.501	177	2	0.73	0.03	176	7	0.18	0.07
4star	16	17cmB	0.505	188	2	0.83	0.03	187	7	0.22	0.08
4	18	19cmA	0.506	185	2	1.58	0.06	183	7	0.41	0.16
4star	20	21cmA	0.507	186	2	0.72	0.03	185	7	0.18	0.07
4star	20	21cmB	0.505	209	2	1.19	0.05	207	8	0.34	0.13
4	22	23cmA	0.503	140	1	0.64	0.03	139	6	0.12	0.05
4	22	23cmB	0.507	141	1	0.43	0.02	141	6	0.08	0.03
4star	22	23cmA	0.501	140	1	0.76	0.03	140	6	0.15	0.06
4star	24	25cmA	0.505	129	1	0.97	0.04	128	5	0.17	0.07
4star	24	25cmB	0.500	136	1	0.66	0.03	135	5	0.12	0.05
4	26	27cmA	0.504	119	1	1.13	0.05	119	5	0.19	0.07
4star	28	29cmA	0.502	134	1	1.02	0.04	133	5	0.19	0.07
4star	28	29cmB	0.506	125	1	0.75	0.03	125	5	0.13	0.05
4	30	31cmA	0.508	150	2	0.64	0.03	150	6	0.13	0.05
4	30	31cmB	0.502	156	2	0.95	0.04	155	6	0.20	0.08
4star	30	31cmA	0.509	149	1	1.91	0.08	148	6	0.40	0.15
4star	32	33cmA	0.506	147	1	1.43	0.06	145	6	0.29	0.11
4star	32	33cmB	0.501	142	1	2.03	0.08	140	6	0.40	0.16
4	34	35cmA	0.510	153	2	0.76	0.03	153	6	0.16	0.06
4	34	35cmB	0.507	151	2	1.24	0.05	150	6	0.26	0.10
4star	36	37cmA	0.505	142	1	2.27	0.09	140	6	0.45	0.17
4star	36	37cmB	0.509	142	1	2.04	0.08	140	6	0.40	0.16
4	38	39cmA	0.505	145	1	1.33	0.05	144	6	0.27	0.10
4	38	39cmB	0.506	139	1	2.62	0.10	137	5	0.51	0.20
4star	38	39cmA	0.503	134	1	1.03	0.04	133	5	0.19	0.07

Table D.1 (continued): Helium analyses of individual sediment aliquots

Sample Interval (section:depths)[a]			Mass (g)	^{4}He total (ncc/g)[b]	1σ[c]	^{3}He/^{4}He (R_A)[d]	1σ[c]	^{4}He$_{terr}$ (ncc/g)[b,e]	1σ[f]	^{3}He$_{ET}$ (pcc/g)[b,e]	1σ[f]
Core: AT26-19-12PC (continued)											
4star	40	41cmA	0.509	140	1	1.43	0.06	139	6	0.28	0.11
4star	40	41cmB	0.505	134	1	1.26	0.05	133	5	0.23	0.09
4	42	43cmA	0.503	158	2	5.04	0.20	154	6	1.11	0.43
4	42	43cmB	0.504	157	2	2.52	0.10	154	6	0.55	0.21
4star	42	43cmA	0.502	150	1	2.37	0.09	148	6	0.49	0.19
4star	44	45cmA	0.507	137	1	2.27	0.09	135	5	0.43	0.17
4star	44	45cmA	0.504	141	1	2.20	0.09	140	6	0.43	0.17
4	46	47cmA	0.504	137	1	3.03	0.12	135	5	0.58	0.23
4	46	47cmB	0.506	135	1	2.49	0.10	133	5	0.47	0.18
4star	46	47cmA	0.508	140	1	1.60	0.06	139	6	0.31	0.12
4star	48	49cmA	0.504	161	2	1.28	0.05	160	6	0.29	0.11
4star	48	49cmB	0.502	164	2	1.84	0.07	163	7	0.42	0.16
4	50	51cmA	0.507	156	2	1.96	0.08	154	6	0.42	0.17
4	50	51cmB	0.509	156	2	4.04	0.16	153	6	0.88	0.34
4star	52	53cmA	0.501	161	2	1.77	0.07	159	6	0.40	0.15
4	54	55cmA	0.507	186	2	1.48	0.06	184	7	0.38	0.15
4star	56	57cmA	0.504	201	2	1.28	0.05	199	8	0.35	0.14
4star	56	57cmB	0.508	207	2	1.60	0.06	205	8	0.46	0.18
4	58	59cmA	0.512	273	3	1.51	0.06	271	11	0.57	0.22
4	58	59cmB	0.507	278	3	4.30	0.17	271	11	1.66	0.65
4star	60	61cmA	0.506	262	3	1.37	0.05	260	10	0.50	0.19
4	62	63cmA	0.503	258	3	2.76	0.11	254	10	0.99	0.39
4	62	63cmB	0.504	256	3	1.71	0.07	254	10	0.61	0.24
4star	62	63cmA	0.506	254	3	1.54	0.06	252	10	0.54	0.21
4star	64	65cmA	0.503	268	3	2.68	0.11	264	11	1.00	0.39
4star	64	65cmB	0.504	262	3	1.69	0.07	259	10	0.61	0.24
4	66	67cmA	0.506	200	2	1.90	0.08	197	8	0.53	0.21
4star	68	69cmA	0.503	193	2	4.87	0.19	188	8	1.31	0.51
4	70	71cmB	0.500	211	2	2.58	0.10	208	8	0.76	0.30
4star	70	71cmA	0.508	204	2	1.43	0.06	202	8	0.40	0.16
4star	72	73cmA	0.501	196	2	3.01	0.12	193	8	0.82	0.32
4star	72	73cmB	0.507	205	2	3.10	0.12	202	8	0.88	0.34
4	74	75cmA	0.504	222	2	1.79	0.07	219	9	0.55	0.21
4star	76	77cmA	0.508	227	2	1.32	0.05	225	9	0.42	0.16
4	78	79cmA	0.501	240	2	1.61	0.06	238	10	0.53	0.21
4star	80	81cmA	0.506	209	2	1.72	0.07	207	8	0.50	0.19
4	82	83cmA	0.507	269	3	1.74	0.07	266	11	0.65	0.25
4	82	83cmB	0.503	253	3	1.40	0.06	250	10	0.49	0.19
4star	84	85cmA	0.506	260	3	1.76	0.07	257	10	0.64	0.25

Table D.1 (continued): Helium analyses of individual sediment aliquots

Sample Interval (section:depths)[a]			Mass (g)	^{4}He total (ncc/g)[b]	1σ[c]	^{3}He/^{4}He (R_A)[d]	1σ[c]	^{4}He$_{terr}$ (ncc/g)[b,e]	1σ[f]	^{3}He$_{ET}$ (pcc/g)[b,e]	1σ[f]
Core: AT26-19-12PC (continued)											
4	86	87cmA	0.506	213	2	2.18	0.09	210	8	0.65	0.25
4	86	87cmB	0.504	204	2	2.73	0.11	201	8	0.78	0.30
4	90	91cmA	0.492	210	2	2.14	0.09	207	8	0.62	0.24
4	90	91cmB	0.505	217	2	2.04	0.08	214	9	0.62	0.24
4star	90	91cmA	0.501	213	2	4.78	0.19	207	8	1.42	0.55
4star	92	93cmA	0.505	221	2	3.14	0.13	217	9	0.97	0.38
4	94	95cmA	0.501	257	3	2.85	0.11	253	10	1.02	0.40
4star	96	97cmA	0.504	228	2	1.85	0.07	225	9	0.59	0.23
4star	96	97cmB	0.506	225	2	2.54	0.10	222	9	0.80	0.31

[a]A and B indicate separate aliquots of the same depth interval, 'star' samples of 12PC section 4 were not sieved.

[b] cc's refer to cm^3 of gas at standard temperature and pressure (STP) of 273K and 1 atm.

[c]1σ values reflect analytical uncertainty derived from the reproducibility of an 8.81 R_A internal standard.

[d]R_A is the ratio normalized to the atmospheric ^{3}He/^{4}He value of 1.39 x $10^{-6.}$

[e,]^{4}He$_{terr}$ and ^{3}He$_{ET}$ were calculated assuming two component mixing of IDP He (^{3}He/^{4}He = 170 R_A) and terrigenous He (^{3}He/^{4}He = 0.01 R_A), see Section 4.2

[f]1σ values are determined from the reproducibility of a population of 101 replicated samples, see Section 4.2.

Table D.2: Sample averaged helium isotope results

Sample Interval (section:depths)			Age (ka)	*n*[a]	Avg.[b] $^4He_{terr}$ (ncc/g)[c]	1σ[d]	Avg.[b] $^3He_{ET}$ (pcc/g)[c]	1σ[d]	Vertical Sed. Rain Rate[b,e] (g cm^{-2} ka^{-1})	1σ	$^3He_{ET}$/ $^{230}Th_{XS}$ (mcc/g)[b,f]	1σ
Core: AT26-19-09PC												
2	25	26cm	47	1	369	15	1.13	0.44	0.71	0.30	5.6	2.2
2	45	46cm	55	1	340	14	3.34	1.30	0.24	0.10	17.7	7.0
2	57	58cm	59	1	295	12	1.02	0.40	0.79	0.33	5.2	2.1
2	69	70cm	62	2	403	11	0.90	0.25	0.89	0.28	4.8	1.3
2	93	94cm	70	2	646	18	1.59	0.44	0.50	0.16	8.0	2.2
3	99	100cm	110	1	859	34	1.19	0.46	0.68	0.28	3.0	1.2
4	29	30cm	133	2	481	14	0.66	0.18	1.21	0.38	4.3	1.2
4	37	38cm	137	1	463	19	1.02	0.40	0.79	0.33	7.0	2.7
4	41	42cm	139	2	422	12	0.75	0.21	1.07	0.34	5.3	1.5
4	45	46cm	141	2	375	11	0.64	0.18	1.26	0.40	4.5	1.2
4	49	50cm	143	2	370	10	0.67	0.18	1.20	0.38	4.9	1.4
4	53	54cm	145	1	327	13	2.95	1.15	0.27	0.11	23.7	9.3
4	57	58cm	147	2	316	9	0.53	0.15	1.52	0.48	3.7	1.0
4	61	62cm	149	2	313	9	0.49	0.13	1.65	0.52	3.3	0.9
4	65	66cm	151	2	347	10	0.51	0.14	1.59	0.50	3.2	0.9
4	89	90cm	163	2	358	10	2.33	0.64	0.34	0.11	13.8	3.8
4	113	114cm	175	1	419	17	0.79	0.31	1.01	0.43	4.4	1.7
4	117	118cm	177	2	397	11	1.11	0.31	0.72	0.23	6.4	1.8
4	133	134cm	185	2	923	26	1.60	0.44	0.50	0.16	5.5	1.5
5	7	8cm	198	1	1164	47	3.12	1.22	0.26	0.11	7.1	2.8
5	23	24cm	206	1	1174	47	1.75	0.68	0.46	0.19	4.1	1.6
5	47	48cm	217	1	1066	43	1.53	0.60	0.52	0.22	4.5	1.8
5	87	88cm	258	1	387	15	0.95	0.37	0.85	0.36	5.6	2.2
5	111	112cm	272	2	955	27	0.56	0.16	1.42	0.45	4.4	1.3
6	1	2cm	288	1	591	24	2.85	1.11	0.28	0.12	11.2	4.5
6	9	10cm	300	2	546	15	1.64	0.45	0.49	0.16	5.2	1.5
6	17	18cm	310	1	691	28	1.62	0.63	0.49	0.21	5.1	2.0
6	25	26cm	321	2	729	21	3.26	0.90	0.25	0.08	7.8	2.3
6	29	30cm	326	2	669	19	1.26	0.35	0.64	0.20	3.9	1.1
6	33	34cm	331	2	618	17	1.34	0.37	0.60	0.19	4.3	1.2
6	37	38cm	336	1	642	26	1.38	0.54	0.58	0.25	6.4	2.6
6	41	42cm	341	2	646	18	0.71	0.20	1.12	0.36	4.0	1.2
6	45	46cm	347	1	548	22	0.65	0.25	1.23	0.52	4.4	1.9
6	53	54cm	358	2	720	20	1.15	0.32	0.70	0.22	5.9	1.8
6	57	58cm	363	2	692	20	0.97	0.27	0.82	0.26	4.6	1.4
6	61	62cm	369	1	574	23	2.18	0.85	0.37	0.16	10.6	4.3
6	65	66cm	375	1	548	22	0.71	0.28	1.12	0.47	3.4	1.5
6	69	70cm	380	2	519	15	4.06	1.12	0.20	0.06	17.8	5.8

Table D.2 (continued): Sample averaged helium isotope results

Sample Interval (section:depths)			Age (ka)	*n*[a]	Avg.[b] $^4He_{terr}$ (ncc/g)[c]	1σ[d]	Avg.[b] $^3He_{ET}$ (pcc/g)[c]	1σ[d]	Vertical Sed. Rain Rate[b,e] (g cm^{-2} ka^{-1})	1σ	$^3He_{ET}$/ $^{230}Th_{XS}$ (mcc/g)[b,f]	1σ
Core: AT26-19-09PC (continued)												
6	77	78cm	391	2	405	11	3.36	0.93	0.24	0.08	13.8	4.2
6	85	86cm	402	1	503	20	1.84	0.72	0.44	0.18	6.9	2.9
6	89	90cm	407	2	457	13	1.74	0.48	0.46	0.15	5.1	1.6
6	93	94cm	410	2	252	7	0.85	0.24	0.94	0.30	3.6	1.1
6	97	98cm	413	1	164	7	0.49	0.19	1.63	0.69	2.4	1.0
6	101	102cm	416	2	198	6	0.61	0.17	1.32	0.42	3.1	0.9
6	109	110cm	422	1	235	9	0.45	0.18	1.77	0.74	2.6	1.1
6	117	118cm	428	2	382	11	0.70	0.19	1.14	0.36	7.7	2.6
6	125	126cm	434	1	402	16	0.30	0.12	2.69	1.13	2.6	1.1
6	129	130cm	438	1	433	17	0.41	0.16	1.98	0.83	7.4	3.9
6	133	134cm	441	2	382	11	0.39	0.11	2.04	0.65	3.1	1.1
Core: AT26-19-12TC												
2	52	53cm	107	2	633	18	3.31	0.91	0.24	0.08	10.9	3.0
2	56	57cm	116	2	558	16	1.15	0.32	0.70	0.22	3.4	0.9
2	60	61cm	125	2	533	15	2.02	0.56	0.40	0.13	5.6	1.6
2	64	65cm	128	2	815	23	2.33	0.64	0.34	0.11	13.4	3.7
2	68	69cm	131	2	435	12	0.95	0.26	0.85	0.27	6.6	1.8
Core: AT26-19-12PC												
1	43	44cm	113	1	622	25	1.11	0.43	0.73	0.31	3.8	1.5
1	45	46cm	121	1	774	31	1.67	0.65	0.48	0.20	5.9	2.3
1	47	48cm	125	2	691	20	1.35	0.37	0.59	0.19	4.3	1.2
1	49	50cm	129	1	582	23	1.04	0.40	0.77	0.33	4.9	1.9
1	51	52cm	130	2	386	11	0.91	0.25	0.88	0.28	5.4	1.5
1	53	54cm	132	1	311	12	0.77	0.30	1.04	0.44	7.1	2.8
1	55	56cm	135	2	289	8	0.74	0.20	1.09	0.35	6.4	1.8
1	57	58cm	137	1	312	12	0.52	0.20	1.55	0.65	4.5	1.8
1	59	60cm	139	1	310	12	0.63	0.24	1.28	0.54	5.2	2.1
1	61	62cm	141	1	338	14	0.70	0.27	1.14	0.48	6.0	2.4
1	63	64cm	144	1	317	13	1.39	0.54	0.58	0.24	12.2	4.8
1	65	66cm	146	1	322	13	0.97	0.38	0.83	0.35	8.3	3.3
1	67	68cm	148	1	406	16	0.48	0.19	1.68	0.71	4.3	1.7
1	69	70cm	150	2	400	11	1.23	0.34	0.65	0.21	10.7	3.0
1	71	72cm	153	1	441	18	2.71	1.06	0.30	0.12	23.1	9.1
1	73	74cm	155	2	453	13	1.65	0.45	0.49	0.15	13.6	3.8
1	75	76cm	157	1	465	19	1.73	0.68	0.46	0.20	13.7	5.4
1	77	78cm	159	2	448	13	0.74	0.20	1.09	0.35	5.9	1.7
1	79	80cm	162	2	575	16	1.06	0.29	0.76	0.24	7.5	2.1
1	81	82cm	164	2	474	13	0.74	0.20	1.09	0.35	5.8	1.6
1	83	84cm	166	1	490	20	0.61	0.24	1.31	0.55	4.1	1.6

Table D.2 (continued): Sample averaged helium isotope results

Sample Interval (section:depths)			Age (ka)	*n*[a]	Avg.[b] $^4He_{terr}$ (ncc/g)[c]	1σ[d]	Avg.[b] $^3He_{ET}$ (pcc/g)[c]	1σ[d]	Vertical Sed. Rain Rate[b,e] (g cm^{-2} ka^{-1})	1σ	$^3He_{ET}$/ $^{230}Th_{XS}$ (mcc/g)[b,f]	1σ
Core: AT26-19-12PC (continued)												
1	85	86cm	168	2	506	14	0.66	0.18	1.22	0.39	4.3	1.2
1	87	88cm	171	2	489	14	1.09	0.30	0.74	0.23	7.2	2.0
1	89	90cm	173	1	503	20	0.77	0.30	1.04	0.44	4.9	1.9
1	91	92cm	175	2	521	15	0.85	0.23	0.95	0.30	4.6	1.3
1	93	94cm	177	1	521	21	1.05	0.41	0.76	0.32	6.5	2.6
1	95	96cm	178	2	441	12	2.05	0.57	0.39	0.12	9.8	2.7
1	97	98cm	179	1	530	21	2.03	0.79	0.39	0.17	9.8	3.9
1	99	100cm	179	1	620	25	1.48	0.58	0.54	0.23	6.1	2.4
1	101	102cm	181	2	599	17	1.77	0.49	0.45	0.14	7.8	2.2
1	103	104cm	182	1	688	28	1.23	0.48	0.65	0.28	4.9	1.9
1	105	106cm	184	1	789	32	1.27	0.49	0.63	0.27	4.9	1.9
1	107	108cm	186	2	879	25	2.12	0.58	0.38	0.12	7.1	2.0
1	109	110cm	188	1	874	35	2.40	0.94	0.33	0.14	9.6	3.8
1	111	112cm	189	1	908	36	2.69	1.05	0.30	0.13	9.3	3.7
1	113	114cm	193	2	832	24	3.01	0.83	0.27	0.08	10.5	2.9
1	117	118cm	202	2	816	23	3.99	1.10	0.20	0.06	13.6	3.8
1	124	125cm	217	1	1116	45	2.08	0.81	0.39	0.16	7.1	2.8
1	129	130cm	228	1	910	36	6.33	2.47	0.13	0.05	25.5	10.1
1	133	134cm	237	2	893	25	1.69	0.47	0.48	0.15	5.7	1.6
1	137	138cm	245	2	997	28	1.68	0.46	0.48	0.15	7.9	2.2
1	145	146cm	255	1	309	12	0.38	0.15	2.09	0.88	4.7	1.9
2	1	2cm	261	2	417	12	0.64	0.18	1.25	0.40	7.8	2.3
2	9	10cm	268	2	717	20	0.85	0.23	0.95	0.30	8.8	2.6
2	17	18cm	272	2	1099	31	0.89	0.25	0.90	0.29	8.2	2.4
2	61	62cm	273	1	1010	40	1.88	0.73	0.43	0.18	10.1	4.1
2	69	70cm	283	1	735	29	1.44	0.56	0.56	0.24	6.5	2.6
2	77	78cm	291	2	499	14	4.34	1.20	0.18	0.06	20.2	5.9
2	89	90cm	299	2	511	14	1.53	0.42	0.53	0.17	7.7	2.2
2	93	94cm	301	1	526	21	1.26	0.49	0.64	0.27	8.7	3.5
2	97	98cm	304	1	569	23	1.82	0.71	0.44	0.19	8.5	3.4
2	101	102cm	306	2	672	19	6.36	1.75	0.13	0.04	32.2	9.7
2	105	106cm	309	1	501	20	10.29	4.01	0.08	0.03	48.0	19.3
2	109	110cm	313	1	541	22	2.19	0.85	0.37	0.15	14.6	6.0
2	113	114cm	318	2	510	14	3.59	0.99	0.22	0.07	16.6	4.9
2	117	118cm	322	1	529	21	1.71	0.67	0.47	0.20	9.8	4.0
2	121	122cm	327	1	531	21	1.62	0.63	0.50	0.21	9.7	4.0
2	125	126cm	332	2	559	16	2.37	0.65	0.34	0.11	16.0	5.1
2	129	130cm	337	2	607	17	1.07	0.29	0.75	0.24	11.1	3.7
2	133	134cm	343	2	857	24	1.52	0.42	0.53	0.17	20.3	7.3
2	136	137cm	348	1	609	24	1.96	0.77	0.41	0.17	26.3	11.9
2	137	138cm	350	2	634	18	1.63	0.45	0.49	0.16	19.3	6.2

Table D.2 (continued): Sample averaged helium isotope results

Sample Interval (section:depths)			Age (ka)	n[a]	Avg.[b] $^4He_{terr}$ (ncc/g)[c]	1σ[d]	Avg.[b] $^3He_{ET}$ (pcc/g)[c]	1σ[d]	Vertical Sed. Rain Rate[b,e] (g cm^{-2} ka^{-1})	1σ	$^3He_{ET}$/ $^{230}Th_{XS}$ (mcc/g)[b,f]	1σ
Core: AT26-19-12PC (continued)												
2	139	140cm	354	2	608	17	1.14	0.31	0.71	0.22	13.4	4.3
2	141	142cm	358	1	643	26	1.21	0.47	0.66	0.28	16.2	7.1
2	142	143cm	360	1	645	26	0.84	0.33	0.95	0.40	11.2	4.9
2	145	146cm	366	2	518	15	1.21	0.33	0.66	0.21	12.4	4.0
2	148	149cm	372	1	473	19	1.30	0.51	0.62	0.26	13.3	5.6
2	149	150cm	374	1	516	21	2.25	0.88	0.36	0.15	26.1	12.5
3	1	2cm	378	2	482	14	2.19	0.60	0.37	0.12	16.6	5.6
3	3	4cm	382	1	490	20	2.14	0.83	0.38	0.16	16.2	7.1
3	5	6cm	386	2	489	14	1.74	0.48	0.46	0.15	18.2	5.9
3	7	8cm	389	1	477	19	3.12	1.22	0.26	0.11	32.7	14.0
3	9	10cm	393	2	500	14	3.00	0.83	0.27	0.08	33.8	12.9
3	10	10.5cm	394	1	496	20	1.40	0.54	0.57	0.24	15.7	7.4
3	13	14cm	400	2	466	13	6.78	1.87	0.12	0.04	93.4	34.4
3	15	16cm	403	1	215	9	3.25	1.27	0.25	0.10	-	-
3	17	18cm	407	1	528	21	1.80	0.70	0.45	0.19	25.3	11.5
3	19	20cm	410	1	235	9	0.60	0.24	1.33	0.56	-	-
3	21	22cm	413	2	598	17	1.73	0.48	0.46	0.15	20.8	7.0
3	23	24cm	415	2	248	7	0.59	0.16	1.35	0.43	-	-
3	25	26cm	417	1	336	13	0.60	0.23	1.35	0.57	15.7	8.3
3	27	28cm	419	1	250	10	0.69	0.27	1.17	0.49	-	-
3	29	30cm	422	1	282	11	0.78	0.30	1.03	0.44	-	-
3	33	34cm	426	1	351	14	0.61	0.24	1.32	0.56	-	-
3	37	38cm	428	2	342	10	0.53	0.15	1.52	0.48	-	-
3	41	42cm	429	2	358	10	1.01	0.28	0.79	0.25	-	-
3	45	46cm	431	1	409	16	0.40	0.15	2.03	0.85	-	-
3	49	50cm	432	1	420	17	0.34	0.13	2.33	0.98	-	-
3	53	54cm	434	2	430	12	0.55	0.15	1.46	0.46	-	-
3	57	58cm	435	1	389	16	0.85	0.33	0.95	0.40	-	-
3	61	62cm	437	2	302	9	0.73	0.20	1.10	0.35	-	-
3	65	66cm	439	1	342	14	0.49	0.19	1.63	0.69	-	-
3	69	70cm	440	2	276	8	0.95	0.26	0.84	0.27	-	-
3	73	74cm	442	1	357	14	0.50	0.19	1.61	0.68	-	-
3	77	78cm	445	2	412	12	0.88	0.24	0.91	0.29	-	-
3	81	82cm	447	1	372	15	1.03	0.40	0.78	0.33	-	-
3	85	86cm	449	2	254	7	0.34	0.09	2.39	0.76	-	-
3	89	90cm	452	1	227	9	0.48	0.19	1.67	0.70	-	-
3	93	94cm	454	2	284	8	0.65	0.18	1.24	0.39	-	-
3	97	98cm	456	1	283	11	0.50	0.20	1.59	0.67	-	-
3	101	102cm	459	1	286	11	1.04	0.41	0.77	0.32	-	-
3	105	106cm	461	1	241	10	0.41	0.16	1.94	0.82	-	-
3	109	110cm	463	1	364	15	8.19	3.19	0.10	0.04	-	-

Table D.2 (continued): Sample averaged helium isotope results

Sample Interval (section:depths)			Age (ka)	*n*[a]	Avg.[b] $^4He_{terr}$ (ncc/g)[c]	1σ[d]	Avg.[b] $^3He_{ET}$ (pcc/g)[c]	1σ[d]	Vertical Sed. Rain Rate[b,e] (g cm^{-2} ka^{-1})	1σ	$^3He_{ET}$/ $^{230}Th_{XS}$ (mcc/g)[b,f]	1σ
Core: AT26-19-12PC (continued)												
3	113	114cm	466	2	554	16	1.07	0.30	0.75	0.24	-	-
3	117	118cm	468	2	618	17	2.00	0.55	0.40	0.13	-	-
3	121	122cm	470	1	590	24	0.89	0.35	0.90	0.38	-	-
3	125	126cm	473	2	646	18	0.94	0.26	0.85	0.27	-	-
3	129	130cm	475	2	718	20	1.00	0.28	0.80	0.25	-	-
3	133	134cm	478	1	748	30	1.05	0.41	0.77	0.32	-	-
3	135	136cm	480	2	780	22	1.00	0.28	0.80	0.25	-	-
3	137	138cm	483	2	712	20	1.71	0.47	0.47	0.15	-	-
3	139	140cm	486	1	625	25	1.72	0.67	0.47	0.20	-	-
3	141	142cm	490	2	566	16	1.10	0.30	0.73	0.23	-	-
3	142	143cm	492	2	232	7	0.42	0.12	1.91	0.61	-	-
3	145	146cm	497	2	104	3	0.27	0.07	3.02	0.96	-	-
4	1	2cm	512	1	98	4	0.41	0.16	1.97	0.83	-	-
4	3	4cm	515	1	93	4	0.36	0.14	2.24	0.95	-	-
4	5	6cm	519	2	93	3	0.18	0.05	4.46	1.41	-	-
4	7	8cm	522	2	117	3	0.14	0.04	5.82	1.85	-	-
4	10	11cm	527	1	152	6	0.21	0.08	3.87	1.63	-	-
4	12	13cm	529	2	162	5	0.19	0.05	4.31	1.37	-	-
4	14	15cm	531	2	180	5	0.80	0.22	1.00	0.32	-	-
4	16	17cm	533	2	182	5	0.20	0.05	4.09	1.30	-	-
4	18	19cm	535	1	183	7	0.41	0.16	1.97	0.83	-	-
4	20	21cm	537	2	196	6	0.26	0.07	3.06	0.97	-	-
4	22	23cm	539	3	140	3	0.12	0.03	6.86	1.88	-	-
4	24	25cm	542	2	132	4	0.15	0.04	5.43	1.72	-	-
4	26	27cm	544	1	119	5	0.19	0.07	4.33	1.82	-	-
4	28	29cm	546	2	129	4	0.16	0.04	5.06	1.61	-	-
4	30	31cm	548	3	151	3	0.24	0.05	3.29	0.90	-	-
4	32	33cm	550	2	143	4	0.35	0.10	2.32	0.74	-	-
4	34	35cm	552	2	151	4	0.21	0.06	3.83	1.21	-	-
4	36	37cm	554	2	140	4	0.43	0.12	1.89	0.60	-	-
4	38	39cm	556	3	138	3	0.32	0.07	2.49	0.68	-	-
4	40	41cm	557	2	136	4	0.26	0.07	3.14	1.00	-	-
4	42	43cm	561	3	152	4	0.72	0.16	1.12	0.31	-	-
4	44	45cm	564	2	137	4	0.43	0.12	1.85	0.59	-	-
4	46	47cm	567	3	136	3	0.45	0.10	1.77	0.49	-	-
4	48	49cm	570	2	161	5	0.35	0.10	2.27	0.72	-	-
4	50	51cm	573	2	153	4	0.65	0.18	1.23	0.39	-	-
4	52	53cm	576	1	159	6	0.40	0.15	2.03	0.85	-	-
4	54	55cm	580	1	184	7	0.38	0.15	2.10	0.89	-	-
4	56	57cm	583	2	202	6	0.41	0.11	1.97	0.63	-	-
4	58	59cm	586	2	271	8	1.12	0.31	0.72	0.23	-	-

Table D.2 (continued): Sample averaged helium isotope results

Sample Interval (section:depths)			Age (ka)	n[a]	Avg.[b] $^4He_{terr}$ (ncc/g)[c]	1σ[d]	Avg.[b] $^3He_{ET}$ (pcc/g)[c]	1σ[d]	Vertical Sed. Rain Rate[b,e] (g cm^{-2} ka^{-1})	1σ	$^3He_{ET}$/ $^{230}Th_{XS}$ (mcc/g)[b,f]	1σ
Core: AT26-19-12PC (continued)												
4	60	61cm	589	1	260	10	0.50	0.19	1.61	0.68	-	-
4	62	63cm	591	3	253	6	0.71	0.16	1.12	0.31	-	-
4	64	65cm	591	2	262	7	0.81	0.22	0.99	0.32	-	-
4	66	67cm	592	1	197	8	0.53	0.21	1.52	0.64	-	-
4	68	69cm	593	1	188	8	1.31	0.51	0.61	0.26	-	-
4	70	71cm	594	2	205	6	0.58	0.16	1.38	0.44	-	-
4	72	73cm	595	2	197	6	0.85	0.24	0.94	0.30	-	-
4	74	75cm	596	1	219	9	0.55	0.21	1.46	0.61	-	-
4	76	77cm	597	1	225	9	0.42	0.16	1.93	0.81	-	-
4	78	79cm	598	1	238	10	0.53	0.21	1.50	0.63	-	-
4	80	81cm	599	1	207	8	0.50	0.19	1.61	0.68	-	-
4	82	83cm	600	2	258	7	0.57	0.16	1.41	0.45	-	-
4	84	85cm	601	1	257	10	0.64	0.25	1.26	0.53	-	-
4	86	87cm	602	1	210	8	0.65	0.25	1.24	0.52	-	-
4	90	91cm	604	3	210	5	0.89	0.20	0.90	0.25	-	-
4	92	93cm	606	1	217	9	0.97	0.38	0.83	0.35	-	-
4	94	95cm	607	1	253	10	1.02	0.40	0.79	0.33	-	-
4	96	97cm	608	2	223	6	0.69	0.19	1.16	0.37	-	-

[a]*n* indicates the number of helium aliquots analyzed for each sediment interval.
[b]Values reflect average over the number of aliquots analyzed for each sample.
[c]cc's refer to cm^3 of gas at standard temperature and pressure (STP) of 273K and 1 atm.
[d]1σ values are determined from the reproducibility of a population of 101 replicated samples and the number of helium aliquots measured, see Section 4.2.
[e,]$^3He_{ET}$-derived vertical sediment rain rates were calculated assuming an $^3He_{ET}$ influx from space of 8.0 ± 1.2 x 10^{-13} cm^3 STP cm^{-2} ka^{-1} (McGee and Mukhopadhyay, 2013)
[f]where available, $^{230}Th_{XS}$ data from Costa and McManus (2017)

Table D.3: Combined-proxy 600 ka flux record of 12PC

	Constant flux proxy-derived			Elemental concentration data[c]					
Age[a]	Vertical sediment rain rate[b]			$CaCO_3$	Ti	Fe	Fe_{HT}[d]	Cu	Cu_{HT}[d]
(ka)	(g cm^{-2} ka^{-1})	1 σ	Proxy	(wt.%)	(wt.%)	(wt.%)	(wt.%)	(ppm)	(ppm)
22.5	1.36	0.01	$^{230}Th_{XS}$	62.7	0.164	2.22	0.30	78.5	64.8
24.1	1.31	0.01	$^{230}Th_{XS}$	63.5	0.173	2.24	0.23	82.2	67.8
25.7	1.20	0.01	$^{230}Th_{XS}$	61.8	0.166	2.28	0.34	76.9	63.1
26.4	1.04	0.01	$^{230}Th_{XS}$	61.7	0.169	2.29	0.32	83.3	69.2
27.3	1.27	0.01	$^{230}Th_{XS}$	61.0	0.173	2.33	0.31	89.1	74.7
28.9	0.77	0.01	$^{230}Th_{XS}$	60.8	0.184	2.42	0.27	89.8	74.5
30.5	1.02	0.01	$^{230}Th_{XS}$	60.2	0.186	2.49	0.32	101.9	86.4
32.1	1.06	0.01	$^{230}Th_{XS}$	59.8	0.184	2.53	0.39	94.3	79.0
35.3	1.00	0.01	$^{230}Th_{XS}$	59.9	0.177	2.46	0.40	89.3	74.6
38.5	0.88	0.01	$^{230}Th_{XS}$	59.8	0.165	2.37	0.45	84.1	70.3
41.7	0.87	0.01	$^{230}Th_{XS}$	59.9	0.163	2.35	0.45	91.3	77.7
43.3	0.86	0.01	$^{230}Th_{XS}$	59.0	0.168	2.42	0.46	86.1	72.1
44.9	0.79	0.01	$^{230}Th_{XS}$	58.9	0.174	2.42	0.39	89.3	74.8
47.6	0.82	0.01	$^{230}Th_{XS}$	59.5	0.170	2.38	0.40	86.4	72.2
48.1	0.79	0.01	$^{230}Th_{XS}$	60.4	0.163	2.35	0.45	93.4	79.8
51.3	0.77	0.01	$^{230}Th_{XS}$	61.5	0.154	2.26	0.47	96.2	83.4
54.5	0.76	0.01	$^{230}Th_{XS}$	60.2	0.142	2.36	0.69	109.4	97.5
55.8	0.75	0.01	$^{230}Th_{XS}$	59.8	0.149	2.23	0.50	119.9	107.4
56.4	0.76	0.01	$^{230}Th_{XS}$	60.5	0.145	2.25	0.56	148.7	136.6
58.3	0.77	0.01	$^{230}Th_{XS}$	59.2	0.137	2.18	0.57	50.0	38.5
58.9	0.84	0.01	$^{230}Th_{XS}$	62.3	0.134	2.11	0.55	86.7	75.6
60.8	0.87	0.01	$^{230}Th_{XS}$	60.9	0.142	2.32	0.66	100.3	88.4
61.4	0.92	0.01	$^{230}Th_{XS}$	59.8	0.150	2.37	0.62	88.1	75.6
63.3	0.89	0.01	$^{230}Th_{XS}$	61.0	0.143	2.31	0.63	58.2	46.3
64.6	1.01	0.01	$^{230}Th_{XS}$	59.8	0.152	2.45	0.68	82.2	69.6
65.8	0.86	0.01	$^{230}Th_{XS}$	42.8	0.234	3.68	0.94	134.7	115.2
66.9	0.96	0.01	$^{230}Th_{XS}$	49.3	0.216	3.25	0.72	121.8	103.7
68.9	0.53	0.01	$^{230}Th_{XS}$	44.8	0.221	3.45	0.88	113.6	95.2
69.9	0.75	0.01	$^{230}Th_{XS}$	45.3	0.214	3.42	0.92	115.0	97.1
72.7	0.77	0.01	$^{230}Th_{XS}$	45.6	0.194	3.45	1.18	129.4	113.2
73.6	0.89	0.01	$^{230}Th_{XS}$	45.6	0.197	3.46	1.16	126.8	110.3
75.5	0.67	0.01	$^{230}Th_{XS}$	44.6	0.206	3.64	1.24	146.5	129.4
77.4	0.88	0.01	$^{230}Th_{XS}$	44.8	0.213	3.70	1.22	166.7	149.0
78.4	0.68	0.01	$^{230}Th_{XS}$	47.2	0.203	3.57	1.21	177.9	161.1

Table D.3 (continued): Combined-proxy 600 ka flux record of 12PC

	Constant flux proxy-derived			Elemental concentration data[c]					
Age[a] (ka)	Vertical sediment rain rate[b] (g cm^{-2} ka^{-1})	1 σ	Proxy	$CaCO_3$ (wt.%)	Ti (wt.%)	Fe (wt.%)	Fe_{HT}[d] (wt.%)	Cu (ppm)	Cu_{HT}[d] (ppm)
81.2	0.77	0.01	$^{230}Th_{XS}$	49.2	0.197	3.42	1.13	163.2	146.8
85.6	0.73	0.01	$^{230}Th_{XS}$	44.9	0.213	3.76	1.27	120.5	102.8
89.3	0.71	0.01	$^{230}Th_{XS}$	41.4	0.209	3.84	1.40	92.5	75.1
91.9	0.66	0.01	$^{230}Th_{XS}$	38.6	0.221	4.04	1.47	84.4	66.0
94.6	0.63	0.01	$^{230}Th_{XS}$	35.4	0.238	4.41	1.63	80.8	60.9
97.2	0.62	0.01	$^{230}Th_{XS}$	32.4	0.270	4.71	1.56	70.3	47.8
99.8	0.54	0.01	$^{230}Th_{XS}$	28.0	0.291	4.98	1.58	74.5	50.2
106.6	0.24	0.08	$^{3}He_{ET}$	12.1	0.322	6.15	2.39	92.3	65.5
113.2	0.73	0.31	$^{3}He_{ET}$	24.4	0.243	4.44	1.61	88.1	67.9
115.7	0.70	0.22	$^{3}He_{ET}$	25.2	0.223	4.38	1.77	83.7	65.0
120.9	0.53	0.01	$^{230}Th_{XS}$	29.1	0.236	4.23	1.47	84.8	65.1
121.1	0.48	0.20	$^{3}He_{ET}$	29.1	0.236	4.23	1.47	84.8	65.1
124.9	0.40	0.13	$^{3}He_{ET}$	29.8	0.258	3.89	0.88	81.9	60.4
125.1	0.59	0.19	$^{3}He_{ET}$	33.3	0.251	3.74	0.81	81.6	60.6
127.8	0.34	0.11	$^{3}He_{ET}$	45.6	0.221	2.93	0.34	79.2	60.7
128.6	0.77	0.33	$^{3}He_{ET}$	34.3	0.270	3.79	0.64	96.4	74.0
130.5	0.88	0.28	$^{3}He_{ET}$	36.6	0.275	4.16	0.95	89.0	66.1
130.5	0.85	0.27	$^{3}He_{ET}$	36.6	0.275	4.16	0.95	89.0	66.1
132.3	1.36	0.03	$^{230}Th_{XS}$	60.9	0.169	2.77	0.80	56.7	42.6
132.4	1.04	0.44	$^{3}He_{ET}$	60.9	0.169	2.77	0.80	56.7	42.6
134.7	1.09	0.35	$^{3}He_{ET}$	64.4	0.160	2.50	0.63	59.9	46.5
136.9	1.55	0.65	$^{3}He_{ET}$	64.3	0.165	2.54	0.61	98.9	85.2
139.2	1.28	0.54	$^{3}He_{ET}$	63.4	0.162	2.44	0.55	116.4	102.9
141.4	1.14	0.48	$^{3}He_{ET}$	62.7	0.149	2.19	0.45	89.7	77.3
143.7	0.58	0.24	$^{3}He_{ET}$	62.6	0.156	2.19	0.38	76.0	63.0
145.9	0.83	0.35	$^{3}He_{ET}$	63.2	0.154	2.32	0.52	64.5	51.6
148.2	1.68	0.71	$^{3}He_{ET}$	63.0	0.181	2.52	0.40	80.3	65.2
150.4	0.65	0.21	$^{3}He_{ET}$	58.4	0.174	2.64	0.62	70.0	55.6
152.7	0.30	0.12	$^{3}He_{ET}$	57.1	0.181	2.70	0.58	79.0	63.8
154.9	0.49	0.15	$^{3}He_{ET}$	59.5	0.181	2.64	0.53	65.2	50.1
157.2	0.46	0.20	$^{3}He_{ET}$	56.7	0.202	2.95	0.59	82.1	65.3
159.4	1.09	0.35	$^{3}He_{ET}$	53.3	0.197	3.06	0.76	91.4	75.0
161.7	0.76	0.24	$^{3}He_{ET}$	55.5	0.204	3.01	0.63	86.4	69.4
164.0	1.09	0.35	$^{3}He_{ET}$	54.2	0.202	3.06	0.70	76.9	60.1

Table D.3 (continued): Combined-proxy 600 ka flux record of 12PC

	Constant flux proxy-derived			Elemental concentration data[c]					
Age[a] (ka)	Vertical sediment rain rate[b] (g cm^{-2} ka^{-1})	1 σ	Proxy	$CaCO_3$ (wt.%)	Ti (wt.%)	Fe (wt.%)	Fe_{HT}[d] (wt.%)	Cu (ppm)	Cu_{HT}[d] (ppm)
166.2	1.31	0.55	$^3He_{ET}$	56.6	0.199	3.01	0.69	79.3	62.8
168.5	1.22	0.39	$^3He_{ET}$	55.4	0.215	3.25	0.74	96.9	79.0
170.7	0.74	0.23	$^3He_{ET}$	51.6	0.222	3.43	0.85	100.7	82.2
173.0	1.04	0.44	$^3He_{ET}$	52.6	0.224	3.38	0.77	99.2	80.6
175.2	0.95	0.30	$^3He_{ET}$	47.7	0.234	3.68	0.95	103.8	84.3
176.6	0.76	0.32	$^3He_{ET}$	46.7	0.236	3.57	0.82	110.5	90.9
177.6	0.39	0.12	$^3He_{ET}$	53.2	0.216	3.10	0.58	84.9	66.9
178.5	0.39	0.17	$^3He_{ET}$	44.5	0.244	3.66	0.82	112.4	92.1
179.5	0.54	0.23	$^3He_{ET}$	39.8	0.258	3.90	0.89	109.8	88.3
180.8	0.45	0.14	$^3He_{ET}$	32.8	0.288	4.59	1.24	131.8	107.8
182.5	0.65	0.28	$^3He_{ET}$	35.1	0.291	4.40	1.01	128.3	104.1
184.2	0.63	0.27	$^3He_{ET}$	28.8	0.300	4.84	1.35	126.9	101.9
186.0	0.38	0.12	$^3He_{ET}$	13.0	0.367	6.21	1.93	151.6	121.1
187.7	0.33	0.14	$^3He_{ET}$	21.6	0.337	5.58	1.65	150.4	122.3
189.4	0.30	0.13	$^3He_{ET}$	21.6	0.330	5.46	1.61	138.4	110.9
193.0	0.27	0.08	$^3He_{ET}$	23.4	0.342	5.35	1.36	149.5	121.0
197.4	0.49	0.02	$^{230}Th_{XS}$	21.0	0.345	5.45	1.42	152.9	124.1
201.7	0.20	0.06	$^3He_{ET}$	20.5	0.354	5.66	1.53	153.0	123.5
206.1	0.45	0.02	$^{230}Th_{XS}$	19.8	0.343	5.58	1.57	147.0	118.4
210.4	0.46	0.02	$^{230}Th_{XS}$	15.8	0.356	5.85	1.69	168.6	138.9
214.8	0.38	0.01	$^{230}Th_{XS}$	7.4	0.386	6.45	1.95	168.1	136.0
216.9	0.39	0.16	$^3He_{ET}$	7.8	0.379	6.41	1.99	168.6	137.1
223.5	0.45	0.02	$^{230}Th_{XS}$	16.5	0.343	5.88	1.89	157.3	128.7
227.8	0.13	0.05	$^3He_{ET}$	21.7	0.273	4.99	1.81	144.2	121.5
232.2	0.39	0.01	$^{230}Th_{XS}$	14.8	0.315	5.66	1.98	147.0	120.7
236.5	0.48	0.15	$^3He_{ET}$	14.0	0.327	5.64	1.83	139.3	112.1
240.9	0.30	0.01	$^{230}Th_{XS}$	19.4	0.306	5.30	1.72	138.9	113.3
245.2	0.48	0.15	$^3He_{ET}$	26.2	0.296	5.03	1.58	134.5	109.9
251.2	0.92	0.05	$^{230}Th_{XS}$	49.0	0.241	3.42	0.61	107.4	87.3
253.0	0.84	0.04	$^{230}Th_{XS}$	66.1	0.126	2.29	0.83	68.0	57.6
254.8	2.09	0.88	$^3He_{ET}$	68.4	0.139	2.17	0.55	87.1	75.6
256.6	1.34	0.08	$^{230}Th_{XS}$	66.3	0.148	2.36	0.63	77.4	65.1
258.5	1.71	0.13	$^{230}Th_{XS}$	66.7	0.161	2.45	0.58	88.1	74.7
261.1	1.25	0.40	$^3He_{ET}$	65.2	0.164	2.45	0.54	73.3	59.7

Table D.3 (continued): Combined-proxy 600 ka flux record of 12PC

	Constant flux proxy-derived			Elemental concentration data[c]					
Age[a]	Vertical sediment rain rate[b]			$CaCO_3$	Ti	Fe	Fe_{HT}[d]	Cu	Cu_{HT}[d]
(ka)	(g cm^{-2} ka^{-1})	1 σ	Proxy	(wt.%)	(wt.%)	(wt.%)	(wt.%)	(ppm)	(ppm)
264.8	1.51	0.13	$^{230}Th_{XS}$	55.3	0.242	3.30	0.47	110.4	90.1
268.4	0.95	0.30	$^{3}He_{ET}$	54.6	0.257	3.29	0.29	103.1	81.6
271.9	1.37	0.16	$^{230}Th_{XS}$	38.5	0.305	4.25	0.69	121.0	95.6
273.5	0.80	0.09	$^{230}Th_{XS}$	5.4	0.383	6.51	2.04	139.1	107.1
275.7	0.90	0.29	$^{3}He_{ET}$	5.9	0.371	6.53	2.21	138.6	107.7
278.1	0.59	0.05	$^{230}Th_{XS}$	7.9	0.345	6.21	2.18	156.1	127.4
282.6	0.68	0.06	$^{230}Th_{XS}$	16.3	0.307	5.71	2.13	150.4	124.8
287.2	0.69	0.06	$^{230}Th_{XS}$	24.4	0.266	4.92	1.82	135.6	113.5
291.0	0.69	0.06	$^{230}Th_{XS}$	24.3	0.264	4.86	1.77	127.4	105.4
293.6	0.66	0.06	$^{230}Th_{XS}$	22.1	0.283	5.22	1.91	138.5	114.9
296.1	0.87	0.09	$^{230}Th_{XS}$	32.2	0.237	4.33	1.57	132.8	113.1
298.7	0.75	0.06	$^{230}Th_{XS}$	31.5	0.250	4.52	1.60	137.8	117.0
301.3	1.03	0.12	$^{230}Th_{XS}$	31.2	0.246	4.48	1.61	127.0	106.5
303.8	0.69	0.06	$^{230}Th_{XS}$	19.7	0.296	5.45	2.00	150.5	125.8
306.4	0.76	0.09	$^{230}Th_{XS}$	20.0	0.293	5.45	2.04	145.5	121.1
309.0	0.70	0.06	$^{230}Th_{XS}$	19.4	0.274	5.56	2.37	154.1	131.3
312.9	1.00	0.13	$^{230}Th_{XS}$	21.9	0.257	4.80	1.80	130.8	109.4
316.0	0.43	0.18	$^{3}He_{ET}$	30.1	0.228	4.81	2.15	123.3	104.3
323.3	0.56	0.24	$^{3}He_{ET}$	25.2	0.255	4.97	2.00	140.2	119.0
330.6	0.18	0.06	$^{3}He_{ET}$	29.2	0.257	4.88	1.88	131.8	110.4
341.6	0.53	0.17	$^{3}He_{ET}$	32.6	0.238	5.56	2.79	132.2	112.4
345.2	0.64	0.27	$^{3}He_{ET}$	36.9	0.252	4.46	1.53	125.9	104.9
348.9	0.44	0.19	$^{3}He_{ET}$	35.5	0.250	4.78	1.87	125.6	104.8
352.5	0.13	0.04	$^{3}He_{ET}$	35.3	0.259	4.30	1.28	119.4	97.8
356.2	0.08	0.03	$^{3}He_{ET}$	34.7	0.260	4.43	1.40	120.5	98.9
359.9	0.37	0.15	$^{3}He_{ET}$	34.8	0.264	4.34	1.25	119.7	97.6
363.5	0.22	0.07	$^{3}He_{ET}$	33.2	0.253	4.38	1.43	110.9	89.8
367.2	0.47	0.20	$^{3}He_{ET}$	32.9	0.247	4.39	1.51	127.6	107.1
370.8	0.50	0.21	$^{3}He_{ET}$	28.2	0.237	5.18	2.42	138.2	118.5
374.5	0.34	0.11	$^{3}He_{ET}$	33.0	0.267	4.74	1.62	130.2	108.0
378.1	0.37	0.12	$^{3}He_{ET}$	37.8	0.274	4.60	1.40	119.6	96.7
378.1	0.75	0.24	$^{3}He_{ET}$	37.8	0.274	4.60	1.40	119.6	96.7
381.8	0.53	0.17	$^{3}He_{ET}$	28.5	0.292	5.12	1.72	141.3	117.0
382.0	0.38	0.16	$^{3}He_{ET}$	28.5	0.292	5.12	1.72	141.3	117.0

Table D.3 (continued): Combined-proxy 600 ka flux record of 12PC

	Constant flux proxy-derived			Elemental concentration data[c]					
Age[a] (ka)	Vertical sediment rain rate[b] (g cm^{-2} ka^{-1})	1 σ	Proxy	$CaCO_3$ (wt.%)	Ti (wt.%)	Fe (wt.%)	Fe_{HT}[d] (wt.%)	Cu (ppm)	Cu_{HT}[d] (ppm)
384.5	0.41	0.17	$^3He_{ET}$	31.6	0.266	4.77	1.66	137.0	114.8
385.4	0.49	0.16	$^3He_{ET}$	31.9	0.265	4.76	1.67	131.8	109.7
385.9	0.46	0.15	$^3He_{ET}$	32.2	0.266	4.79	1.68	129.0	106.8
387.3	0.71	0.22	$^3He_{ET}$	31.3	0.268	4.91	1.78	133.7	111.3
389.1	0.66	0.28	$^3He_{ET}$	33.1	0.274	4.89	1.69	141.7	118.9
389.3	0.26	0.11	$^3He_{ET}$	33.1	0.274	4.89	1.69	141.7	118.9
390.0	0.95	0.40	$^3He_{ET}$	33.6	0.275	4.88	1.67	143.1	120.2
392.7	0.27	0.08	$^3He_{ET}$	31.5	0.274	5.03	1.83	134.7	111.9
392.8	0.66	0.21	$^3He_{ET}$	31.5	0.274	5.03	1.83	134.7	111.9
393.6	0.57	0.24	$^3He_{ET}$	30.9	0.281	5.01	1.73	142.6	119.2
395.5	0.62	0.26	$^3He_{ET}$	29.4	0.284	5.10	1.79	130.1	106.5
396.4	0.36	0.15	$^3He_{ET}$	28.4	0.282	5.14	1.85	141.2	117.7
399.6	0.12	0.04	$^3He_{ET}$	25.9	0.270	5.22	2.07	131.2	108.7
403.1	0.25	0.10	$^3He_{ET}$	32.0	0.253	5.00	2.05	139.8	118.8
406.5	0.45	0.19	$^3He_{ET}$	52.8	0.168	3.58	1.62	103.7	89.7
410.0	1.33	0.56	$^3He_{ET}$	49.9	0.162	3.62	1.73	106.6	93.1
412.9	0.46	0.15	$^3He_{ET}$	19.2	0.300	5.73	2.23	151.2	126.2
415.1	1.35	0.43	$^3He_{ET}$	54.4	0.181	3.66	1.54	106.6	91.5
417.2	1.35	0.57	$^3He_{ET}$	69.2	0.118	2.49	1.12	74.9	65.1
419.4	1.17	0.49	$^3He_{ET}$	69.0	0.133	2.50	0.95	82.3	71.2
421.5	1.03	0.44	$^3He_{ET}$	69.3	0.132	2.55	1.01	74.8	63.8
425.5	1.32	0.56	$^3He_{ET}$	68.0	0.147	2.63	0.92	83.1	70.9
427.7	1.52	0.48	$^3He_{ET}$	67.6	0.140	2.67	1.03	79.9	68.2
429.2	0.79	0.25	$^3He_{ET}$	59.9	0.186	3.11	0.93	81.8	66.3
430.8	2.03	0.85	$^3He_{ET}$	64.4	0.147	2.54	0.83	80.9	68.6
432.3	2.33	0.98	$^3He_{ET}$	65.4	0.152	2.61	0.83	70.3	57.6
433.9	1.46	0.46	$^3He_{ET}$	64.7	0.164	3.01	1.09	84.4	70.7
435.4	0.95	0.40	$^3He_{ET}$	57.9	0.188	3.21	1.01	89.5	73.8
437.0	1.10	0.35	$^3He_{ET}$	61.6	0.169	2.93	0.95	74.6	60.5
438.5	1.63	0.69	$^3He_{ET}$	63.8	0.160	2.78	0.91	71.4	58.0
440.1	0.84	0.27	$^3He_{ET}$	60.3	0.153	2.92	1.13	68.1	55.4
442.4	1.61	0.68	$^3He_{ET}$	57.2	0.162	3.11	1.22	70.2	56.7
444.7	0.91	0.29	$^3He_{ET}$	55.3	0.175	3.24	1.19	77.6	63.0
447.0	0.78	0.33	$^3He_{ET}$	55.3	0.190	3.21	0.99	88.7	72.8

Table D.3 (continued): Combined-proxy 600 ka flux record of 12PC

Age[a] (ka)	Constant flux proxy-derived Vertical sediment rain rate[b] (g cm^{-2} ka^{-1})	1 σ	Proxy	Elemental concentration data[c] $CaCO_3$ (wt.%)	Ti (wt.%)	Fe (wt.%)	Fe_{HT}[d] (wt.%)	Cu (ppm)	Cu_{HT}[d] (ppm)
449.3	2.39	0.76	$^3He_{ET}$	62.6	0.154	2.52	0.73	73.9	61.1
451.7	1.67	0.70	$^3He_{ET}$	68.0	0.124	2.09	0.64	68.6	58.2
454.0	1.24	0.39	$^3He_{ET}$	64.8	0.145	2.49	0.80	68.8	56.7
456.3	1.59	0.67	$^3He_{ET}$	62.2	0.163	2.74	0.84	69.9	56.4
458.6	0.77	0.32	$^3He_{ET}$	58.7	0.156	2.89	1.08	64.9	51.9
460.9	1.94	0.82	$^3He_{ET}$	59.1	0.165	2.98	1.05	65.3	51.5
463.3	0.10	0.04	$^3He_{ET}$	55.1	0.170	3.21	1.23	83.9	69.7
465.6	0.75	0.24	$^3He_{ET}$	41.5	0.223	4.22	1.62	105.7	87.1
467.9	0.40	0.13	$^3He_{ET}$	32.4	0.286	5.13	1.80	112.0	88.2
470.2	0.90	0.38	$^3He_{ET}$	29.6	0.295	5.43	1.99	128.6	104.0
472.6	0.85	0.27	$^3He_{ET}$	28.2	0.302	5.58	2.06	113.3	88.2
475.4	0.80	0.25	$^3He_{ET}$	27.4	0.291	5.55	2.15	132.9	108.6
478.2	0.77	0.32	$^3He_{ET}$	25.5	0.273	5.68	2.49	120.6	97.8
479.6	0.80	0.25	$^3He_{ET}$	23.7	0.287	6.11	2.77	133.6	109.7
482.7	0.47	0.15	$^3He_{ET}$	20.9	0.295	5.97	2.53	123.8	99.2
486.3	0.47	0.20	$^3He_{ET}$	31.5	0.253	5.14	2.18	117.7	96.6
489.9	0.73	0.23	$^3He_{ET}$	30.2	0.240	4.99	2.20	131.7	111.7
491.7	1.91	0.61	$^3He_{ET}$	33.2	0.248	4.91	2.02	122.6	102.0
497.1	3.02	0.96	$^3He_{ET}$	68.6	0.097	2.14	1.01	76.8	68.7
511.6	1.97	0.83	$^3He_{ET}$	67.4	0.116	2.44	1.08	100.1	90.4
515.2	2.24	0.95	$^3He_{ET}$	67.3	0.123	2.49	1.06	97.6	87.4
518.9	4.46	1.41	$^3He_{ET}$	64.2	0.083	1.52	0.55	66.3	59.3
522.5	5.82	1.85	$^3He_{ET}$	64.6	0.094	1.57	0.48	49.9	42.1
526.7	3.87	1.63	$^3He_{ET}$	57.9	0.118	2.22	0.84	72.4	62.6
528.8	4.31	1.37	$^3He_{ET}$	57.9	0.108	2.31	1.05	68.5	59.5
530.9	1.00	0.32	$^3He_{ET}$	60.3	0.106	2.28	1.04	52.0	43.1
533.1	4.09	1.30	$^3He_{ET}$	64.5	0.097	2.10	0.98	43.1	35.0
535.2	1.97	0.83	$^3He_{ET}$	69.8	0.083	1.41	0.44	35.0	28.1
537.3	3.06	0.97	$^3He_{ET}$	72.9	0.075	1.02	0.14	30.9	24.6
539.4	6.86	1.88	$^3He_{ET}$	74.6	0.080	0.82	-0.12	30.0	23.3
541.5	5.43	1.72	$^3He_{ET}$	74.6	0.077	0.90	0.01	31.8	25.4
543.7	4.33	1.82	$^3He_{ET}$	72.9	0.079	1.00	0.08	30.6	24.0
545.8	5.06	1.61	$^3He_{ET}$	72.0	0.088	1.07	0.05	38.1	30.8
547.9	3.29	0.90	$^3He_{ET}$	69.8	0.100	1.24	0.07	40.9	32.5

Table D.3 (continued): Combined-proxy 600 ka flux record of 12PC

	Constant flux proxy-derived			Elemental concentration data[c]					
Age[a] (ka)	Vertical sediment rain rate[b] (g cm^{-2} ka^{-1})	1 σ	Proxy	$CaCO_3$ (wt.%)	Ti (wt.%)	Fe (wt.%)	Fe_{HT}[d] (wt.%)	Cu (ppm)	Cu_{HT}[d] (ppm)
550.0	2.32	0.74	$^3He_{ET}$	69.5	0.091	1.18	0.12	43.9	36.4
552.2	3.83	1.21	$^3He_{ET}$	69.0	0.108	1.31	0.05	37.1	28.1
554.3	1.89	0.60	$^3He_{ET}$	68.0	0.115	1.34	-0.01	39.7	30.1
556.4	2.49	0.68	$^3He_{ET}$	65.1	0.128	1.39	-0.11	60.2	49.6
557.5	3.14	1.00	$^3He_{ET}$	62.7	0.148	1.68	-0.05	60.5	48.2
560.6	1.12	0.31	$^3He_{ET}$	52.5	0.246	2.94	0.07	83.5	63.0
563.6	1.85	0.59	$^3He_{ET}$	55.0	0.217	2.44	-0.10	78.7	60.6
566.8	1.77	0.49	$^3He_{ET}$	43.1	0.289	3.18	-0.19	81.2	57.1
570.0	2.27	0.72	$^3He_{ET}$	48.4	0.203	2.87	0.50	78.7	61.8
573.3	1.23	0.39	$^3He_{ET}$	52.6	0.226	3.35	0.71	85.7	66.9
576.5	2.03	0.85	$^3He_{ET}$	48.9	0.231	3.83	1.14	86.5	67.2
579.7	2.10	0.89	$^3He_{ET}$	44.2	0.235	4.04	1.30	86.4	66.8
582.9	1.97	0.63	$^3He_{ET}$	41.4	0.251	4.34	1.41	85.3	64.4
586.2	0.72	0.23	$^3He_{ET}$	38.1	0.268	4.85	1.73	96.1	73.8
589.4	1.61	0.68	$^3He_{ET}$	38.5	0.289	5.38	2.01	107.6	83.5
590.6	1.12	0.31	$^3He_{ET}$	39.1	0.246	5.43	2.56	93.9	73.5
591.3	0.99	0.32	$^3He_{ET}$	51.3	0.241	3.95	1.13	79.4	59.3
592.0	1.52	0.64	$^3He_{ET}$	51.7	0.268	3.74	0.61	87.8	65.4
592.7	0.61	0.26	$^3He_{ET}$	55.8	0.235	3.49	0.74	72.8	53.2
593.7	1.38	0.44	$^3He_{ET}$	56.8	0.223	3.21	0.60	83.5	64.9
594.8	0.94	0.30	$^3He_{ET}$	54.6	0.221	3.42	0.84	76.8	58.4
595.8	1.46	0.61	$^3He_{ET}$	50.5	0.248	3.59	0.70	92.2	71.6
596.9	1.93	0.81	$^3He_{ET}$	52.9	0.213	3.08	0.59	75.9	58.1
598.0	1.50	0.63	$^3He_{ET}$	49.0	0.281	3.67	0.39	77.6	54.2
599.1	1.61	0.68	$^3He_{ET}$	50.1	0.261	3.81	0.77	89.5	67.8
600.1	1.41	0.45	$^3He_{ET}$	40.0	0.301	4.55	1.04	106.1	81.1
601.2	1.26	0.53	$^3He_{ET}$	36.4	0.317	4.89	1.20	115.6	89.2
602.3	1.24	0.52	$^3He_{ET}$	39.1	0.294	4.36	0.93	115.1	90.6

Table D.3 (continued): Combined-proxy 600 ka flux record of 12PC

	Constant flux proxy-derived			Elemental concentration data[c]					
Age[a] (ka)	Vertical sediment rain rate[b] ($g\ cm^{-2}\ ka^{-1}$)	1 σ	Proxy	$CaCO_3$ (wt.%)	Ti (wt.%)	Fe (wt.%)	Fe_{HT}[d] (wt.%)	Cu (ppm)	Cu_{HT}[d] (ppm)
604.5	0.90	0.25	$^3He_{ET}$	35.2	0.259	4.45	1.43	111.2	89.6
605.5	0.83	0.35	$^3He_{ET}$	29.1	0.304	5.16	1.62	122.8	97.5
606.6	0.79	0.33	$^3He_{ET}$	27.9	0.281	4.89	1.61	120.7	97.3

[a]The 600 ka record includes samples from both 12PC and the simultaneously recovered trigger core 12TC

[b]Vertical sediment rain rates are calculated using $^{230}Th_{XS}$ (Costa and McManus, 2017) in samples for which $^3He_{ET}$ data (this study) is unavailable

[c]Concentrations reflect average values over the sampled interval as determined by x-ray fluorescence scanning (Costa and McManus, 2017; Costa et al., 2017)

[d]HT denotes the hydrothermal component of each element determined using a Ti-based lithogenic correction (see Section 4.2)

Table D.4: Combined-proxy 600 ka sediment component flux record of 12PC

	Sediment component fluxes[b]									
Age[a] (ka)	$CaCO_3$ (g cm^{-2} ka^{-1})	1 σ	non-$CaCO_3$ (g cm^{-2} ka^{-1})	1σ	Ti (mg cm^{-2} ka^{-1})	1 σ	Fe_{HT}[c] (mg cm^{-2} ka^{-1})	1 σ	Cu_{HT}[c] (µg cm^{-2} ka^{-1})	1 σ
22.5	0.851	0.007	0.505	0.004	2.23	0.02	4.09	0.04	87.8	0.8
24.1	0.830	0.007	0.478	0.004	2.26	0.02	3.00	0.03	88.7	0.8
25.7	0.741	0.006	0.458	0.004	1.99	0.02	4.12	0.04	75.7	0.6
26.4	0.638	0.006	0.397	0.004	1.75	0.02	3.28	0.03	71.6	0.6
27.3	0.776	0.007	0.495	0.004	2.20	0.02	3.93	0.03	94.9	0.8
28.9	0.469	0.004	0.302	0.002	1.42	0.01	2.10	0.02	57.5	0.5
30.5	0.614	0.006	0.406	0.004	1.90	0.02	3.23	0.03	88.1	0.8
32.1	0.636	0.006	0.427	0.004	1.96	0.02	4.13	0.04	84.0	0.8
35.3	0.600	0.006	0.401	0.004	1.77	0.02	4.02	0.04	74.7	0.7
38.5	0.526	0.005	0.353	0.003	1.45	0.01	3.92	0.04	61.8	0.6
41.7	0.518	0.005	0.347	0.003	1.41	0.01	3.91	0.04	67.2	0.6
43.3	0.509	0.005	0.354	0.003	1.45	0.01	3.99	0.04	62.2	0.6
44.9	0.465	0.004	0.324	0.003	1.37	0.01	3.05	0.03	59.1	0.6
47.6	0.487	0.005	0.331	0.003	1.39	0.01	3.29	0.03	59.0	0.6
48.1	0.474	0.005	0.311	0.003	1.28	0.01	3.51	0.03	62.7	0.6
51.3	0.476	0.005	0.298	0.003	1.19	0.01	3.60	0.03	64.6	0.6
54.5	0.455	0.004	0.300	0.003	1.08	0.01	5.25	0.05	73.7	0.7
55.8	0.448	0.004	0.301	0.003	1.12	0.01	3.72	0.04	80.5	0.8
56.4	0.461	0.005	0.301	0.003	1.11	0.01	4.23	0.04	104.0	1.1
58.3	0.454	0.005	0.312	0.003	1.05	0.01	4.40	0.05	29.5	0.3
58.9	0.525	0.006	0.317	0.003	1.13	0.01	4.59	0.05	63.6	0.7
60.8	0.528	0.006	0.339	0.004	1.23	0.01	5.74	0.06	76.7	0.8
61.4	0.552	0.006	0.371	0.004	1.38	0.02	5.69	0.06	69.7	0.8
63.3	0.545	0.006	0.349	0.004	1.28	0.01	5.65	0.07	41.4	0.5
64.6	0.602	0.007	0.404	0.005	1.53	0.02	6.85	0.08	70.1	0.8
65.8	0.369	0.005	0.494	0.006	2.02	0.03	8.16	0.10	99.5	1.2
66.9	0.471	0.006	0.485	0.007	2.07	0.03	6.90	0.09	99.1	1.3
68.9	0.238	0.002	0.293	0.003	1.17	0.01	4.66	0.05	50.5	0.5
69.9	0.339	0.004	0.409	0.005	1.60	0.02	6.92	0.08	72.6	0.8
72.7	0.353	0.004	0.420	0.005	1.50	0.02	9.11	0.11	87.5	1.0
73.6	0.406	0.006	0.485	0.007	1.76	0.02	10.29	0.14	98.3	1.3
75.5	0.298	0.004	0.370	0.005	1.37	0.02	8.31	0.10	86.5	1.1
77.4	0.394	0.005	0.485	0.007	1.87	0.03	10.69	0.14	130.9	1.8
78.4	0.322	0.004	0.360	0.005	1.38	0.02	8.23	0.11	109.9	1.4

Table D.4 (continued): Combined-proxy 600 ka sediment component flux record of 12PC

	Sediment component fluxes[b]									
Age[a] (ka)	$CaCO_3$ (g cm^{-2} ka^{-1})	1 σ	non-$CaCO_3$ (g cm^{-2} ka^{-1})	1σ	Ti (mg cm^{-2} ka^{-1})	1 σ	Fe_{HT}[c] (mg cm^{-2} ka^{-1})	1 σ	Cu_{HT}[c] (µg cm^{-2} ka^{-1})	1 σ
81.2	0.378	0.005	0.389	0.005	1.51	0.02	8.63	0.12	112.6	1.5
85.6	0.328	0.005	0.402	0.006	1.55	0.02	9.28	0.13	75.0	1.0
89.3	0.294	0.004	0.416	0.006	1.48	0.02	9.96	0.14	53.3	0.8
91.9	0.256	0.004	0.408	0.006	1.47	0.02	9.73	0.14	43.8	0.6
94.6	0.222	0.003	0.405	0.006	1.49	0.02	10.25	0.15	38.2	0.6
97.2	0.199	0.003	0.416	0.006	1.66	0.02	9.59	0.14	29.4	0.4
99.8	0.151	0.002	0.389	0.006	1.57	0.02	8.55	0.13	27.1	0.4
106.6	0.029	0.009	0.213	0.068	0.78	0.25	5.79	1.84	15.8	5.0
113.2	0.177	0.075	0.548	0.231	1.76	0.74	11.69	4.93	49.2	20.7
115.7	0.177	0.056	0.523	0.166	1.56	0.50	12.41	3.94	45.5	14.4
120.9	0.154	0.003	0.375	0.007	1.25	0.02	7.79	0.14	34.4	0.6
121.1	0.140	0.059	0.341	0.144	1.14	0.48	7.09	2.99	31.4	13.2
124.9	0.118	0.038	0.278	0.088	1.03	0.33	3.49	1.11	24.0	7.6
125.1	0.198	0.063	0.395	0.125	1.49	0.47	4.79	1.52	35.9	11.4
127.8	0.157	0.050	0.187	0.059	0.76	0.24	1.18	0.37	20.9	6.6
128.6	0.265	0.112	0.509	0.215	2.09	0.88	4.99	2.10	57.3	24.1
130.5	0.323	0.102	0.560	0.178	2.43	0.77	8.39	2.66	58.4	18.5
130.5	0.310	0.098	0.538	0.171	2.33	0.74	8.07	2.56	56.1	17.8
132.3	0.827	0.018	0.532	0.011	2.29	0.05	10.91	0.24	57.9	1.2
132.4	0.631	0.266	0.406	0.171	1.75	0.74	8.33	3.51	44.2	18.6
134.7	0.702	0.223	0.389	0.123	1.75	0.55	6.86	2.18	50.8	16.1
136.9	0.995	0.419	0.554	0.233	2.56	1.08	9.52	4.01	131.9	55.6
139.2	0.813	0.343	0.469	0.198	2.08	0.88	7.00	2.95	131.9	55.6
141.4	0.715	0.301	0.426	0.180	1.70	0.72	5.17	2.18	88.2	37.2
143.7	0.362	0.153	0.216	0.091	0.90	0.38	2.18	0.92	36.4	15.4
145.9	0.521	0.220	0.304	0.128	1.27	0.54	4.27	1.80	42.6	18.0
148.2	1.057	0.445	0.620	0.261	3.04	1.28	6.79	2.86	109.3	46.1
150.4	0.382	0.121	0.272	0.086	1.14	0.36	4.05	1.28	36.4	11.5
152.7	0.169	0.071	0.127	0.053	0.54	0.23	1.71	0.72	18.9	8.0
154.9	0.290	0.092	0.197	0.062	0.88	0.28	2.58	0.82	24.4	7.7
157.2	0.263	0.111	0.201	0.085	0.94	0.40	2.72	1.15	30.2	12.7
159.4	0.581	0.184	0.509	0.162	2.15	0.68	8.33	2.64	81.8	25.9
161.7	0.422	0.134	0.338	0.107	1.55	0.49	4.80	1.52	52.7	16.7
164.0	0.590	0.187	0.499	0.158	2.20	0.70	7.61	2.41	65.4	20.8

Table D.4 (continued): Combined-proxy 600 ka sediment component flux record of 12PC

	Sediment component fluxes[b]									
Age[a] (ka)	$CaCO_3$ (g cm^{-2} ka^{-1})	1 σ	non-$CaCO_3$ (g cm^{-2} ka^{-1})	1σ	Ti (mg cm^{-2} ka^{-1})	1 σ	Fe_{HT}[c] (mg cm^{-2} ka^{-1})	1 σ	Cu_{HT}[c] (µg cm^{-2} ka^{-1})	1 σ
166.2	0.740	0.312	0.567	0.239	2.60	1.09	9.04	3.81	82.0	34.6
168.5	0.674	0.214	0.544	0.172	2.62	0.83	9.01	2.86	96.2	30.5
170.7	0.380	0.120	0.356	0.113	1.63	0.52	6.24	1.98	60.5	19.2
173.0	0.549	0.232	0.495	0.209	2.34	0.99	8.08	3.41	84.2	35.5
175.2	0.452	0.143	0.495	0.157	2.22	0.70	9.03	2.87	79.8	25.3
176.6	0.356	0.150	0.406	0.171	1.80	0.76	6.24	2.63	69.3	29.2
177.6	0.208	0.066	0.183	0.058	0.85	0.27	2.26	0.72	26.1	8.3
178.5	0.176	0.074	0.219	0.092	0.96	0.41	3.25	1.37	36.4	15.3
179.5	0.216	0.091	0.326	0.137	1.40	0.59	4.82	2.03	47.8	20.2
180.8	0.148	0.047	0.304	0.097	1.30	0.41	5.60	1.78	48.8	15.5
182.5	0.230	0.097	0.425	0.179	1.90	0.80	6.58	2.78	68.1	28.7
184.2	0.182	0.077	0.450	0.190	1.89	0.80	8.51	3.59	64.5	27.2
186.0	0.049	0.016	0.330	0.105	1.39	0.44	7.33	2.32	45.9	14.6
187.7	0.072	0.030	0.262	0.110	1.13	0.47	5.51	2.32	40.9	17.2
189.4	0.065	0.027	0.234	0.099	0.99	0.42	4.80	2.03	33.1	13.9
193.0	0.063	0.020	0.204	0.065	0.91	0.29	3.64	1.16	32.3	10.2
197.4	0.102	0.003	0.384	0.013	1.68	0.06	6.90	0.23	60.3	2.0
201.7	0.041	0.013	0.160	0.051	0.71	0.23	3.07	0.97	24.8	7.9
206.1	0.089	0.003	0.359	0.012	1.54	0.05	7.03	0.24	53.0	1.8
210.4	0.073	0.003	0.391	0.015	1.65	0.06	7.85	0.30	64.4	2.4
214.8	0.028	0.001	0.349	0.012	1.45	0.05	7.35	0.26	51.2	1.8
216.9	0.030	0.013	0.355	0.150	1.46	0.61	7.66	3.23	52.8	22.3
223.5	0.075	0.003	0.378	0.015	1.55	0.06	8.55	0.35	58.3	2.4
227.8	0.028	0.012	0.099	0.042	0.35	0.15	2.29	0.97	15.4	6.5
232.2	0.057	0.002	0.328	0.013	1.21	0.05	7.61	0.30	46.5	1.8
236.5	0.067	0.021	0.409	0.130	1.55	0.49	8.68	2.75	53.3	16.9
240.9	0.058	0.002	0.241	0.009	0.92	0.03	5.16	0.19	33.9	1.3
245.2	0.125	0.040	0.353	0.112	1.42	0.45	7.54	2.39	52.5	16.6
251.2	0.449	0.026	0.467	0.027	2.21	0.13	5.58	0.33	80.0	4.7
253.0	0.556	0.028	0.285	0.014	1.06	0.05	6.95	0.35	48.4	2.4
254.8	1.429	0.603	0.660	0.278	2.90	1.22	11.42	4.81	157.9	66.5
256.6	0.889	0.051	0.451	0.026	1.99	0.11	8.40	0.48	87.2	5.0
258.5	1.142	0.084	0.570	0.042	2.75	0.20	9.86	0.72	127.9	9.4
261.1	0.815	0.259	0.436	0.138	2.05	0.65	6.77	2.15	74.7	23.7

Table D.4 (continued): Combined-proxy 600 ka sediment component flux record of 12PC

	Sediment component fluxes[b]									
Age[a] (ka)	$CaCO_3$ (g cm^{-2} ka^{-1})	1 σ	non-$CaCO_3$ (g cm^{-2} ka^{-1})	1σ	Ti (mg cm^{-2} ka^{-1})	1 σ	Fe_{HT}[c] (mg cm^{-2} ka^{-1})	1 σ	Cu_{HT}[c] (µg cm^{-2} ka^{-1})	1 σ
264.8	0.833	0.073	0.673	0.059	3.65	0.32	7.09	0.62	135.7	11.9
268.4	0.517	0.164	0.429	0.136	2.44	0.77	2.71	0.86	77.2	24.5
271.9	0.526	0.062	0.840	0.099	4.17	0.49	9.42	1.11	130.6	15.4
273.5	0.043	0.005	0.760	0.088	3.08	0.36	16.35	1.89	86.1	9.9
275.7	0.053	0.017	0.846	0.268	3.33	1.06	19.89	6.31	96.8	30.7
278.1	0.047	0.004	0.543	0.046	2.03	0.17	12.88	1.08	75.1	6.3
282.6	0.110	0.010	0.566	0.049	2.08	0.18	14.38	1.25	84.4	7.4
287.2	0.169	0.014	0.524	0.044	1.84	0.15	12.65	1.06	78.7	6.6
291.0	0.169	0.015	0.525	0.047	1.84	0.16	12.32	1.11	73.2	6.6
293.6	0.146	0.013	0.515	0.044	1.87	0.16	12.63	1.09	75.9	6.5
296.1	0.279	0.028	0.587	0.059	2.05	0.21	13.59	1.37	98.0	9.9
298.7	0.237	0.020	0.516	0.044	1.89	0.16	12.08	1.03	88.1	7.5
301.3	0.321	0.038	0.707	0.084	2.53	0.30	16.58	1.97	109.5	13.0
303.8	0.137	0.012	0.557	0.050	2.05	0.18	13.89	1.24	87.4	7.8
306.4	0.152	0.019	0.606	0.074	2.22	0.27	15.41	1.89	91.7	11.2
309.0	0.136	0.012	0.562	0.052	1.91	0.18	16.51	1.51	91.6	8.4
312.9	0.218	0.028	0.779	0.102	2.56	0.33	17.99	2.35	109.1	14.2
316.0	0.129	0.054	0.299	0.126	0.97	0.41	9.19	3.88	44.6	18.8
323.3	0.141	0.059	0.417	0.176	1.42	0.60	11.13	4.69	66.4	28.0
330.6	0.054	0.017	0.131	0.041	0.47	0.15	3.48	1.10	20.4	6.5
341.6	0.171	0.054	0.354	0.112	1.25	0.40	14.65	4.65	59.1	18.7
345.2	0.235	0.099	0.402	0.170	1.61	0.68	9.73	4.10	66.9	28.2
348.9	0.156	0.066	0.284	0.120	1.10	0.46	8.22	3.47	46.1	19.5
352.5	0.044	0.014	0.082	0.026	0.33	0.10	1.61	0.51	12.3	3.9
356.2	0.027	0.011	0.051	0.021	0.20	0.09	1.09	0.46	7.7	3.2
359.9	0.128	0.054	0.239	0.101	0.97	0.41	4.60	1.94	35.8	15.1
363.5	0.074	0.024	0.149	0.047	0.57	0.18	3.20	1.01	20.1	6.4
367.2	0.154	0.065	0.315	0.133	1.16	0.49	7.09	2.99	50.3	21.2
370.8	0.140	0.059	0.356	0.150	1.17	0.50	12.00	5.06	58.8	24.8
374.5	0.112	0.035	0.227	0.072	0.91	0.29	5.50	1.74	36.6	11.6
378.1	0.139	0.044	0.228	0.072	1.01	0.32	5.12	1.62	35.5	11.2
378.1	0.284	0.090	0.467	0.148	2.06	0.65	10.48	3.32	72.6	23.0
381.8	0.151	0.048	0.378	0.120	1.54	0.49	9.07	2.88	61.8	19.6
382.0	0.107	0.045	0.268	0.113	1.09	0.46	6.44	2.71	43.9	18.5

Table D.4 (continued): Combined-proxy 600 ka sediment component flux record of 12PC

	Sediment component fluxes[b]									
Age[a] (ka)	$CaCO_3$ (g cm^{-2} ka^{-1})	1 σ	non-$CaCO_3$ (g cm^{-2} ka^{-1})	1σ	Ti (mg cm^{-2} ka^{-1})	1 σ	Fe_{HT}[c] (mg cm^{-2} ka^{-1})	1 σ	Cu_{HT}[c] (µg cm^{-2} ka^{-1})	1 σ
384.5	0.129	0.054	0.280	0.118	1.09	0.46	6.79	2.86	46.9	19.8
385.4	0.157	0.050	0.335	0.106	1.30	0.41	8.22	2.61	54.0	17.1
385.9	0.149	0.047	0.313	0.099	1.23	0.39	7.78	2.47	49.3	15.7
387.3	0.221	0.070	0.485	0.154	1.90	0.60	12.58	3.99	78.6	24.9
389.1	0.219	0.092	0.442	0.186	1.81	0.76	11.19	4.72	78.6	33.1
389.3	0.085	0.036	0.172	0.072	0.70	0.30	4.35	1.83	30.5	12.9
390.0	0.320	0.135	0.633	0.267	2.62	1.11	15.95	6.73	114.6	48.3
392.7	0.084	0.027	0.184	0.058	0.73	0.23	4.89	1.55	30.0	9.5
392.8	0.209	0.066	0.455	0.144	1.82	0.58	12.11	3.84	74.2	23.5
393.6	0.177	0.075	0.397	0.167	1.61	0.68	9.92	4.18	68.5	28.9
395.5	0.181	0.076	0.435	0.183	1.75	0.74	11.03	4.65	65.6	27.7
396.4	0.101	0.043	0.255	0.108	1.00	0.42	6.60	2.78	42.0	17.7
399.6	0.031	0.010	0.088	0.028	0.32	0.10	2.46	0.78	12.9	4.1
403.1	0.079	0.033	0.168	0.071	0.62	0.26	5.06	2.13	29.3	12.3
406.5	0.235	0.099	0.211	0.089	0.75	0.32	7.23	3.05	40.0	16.9
410.0	0.662	0.279	0.664	0.280	2.15	0.91	22.93	9.67	123.4	52.0
412.9	0.089	0.028	0.375	0.119	1.39	0.44	10.35	3.28	58.5	18.6
415.1	0.737	0.234	0.617	0.196	2.45	0.78	20.90	6.63	123.9	39.3
417.2	0.930	0.392	0.415	0.175	1.59	0.67	15.00	6.32	87.5	36.9
419.4	0.808	0.340	0.363	0.153	1.56	0.66	11.07	4.67	83.3	35.1
421.5	0.716	0.302	0.317	0.134	1.36	0.57	10.46	4.41	66.0	27.8
425.5	0.898	0.379	0.423	0.178	1.94	0.82	12.15	5.12	93.6	39.5
427.7	1.030	0.327	0.493	0.157	2.14	0.68	15.68	4.97	103.9	33.0
429.2	0.474	0.150	0.318	0.101	1.47	0.47	7.39	2.35	52.5	16.6
430.8	1.305	0.550	0.723	0.305	2.98	1.26	16.82	7.09	139.2	58.7
432.3	1.523	0.642	0.804	0.339	3.55	1.50	19.39	8.17	134.1	56.5
433.9	0.947	0.300	0.517	0.164	2.41	0.76	15.97	5.07	103.5	32.8
435.4	0.548	0.231	0.398	0.168	1.78	0.75	9.54	4.02	69.8	29.4
437.0	0.678	0.215	0.422	0.134	1.86	0.59	10.48	3.32	66.6	21.1
438.5	1.040	0.438	0.590	0.249	2.61	1.10	14.85	6.26	94.6	39.9
440.1	0.509	0.161	0.335	0.106	1.29	0.41	9.56	3.03	46.7	14.8
442.4	0.922	0.389	0.689	0.290	2.62	1.10	19.59	8.26	91.3	38.5
444.7	0.505	0.160	0.407	0.129	1.60	0.51	10.90	3.46	57.5	18.2
447.0	0.431	0.182	0.348	0.147	1.48	0.63	7.69	3.24	56.7	23.9

Table D.4 (continued): Combined-proxy 600 ka sediment component flux record of 12PC

	Sediment component fluxes[b]									
Age[a] (ka)	$CaCO_3$ (g cm^{-2} ka^{-1})	1 σ	non-$CaCO_3$ (g cm^{-2} ka^{-1})	1σ	Ti (mg cm^{-2} ka^{-1})	1 σ	Fe_{HT}[c] (mg cm^{-2} ka^{-1})	1 σ	Cu_{HT}[c] (µg cm^{-2} ka^{-1})	1 σ
449.3	1.497	0.475	0.896	0.284	3.68	1.17	17.52	5.56	146.1	46.4
451.7	1.135	0.479	0.534	0.225	2.08	0.88	10.63	4.48	97.2	41.0
454.0	0.804	0.255	0.437	0.139	1.80	0.57	9.95	3.16	70.4	22.3
456.3	0.990	0.417	0.601	0.254	2.59	1.09	13.36	5.63	89.7	37.8
458.6	0.451	0.190	0.317	0.133	1.19	0.50	8.27	3.48	39.8	16.8
460.9	1.149	0.485	0.796	0.335	3.22	1.36	20.39	8.59	100.3	42.3
463.3	0.054	0.023	0.044	0.019	0.17	0.07	1.20	0.51	6.8	2.9
465.6	0.310	0.098	0.437	0.139	1.67	0.53	12.10	3.84	65.1	20.7
467.9	0.130	0.041	0.271	0.086	1.15	0.36	7.22	2.29	35.4	11.2
470.2	0.267	0.113	0.636	0.268	2.67	1.13	17.97	7.57	93.9	39.6
472.6	0.239	0.076	0.610	0.193	2.56	0.81	17.48	5.54	74.8	23.7
475.4	0.219	0.070	0.581	0.184	2.33	0.74	17.19	5.45	87.0	27.6
478.2	0.195	0.082	0.571	0.241	2.10	0.88	19.08	8.04	75.0	31.6
479.6	0.190	0.060	0.611	0.194	2.30	0.73	22.18	7.04	87.9	27.9
482.7	0.098	0.031	0.372	0.118	1.39	0.44	11.88	3.77	46.7	14.8
486.3	0.147	0.062	0.320	0.135	1.18	0.50	10.18	4.29	45.1	19.0
489.9	0.219	0.069	0.507	0.161	1.74	0.55	15.96	5.06	81.1	25.7
491.7	0.634	0.201	1.276	0.405	4.74	1.50	38.53	12.22	194.8	61.8
497.1	2.072	0.657	0.946	0.300	2.93	0.93	30.52	9.68	207.3	65.8
511.6	1.327	0.560	0.642	0.271	2.29	0.97	21.31	8.98	178.0	75.0
515.2	1.509	0.636	0.735	0.310	2.76	1.16	23.75	10.01	196.0	82.6
518.9	2.863	0.908	1.595	0.506	3.72	1.18	24.45	7.76	264.6	83.9
522.5	3.760	1.193	2.059	0.653	5.45	1.73	28.00	8.88	244.8	77.6
526.7	2.244	0.946	1.629	0.687	4.57	1.92	32.71	13.79	242.5	102.2
528.8	2.492	0.790	1.815	0.576	4.66	1.48	45.35	14.39	256.2	81.3
530.9	0.601	0.191	0.396	0.126	1.06	0.34	10.34	3.28	43.0	13.6
533.1	2.636	0.836	1.452	0.461	3.95	1.25	39.86	12.65	143.1	45.4
535.2	1.376	0.580	0.597	0.251	1.63	0.69	8.73	3.68	55.5	23.4
537.3	2.232	0.708	0.831	0.263	2.29	0.73	4.34	1.38	75.4	23.9
539.4	5.118	1.401	1.743	0.477	5.49	1.50	-7.95	-2.18	160.1	43.8
541.5	4.051	1.285	1.383	0.439	4.18	1.32	0.47	0.15	138.2	43.8
543.7	3.151	1.328	1.174	0.495	3.42	1.44	3.46	1.46	103.8	43.7
545.8	3.642	1.155	1.419	0.450	4.44	1.41	2.39	0.76	155.6	49.4
547.9	2.294	0.628	0.994	0.272	3.29	0.90	2.34	0.64	106.9	29.3

Table D.4 (continued): Combined-proxy 600 ka sediment component flux record of 12PC

	Sediment component fluxes[b]									
Age[a] (ka)	$CaCO_3$ (g cm^{-2} ka^{-1})	1 σ	non-$CaCO_3$ (g cm^{-2} ka^{-1})	1σ	Ti (mg cm^{-2} ka^{-1})	1 σ	Fe_{HT}[c] (mg cm^{-2} ka^{-1})	1 σ	Cu_{HT}[c] (µg cm^{-2} ka^{-1})	1 σ
550.0	1.613	0.512	0.707	0.224	2.10	0.67	2.89	0.92	84.4	26.8
552.2	2.641	0.838	1.189	0.377	4.13	1.31	1.93	0.61	107.7	34.2
554.3	1.282	0.407	0.603	0.191	2.18	0.69	-0.16	-0.05	56.7	18.0
556.4	1.622	0.444	0.871	0.238	3.19	0.87	-2.63	-0.72	123.6	33.8
557.5	1.972	0.626	1.172	0.372	4.66	1.48	-1.56	-0.49	151.5	48.1
560.6	0.586	0.160	0.531	0.145	2.75	0.75	0.81	0.22	70.3	19.2
563.6	1.020	0.323	0.835	0.265	4.03	1.28	-1.77	-0.56	112.3	35.6
566.8	0.765	0.209	1.009	0.276	5.12	1.40	-3.44	-0.94	101.3	27.7
570.0	1.097	0.348	1.171	0.371	4.59	1.46	11.45	3.63	140.2	44.5
573.3	0.646	0.205	0.583	0.185	2.77	0.88	8.74	2.77	82.2	26.1
576.5	0.991	0.418	1.035	0.436	4.67	1.97	23.07	9.73	136.2	57.4
579.7	0.930	0.392	1.175	0.496	4.94	2.08	27.37	11.54	140.6	59.3
582.9	0.815	0.259	1.157	0.367	4.95	1.57	27.82	8.83	127.0	40.3
586.2	0.273	0.087	0.444	0.141	1.92	0.61	12.38	3.93	52.9	16.8
589.4	0.618	0.260	0.989	0.417	4.65	1.96	32.26	13.60	134.1	56.5
590.6	0.440	0.120	0.685	0.188	2.77	0.76	28.80	7.88	82.6	22.6
591.3	0.509	0.162	0.484	0.154	2.40	0.76	11.26	3.57	59.0	18.7
592.0	0.788	0.332	0.735	0.310	4.09	1.72	9.28	3.91	99.6	42.0
592.7	0.340	0.144	0.270	0.114	1.44	0.61	4.52	1.91	32.5	13.7
593.7	0.784	0.249	0.596	0.189	3.08	0.98	8.30	2.63	89.5	28.4
594.8	0.514	0.163	0.426	0.135	2.08	0.66	7.91	2.51	54.9	17.4
595.8	0.736	0.310	0.720	0.303	3.60	1.52	10.24	4.31	104.2	43.9
596.9	1.022	0.431	0.910	0.384	4.12	1.74	11.41	4.81	112.3	47.3
598.0	0.735	0.310	0.766	0.323	4.22	1.78	5.80	2.45	81.3	34.3
599.1	0.804	0.339	0.802	0.338	4.18	1.76	12.36	5.21	108.9	45.9
600.1	0.563	0.179	0.844	0.268	4.23	1.34	14.60	4.63	114.0	36.2
601.2	0.459	0.194	0.803	0.339	4.00	1.69	15.13	6.38	112.6	47.5
602.3	0.486	0.205	0.756	0.319	3.65	1.54	11.59	4.89	112.5	47.4

Table D.4 (continued): Combined-proxy 600 ka sediment component flux record of 12PC

	Sediment component fluxes[b]									
Age[a] (ka)	**$CaCO_3$ (g cm^{-2} ka^{-1})**	**1 σ**	**non-$CaCO_3$ 1σ (g cm^{-2} ka^{-1})**		**Ti (mg cm^{-2} ka^{-1})**	**1 σ**	**Fe_{HT}[c] (mg cm^{-2} ka^{-1})**	**1 σ**	**Cu_{HT}[c] (µg cm^{-2} ka^{-1})**	**1 σ**
604.5	0.318	0.087	0.586	0.160	2.34	0.64	12.89	3.53	81.0	22.2
605.5	0.241	0.102	0.587	0.248	2.52	1.06	13.39	5.65	80.8	34.1
606.6	0.219	0.092	0.567	0.239	2.21	0.93	12.67	5.34	76.5	32.2

[a]The 600 ka record includes samples from both 12PC and the simultaneously recovered trigger core 12TC

[b]Vertical sediment rain rates are calculated using $^{230}Th_{XS}$ (Costa and McManus, 2017) in samples for which $^{3}He_{ET}$ data (this study) is unavailable

[c]HT denotes the hydrothermal component of each element determined using a Ti-based lithogenic correction (see Section 4.2)